

THE UNIVERSITY OF HULL

One-Dimensional, Mixed-Metal Sulphides – Structural
and Physical Properties

being a Thesis submitted for the Degree of PhD

in the University of Hull

by

Mark Robert Harrison MChem (Hons)

February 2011

Abstract

New one-dimensional sulphides based on Ba_2CoS_3 have been synthesised and their structural and electronic properties investigated. The starting point was the one-dimensional sulphide Ba_2CoS_3 , which shows one-dimensional anti-ferromagnetism, metallic-like behaviour and a small negative magnetoresistance. Cationic substitutions were carried out on both the barium and cobalt sites of Ba_2CoS_3 . The substitution of zinc for cobalt into Ba_2CoS_3 resulted in the formation of the series $\text{Ba}_2\text{Co}_{1-x}\text{Zn}_x\text{S}_3$ ($x = 0.0-1.0$). $\text{Ba}_2\text{Co}_{1-x}\text{Zn}_x\text{S}_3$ compounds maintain the one-dimensional structure but become paramagnetic and show semiconducting properties. Interestingly significant values of magnetoresistance (up to -25%) are found in the series. The origin of the magnetoresistance is currently unknown although it is suspected that there is some extrinsic contribution. The compound $\text{Ba}_2\text{Co}_{0.75}\text{Fe}_{0.25}\text{S}_3$ has also been successfully synthesised although attempts to form compounds with higher iron content were not successful. A large number of compounds in the series $\text{Ba}_2\text{Zn}_{1-x}\text{M}_x\text{S}_3$ ($M = \text{Fe}, \text{Mn}, \text{Cr}, \text{Ni}$) have also been synthesised and initial investigations into the properties of these materials show that again they exhibit negative magnetoresistance. Finally $\text{Ba}_{1.9}\text{K}_{0.1}\text{CoS}_3$ has been synthesised although no investigation into the properties has yet been carried out.

Acknowledgements

I wish to thank my supervisor, Dr M. Grazia Francesconi, for all of her help and support throughout my PhD.

I would like to acknowledge the collaborators Prof. Antoine Maignan and Dr Vincent Hardy at Laboratoire CRISMAT, ENSICAEN for the measurements of magnetic and physical properties and Dr Oleg Lebedev also at Laboratoire CRISMAT, ENSICAEN for TEM measurements. In addition, I would like to thank Dr Nigel Young, of the University of Hull for his assistance with XAFS data collection and analysis and Dr Ron Smith and Dr Stephen Hull at ISIS, Rutherford Appleton Laboratories for their assistance with collection of neutron diffraction data.

I would also like to thank all of the people I have worked with at the University of Hull, especially Dave, Chris, Becky, Tim, Vincent, Phil, Steve, Graeme, Antony and Aaron, and the project students, particularly James and Tai. For helping me enjoy coffee breaks I wish to thank Ben and James. I would like to thank all of the technical staff in the chemistry department for their help over the last three years, particularly Anthony Sinclair for the EDX spectroscopy measurements, Carol Kennedy for elemental analysis and Bob Knight for ICP-MS.

I would also like to thank the EPSRC for financial support and acknowledge the use of the EPSRC's Chemical Database Service at Daresbury.

Finally, I would like to thank my Mum and Dad, Tracie, Jonathan, Luke and Barney, Nanny and Bumpy, and Evelyn.

Abbreviations

EDX	Energy Dispersive X-ray
EXAFS	Extended X-ray Absorption Fine Structure
FT	Fourier Transform
NPD	Neutron Powder Diffraction
PXRD	Powder X-ray Diffraction
RT	Room Temperature
SQUID	Superconducting Quantum Interference Device
TEM	Transmission Electron Microscopy
TM	Transition Metal
XAFS	X-ray Absorption Fine Structure
XANES	X-ray Absorption Near-Edge Structure
XAS	X-ray Absorption Spectroscopy
XPS	X-ray Photoemission Spectroscopy
XRD	X-ray Diffraction

Contents

1.0 Introduction	10
1.1 Magnetism.....	10
1.1.1 Diamagnetism	10
1.1.2 Paramagnetism	11
1.1.3 Ferromagnetism.....	11
1.1.4 Anti-Ferromagnetism	12
1.1.5 Magnetic Susceptibility.....	14
1.1.6 Lower Dimensional Magnetism.....	16
1.2 Conductivity	18
1.3 Magnetoresistance.....	21
1.3.1 Anisotropic Magnetoresistance	22
1.3.2 Giant Magnetoresistance	23
1.3.3 Colossal Magnetoresistance	25
1.4 Sulphide Synthesis	27
1.4.1 Conventional Solid-State Synthesis	27
1.4.2 Solid-Gas Reactions	27
1.4.3 Co-Precipitation Reactions.....	28
1.5 One-Dimensional Sulphides.....	28
1.5.1 Introduction	28
1.5.2 Ternary One-Dimensional Sulphides $A_xM_yS_z$ Where $A:M = 1$	31
1.5.2.1 $BaMS_3$ ($M = Ti, V, Nb, Ta$)	31
1.5.2.2 $K_2Ta_2S_{10}$	33
1.5.2.3 AMS_3 ($A = Sr, Sn, Pb, M = Hf, Zr$)	33
1.5.2.4 $La_2Fe_2S_5$	34
1.5.2.5 $BaPdS_2$	35
1.5.2.6 $AFeS_2$ ($A = K, Rb, Cs, Tl$)	36
1.5.2.7 $KCuS$ and $KAuS$	38
1.5.3 Ternary One-Dimensional Sulphides $A_xM_yS_z$ Where $A:M < 1$	40
1.5.3.1 AFe_2S_3 ($A = K, Rb, Cs, Ba$)	40
1.5.3.2 $Ba_{1+x}Fe_2S_4$ ($0.072 \leq x \leq 0.142$)	41

1.5.3.3 AV_6S_8 (A = In, Tl, Na, K, Rb, Cs).....	42
1.5.3.4 $Na_3Cu_4S_4$	44
1.5.4 Ternary One-Dimensional Sulphides $A_xM_yS_z$ Where A:M >1.....	45
1.5.4.1 Ba_3CrS_5 and $Ba_3Cr_2S_6$	45
1.5.4.2 A_2TiS_3 (A = Cs, K).....	45
1.5.4.3 Tl_2TiS_4	46
1.5.4.4 $A_3Fe_2S_4$ (A = Na, K, Rb, Cs, Tl).....	48
1.5.4.5 A_2MnS_2 (A = K, Rb, Cs).....	49
1.5.4.6 Na_2ZnS_2	50
1.5.4.7 $Na_5Co_2S_5$	50
1.5.4.8 A_2CoS_2 (A = Na, K, Rb, Cs).....	51
1.5.4.9 A_2MS_2 (A = Na, K, Rb, M = Pt, Pd).....	52
1.5.4.10 $Ba_7Fe_6S_{14}$	53
1.5.4.11 $Ba_6Fe_8S_{15}$	54
1.5.4.12 Ba_2MS_3 (M = Mn, Hg, Cd, and Fe, Co, Zn).....	55
1.5.5 Conclusion.....	57
1.6 Ba_2CoS_3	59
1.7 Project Aims and Outline.....	66
2.0 Experimental Techniques.....	67
2.1 Synthesis and characterisation.....	67
2.2 Structural Characterisation.....	70
2.2.1 Crystallography.....	70
2.2.1.1 Symmetry.....	70
2.2.1.2 Symmetry Operations.....	70
2.2.1.3 Unit Cell.....	71
2.2.1.4 Lattice Notations.....	75
2.2.1.5 Diffraction.....	76
2.2.2 Powder X-ray Diffraction (PXRD).....	78
2.2.2.1 X-ray Generation.....	78
2.2.2.2 Diffractometer.....	83
2.2.2.3 X-ray Detection.....	83

2.2.3 Neutron Powder Diffraction (NPD)	84
2.2.4 Rietveld Refinement	87
2.2.4.1 Criteria of Fit	90
2.2.5 X-ray Absorption Spectroscopy	91
2.3 Physical Characterisation	95
2.3.1 Magnetic Measurements	95
2.3.2 Transport Measurements	96
3.0 Ba ₂ Co _{1-x} Zn _x S ₃	99
3.1 Synthesis and Characterisation	99
3.2 Results and Discussion	99
3.2.1 Powder X-ray Diffraction (PXRD)	99
3.2.2 Neutron Powder Diffraction (NPD)	102
3.2.3 X-ray Absorption Spectroscopy (XAS)	107
3.2.3.1 XANES	108
3.2.3.2 EXAFS	110
3.2.4 Transition Electron Microscopy (TEM)	123
3.3 Physical Properties	124
3.3.1 Magnetic Susceptibility	124
3.3.2 Transport Properties	132
3.3.3 Conclusion	138
4.0 Ba ₂ Co _{1-x} Fe _x S ₃	139
4.1 Synthesis and Characterisation	139
4.2 Results and Discussion	139
4.2.1 Powder X-ray Diffraction (PXRD)	139
4.2.2 Neutron Powder Diffraction (NPD)	141
4.2.3 X-ray Absorption Spectroscopy (XAS)	143
4.2.3.1 XANES	144
4.2.3.2 EXAFS	145
4.2.4 Physical Properties	147
4.2.4.1 Transport Properties	147
4.2.5 Conclusion	150
5.0 Ba ₂ Zn _{1-x} M _x S ₃ (M = Fe, Mn, Cr, Ni)	151

5.1 Synthesis and Characterisation	151
5.2 Results and Discussion.....	151
5.2.1 Powder X-ray Diffraction (PXRD)	151
5.2.1.1 $\text{Ba}_2\text{Zn}_{1-x}\text{Fe}_x\text{S}_3$ ($x = 0.25, 0.5, 0.75$).....	152
5.2.1.2 $\text{Ba}_2\text{Zn}_{1-x}\text{Mn}_x\text{S}_3$ ($x = 0.25, 0.5, 0.75$)	154
5.2.1.3 $\text{Ba}_2\text{Zn}_{1-x}\text{Cr}_x\text{S}_3$ ($x = 0.25, 0.5, 0.75$).....	156
5.2.1.4 $\text{Ba}_2\text{Zn}_{1-x}\text{Ni}_x\text{S}_3$ ($x = 0.25, 0.5, 0.75$).....	157
5.2.2 Neutron Powder Diffraction (NPD)	159
5.2.2.1 $\text{Ba}_2\text{Zn}_{1-x}\text{Fe}_x\text{S}_3$ ($x = 0.25, 0.5, 0.75$).....	159
5.2.2.2 $\text{Ba}_2\text{Zn}_{1-x}\text{Mn}_x\text{S}_3$ ($x = 0.25, 0.5$)	164
5.2.2.3 $\text{Ba}_2\text{Zn}_{0.75}\text{Cr}_{0.25}\text{S}_3$	168
5.2.2.4 $\text{Ba}_2\text{Zn}_{0.75}\text{Ni}_{0.25}\text{S}_3$	170
5.2.3 Physical Properties	172
5.2.3.1 Magnetic Susceptibility.....	172
5.2.3.2 Transport Properties	172
5.2.4 Conclusions	174
6.0 $\text{Ba}_{2-y}\text{A}_y\text{CoS}_3$ ($A = \text{Ca}, \text{Mg}, \text{Sr}, \text{K}$).....	175
6.1 Synthesis and Characterisation	175
6.3 Results and Discussion.....	175
6.1.1 Powder X-ray Diffraction (PXRD)	175
6.1.2 Neutron Powder Diffraction (NPD)	176
7.0 Overall Conclusions	179
8.0 Further Work.....	182
9.0 References	183
10.0 Appendices.....	188
10.1 Appendix 1	188
10.2 Appendix 2	196
10.3 Appendix 3	206
10.4 Appendix 4	210
10.5 Appendix 5	212
10.6 Appendix 6	213
10.7 Appendix 7	225
10.8 Appendix 8	233
10.9 Appendix 9	237

10.10 Appendix 10.....239

1.0 Introduction

1.1 Magnetism

All atoms exhibit some degree of intrinsic magnetic behaviour due to the spin and orbital motion of their electrons. This spin and orbital motion creates ‘atomic magnetic dipoles’ and these dipoles can interact with one another and with applied external magnetic fields in a number of ways.¹ In a material where there is no interaction between spins either diamagnetism or paramagnetism result (although diamagnetism may also result where interactions do occur).

1.1.1 Diamagnetism

Diamagnetism is a magnetic property which occurs in almost all materials as it is due to the orbital motion of paired electrons. It is generally a weak effect which occurs along with other interactions and is often overshadowed by these other stronger magnetic interactions within a material i.e. those caused by the spin of unpaired electrons. In materials with atoms containing only paired electrons the spins of these paired electrons align anti-parallel to one another and cancel each other out, there is no spin contribution to the magnetic properties and diamagnetism is the only property exhibited. The orbital motion of the paired electrons creates a magnetic dipole and this gives the material its magnetic properties. In the absence of an applied magnetic field these dipoles will tend to order randomly with respect to one another within the material and cancel each other out to minimise the energy of the material; the material will therefore have zero net magnetic moment.

When a magnetic field is applied to a diamagnetic material it will repel it. This is as a result of Lenz’s law which states that an induced electric current will always flow in such a direction as to oppose the change which produces it. When an external magnetic flux density is applied to a material the orbit of the electrons is affected such that they precess and a tiny current is induced, and, in turn this current creates its own lines of magnetic flux. These lines of magnetic flux act in opposition to those of the applied field. In addition, the external magnetic field causes the dipoles within the material to align, meaning the induced magnetic flux and therefore the repulsion is greater for stronger applied fields. Diamagnetism is independent of temperature.

1.1.2 Paramagnetism

Paramagnetism occurs in materials which have unpaired electrons; the spin of these electrons gives rise to permanent atomic magnetic dipoles. These dipoles are, in the absence of an applied field, randomly ordered throughout the material and so as with diamagnetism there is no net magnetic moment in the material. If a magnetic field is applied the dipoles align with the applied field and the material is attracted to the magnetic field, when the field is removed the dipoles return to their disordered state. Paramagnetism is dependent on the strength of the applied field as a stronger field will cause more dipoles to align, up until a saturation point. Paramagnetism is also temperature dependent as thermally induced motion leads to a greater randomisation of the dipoles. Paramagnetism is usually a stronger effect than diamagnetism.²

At 0 K all materials must show some degree of magnetic order (i.e. ordered arrangement of the spins) in order that entropy is zero. This results in either parallel or anti-parallel arrangement of the spins and often occurs at temperatures well above 0 K, leading to ferromagnetism and anti-ferromagnetism.

1.1.3 Ferromagnetism

In ferromagnetism there is an interaction between dipoles which causes them to line up parallel to one another. This magnetic interaction is temperature dependent and only occurs below a point known as the Curie temperature (T_c) above this point the dipoles are randomly aligned due to the thermal energy being greater than the interaction energy.

Whilst neighbouring dipole spins tend to line up in parallel this does not necessarily propagate over the entire volume of a ferromagnetic material, known as long-range order. Areas of uniform magnetisation called domains may form and are separated from other domains by domain walls, see figure 1.1. Upon applying an external magnetic field these domains can be aligned with one another to give permanent magnets. As the field is increased there are two effects upon the domains. The first is that those domains which are parallel or at a small angle to the field increase in size whilst those aligned anti-parallel get smaller. The second effect is that at high external field strengths some domains will rotate to align with the external field, this however requires a large amount of energy. These processes are known as magnetisation.

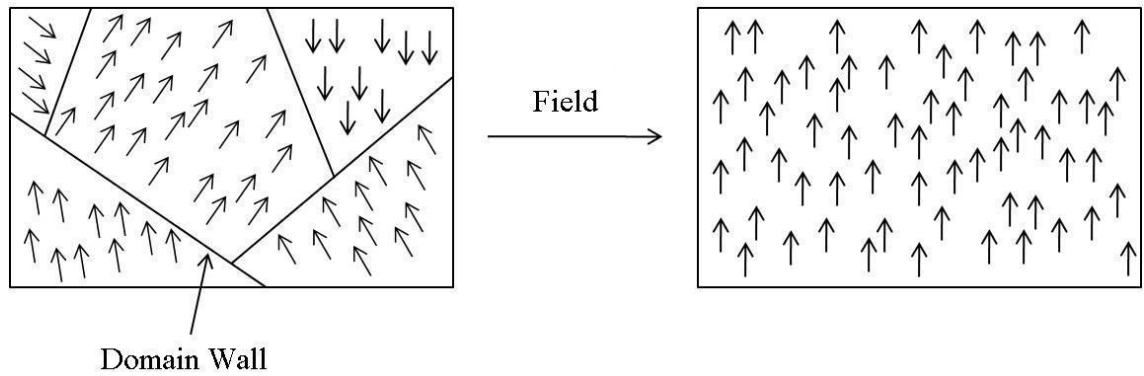


Figure 1.1 Domains within a ferromagnetic material affected by the application of an external magnetic field

There are two broad classes of ferromagnetic materials. Magnetically soft materials have a high magnetic permeability and are easily magnetised and demagnetised, whilst magnetically hard materials have a lower permeability and as such are harder to magnetise but maintain magnetisation more readily. The ease of magnetisation is determined by the strength of the interaction between the dipoles, known as the exchange interaction, J .

1.1.4 Anti-Ferromagnetism

In anti-ferromagnetic materials the neighbouring spins align in an anti-parallel fashion. As with ferromagnetism the interactions only occur below a set temperature, in this case known as the Néel temperature, T_N . This anti-parallel alignment between the spins is often mediated by a bridging atom. Figure 1.2 shows the most common mechanism by which this mediation occurs, known as superexchange, in which two metal centres with unpaired electrons are coupled anti-parallel *via* the mediation of a p-block atom. The p-block atom donates two electrons, each with opposite spin, one to each metal. The donated electrons must have the opposite spin to that of the metal centre to which they are donated (Pauli Exclusion Principle). Since the donated electrons have opposite spin to one another so must the metal centres and the anti-parallel arrangement results. A more polarisable ligand generally leads to a greater interaction between the metal centres.

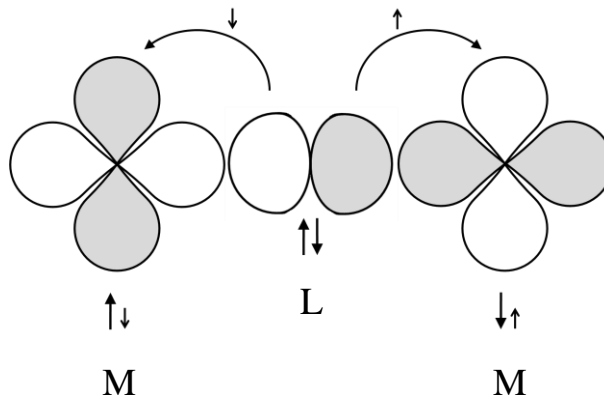


Figure 1.2 The Superexchange mechanism, resulting in an anti-ferromagnetic material

A special kind of anti-ferromagnetism known as ferrimagnetism also exists in which two different metals, with unequal spins, align anti-parallel. This creates a permanent magnet when the spins are ordered despite the anti-parallel alignment of those spins.

The different kinds of magnetism resulting from unpaired electrons are represented in figure 1.3.

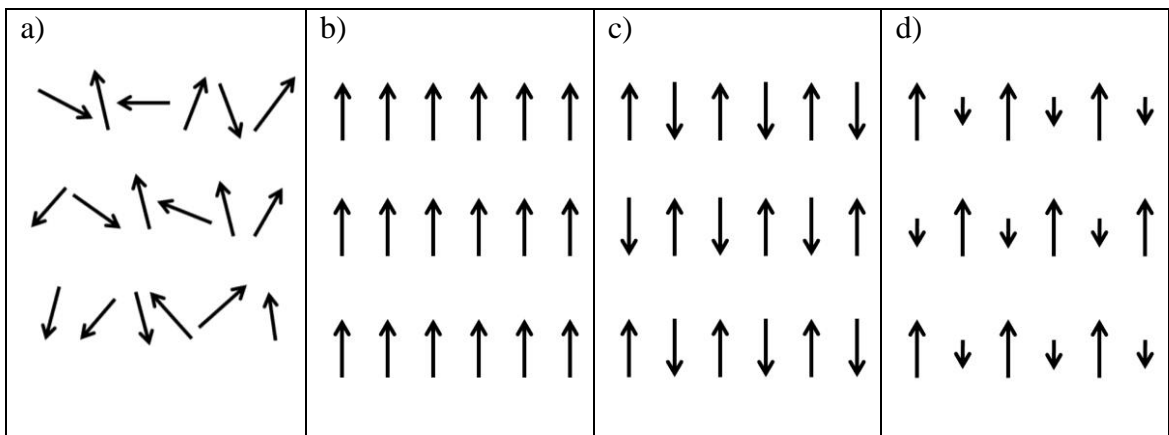


Figure 1.3 Representations of the spin arrangements in a) paramagnetism b) ferromagnetism c) anti-ferromagnetism and d) ferrimagnetism

Finally, a special type of paramagnetism known as Pauli paramagnetism is associated with some metals. When a Pauli paramagnet is placed in an external field delocalised electrons in the partially filled conduction band undergo polarisation and those electrons which line up with the field have lower energy. This leads to some electrons at the Fermi surface reorienting to line up with the field and reduce their energy which leads to an increase in the population of those spins and therefore weak magnetisation.

1.1.5 Magnetic Susceptibility

The most common way of describing a materials magnetic behaviour is in terms of magnetic susceptibility, χ . This is a measure of how easily a compound is magnetised, i.e. how affected by a magnetic field the dipoles are. The volume susceptibility is given by the equation;

—

where M is the magnetisation, measured in Amperes/metre (A/m) and H is the strength of the applied magnetic field also measured in A/m. The susceptibility can also be expressed as molar susceptibility;

—————

where ρ is the density. and RRM is the relative molecular mass. An alternative description of susceptibility involves comparing the strength of field inside the material, B , to that of the applied field, B_0 .

i.e. when χ is negative the field inside the material is lower than the applied field, the material repels the applied field and is diamagnetic. When χ is positive the applied field is enhanced and the material is attracted.

The molar susceptibility of a material can also be used to determine the effective magnetic moment, μ_{eff} , of a material;

—————

This gives the μ_{eff} in Bohr magnetons where one Bohr magneton is $9.274 \times 10^{-21} \text{ ErgG}^{-1}$. For paramagnetic and diamagnetic materials the effective magnetic moment is independent of temperature and field strength.

For paramagnetic materials the number of unpaired electrons can be estimated by using the effective magnetic moment using the spin only formula.

—————

For transition metals (i.e. atoms containing 3d electrons) $\mu_{\text{eff}} \approx \mu_s$ and this equation can be used to estimate the number of unpaired electrons in a material. $S=1/2$ for one unpaired electron, 1 for two unpaired electrons, $3/2$ for three unpaired electrons, etc.

Whilst magnetic susceptibility describes the susceptibility of a material it is also possible to define susceptibility in terms of individual spins. The energy of an individual spin in an external field H is;

where μ_B is the Bohr magneton, a constant equal to $eh^2/4m$ (e = charge on an electron, h = Planck's constant, m = mass of electron and c = speed of light) and g is a number characteristic of each atom (e.g. 2.0023 for a free electron and often close to 2 for many metal ions). The value of g may vary with orientation if the atom possesses significant magnetic anisotropy.

The temperature dependence of the susceptibility is a useful way to categorise and study materials and for a paramagnetic material is shown by the Curie law;

—

where C is the Curie constant in $\text{emu}\cdot\text{mol}^{-1}\text{K}$ and T is the temperature in K .

In reality the susceptibility of materials, particularly those exhibiting ferro- and anti-ferromagnetism, is more complex but can be modelled above the transition temperature, where the materials are paramagnetic, using a modified version of the Curie-Law known as the Curie-Weiss law;

—————

where θ is the Weiss constant.

This equation becomes less accurate as the transition temperature is approached. For both ferro- and anti-ferromagnetic materials the susceptibility shows a sharp change at the transition temperature. For ferromagnetic materials the susceptibility rapidly increases as the dipoles align in parallel with the field and for anti-ferromagnetic materials the susceptibility decreases as the spins align anti-parallel to one another and cancel each other out. These behaviours are represented graphically in figure 1.4 and

typical values for the susceptibility for materials exhibiting the different types of magnetism are shown in table 1.1.

Table 1.1 Typical values of volume susceptibility for different types of magnetism

Type of Magnetism	Typical values
Diamagnetism	-1×10^{-6}
Paramagnetism	10^{-2} to 10^{-5}
Ferromagnetism	10^2 to 10^6
Anti-ferromagnetism	0 to 10^{-2}

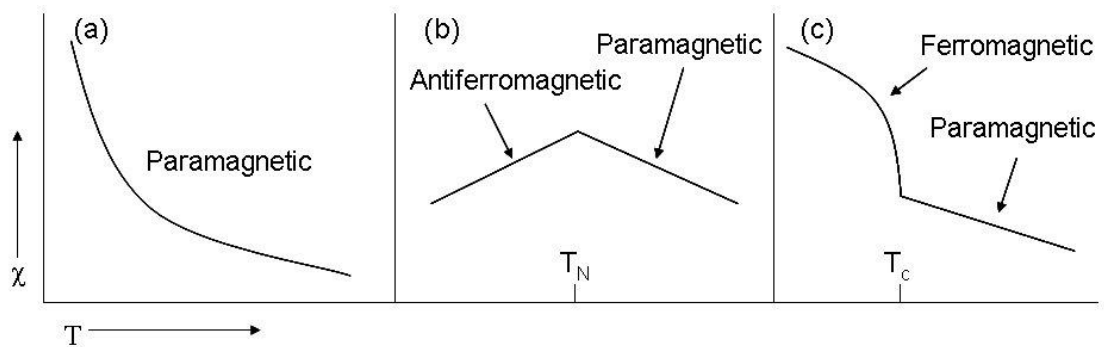


Figure 1.4 Schematic diagram of magnetic susceptibility versus temperature for (a) paramagnetic (b) antiferromagnetic and (c) ferromagnetic materials

Another common way of determining magnetic properties and specifically magnetic transitions is by analysing specific heat (C). Specific heat is the amount of energy required to raise the temperature of a material by one Kelvin. In a solid, this is influenced by both the Debye lattice specific heat (caused by the vibrations in the solid) and also by the entropy or ordering of electron spins. As these spins align during a magnetic transition (at T_C or T_N) sharp changes in the specific heat occur, represented by peaks in a specific heat versus temperature plot.

1.1.6 Lower Dimensional Magnetism

The magnetic ordering described above usually propagates through a material in three dimensions, i.e. if something is anti-ferromagnetically ordered the spins align anti-parallel to their neighbouring spins in all three spatial directions. It is however possible for exchange interactions to occur in just two or one dimensions and recently there has been a great deal of interest in such systems.^{3,4} In general, the strength of magnetic

interactions between spins either *via* direct or indirect exchange is measured in terms of the exchange constant, J , and the spin operators, S , of the two ions i and j interacting. This is shown by the Hamiltonian;

For a linear chain model the two ions are neighbouring atoms in a chain and the exchange term can be expanded to introduce the concept of spin dimensionality and give;

This gives rise to three possible combinations depending on the values of α and β . If $\alpha = 1$ and $\beta = 0$ the spin is only considered in the z direction, this is the basis for the Ising model. If $\alpha = 0$ and $\beta = 1$ the spins can vary in both the x and y directions and the model used to describe this is called the XY Hamiltonian. When both α and $\beta = 1$ the model is isotropic and called the Heisenberg model. The spin dimensionalities in these three models are one, two and three respectively. For example, for the Ising model the spins on atoms can only point up or down with respect to the principal axis of the chain. The type of system which forms is largely dependent on the nature of the magnetic atom, for example manganese is more isotropic in nature than cobalt and so manganese and cobalt tend to form Heisenberg and Ising type systems respectively.

In a perfect theoretical Ising model with no interchain interaction the system will only undergo three-dimensional ordering, i.e. ordering between the chains as well as within them, at absolute zero, 0 K. In reality three-dimensional interactions increase as temperature is lowered and all low-dimensional systems undergo this transition to 3-D order above 0 K.

One-dimensional interactions are seen in susceptibility measurements as broad curves rather than the sharp changes in gradient seen for three-dimensional magnetic transitions. In specific heat measurements the interactions are indicated by the system gaining entropy as is it heated, with perfect one-dimensional systems having zero entropy at 0 K.

The presence of one or two-dimensional magnetic interactions in materials is of interest due to the greater simplicity of modelling these interactions but also the usefulness of such systems. Commonly the properties are linked to the structure and so there is

interest in synthesising systems with one-dimensional structures and properties, see section 1.5.

1.2 Conductivity

Electrical conductivity is a measure of how easy it is for a material to carry an electric current and is measured in units of Siemens per metre, Sm^{-1} . The reciprocal of conductivity is resistivity which is measured in ohm metres, Ωm .

Conductivity can be used to classify materials into three general areas; conductors, semi-conductors and insulators.

Materials which conduct well, typically $>10^3 \text{ Sm}^{-1}$, and show a decrease in conductivity as temperature is increased are known as conductors. Materials which conduct fairly well but show an increase in conductivity as temperature is increased are known as semiconductors and materials which show very low levels of conductivity, typically $<1 \text{ Sm}^{-1}$, are known as insulators. These are very broad definitions and many materials fall in between or do not fit into these categories.

These three classes of conductivity can be explained up to a basic level using band theory. By treating a material as consisting of a large number of overlapping atomic orbitals and including a large number of these orbitals we can see that there essentially exist bands of energy where for an individual atom there are discrete energy levels, see figure 1.5.

For a material containing n atoms there are n molecular orbitals, bonding, non-bonding and anti-bonding. Where there is strong overlap between the molecular orbitals wide energy bands are created and for weak overlap the bands are narrower. At energy levels where there are no orbitals there exists a 'band gap', figure 1.6.

An insulator exists where a material contains only fully occupied bands combined with a large band gap. As it is not possible for electrons to move freely within a fully occupied energy band, figure 1.6a, the material is a poor conductor.

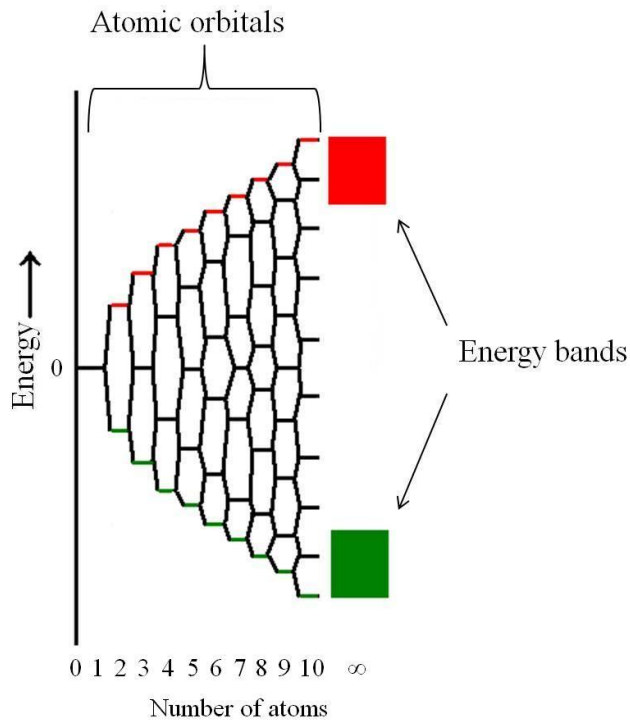


Figure 1.5 Molecular orbital overlap for an extended system resulting in energy bands

Materials which have either partially filled bands or have overlapping full and empty bands are conductors, figure 1.6b and 1.6c. Within the partially filled or conduction band electrons are essentially free to move within the cation lattice and, according to assumptions made in the Drude model, there is no electron-cation interaction and no electron-electron interaction. The electrons move under an applied electrical potential and are slowed only by collisions. In a metal collisions occur due to defects within the cation lattice and due to electrons interacting with the vibration of the cation lattice, known as electron-phonon interactions. The prevalence of defects is temperature dependent, with more occurring at higher temperature and electron-phonon interactions also increase with temperature; as the cation lattice gains energy it vibrates more and collisions are more frequent. These two factors explain the temperature dependence of conductors. There are also other factors which influence the conductivity and in general in this model the conductivity is seen to be dependent on the mean free path, i.e. the average distance an electron can move before undergoing a collision.

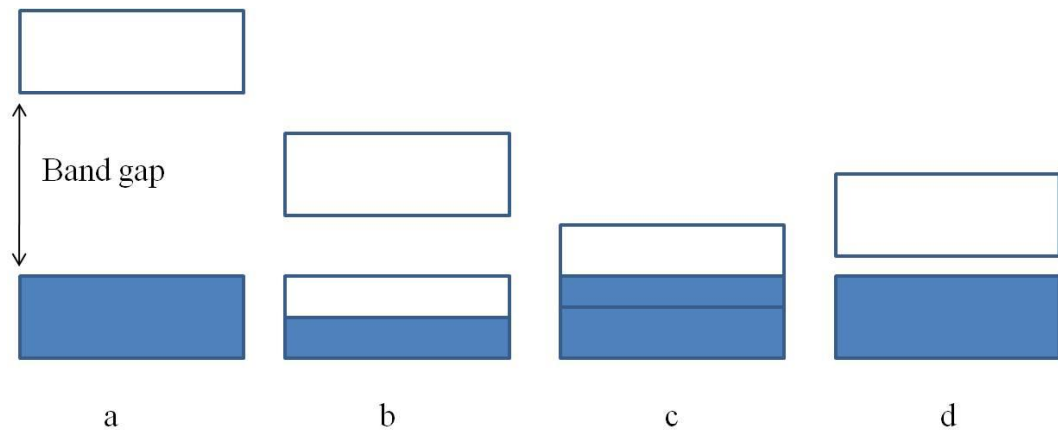


Figure 1.6 Representation of the band structure of a) insulator b) conductor with half filled band c) conductor with overlapping bands d) semiconductor

In semiconductors there is a fully occupied lower band but a small band gap, figure 1.6d, and this band gap can be overcome and conduction induced by promoting electrons, in one of two ways, into the unoccupied conduction band. The first is by heating the material which increases the energy of some electrons and promotes them into the conduction band. As these electrons are promoted they also leave behind a ‘hole’ in the valence band and the electrons remaining in the valence band can hop into these vacancies, with the ‘holes’ effectively moving in the opposite direction to the electrons in the conduction band; this is known as hole conduction. As the temperature is increased the number of electrons promoted and the number of holes created increases and so, therefore, does the conductivity of the material. Materials which behave in this way are known as intrinsic semiconductors and include silicon and germanium. The second method of promoting electrons involves doping the material, either with an electron-rich element or an electron-poor element, for example doping silicon, a group IV element, with a group III or group V element. This introduces either an extra electron which goes into the conduction band or an extra ‘hole’ in the valence band which allows for conduction; these are known as n- and p- type extrinsic semiconductors respectively.

A further type of conductivity known as superconductivity is also present in some materials, where the resistance drops to zero at low temperature (<40 K). As they reach this transition temperature, T_c , these materials also become perfect diamagnets, this is known as the Meissner effect. Conventional superconductivity is seen in some metals and alloys such as mercury⁵ and Nb_3Ge ⁶, which has the highest known transition temperature for a ‘conventional’ superconductor at 23 K. Conventional superconductivity can be explained with the Bardeen-Cooper-Schrieffer (BCS) theory,

established in 1957.⁷ At low temperature there is very little vibration of the cation lattice through which an electron passes and as such there is little scattering of the electron. As the electron passes through the cation lattice it slightly attracts nearby cations and effectively creates a region of higher density positive charge which travels behind the electron through the cation lattice as a phonon. This positive charge in turn attracts another electron (of opposite spin) and the two electrons are said to form a Cooper pair. As the electrons possess opposite spin and have now paired up they can be treated as having zero spin and so can exist with other Cooper pairs at the same energy state. This is known as a Bose-Einstein condensate and is a highly ordered ground state. All the Cooper pairs in the condensate can then pass through the material without scattering one another, i.e. a zero resistance state has been created.

Although this theory is very successful at explaining superconductivity in these materials up to 40 K there are other materials known as high-temperature superconductors (HTSC) which show much higher transition temperatures that cannot be explained by this theory. HTSC is a well researched field with initial interest in copper containing oxides resulting in the highest transition temperature material, Hg-Ba₂Ca₂Cu₃O_{8+δ} with a T_c of 135 K.⁸ More recent research has focussed on materials containing arsenic as well as other materials and currently no known explanation exists for the superconductivity in these materials.

1.3 Magnetoresistance

Magnetoresistance (MR) is defined as a change in the resistivity (ρ) of a material when a magnetic field (H) is applied; this change can be positive or negative and is often expressed as a percentage:

In general terms the effect arises from the interaction between the magnetic and electronic structure of a material. Materials exhibiting this effect are technologically useful with a variety of applications including read heads for hard disk drives as well as in magnetoresistive random access memory (MRAM).

1.3.1 Anisotropic Magnetoresistance

The first evidence of magnetoresistance was discovered in 1856 by William Thomson (Lord Kelvin) who showed that the resistance of iron and chromium varies depending on the direction of the applied magnetic field relative to the direction of electric current.⁹ This effect is now known as ‘anisotropic magnetoresistance’ and although no explanation was given at the time (the electron was not discovered for another 40 years) the mechanism is now known. Anisotropic magnetoresistance occurs in all metallic ferromagnets and is due to the increased scattering cross-section conduction electrons experience when moving parallel to the magnetisation compared with moving perpendicular. The scattering cross-section is influenced by the applied magnetic field interacting with spin-orbit coupling causing the electron cloud of bound electrons to deform, becoming larger perpendicular to the magnetic field and smaller parallel to it, see figure 1.7. This leads to an increase in resistance when the magnetic field is applied parallel to the current direction and a decrease when the field is applied perpendicularly. Alloys of nickel and iron, known as permalloys, have shown anisotropic magnetoresistance of up to 20% at around 183 K¹⁰ and the largest anisotropic magnetoresistance seen so far occurs in uranium phosphide and arsenide, U_3P_4 and U_3As_4 reaching values of up to 50%.¹¹

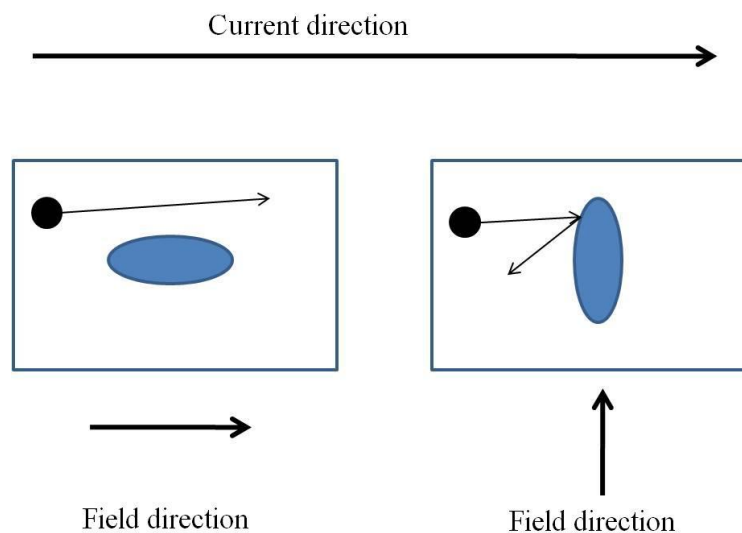


Figure 1.7 Diagram showing anisotropic magnetoresistance. Blue ovals represent the electron orbitals of bound electrons which can scatter the black conduction electrons. The applied magnetic field distorts the electron clouds and changes the cross section presented to the conduction electrons and therefore the resistance of the material

A similar effect known as ‘ordinary magnetoresistance’ occurs in non-magnetic metals and is due to the Lorentz force acting on the conduction electrons. In this case the

applied magnetic field interacts with the conduction electrons and leads to increased resistance for all geometries of magnetic and electric field. The Lorentz force acts upon a moving electron in a magnetic field and leads to a spiralling motion in the electron, increasing the resistance.

1.3.2 Giant Magnetoresistance

‘Giant magnetoresistance’ occurs in multilayer materials consisting of alternate layers of ferro- and non ferro- magnetic materials and arises due to differences in the scattering probabilities for electrons with different spins. In a ferromagnetic material there is an excess of either up or down spin electrons at the Fermi level (the energy level of the highest occupied orbitals at 0 K) and the scattering probability is greater for the minority electrons. According to Mott’s theory electric current can be considered as two different channels, spin up and spin down, and as there is little ‘spin flip’ scattering between the two conduction paths they can be considered independent.¹² In these multilayer materials, if the two ferromagnetic layers are anti-ferromagnetically aligned with respect to one another any electron moving between the two layers will experience significantly higher resistance in one of the layers. For example, a spin up electron starting in a layer with majority spin up electrons will pass from a layer of low resistance to one of high resistance when it goes into the layer with majority spin down electrons. If, however, the two layers have their spins aligned parallel to one another the minority spin electrons will flow much more easily. This effect is illustrated in figure 1.8.

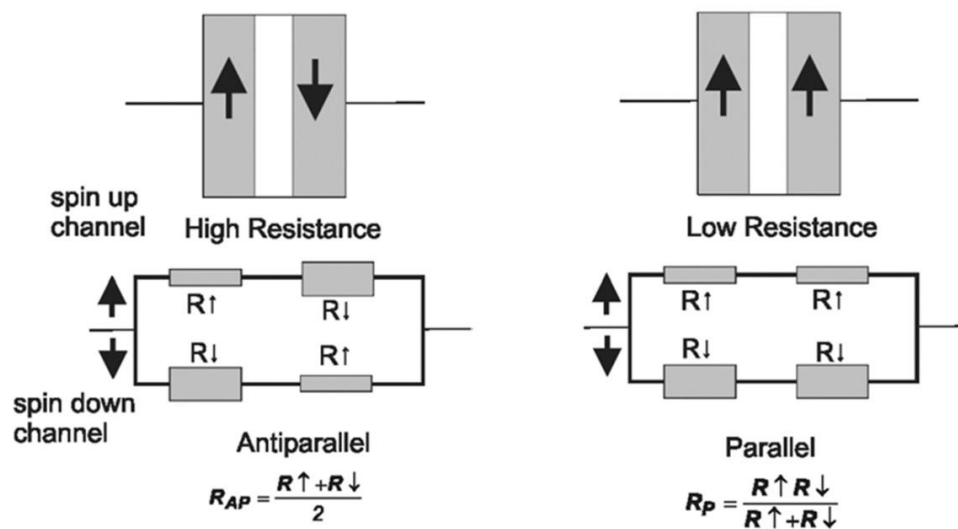


Figure 1.8 Representation of the high and low resistance states for a multilayer material showing the spin up and spin down channels as a parallel electronic circuit. Reproduced from the literature.¹³

In order to switch the coupling between the layers from anti-ferromagnetic to ferromagnetic the thickness of the non-ferromagnetic spacer material is chosen to exploit the RKKY interaction. This relatively weak interaction results in anti-ferromagnetic coupling which can be overcome with the application of an external magnetic field resulting in ferromagnetic interlayer coupling. The first samples to show this effect were Fe-Cr-Fe multilayers discovered by Grunberg¹⁴ and Fert¹⁵ independently and they later jointly received the Nobel prize for Physics in 2007 for their work in this field. The effect can reach values of 50% in Fe-Cr-Fe multilayers (Cr layer thickness 9 Å) at 4.2 K in a 2 T field.¹⁵

There have since been modified versions of this system involving additional layers which show increased magnetoresistance and are widely commercially used in hard disk drive read heads. One such system known as a 'spin valve' system utilises a fourth so-called pinning layer; this layer has fixed magnetisation and is coupled to the first magnetic layer anti-ferromagnetically. A thicker spacer than in the original system is then used followed by the final magnetic layer which is uncoupled and known as the free layer. This layer is then able to freely rotate in response to an external magnetic field. As with the initial configuration the resistance is higher when the layers are anti-ferromagnetically aligned and lowered when an external field is applied to align the two layers.

In addition, this giant magnetoresistance effect has been seen in non-multilayer materials consisting of single domain ferromagnetic entities contained within inhomogeneous materials. The mechanism is similar to that in the layered materials as in the absence of an external field the domains are not aligned with respect to one another and the resistance is high due to scattering of electrons as they pass through the domains. When an external field is applied the domains align and the scattering and therefore resistance is reduced.¹⁶

'Tunnelling magnetoresistance' also works in a similar way with two layers of ferromagnetic material separated by an insulator. If the two ferromagnetic layers are aligned with one another the chances of a tunnelling event occurring are greater and the resistivity is reduced, this is illustrated in figure 1.9.¹⁷ This effect can reach levels of up to 600% in layered structures of CoFeB/MgO/CoFeB.¹⁸

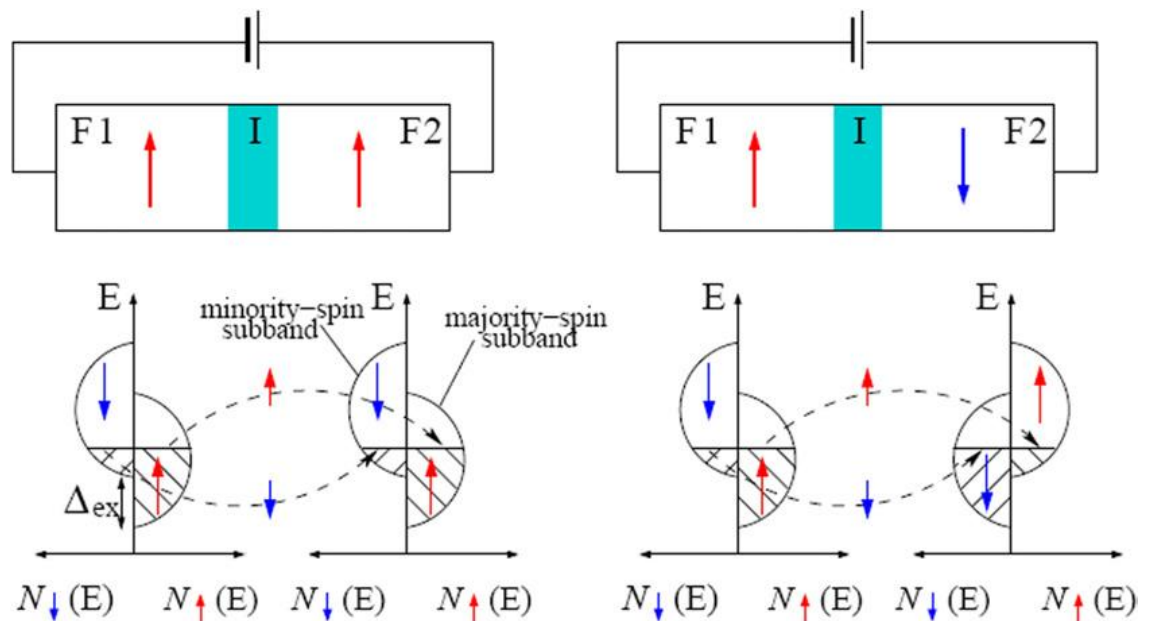


Figure 1.9 Representation of a tunnelling magnetoresistive material and the low and high resistance states. F represents the ferromagnetic layers and I the insulating layer. Reproduced from the literature.¹³

1.3.3 Colossal Magnetoresistance

Finally, the most recently discovered ‘colossal magnetoresistance’ is the name given to a magnetoresistive effect, most commonly occurring in perovskite manganites, which is associated with ferromagnetic-paramagnetic phase transitions and can show changes in resistivity of over 100,000%. The first group of compounds to show this effect were based on $\text{Ln}_{1-x}\text{A}_x\text{MnO}_3$ where Ln is a trivalent lanthanide and A is a divalent metal, usually an alkaline earth. With no substitution the compounds LnMnO_3 have an antiferromagnetic ground state but doping leads to a ferromagnetic ground state with the paramagnet-ferromagnetic transition accompanied by a large drop in the resistivity. The optimum values for substitution are between 20 and 40%.¹⁹ Part of the possible explanation for the magnetoresistance, which is at its greatest near to the transition (i.e. T_N), lies in the mixed oxidation state of manganese in these materials and the double exchange mechanism. The distance between the manganese atoms means there is no Mn-Mn overlap in these materials and electron transfer is mediated by oxygen atoms. As one electron is passed from Mn^{3+} to the bridging oxygen another is passed from the oxygen atom to a Mn^{4+} , i.e. a double exchange.²⁰ Because of the interaction between the e_g and t_{2g} electrons this exchange is more favourable when the electrons of both manganese ions have their spins aligned, see figure 1.10.

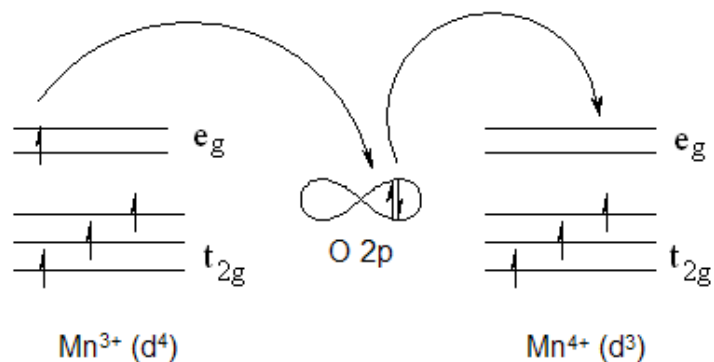


Figure 1.10 Mechanism of double exchange. An electron is simultaneously passed from the Mn^{3+} atom to the oxygen and from the oxygen to the Mn^{4+} resulting in a parallel arrangement of the spins on the manganese atoms

In addition there is believed to be considerable electron-phonon coupling due to the Jahn-Teller distortion in these materials which may add to the magnetoresistive effect.²¹

This is only a part explanation of the mechanism and an effect similar to this is seen in some chromium based chalcogenides which have the spinel structure and do not contain mixed oxidation state metals and cannot therefore be governed by the same mechanism.²²

The link between these compounds is the presence of a magnetic transition and a metal-insulator transition. The application of a magnetic field to some magnetic semiconductors as well as producing a change in the level of conductance often also produces a change in the conduction mechanism and there are often magnetothermal effects as well as changes in the band gap associated with the application of a magnetic field. Although colossal magnetoresistance can show larger effects than giant magnetoresistance and does not saturate until much higher fields it is a weaker effect at room temperature and in low field environments.

Each of these different kinds of magnetoresistance has technological uses and although some are understood clearly there is considerable work to be done to fully elucidate the mechanism by which MR occurs in some materials.

1.4 Sulphide Synthesis

The synthesis of sulphides, as with the majority of solid-state materials, can be divided into three main areas, the conventional or ceramic method, solid-gas reactions and co-precipitation reactions.

1.4.1 Conventional Solid-State Synthesis

The vast majority of sulphides are still made *via* conventional solid state techniques i.e., mixing of the elements or binary sulphides and heating to high temperatures ($>750^{\circ}\text{C}$) for long periods of time (up to weeks) (see section 1.5 for examples of the synthesis techniques described here). The starting materials must first be ground to reduce the size of the grains, ensure that they are well mixed together and to ensure close contact between grains. In addition, the choice of starting reagents is important as some binary transition metal sulphides are highly stable and also some metals react extremely vigorously with sulphur. After mixing together the mixture must be placed in a sealed tube that has either been evacuated or filled with an inert gas such as argon, to prevent reaction with oxygen, a common problem with sulphide synthesis. The reactions require high temperature and long reaction times as the reaction rate is essentially controlled by diffusion which is very slow in solids, and occasionally the materials may have to undergo several regrinding and reheating steps to ensure completion. A further limit on this type of reaction is that the product formed will be exclusively the thermodynamically stable product, reducing the control over the reaction and limiting the number of compounds that can be produced in this manner.

1.4.2 Solid-Gas Reactions

The second most common technique for synthesising sulphides involves reacting metal carbonates or oxides with streams of gas or vapour, usually of H_2S or CS_2 .²³ The advantages of this method over the ceramic method are the greater availability of starting materials and the reduced reaction times and temperatures. It is however hard to control the sulphur stoichiometry in the final product and oxide impurities may also remain. This technique has been used throughout this work and is discussed more in the experimental chapter.

1.4.3 Co-Precipitation Reactions

The main alternative to these synthetic techniques involves co-precipitation or solvothermal reactions. These involve dissolving the starting materials (metals or binary sulphides) in a highly polar molecular solvent. This allows the starting materials to mix much more intimately in the solution before the liquid is removed (usually by boiling) and the powder can then be gently heated. These relatively low temperature reactions (100-600°C) can be used to target metastable compounds as well as thermodynamically stable compounds and present significant environmental benefits by using lower reaction temperatures and times.²⁴ Solvothermal synthesis has been used mainly for binary sulphides but is finding more use for the synthesis of ternary and quaternary compounds.²⁵ The main problem associated with this technique is finding a suitable solvent in which to dissolve the starting materials, i.e. one which dissolves all the starting materials to the same extent and does not react with them. A similar technique known as molten flux instead dissolves the metals in molten salts. These types of reaction are particularly useful for performing structural modifications to existing compounds where the thermodynamic requirements of the reaction are low, and in intercalation reactions, see section 1.5.3.3 for an example.

1.5 One-Dimensional Sulphides

1.5.1 Introduction

This section gives an account of one-dimensional ternary sulphides, known to date, defined as the series $A_xM_yS_z$ where A is an alkali, alkaline earth or rare earth metal and M is a transition metal (groups 4-12) with A and M occupying different crystallographic sites. Mixed transition metal ternary sulphides, ternary transition metal polysulphides containing S-S bonds and main group-transition metal sulphides are not included.

The reason for continued interest in sulphides is the wide variety of properties which they exhibit, including superconductivity,²⁶ magnetoresistance,² ferro- and anti-ferromagnetism and catalytic activity.²⁷ Sulphides have also found use in photovoltaics and there is growing interest in nano-particles of sulphides.^{28,29}

One-dimensional compounds are of particular interest as they present ideal systems for studying structure property relationships^{4,30} and can be considered a link between

molecular and solid state chemistry. A one-dimensional solid can be viewed as a condensation of chains in which there is large degree of anisotropy in the bonding, with strong bonding within these chains and weaker (often van der Waals' forces) bonding between them.³¹ The combination of delocalization in some dimensions and quantum-confinement effects in the others results in anisotropic properties and also often results in unusual electronic properties, such as charge density waves.

The ternary sulphides presented here contain a mixture of transition metals and electropositive elements (alkaline or alkaline earth metals) and it is this combination that gives rise to a prevalence of one-dimensional ternary sulphides. Metal-sulphide bonds tend to be more covalent than metal-oxide bonds because of the lower electronegativity of sulphur. For this reason only those binary sulphides with the most electropositive metals, i.e. the alkali metals (A), share the same ionic-like structure as the corresponding oxides and the binary sulphides of transition metals often show a prevalence of covalent or metallic character and their structures tend to differ from those of the corresponding oxides.

The combination of an alkali metal with the covalent structure of a binary transition metal sulphide often leads to the formation of ternary two-dimensional (2D) layered and one-dimensional (1D) chain-like structures. The alkali metals are too electropositive to bond covalently to the sulphur but their addition tends to break up the original bonding, and as such the alkali metals induce the formation of a covalently bonded anisotropic framework of transition metal sulphide interspersed with alkali metal. In addition, the presence of the alkali metal gives the transition metals oxidation states typical of salt-like compounds. It was first observed by Zintl that solid compounds which contain both elements on the borderline between metals and non-metals and electropositive metals contain certain characteristic structural units. These structural units can show structural similarities with units containing atoms of a different nature. For example the network of $[\text{Si}_4^{4-}]$ tetrahedra in NaSi is related to the tetrahedra network in white phosphorous. The Zintl concept has been extended to rationalise the structures of a number of ternary sulphides of general formula $\text{A}_x\text{M}_y\text{S}_z$ in which A is an electropositive metal and M a transition metal.^{32,33} According to this model, sulphides can still be considered, to a certain extent, 'ionic compounds' in which the 'anion' is the $[\text{M}_x\text{S}_z]^{n-}$, gaining electrons from the metal A to give the cation A^{n+} . Interestingly, if sulphur is replaced by a halogen, X, giving rise to the $[\text{M}_x\text{X}_z]^{(n-z)}$ anion, these two structural units in some cases exhibit a close relationship, as observed for $[\text{CoS}_4]^{6-}$ units, related to $[\text{CoCl}_4]^{2-}$ units and

$[\text{PdS}_2]^{2-}$ units related to PdCl_2 units. Also, the $[\text{FeS}_2]^-$ units show isostructurality with the $[\text{MnS}_2]^{2-}$ units, when Fe^{3+} is replaced by the isoelectronic Mn^{2+} .

The validity of the ionic model as a starting point for the description of structural features in ternary sulphides is what allows chemists to apply similar reasoning to oxides and sulphides, such as charge neutrality, ionic size and Vegard's law within families of isostructural compounds, for example the A_2MS_2 ($\text{A} = \text{K}, \text{Rb}, \text{Cs}$; $\text{M} = \text{Mn}, \text{Co}$) series, in which the unit cell parameters increase with the increasing size of the alkali metal.

In general more alkali metal reduces the cross linking³⁴ and this is illustrated by comparing, for example, AFe_2S_3 with AFeS_2 . In AFe_2S_3 (see section 1.5.3.1) the iron forms double tetrahedra³⁵ whereas in AFeS_2 (section 1.5.2.6), which has a higher alkali metal to iron ratio, the chains of tetrahedra are single.³⁶

Strong bonds within the chains and weak bonds between the chains not only favours a large degree of anisotropy in the structure, it also effects the physical properties, as exemplified by the many cases of S^{2-} mediated magnetic interactions located along chains of $[\text{M}_x\text{S}_z]^{n-}$ polyhedra. The lower electronegativity of sulphur compared to oxygen also means that the 3s and 3p energy levels are nearer to the 3d level in the metals allowing for increased orbital overlap. This increased covalency leads to antiferromagnetism in spin unpaired compounds and diamagnetism in spin paired compounds (e.g. planar (Pd, Ni, Pt)S). The increased diffuseness of the metal orbital also increases the metal-metal interaction leading to more metallic-like behaviour than in oxides.

There are a wide variety of sulphides that have already been synthesised but there are clearly many more yet to be discovered. In the Ba-Fe-S system alone there are over 10 different sulphides and whilst this is partially due to the flexibility of iron and its oxidation state it also suggests that a systematic study of other metal-sulphur combinations may yield further products.

In this review, the one-dimensional ternary sulphides included are subdivided according to the metal ratio A/M. Three broad classes of sulphides are identified according to whether A/M is equal to, smaller than or larger than one. Within these groups the sulphides are presented in terms of the connectivity of the polyhedra within the chains.

A brief description of the structure and the main physical properties will be provided for all the sulphides included.

1.5.2 Ternary One-Dimensional Sulphides $A_xM_yS_z$ Where $A:M = 1$

1.5.2.1 $BaMS_3$ (M = Ti, V, Nb, Ta)

These isostructural compounds consist of face linked MS_6 octahedra running in chains along the c axis (Figure 1.11). The space group of the $BaMS_3$ compounds is $P6_3/mmc$, the unit cell parameters are shown below in Table 1.2. $BaTiS_3$ was prepared by heating a mixture of barium carbonate and titanium sponge in a H_2S stream at $1250^\circ C$ for 2 days³⁷ whilst $BaNbS_3$ and $BaVS_3$ are synthesised by heating barium carbonate and niobium oxide (Nb_2O_5) or vanadium oxide (V_2O_5) at $800^\circ C$ for 24 hours in a carbon disulphide/nitrogen stream.³⁸ $BaTaS_3$ is prepared differently by heating a mixture of barium sulphide, tantalum and sulphur at $600^\circ C$ for 2 weeks followed by further heating at $1000^\circ C$ for 1 week in an evacuated silica tube.³⁹

Table 1.2 Unit cell parameters of the isostructural compounds $BaMS_3$

M	Ti ³⁷	V ⁴⁰	Nb ³⁸	Ta ³⁹
a (Å)	6.756(1)	6.7283(5)	6.840(2)	6.846(5)
c (Å)	5.798(1)	5.6263(5)	5.745(2)	5.744(5)

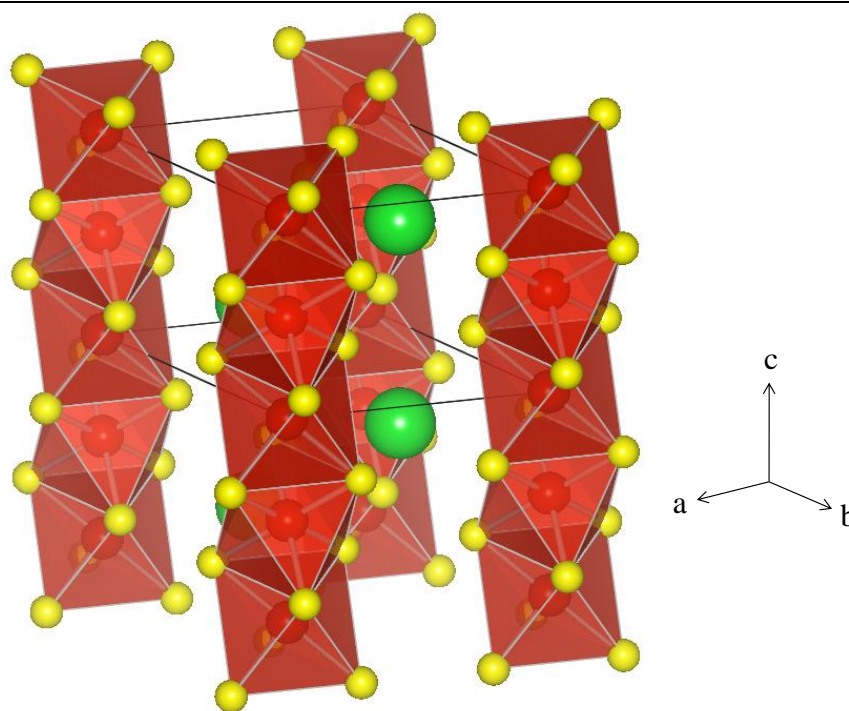


Figure 1.11 Structure of $BaMS_3$; the red polyhedra represent the M-S octahedra with yellow sulphur at the vertices and the green spheres represent Ba cations

These compounds provide a good example of the variation of physical properties as a function of the size or oxidation state of the cations as well as the effects of non-stoichiometry.

BaTiS₃ is the only compound of the series to contain a d⁰ cation, Ti⁴⁺, whilst the other stoichiometric compounds contain d¹ cations. BaTiS₃ shows semiconducting properties.

BaVS₃ is a metallic Pauli paramagnet and undergoes a transition to an antiferromagnetic semiconductor at 70 K with no associated structural (or spin-Peierls) transition. A slight structural distortion which induces some zigzagging of the chains does occur at 250 K.⁴¹

BaTaS₃ is a metallic like conductor as the Ta-Ta distance, 2.872(2) Å, is small enough for some direct d-orbital overlap. The non-stoichiometric BaTa_{0.8}S₃ is semiconductive and diamagnetic. There is no ordering of the Ta vacancies and the tantalum oxidises partially to Ta⁵⁺.

The properties of BaNbS₃ are in doubt due to difficulties in confirming the stoichiometry and the sensitivity of the properties to this stoichiometry. For example, BaNbS₃ was initially reported as diamagnetic and semiconducting¹⁰ but later studies suggested that the composition of that sample was BaNb_{0.8}S₃.⁴² Other workers have reported diamagnetism and a metal-to-semiconductor transition at 620 K due to the formation of Nb-Nb dimers.⁴³ Others have suggested that BaNbS₃ is always stoichiometric with respect to Ba and Nb and is metallic whilst the sulphur deficient compound BaNbS_{3-δ} undergoes a semiconductor-metal transition (at 130 K for BaNbS_{2.89}).⁴⁴ The most recent work suggests that with non-stoichiometry of sulphur, BaNbS_{3+δ}, a semiconductor-to-metal transition occurs (between 146 and 215 K for values of $2.96 \geq 3+\delta \leq 3.06$ with temperature independent magnetic susceptibility).⁴⁵

A partial solid solution of BaV_xTi_{1-x}S₃ was also reported. This series was synthesised by mixing BaCO₃, V₂O₅ and TiO₂ in ethanol and calcining the powder at 600°C for 5 hours in H₂S/Ar gas. To achieve good quality crystals this heating was repeated three times followed by a final annealing of pellets in evacuated quartz tubes at 800°C for 20 hours.⁴⁶ Substitution of 5% V by Ti induces semiconductive behaviour and also destroys the anti-ferromagnetism. Interestingly, BaV_{0.2}Ti_{0.8}S₃ shows negative magnetoresistance of 0.7% at 80 K in a 6 T field.^{46,47}

Further work is needed on this group of compounds to investigate fully the trends occurring in electrical and magnetic properties.

1.5.2.2 $\text{K}_2\text{Ta}_2\text{S}_{10}$

This compound crystallises in the monoclinic space group $P2_1/n$ with $a = 14.9989(13)$ Å, $b = 6.4183(4)$ Å, $c = 15.1365(13)$ Å, $\beta = 117.629(9)^\circ$. There are two crystallographically independent Ta sites which form two different zigzagging (Ta-Ta-Ta angles 139.3° and 139.0°) one dimensional chains (Figure 1.12). Ta is eight coordinated (this is the first example of eight coordinate Ta) to form heavily distorted bi-capped trigonal prisms which are face linked. The intra-chain Ta-Ta distances are $3.432(1)$ and $3.426(1)$ Å not allowing any direct Ta-Ta interaction. $\text{K}_2\text{Ta}_2\text{S}_{10}$ is synthesised from the polysulfide potassium sulphide (K_2S_3), tantalum sulphide, and sulphur heated at 500°C for 6 days in an evacuated sealed ampoule. This is followed by washing with DMF and acetone leaving dark red needles of $\text{K}_2\text{Ta}_2\text{S}_{10}$. So far no study has been made into the properties of this compound.⁴⁸

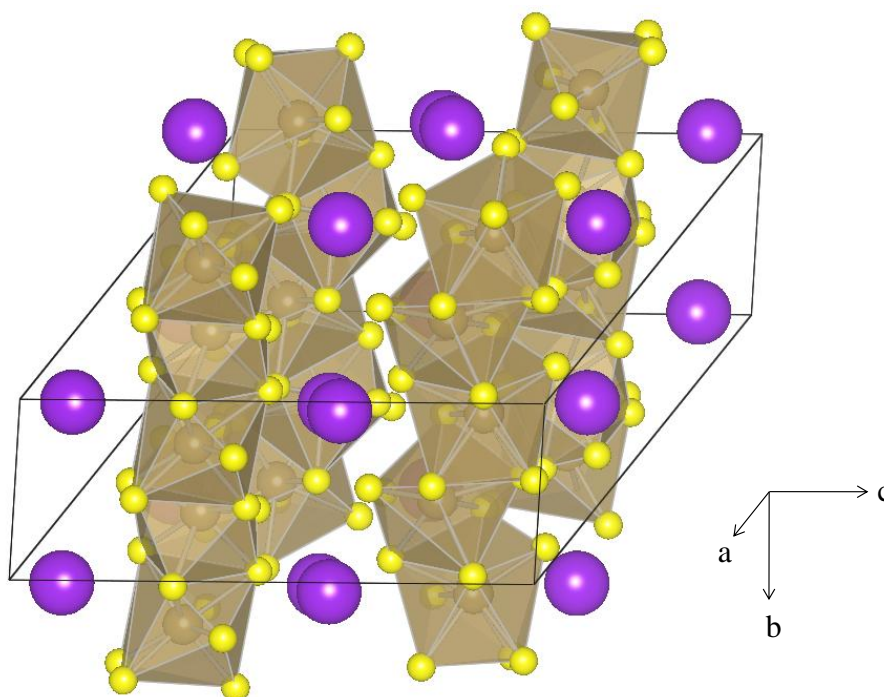


Figure 1.12 Structure of $\text{K}_2\text{Ta}_2\text{S}_{10}$ The brown polyhedra represent M-S bi-capped trigonal prisms, the purple spheres represent K^+ cation and the yellow spheres sulphur

1.5.2.3 AMS_3 (A = Sr, Sn, Pb, M = Hf, Zr)

These compounds adopt the $(\text{NH}_4)\text{CdCl}_3$ type structure, which is common among non sulphides, including a range of selenides. The structure consists of double chains of edge sharing octahedra running along the b axis (Figure 1.13). SrZrS_3 ($Pnma$; $a =$

8.5254(7) Å, $b = 3.8255(3)$ Å, $c = 13.9246(12)$ Å) adopts this structure at temperatures below 980°C⁴⁹ as well as at high pressure and is a semiconductor.⁵⁰ SnZrS₃,⁵¹ PbZrS₃,⁵² SnHfS₃,⁵³ PbHfS₃⁵³ and PbSnS₃⁵⁴ also adopt this structure. The unit cell parameters are shown in table 1.3. These compounds are all synthesised by heating stoichiometric amounts of the elements in evacuated silica tubes and heating to ~700°C for several days.

Table 1.3 Unit cell parameters for some sulphides AMS₃ adopting the (NH₄)CdCl₃ structure (no standard deviations quoted for PbSnS₃)

Formula	SnZrS ₃ ⁵¹	PbZrS ₃ ⁵²	SnHfS ₃ ⁵³	PbHfS ₃ ⁵³	PbSnS ₃ ⁵⁴
a (Å)	9.188(1)	9.0134(7)	9.139(1)	8.988(2)	8.738
b (Å)	3.717(1)	3.7660(2)	3.694(1)	3.739(1)	3.792
c (Å)	13.839(1)	13.9237(10)	13.875(4)	13.924(2)	14.052

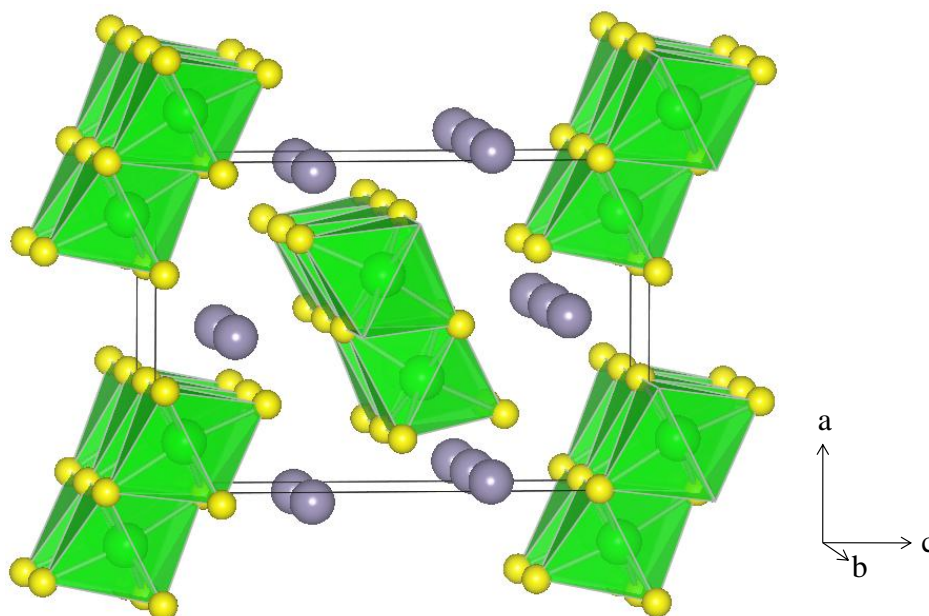


Figure 1.13 Structure of AMS₃ (A = Sr, Sn, Pb, M = Hf, Zr); the green polyhedra are M-S octahedra. The silver spheres represent A atoms and the yellow spheres sulphur

1.5.2.4 La₂Fe₂S₅

This structure consists of edge sharing FeS₆ octahedra running along the a axis which are interlinked with FeS₄ tetrahedra (Figure 1.14). La₂Fe₂S₅ is orthorhombic $Cmc2_1$: $a = 3.997(2)$ Å, $b = 16.485(5)$ Å, $c = 11.394(4)$ Å.⁵⁵ The compound is prepared by heating stoichiometric amounts of the binary sulphides La₂S₃ and FeS in sealed ampoules at 950°C for one month⁵⁶ or alternatively at 300°C for one week followed by 600°C for

one day and 980°C for a further week followed by slow cooling to allow for any dissociated sulphur to recombine.⁵⁷

A study into the magnetic properties revealed a Néel temperature of 11 K and suggested a Fe-S-Fe interaction within the chains and Fe-S-S-Fe interactions between chains.⁵⁷ A neutron diffraction study on $\text{La}_2\text{Fe}_2\text{S}_5$ confirmed these interactions as antiferromagnetic coupling *via* superexchange between the octahedral and tetrahedral Fe cations within the chains and found the magnetic structure to be monoclinic with space group $P2$.⁵⁸

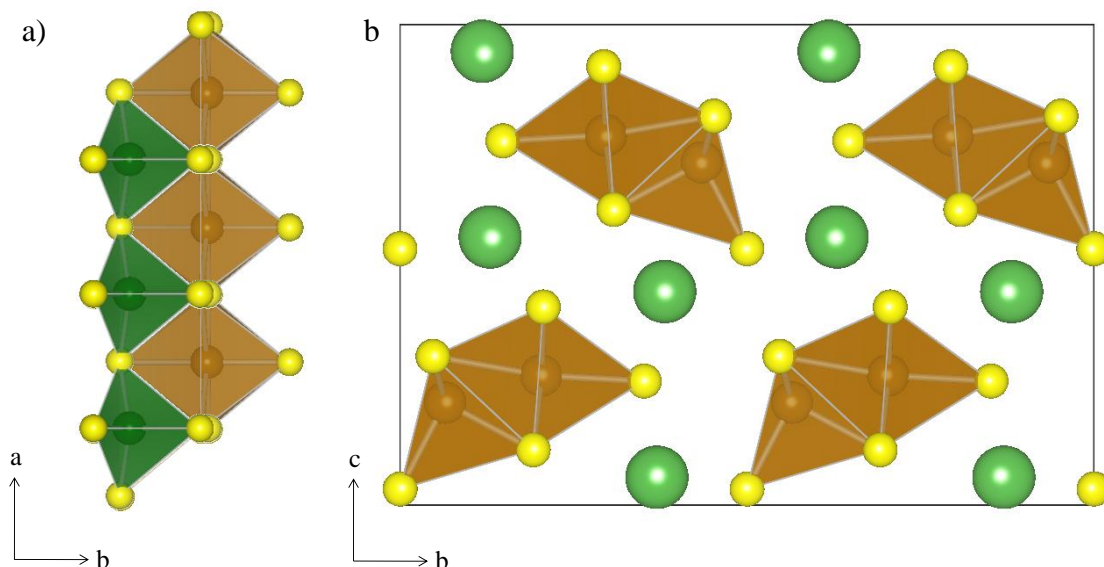


Figure 1.14 Structure of $\text{La}_2\text{Fe}_2\text{S}_5$ showing a) the interlinked FeS_4 tetrahedra and FeS_6 octahedra along the c axis b) the unit cell seen along the a axis

1.5.2.5 BaPdS_2

The structure of BaPdS_2 consists of square planes of PdS_4 edge linked in zigzagging chains (Figure 1.15). No analysis of the properties has yet been carried out. The space group is $Cmcm$, with $a = 6.783(1) \text{ \AA}$, $b = 10.634(2) \text{ \AA}$, $c = 5.327(1) \text{ \AA}$. The synthesis of BaPdS_2 is achieved by heating $\text{BaPd}(\text{CN})_4 \cdot 4\text{H}_2\text{O}$ for 3 hours at 600°C in a stream of H_2S or by mixing with sulphur and heating under argon, again for 3 hours at 600°C.⁵⁹

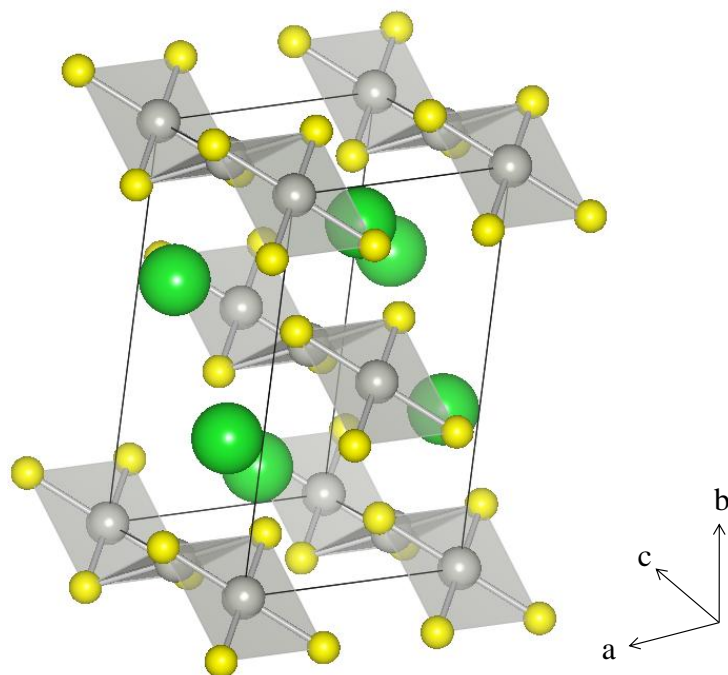


Figure 1.15 Structure of BaPdS_2 . The coordination of PdS_4 units is illustrated with silver square planes. The green spheres represent Ba atoms and the yellow spheres sulphur

1.5.2.6 AFeS_2 (A = K, Rb, Cs, Tl)

These compounds are all structurally related and show FeS_4 tetrahedra edge linked in one-dimensional chains with the alkali metal ions (or Tl) between these chains (Figure 1.16).

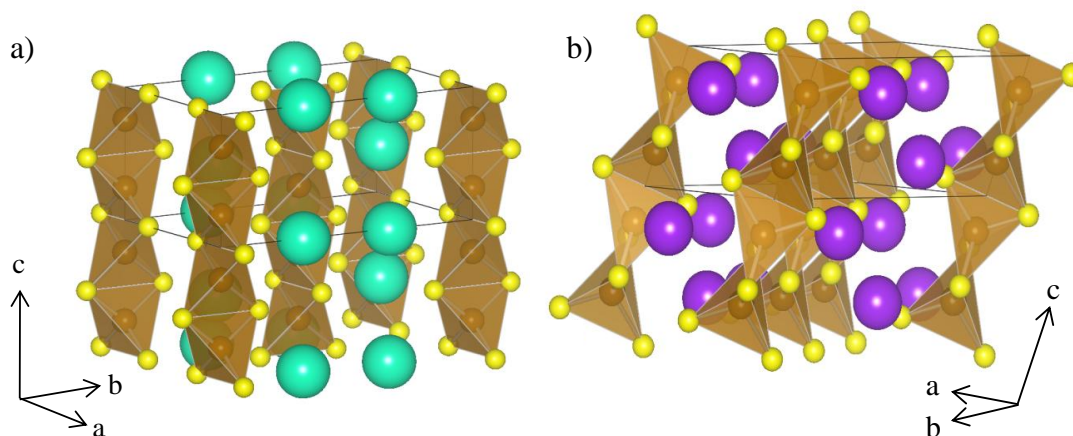


Figure 1.16 Structure of a) CsFeS_2 and b) KFeS_2 ; the brown tetrahedra are FeS_4 with yellow sulphur at the vertices. The blue spheres are Cs atoms and the purple spheres are K atoms

KFeS₂ and RbFeS₂ are isostructural and both monoclinic as is TlFeS₂ whilst CsFeS₂ is orthorhombic. Unit cell parameters and space groups for all the compounds in the AFeS₂ series are shown in table 1.4.

Table 1.4 Unit cell parameters of AFeS₂ (A = K, Rb, Cs, Tl) (No standard deviations quoted)

A	K ⁶⁰	Rb ⁶⁰	Cs ⁶¹	Tl ⁶²
Space group	<i>C2/c</i>	<i>C2/c</i>	<i>Immm</i>	<i>C2/m</i>
<i>a</i> (Å)	7.05	7.215	7.159	11.68
<i>b</i> (Å)	11.28	11.70	11.91	5.32
<i>c</i> (Å)	5.4	5.42	5.409	10.53
β (°)	112.5	112.0	90.0	144.6

These compounds are prepared by reaction of the alkali metal carbonates with iron powder and hydrogen sulphide gas at 725°C for several hours. The products are then extracted with water or ethanol.⁶¹ An alternative technique involving heating the elements has also been used, again followed by extraction using water.⁶⁰

The main difference between the structures of KFeS₂ (and the isostructural RbFeS₂) and CsFeS₂ is in the Fe-Fe distances. In both cases the interchain distances are around 7 Å and the tetrahedra are distorted with Fe-S distances ranging from 2.18 Å to 2.28 Å. In KFeS₂ the Fe-Fe intrachain distance is 2.7 Å whilst in CsFeS₂ the distance alternates between 2.61 Å and 2.82 Å. This difference influences the magnetic properties of the two compounds.⁶³

KFeS₂ and RbFeS₂ are both $S = 1/2$ one-dimensional anti-ferromagnets with characteristic broad peaks in the susceptibility data at ~550 K with a transition to three dimensional (3D) ordered anti-ferromagnet at 250 K and 188 K respectively. The intra- and interchain exchange constants for KFeS₂ have been calculated as $J_{\text{Intra}} = -440.7$ K and $J_{\text{Inter}} = 53.9$ K respectively.³⁶

CsFeS₂ shows a broad maximum in susceptibility at around 800 K but is paramagnetic until a structural and magnetic phase transition at 70 K. The alternating intrachain Fe-Fe distances result in two intrachain exchange constants of $J = -640$ K for the short distance, and $J_2 = 192$ K for the longer distance, which average out to $T_c -440$ K (the value for KFeS₂). The alternating bond lengths in CsFeS₂ remain even at high temperature, unlike a spin-Peierls system where the dimerisation is lost at high

temperatures. CsFeS₂ and KFeS₂ can, however, be viewed as low and high temperature analogues of a spin-Peierls system as the bond lengths are varied in CsFeS₂ and regular in KFeS₂ with roughly the same average distance.⁶³ Interestingly, TlFeS₂ shows the alternating Fe-Fe intrachain distances seen in CsFeS₂, in this case 2.617 Å and 2.703 Å but contains antiferromagnetic covalent chains with a switch to collinear 3D order at T_N = 196(1) K with intrachain coupling constant J = -55(3) meV.⁶²

In all of these compounds the iron is formally trivalent but there is considerable delocalisation due to short Fe-Fe bonds, for example, KFeS₂ can be described with iron present as Fe³⁺ d⁴ with one itinerant electron.³⁶

CsGaS₂ is structurally very similar to these compounds and it contains edge linked gallium centred tetrahedra.⁶⁴ It crystallises in the space group *C2/c* with $a = 7.428(4)$ Å, $b = 12.217(3)$ Å, $c = 5.905(5)$ Å, $\beta = 113.0(1)^\circ$ and substitution of small values of Ga for Fe, and vice versa, is possible. CsGa_{1-x}Fe_xS₂ forms a single monoclinic phase with values of $x \leq 0.25$ and an orthorhombic phase for $x \geq 0.95$.⁶⁵ In both cases the length of the *c* unit cell parameter, i.e. the axis along which the chains run, increases with the amount of Ga in the system. These compounds are unusual because susceptibility, Mössbauer studies and neutron diffraction data indicate that the iron is present in a tetrahedral environment but is low spin.

1.5.2.7 KCuS and KAuS

KCuS consists of chains of Cu-S zigzagging along the *c* axis (Figure 1.17). Each copper atom is co-ordinated linearly by two sulphur atoms. The space group is *Pna2*₁ with $a = 10.66(2)$ Å, $b = 6.20(2)$ Å and $c = 5.32(2)$ Å.⁶⁶ The compound is synthesised from the elements under an argon atmosphere at 700°C for 1 hour and isolated using paraffin oil.

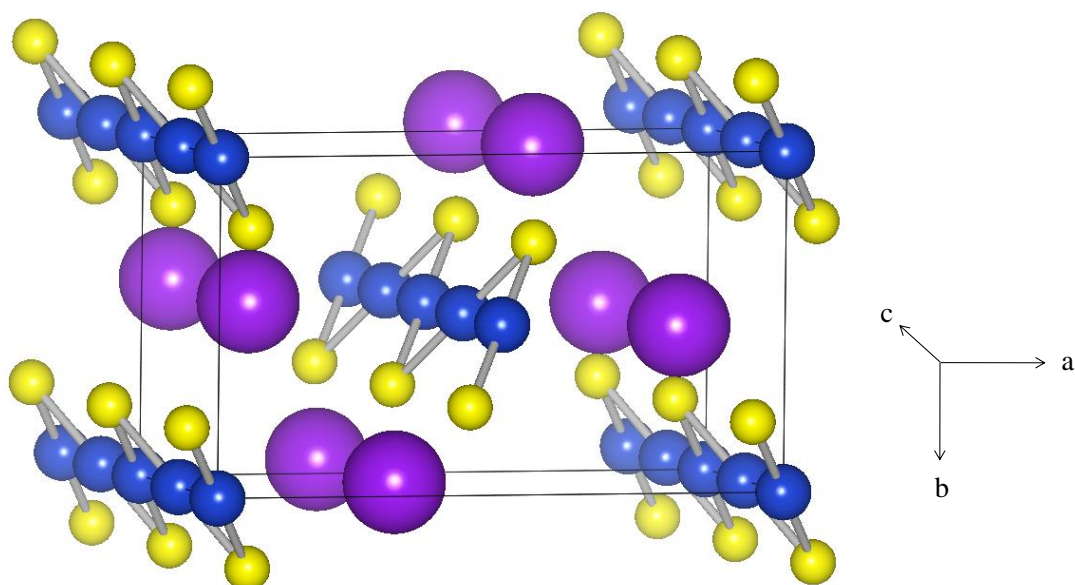


Figure 1.17 Structure of KCuS ; the blue atoms are Cu forming chains with the yellow sulphur spheres with purple K spheres

KAuS is structurally similar to KCuS but the zigzag chains run parallel to the c axis and perpendicular to the a axis without the tilting relative to the b axis seen in KCuS (Figure 1.18). KAuS crystallises in the space group $Cmcm$, with unit cell parameters $a = 6.304(3) \text{ \AA}$, $b = 7.850(4) \text{ \AA}$, $c = 6.520(3) \text{ \AA}$.⁶⁷ This compound is also prepared in an argon atmosphere at 700°C using potassium sulphide (K_2S) and gold as the starting materials.

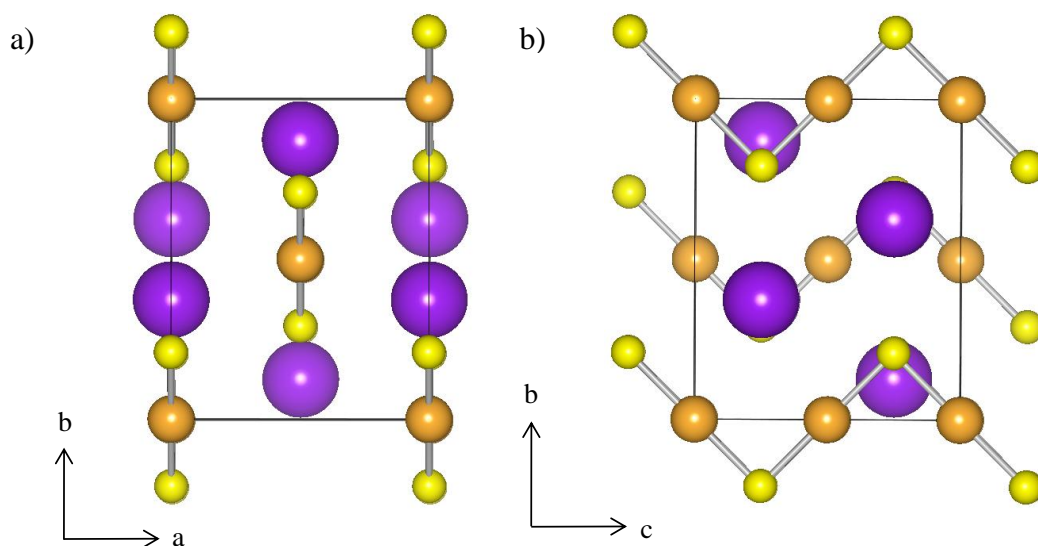


Figure 1.18 Structure of KAuS showing the chains of orange Au and yellow sulphur atoms along the a) c axis and b) a axis. The purple spheres represent potassium cations

1.5.3 Ternary One-Dimensional Sulphides $A_xM_yS_z$ Where $A:M < 1$

1.5.3.1 AFe_2S_3 ($A = K, Rb, Cs, Ba$)

These isostructural compounds are all orthorhombic $Cmcm$ (see table 1.5 for unit cell parameters) and consist of chains of double tetrahedra running along the c axis (Figure 1.19). Mössbauer, resistivity and susceptibility studies have been used to determine the oxidation state of iron in $BaFe_2S_3$. The single quadrupole shift, low resistivity ($\sim 0.5 \Omega\text{cm}$) and magnetic moment of $4.85\mu\text{B}$ all point to significant delocalisation, in this case of one half electron per atom.⁶⁸ In KFe_2S_3 iron is formally in oxidation state +2.5 with a random distribution of Fe^{2+} and Fe^{3+} over the single iron crystallographic site.⁶⁹

Table 1.5 Unit cell parameters for AFe_2S_3 ($A = K, Rb, Cs, Ba$)

A	K ³⁵	Rb ³⁵	Cs ³⁵	Ba ⁶⁹
a (Å)	9.0415(13)	9.2202(7)	9.5193(8)	8.7835(9)
b (Å)	11.0298(17)	11.2429(9)	11.5826(10)	11.219(1)
c (Å)	5.4177(6)	5.4450(3)	5.4820(4)	5.2860(5)

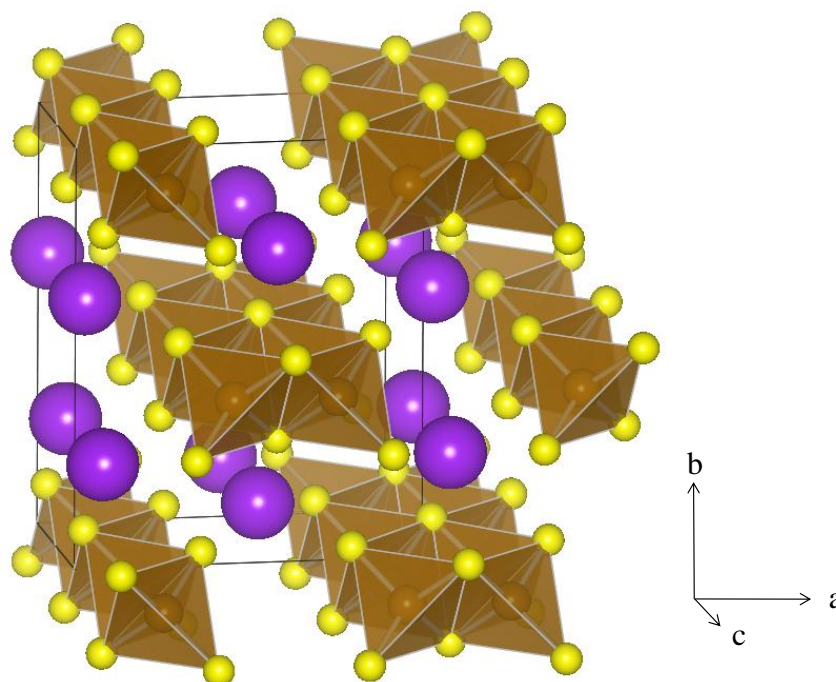


Figure 1.19 Representation of the structure of AFe_2S_3 ($A = K, Rb, Cs, Ba$). The brown tetrahedra are FeS_4 with yellow sulphur at the vertices. The purple spheres are A atoms

These compounds are synthesised in evacuated quartz or graphite coated tubes (to prevent attack on the quartz by barium sulphide) from binary alkali metal sulphides or

AFeS₂, with iron and sulphur. The stoichiometric mixtures are slowly heated to 750-1050°C for up to 5 days and then slowly cooled.

A solid solution of K_xBa_{1-x}Fe₂S₃ exists with *a* and *b* values increasing and *c* decreasing with increasing values of *x* (table 1.6).⁷⁰

Table 1.6 Unit cell parameters and Debye temperatures for the solid solution K_xBa_{1-x}Fe₂S₃⁷⁰

<i>x</i>	<i>a</i> (Å)	<i>b</i> (Å)	<i>c</i> (Å)	D (K)
0	8.795(2)	11.228(3)	5.285(2)	435
0.05	8.790(2)	11.216(3)	5.294(5)	418
0.1	8.808(2)	11.193(3)	5.305(1)	427
0.3	8.824(4)	11.171(5)	5.323(2)	405

1.5.3.2 Ba_{1+x}Fe₂S₄ (0.072 ≤ *x* ≤ 0.142)

The structure of this series of compounds is similar to the structure of the AFeS₂ (A = K, Rb, Cs, Tl) compounds discussed in section 1.5.2.6 as it consists of FeS₄ edge linked tetrahedra forming one-dimensional chains along the *c* axis (Figure 1.20).

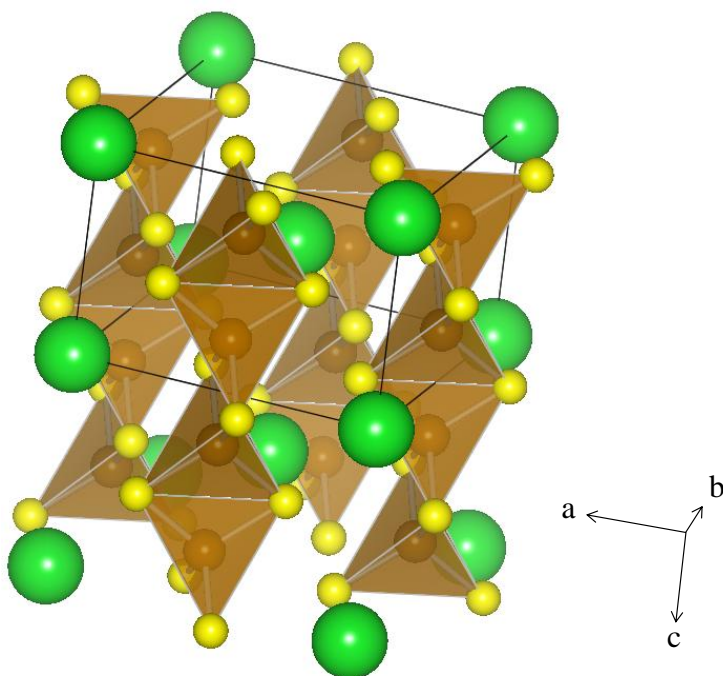


Figure 1.20 Structure of BaFe₂S₄. The brown tetrahedra are FeS₄ with yellow sulphur at the vertices. The green spheres are Ba cations

Initially, the series was thought to exist as a range with 0 ≤ *x* ≤ 0.142, but further study demonstrated that compounds in the range 0 ≤ *x* ≤ 0.072 actually consisted of a mixture

of BaFe_2S_4 and $\text{Ba}_{1.072}\text{Fe}_2\text{S}_4$ whilst the range $0.072 \leq x \leq 0.142$ is “infinitely adaptive” (as defined by Anderson⁷¹).⁷² Below $x = 0.072$ the value of the Ba-S distances becomes too low. They all crystallise in the tetragonal space group $I4/m$ with the stoichiometric end member BaFe_2S_4 having unit cell parameters $a = 7.678(2) \text{ \AA}$, $c = 5.292(4) \text{ \AA}$. For some compounds a superstructure along the c axis has been determined, for example a supercell with $a = 7.776 \text{ \AA}$ and $c = 49.86 \text{ \AA}$ for $\text{Ba}_{10/9}\text{Fe}_2\text{S}_4$, and $a = 7.776 \text{ \AA}$ and $c = 44.41 \text{ \AA}$ for $\text{Ba}_{9/8}\text{Fe}_2\text{S}_4$.⁷³

The preparation of these compounds was first performed by mixing barium sulphide, iron and excess sulphur and heating in an evacuated tube for several days. It was thought that the temperature (540-800°C) and amount of excess sulphur (barium to sulphur ratios of 1:4 to 1:6 were used) used could be used to control the stoichiometry of the reaction product. Further investigation revealed that it is the sulphur pressure inside the reaction vessel which controls the stoichiometry of the product formed with an increase in the sulphur pressure leading to a decrease in the value of x for a given temperature. To prepare the samples barium sulphide and iron are mixed and placed in loosely capped graphite tubes at one end of a silica tube with excess sulphur placed at the other end. The tube is sealed and evacuated and placed in a horizontal furnace with the barium sulphide and iron mixture at a constant temperature and the sulphur temperature varied to maintain a constant pressure within the tube. Varying the relative temperature of the Ba/Fe mixture and the sulphur allows for control over the sulphur pressure and therefore the stoichiometry of the final product. Typically the Ba/Fe mixture is heated between 650°C and 800°C and the sulphur between 130°C and 640°C for two days before being slow cooled.⁷⁴

1.5.3.3 AV_6S_8 (A = In, Tl, Na, K, Rb, Cs)

Crystallising in the hexagonal space group $P6_3$ the main structural feature of these compounds is the interpenetrating edge and face sharing VS_6 octahedra which result in hexagonal channels filled with A atoms (Figure 1.21). The V atoms are also linked in zigzagging chains with an average V-V distances of 2.86 \AA , comparable to the distance in metallic vanadium (2.61 \AA).⁷⁵ TlV_6S_8 is the only one of these compounds that can be synthesised directly and this is achieved by heating the elements at 800°C for 5 days in evacuated tubes.⁷⁶ The TlV_6S_8 is then reacted further to synthesise the other compounds. InV_6S_8 is prepared by de-intercalation of TlV_6S_8 using AlCl_3 and FeCl_3 to

give free V_6S_8 which is then reacted with indium metal at 500°C for 30 days.⁷⁵ The other compounds in this series have been successfully synthesised by performing ion exchange using TlV_6S_8 and Al or ABr ($A = K, Rb, Cs$).⁷⁷

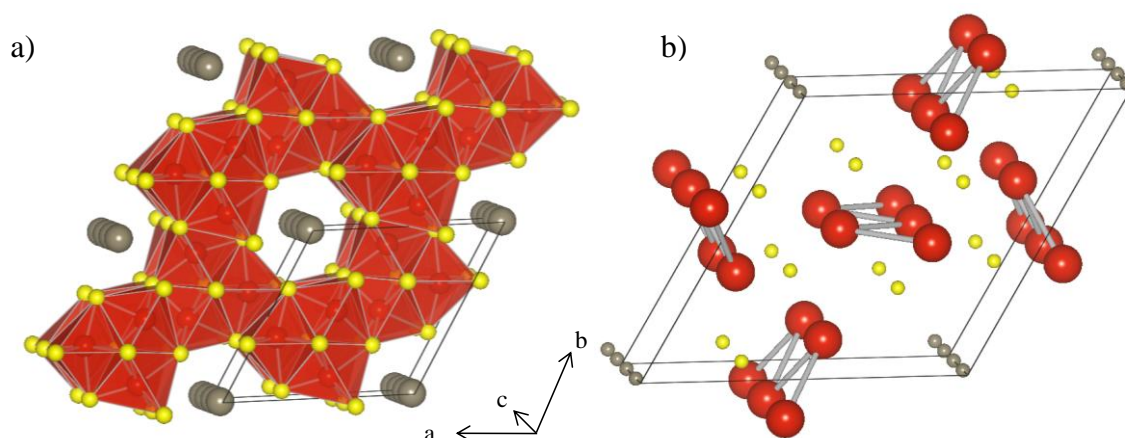


Figure 1.21 Representation of AV_6S_8 structure, showing a) hexagonal channels formed by red, linked VS_8 octahedra with yellow sulphur at the vertices and silver A cations in the channels and b) zigzagging vanadium chains. The sulphur (yellow) and A (silver) cations are represented relatively smaller for clarity

The unit cell parameters of the AV_6S_8 compounds are shown in table 1.7. It can be seen that the value of a increases with increasing ionic radius of the A cation whilst the c axis, which is the direction of the channels, changes only slightly.⁷⁶ These isotypic compounds are all (except for NaV_6S_8) superconductive with the T_c for the stoichiometric compounds shown in table 1.7.

Table 1.7 Unit cell parameters and T_c for compounds in the series AV_6S_8 (no errors quoted for InV_6S_8 and TlV_6S_8)

A	Na ⁷⁷	In ⁷⁸	K ⁷⁷	Tl ⁷⁶	Rb ⁷⁷	Cs ⁷⁷
a (Å)	9.1552(1)	9.1711	9.1897(1)	9.20400	9.2125(1)	9.2572(1)
c (Å)	3.3087(31)	3.2972	3.2800(19)	3.30580	3.3075(20)	3.2847(14)
T_c (K) ⁷⁵	-	3.9	0.71	4.1	0.65	0.32

As well as the stoichiometric compounds these compounds exist as $A_xV_6S_8$ ($x < 1$) with the structure remaining stable for $x \geq 0.2$. Many of these non-stoichiometric compounds are also superconductive. $Tl_xV_6S_8$, has critical temperatures $T_c = 3.5$ K for $x = 0.61$ and $T_c = 0.74$ K for $x = 0.26$. $In_xV_6S_8$ is superconductive at $T_c = 0.95$ K for $x = 0.63$ and at $T_c < 0.02$ K for $x = 0.46$.⁷⁵

1.5.3.4 Na₃Cu₄S₄

This compound has an unusual structure and contains four sided columns with each side made from corner linked S₃ trigonal planes with copper atoms sitting slightly out of the plane of these S₃ units (Figure 3.4).⁷⁹ Na₃Cu₄S₄ is synthesised from sodium carbonate, copper and sulphur, heated under argon to 600°C for 1 hour or under nitrogen to 550°C for 2 hours. The resulting blue-black crystals are washed with water and ethanol and vacuum dried. Initially mixed valency was ascribed to but X-ray photoelectron spectroscopy (XPS) showed mixed valence on the sulphur and therefore the formula is better written as .⁸⁰ This leads to partially filled bands which combined with the short Cu-Cu distance, leads to metallic like conduction. This conduction is significantly anisotropic and considerably higher along the chains.^{80,81}

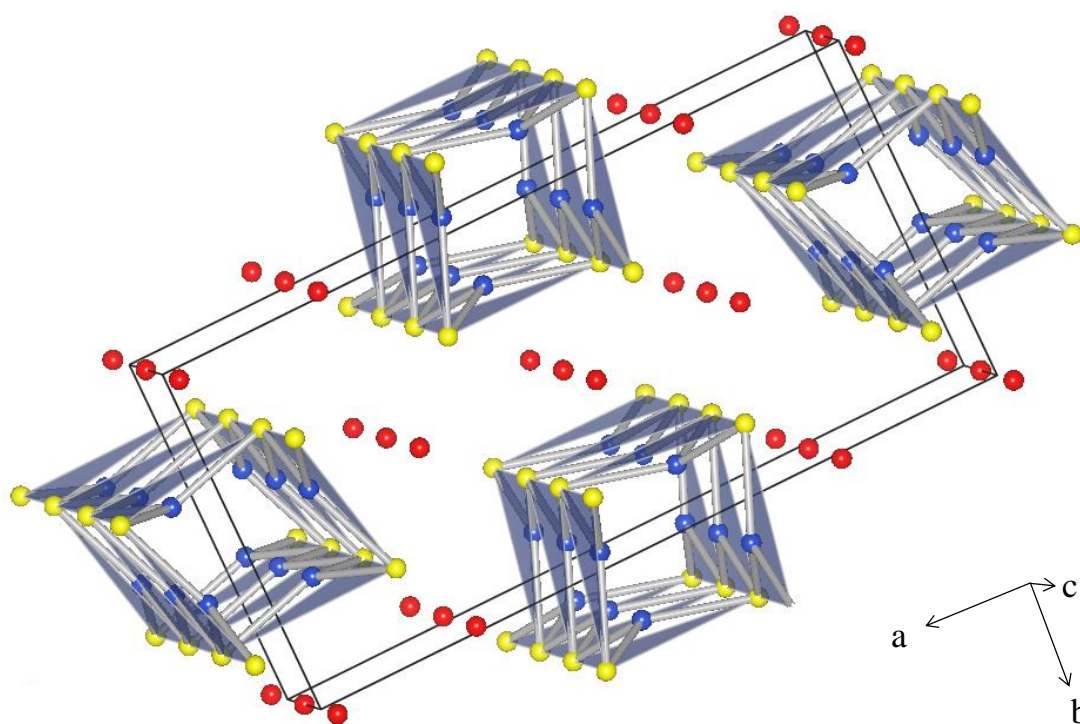


Figure 1.22 Structure of Na₃Cu₄S₄. Columns of S₃ trigonal planes with yellow sulphur at the vertices blue copper situated slightly out of the plane and red sodium cations in between

1.5.4 Ternary One-Dimensional Sulphides $A_xM_yS_z$ Where $A:M > 1$

1.5.4.1 Ba_3CrS_5 and $Ba_3Cr_2S_6$

These two compounds both contain chains of CrS polyhedra running along the c axis. In Ba_3CrS_5 the chains consist of face sharing octahedra (slightly elongated along the chains) (Figure 1.23a) and for $Ba_3Cr_2S_6$ the chains are formed by alternating between octahedra and trigonal prisms (slightly distorted with rotation of approximately 10° between top and bottom S_3 planes) (Figure 1.23b).⁸² Ba_3CrS_5 is hexagonal and crystallises in the space group $P6_3cm$ ($a = 9.1208(3)$ Å and $c = 6.1930(3)$ Å) whilst $Ba_3Cr_2S_6$ crystallises in the trigonal space group $R3c$ ($a = 11.8179(7)$ Å and $c = 12.796(1)$ Å). It is suggested that $Ba_3Cr_2S_6$ may have a superstructure caused by a mismatch in the barium chain and CrS_6 chain lengths although further work is needed to confirm this. The preparation of these compounds is performed at high pressure and temperature. Barium sulphide, chromium and sulphur are mixed and placed in a boron nitride cell which is then placed in a carbon tube heater within a pyrophyllite cube. The mixture is then heated to 1200°C at a pressure of 5GPa for 30 min and quenched to room temperature.⁸²

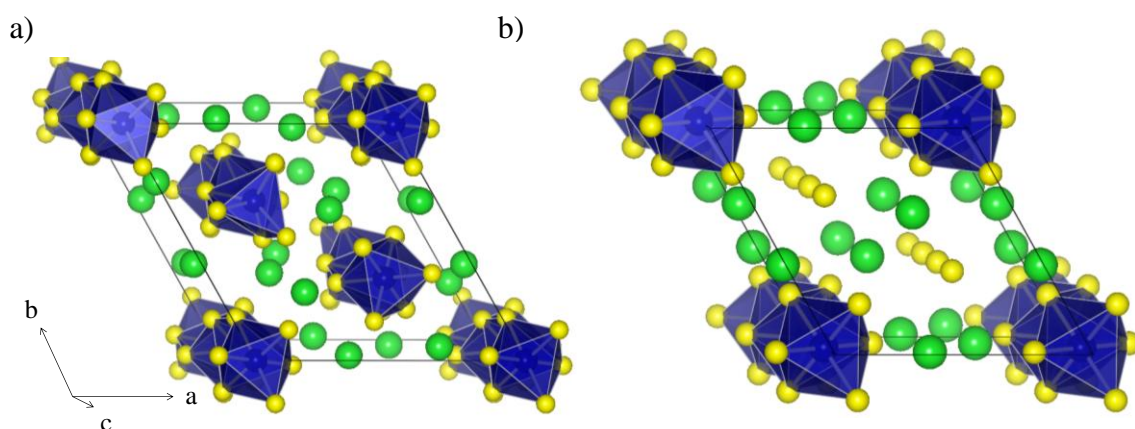


Figure 1.23 Representation of the structures of a) $Ba_3Cr_2S_6$ and b) Ba_3CrS_5 showing the blue chromium sulphide polyhedra with yellow sulphur at the vertices and green barium in between

1.5.4.2 A_2TiS_3 ($A = \text{Cs, K}$)

These two compounds are structurally very similar and consist of chains of TiS_5 square pyramids linked by edges with the apices of alternate pyramids pointing in opposite directions (Figure 1.23). The difference between the two structures is a slight monoclinic distortion from the Cs_2TiS_3 to the K_2TiS_3 structure. The unit cell parameters for K_2TiS_3 are; $a = 11.667(6)$ Å, $b = 8.325(4)$ Å, $c = 6.494(4)$ Å and $\beta = 91.81(4)^\circ$ $C2/c$.

The unit cell parameters for Cs_2TiS_3 are $a = 12.51(8) \text{ \AA}$, $b = 9.03(6) \text{ \AA}$ and $c = 6.55(10) \text{ \AA}$ $Cmc2_1$.^{83,84} There is also a small but significant difference in the apical Ti-S distances, as K_2TiS_3 shows $\text{Ti-S} = 2.188(3) \text{ \AA}$ and Cs_2TiS_3 has $\text{Ti-S} = 2.23(2) \text{ \AA}$.⁸³ K_2TiS_3 is synthesised from titanium, sulphur and potassium sulphide in sealed evacuated quartz ampoules at 800°C for 6 days.⁸³ Cs_2TiS_3 is synthesised by heating the binary sulphides in evacuated tubes for 14-20 days at $\sim 600^\circ\text{C}$.⁸⁴

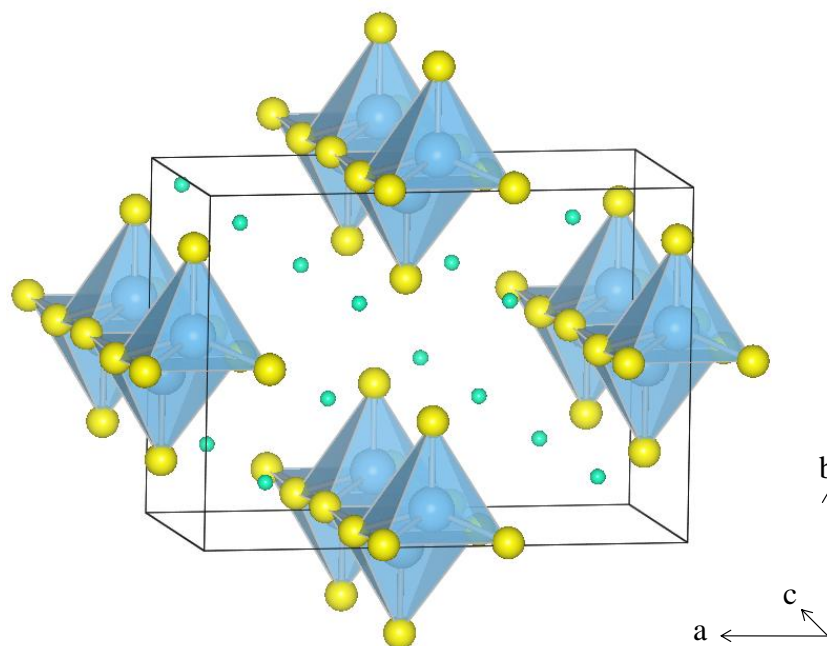


Figure 1.23 Representation of the structure of Cs_2TiS_3 showing blue square pyramids of CsS_5 with yellow sulphur at the vertices and green spheres representing Cs atoms. (The structure of K_2TiS_3 is very similar although the standard unit cell chosen is shifted $+1/2$ along the a axis)

1.5.4.3 Tl_2TiS_4

This compound crystallises in the space group $Pbca$ ($a = 22.176(7) \text{ \AA}$, $b = 9.484(4) \text{ \AA}$, $c = 6.3977(9) \text{ \AA}$) and contains chains of distorted TiS_6 octahedra edge linked in zigzagging chains (Figure 1.24). Tl_2TiS_4 is prepared from the elements in an evacuated tube heated to 1000°C for several days followed by slow cooling to room temperature.⁸⁵

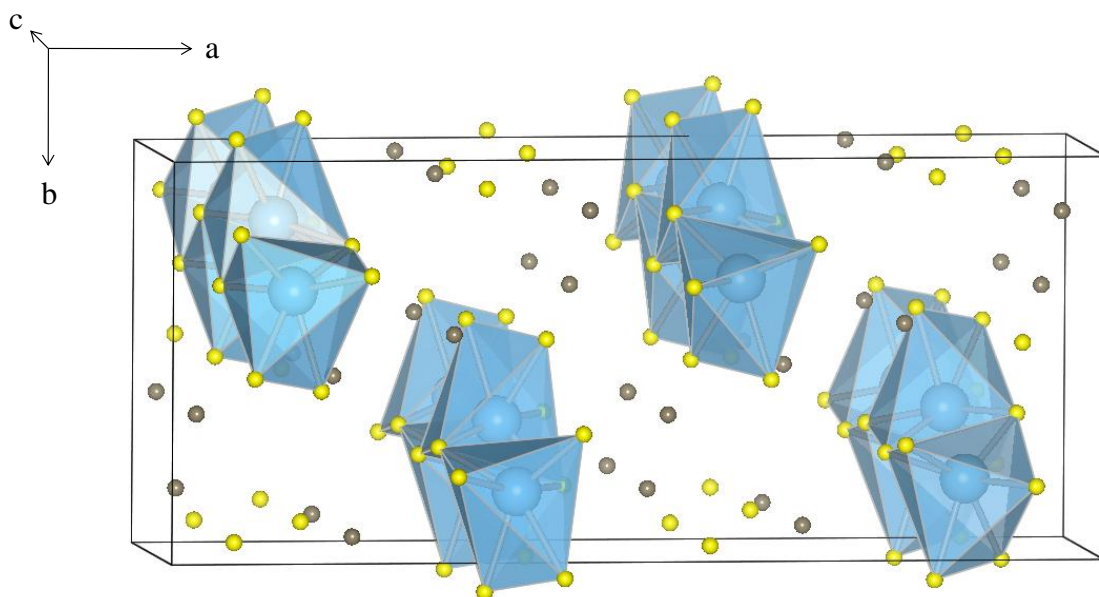


Figure 1.24 Representation of the structure of Tl_2TiS_4 showing blue TiS_6 octahedra with yellow sulphur and grey Tl atoms

It is interesting to note the similarities between this structure and the structure of A_2TiS_3 ($\text{A} = \text{Cs}, \text{K}$) seen in section 1.5.4.2. Figure 1.25 shows a representation of the titanium sulphide chains in the two structures viewed along the a axis. This shows that the coordination around the titanium is very similar in each case with the extra sulphur present in the Tl_2TiS_4 polyhedra sitting very close to the axial sulphur of the square pyramids ($\text{S-S} = 2.11(2) \text{ \AA}$); this positioning also explains the large distortion of the octahedra in Tl_2TiS_4 .

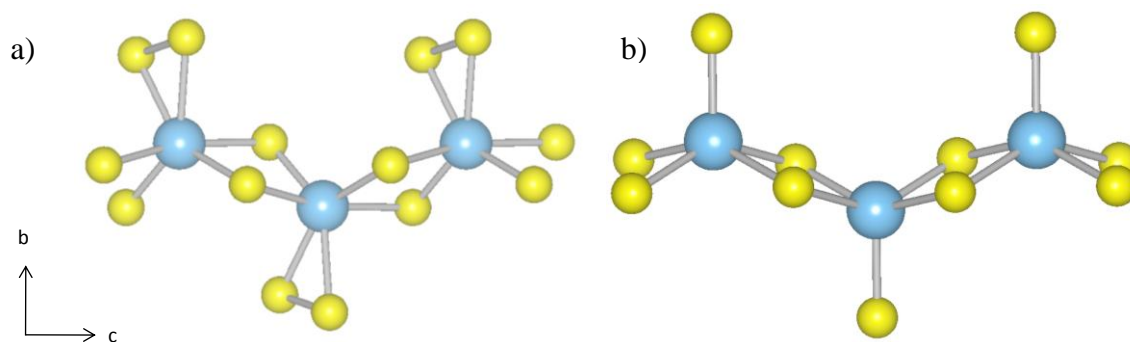


Figure 1.25 Representation of chains of a) TiS_6 in Tl_2TiS_4 and b) TiS_5 in A_2TiS_3 ($\text{A} = \text{Cs}, \text{K}$)

1.5.4.4 $A_3Fe_2S_4$ (A = Na, K, Rb, Cs, Tl)

This series of compounds is synthesised by heating the alkali metal carbonate, iron and sulphur in a hydrogen sulphide atmosphere for 20 hours at 650°C⁸⁶ or from the elements in evacuated tubes, at 900°C for 15-45 hours followed by cooling for 10 hours.⁸⁷ These compounds crystallise in the orthorhombic space group *Pnma* and contain one-dimensional zigzagging edge sharing chains of slightly distorted FeS_4 tetrahedra (Figure 1.26).⁸⁷ The compounds are isotypic except $Cs_3Fe_2S_4$, which has an Fe-Fe-Fe bond angle of 175.3° which is considerably higher than the others at 160° and has slightly different alkali metal-sulphur co-ordination. The lattice parameters are shown in table 1.8.

Table 1.8 Unit cell parameters of the compounds $A_3Fe_2S_4$ (A = Na, K, Rb, Cs, Tl) Standard deviations for $Tl_3Fe_2S_4$ were not reported

A	Na ⁸⁷	K ⁸⁶	Rb ⁸⁶	Cs ⁸⁶	Tl ⁸⁸
a (Å)	6.6333(5)	7.157(3)	7.4069(7)	7.540(2)	7.38
b (Å)	10.675(1)	10.989(4)	11.141(1)	11.168(5)	10.73
c (Å)	10.677(2)	11.560(4)	11.997(1)	12.923(4)	11.14

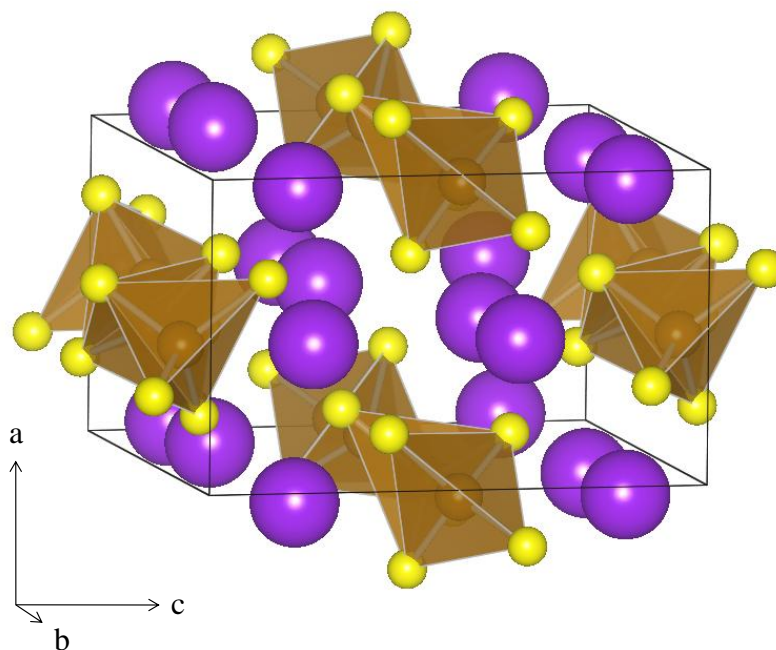


Figure 1.26 Representation of the structure of $A_3Fe_2S_4$ (A = Na, K, Rb, Tl). The brown tetrahedra are FeS_4 with yellow sulphur at the vertices. The purple spheres are A atoms

In $Na_3Fe_2S_4$ the Fe centres are coupled antiferromagnetically with a transition to 3D ferrimagnetism at 149 K. Mössbauer spectroscopy showed only one resonance between

4.2 K and 300 K, indicating that although iron is formally in a mixed valence state (+2/+3), delocalisation of electrons results in an averaging of the oxidation state over the iron atoms.⁸⁹ $\text{Tl}_3\text{Fe}_2\text{S}_4$ shows three-dimensional antiferromagnetic order with a Néel temperature T_N 90(5) K.⁸⁸

1.5.4.5 A_2MnS_2 (A = K, Rb, Cs)

These isotopic compounds crystallise in the space group *Ibam*, and show chains of edge-sharing MnS_4 tetrahedra, which run along the *c* axis (Figure 1.27). The unit cell parameters are shown in table 1.9. They are prepared by heating a mixture of the alkali metal carbonates and manganese under a hydrogen sulphide atmosphere at 800 – 920°C for 6 hours.

Table 1.9 Unit cell parameters for A_2MnS_2 (A = K, Rb, Cs)

A	K ⁹⁰	Rb ⁹⁰	Cs ⁹⁰
a (Å)	6.932(2)	7.119(1)	7.589(2)
b (Å)	12.62(3)	13.140(2)	13.781(4)
c (Å)	6.179(2)	6.295(1)	6.414(3)

The magnetic properties have been characterised and suggest antiferromagnetic interactions between the Mn atoms within the chains.⁹⁰

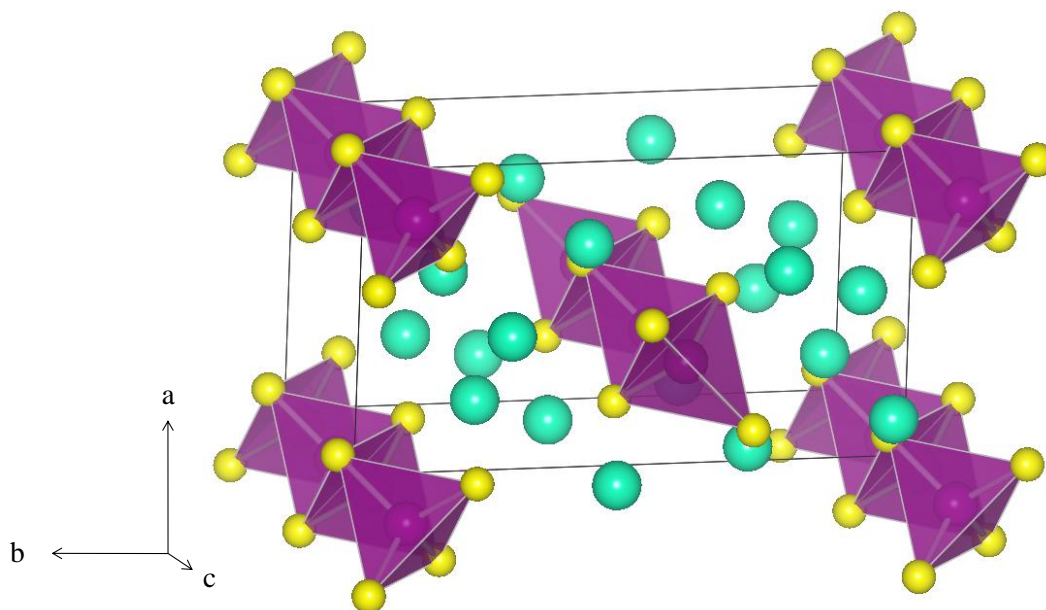


Figure 1.27 Representation of the structure of A_2MnS_2 (A = K, Rb, Cs) with purple Mn-S edge linked tetrahedra with yellow sulphur at the vertices and A cations represented by blue spheres

1.5.4.6 Na₂ZnS₂

This compound consists of chains of edge sharing ZnS₄ tetrahedra and crystallises (Figure 1.28) in the orthorhombic space group *Ibam* ($a = 6.421(2)$ Å, $b = 11.133(6)$ Å and $c = 5.942(4)$ Å).

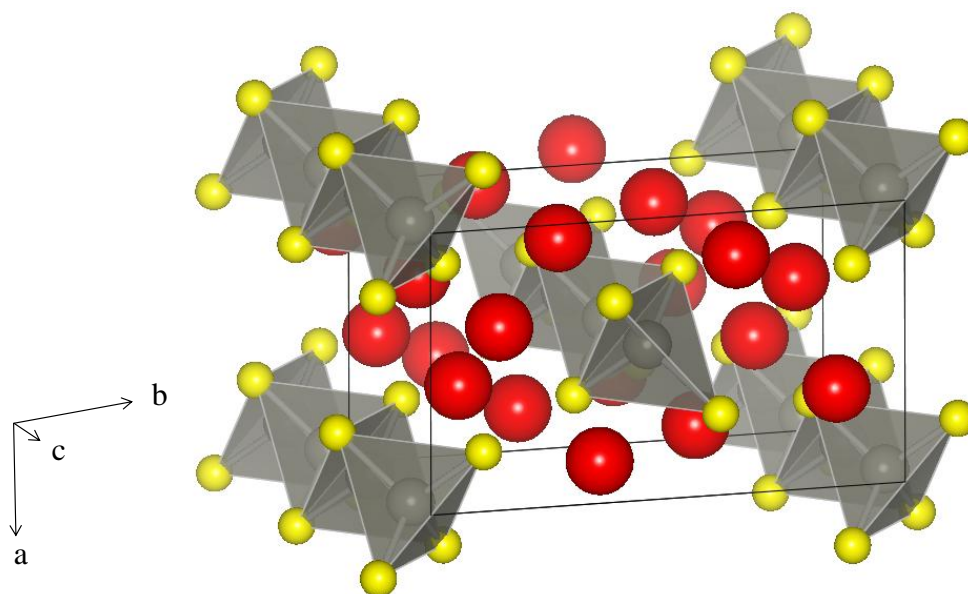


Figure 1.28 Representation of the structure of Na₂ZnS₂ showing grey Zn-S tetrahedra with yellow sulphur at the vertices with sodium atoms represented by red spheres

No properties have so far been reported for this compound. It is synthesised from a mixture of sodium carbonate, zinc sulphide and excess sulphur heated in a sealed tube to 830°C for several hours followed by extraction with paraffin oil.⁹¹

1.5.4.7 Na₅Co₂S₅

This compound crystallises in the space group *I4mm* with $a = 9.150(2)$ Å and $c = 6.222(2)$ Å. There are chains of CoS₄ tetrahedra separated by further sulphur and sodium atoms (Figure 1.29). All the cobalt atoms are crystallographically equivalent and in the +2.5 oxidation state. Na₅Co₂S₅ is prepared from cobalt and sodium carbonate in a hydrogen sulphide atmosphere at 725°C, it forms black shiny needles which are sensitive to air and moisture. No properties have so far been reported for this compound.⁹²

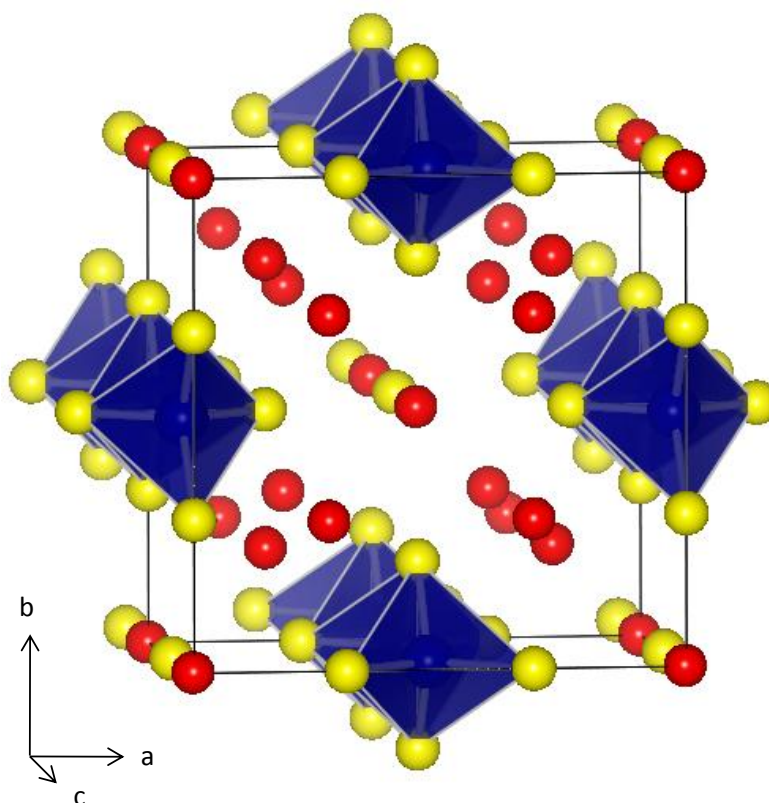


Figure 1.29 Representation of the structure of $\text{Na}_5\text{Co}_2\text{S}_5$ with blue CoS_4 tetrahedra with sulphur represented by yellow spheres and sodium by red spheres

1.5.4.8 A_2CoS_2 (A = Na, K, Rb, Cs)

These isostructural compounds crystallise in the space group *Ibam*. The unit cell parameters are shown in table 1.10 and exhibit the expected increase with increasing ionic radius of the alkali metal. The structure contains chains of edge linked CoS_4 tetrahedra (Figure 1.30). K_2CoS_2 has been analysed by neutron diffraction along with magnetic susceptibility and showed antiferromagnetic coupling of the cobalt ions along the chains with an onset of 3D order at 9.5 K. These compounds are synthesised from a stoichiometric mixture of the alkali metal carbonates and cobalt heated under a hydrogen sulphide atmosphere.⁹³

Table 1.10 Unit cell parameters for A_2CoS_2 (A = Na, K, Rb, Cs)⁹³

A	Na	K	Rb	Cs
a (Å)	6.373(3)	6.710(2)	6.959(1)	7.232(5)
b (Å)	11.208(4)	12.491(5)	13.096(2)	13.722(7)
c (Å)	5.850(2)	6.085(2)	6.219(1)	6.322(4)

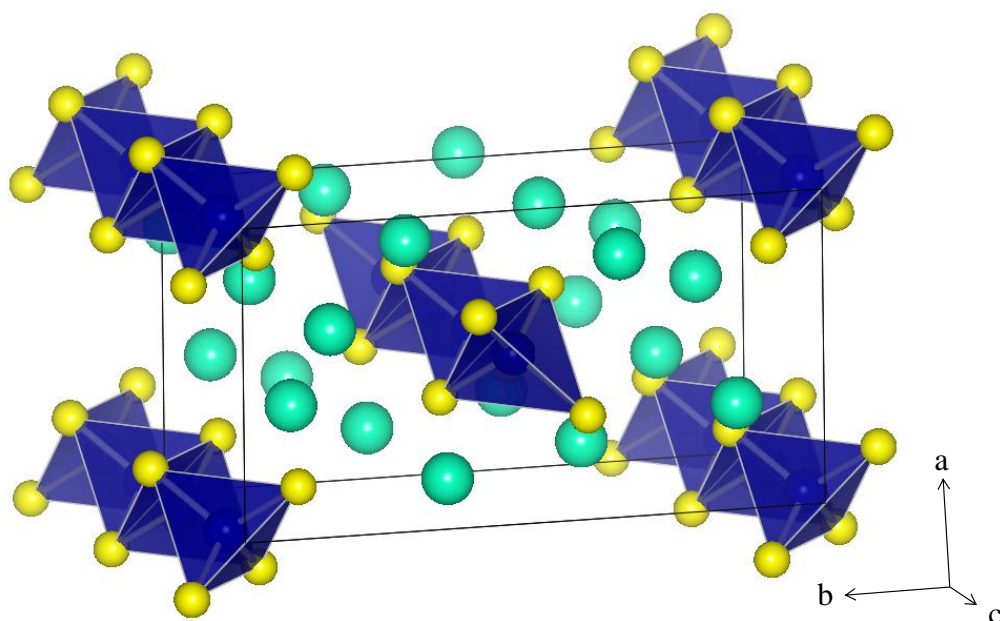


Figure 1.30 Representation of the structure of A_2CoS_2 ($A = Na, K, Rb, Cs$). The dark blue polyhedra represent CoS_4 tetrahedra with yellow sulphur at the vertices and A atoms represented by light blue spheres

1.5.4.9 A_2MS_2 ($A = Na, K, Rb, M = Pt, Pd$)

These compounds all show square planar coordination of the sulphur around the Pt/Pd atoms with the square planes edge-connected in chains running along the short axis. The compounds K_2PtS_2 and Rb_2PtS_2 crystallise in the space group $Immm$ and the square planes are parallel to the c axis (Figure 1.31a).⁹⁴ The compounds Na_2PtS_2 and Na_2PdS_2 are slightly different as the square planes are tilted with respect to the short axis, a , (Figure 1.31b) and crystallise in the space group $Cmc2_1$. The unit cell parameters are shown in table 1.11.⁹⁵ The compounds are synthesised by heating the alkali metal sulphide with sulphur and platinum at $850\text{ }^\circ\text{C}$ ⁹⁴ or with $Pd(NH_3)_2Cl_2$ at $900\text{ }^\circ\text{C}$.⁹⁵

Table 1.11 Unit cell parameters of A_2MS_2 ($A = Na, K, Rb, M = Pt, Pd$) (no errors quoted for K_2PtS_2 and Rb_2PtS_2)

	K_2PtS_2 ⁹⁴	Rb_2PtS_2 ⁹⁴	Na_2PtS_2 ⁹⁵	Na_2PdS_2 ⁹⁵
a (Å)	9.37	9.87	3.548(1)	3.539(2)
b (Å)	7.08	7.33	10.437(1)	10.411(4)
c (Å)	3.59	3.64	10.877(2)	10.886(4)

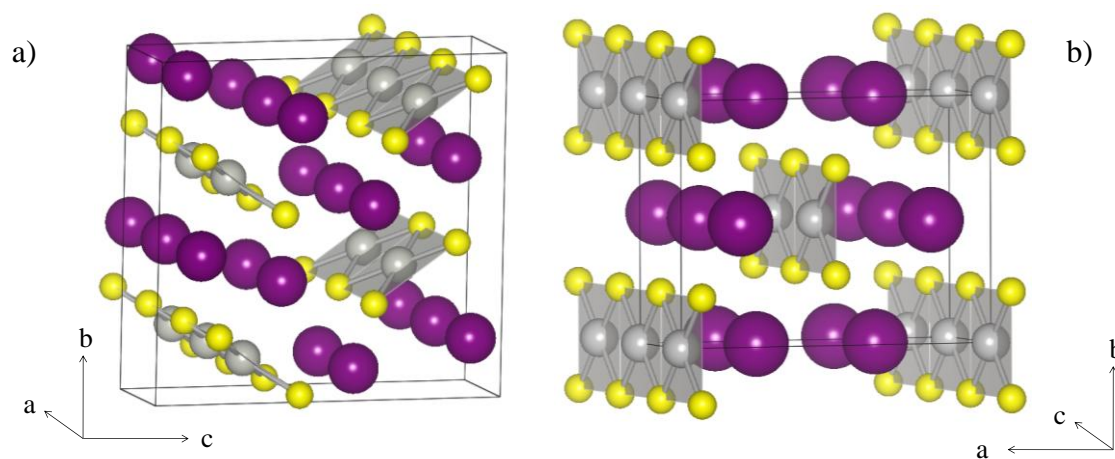


Figure 1.31 Representation of a) A_2PtS_2 ($A = K, Rb$) and b) Na_2MS_2 ($M = Pt, Pd$) structure, showing edge sharing square planes of silver M atoms and yellow sulphur atoms with purple A atoms in chains in between

A theoretical study, using density functional methods, has been undertaken on PtS_2 chain compounds and correctly predicted the structure of K_2PtS_2 and its semiconductive one dimensional behaviour, provided long range Coulomb interactions were considered.⁹⁶

1.5.4.10 $Ba_7Fe_6S_{14}$

$Ba_7Fe_6S_{14}$ is prepared by heating a stoichiometric mixture of barium sulphide, iron and sulphur under vacuum at 800-1100°C. This compound crystallises in the monoclinic space group $C2/c$ with $a = 25.490(2) \text{ \AA}$, $b = 8.244(1) \text{ \AA}$, $c = 14.949(2) \text{ \AA}$, $\beta = 118.85(6)^\circ$ (Figure 1.32).⁹⁷ The iron atoms are in FeS_4 tetrahedra, which are edge linked to form trinuclear units. These groups of three tetrahedra are themselves linked via corners to form infinite chains (Figure 1.33). The Fe-Fe distances between the edge linked tetrahedra are 2.747(7) \AA and 2.829(7) \AA , whilst the distance for the corner linked iron atoms is higher at 3.669(3) \AA . The Fe-S distances also vary; the Fe-S bonds that are not involved in edge or corner sharing are the shortest at 2.24-2.28 \AA . The Fe-S bonds for the corner linked sulphurs are 2.30(2) \AA whilst the longest bonds are those between iron and the edge linked sulphurs which are between 3.2 and 3.6 \AA . Mössbauer spectroscopy has shown that the iron oxidation state is averaged at +2.5 suggesting delocalisation of the electrons but the large resistivity of 10^5 \Omega cm implies that this delocalisation is limited to within the trinuclear units. $Ba_7Fe_6S_{14}$ orders antiferromagnetically at 200 K.⁶⁸

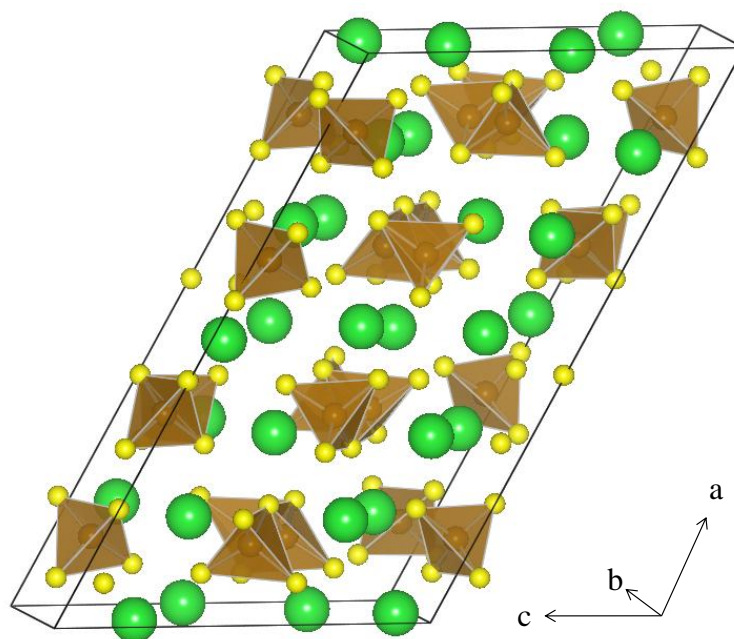


Figure 1.32 Representation of the structure of $\text{Ba}_7\text{Fe}_6\text{S}_{14}$ showing brown iron sulphide tetrahedra with sulphur at the vertices and green barium

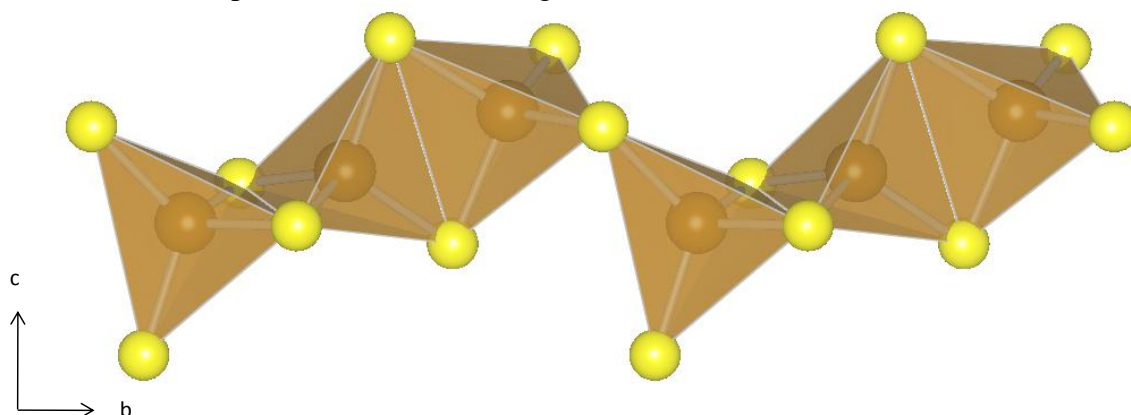


Figure 1.33 Representation of a chain within the $\text{Ba}_7\text{Fe}_6\text{S}_{14}$ structure, formed by corner linked trinuclear units of edge sharing tetrahedra

1.5.4.11 $\text{Ba}_6\text{Fe}_8\text{S}_{15}$

$\text{Ba}_6\text{Fe}_8\text{S}_{15}$ crystallises in the space group $I4/m$, with $a = 11.408(2) \text{ \AA}$, $c = 10.256(2) \text{ \AA}$. In this structure FeS_4 tetrahedra are corner linked into tetranuclear units. These units are then further linked *via* edges to form infinite chains which run along the c axis (Figure 1.34). It is prepared by heating a stoichiometric mixture of barium sulphide, iron and sulphur in a vacuum sealed graphite tube heated to 300°C for 4-5 hours then $750\text{--}1050^\circ\text{C}$ for 2 days.⁹⁸

The low value of electrical resistivity ($\sim 1 \text{ \Omega cm}$) indicates mobile electrons and Mössbauer spectroscopy showed that all the iron atoms are equivalent suggesting ease

of electron delocalisation. The magnetic moment is consistent with an averaging of giving a mean iron oxidation state of +2.25.⁶⁸

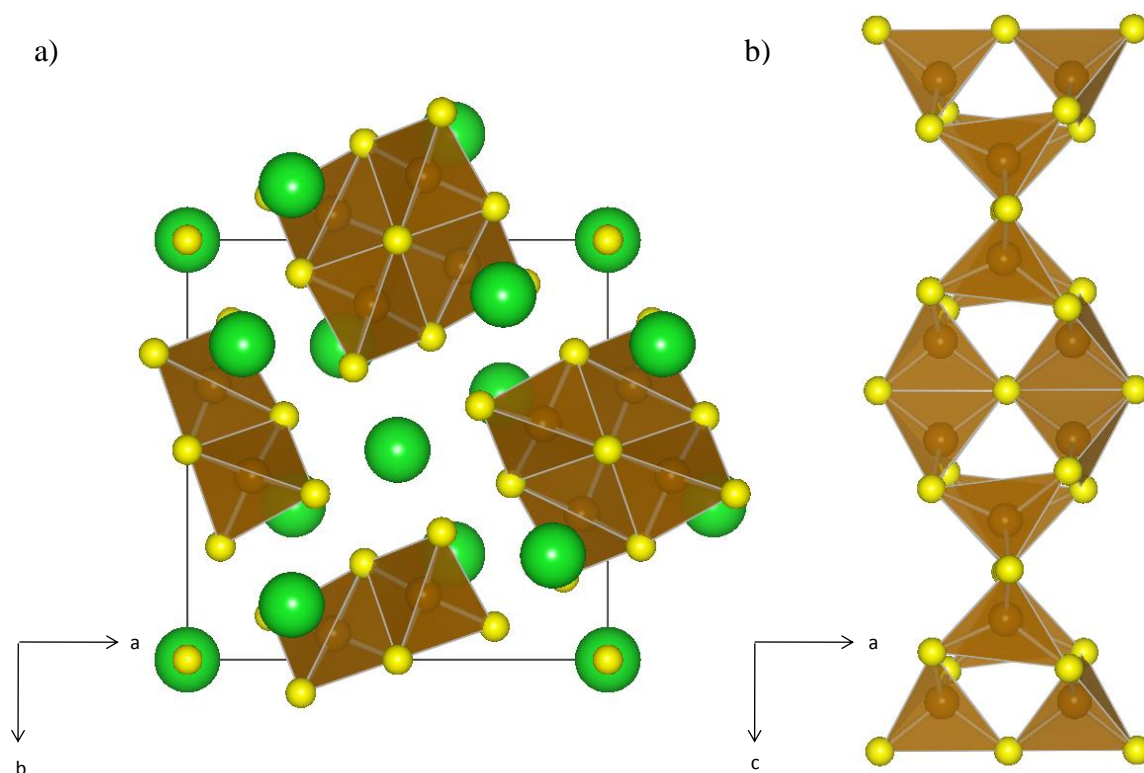


Figure 1.34 Structure of Ba₆Fe₈S₁₅. The brown tetrahedra are Fe-S and the green spheres are Ba cations. Showing a) a projection along the *c* axis and b) along the *b* axis showing how the tetrahedra are linked via corners and edges to form infinite columns

1.5.4.12 Ba₂MS₃ (M = Mn, Hg, Cd, and Fe, Co, Zn)

These compounds can be split into two isostructural groups with only slight structural differences between these groups. The first group contains Ba₂MS₃ with M = Mn, Hg and Cd and the second has M = Fe, Co and Zn but all of these compounds crystallise in the space group *Pnma*. The structural features common to both types consist of distorted MS₄ tetrahedra corner linked in chains running along the *c* axis (Figure 1.35 a and b). The difference between the two structure types arises at the Ba site. In both there are two crystallographically different sites containing Ba²⁺. In the Ba₂MnS₃ type both Ba sites consist of trigonal prisms mono-capped at a rectangular face. In the Ba₂CoS₃ type one site is again a mono-capped trigonal prism whilst the other consists of a distorted trigonal prism with one face capped. The differences in this coordination give rise to differences in the overall structure with the Ba²⁺ polyhedra forming chains in Ba₂MnS₃ and dimeric units in Ba₂CoS₃. Ba₂MnS₃ can be described as a K₂AgI₃ type and Ba₂CoS₃ crystallises as the K₂CuCl₃ type. A study comparing these two structural types has

attributed the reason for the formation of one type over the other to the nature of the transition metal and perhaps the small difference in the geometry of the tetrahedra.⁹⁹ The unit cell parameters of the compounds in both groups are shown in table 1.12. These compounds can be made either from the elements or binary sulphides in evacuated silica or graphite coated tubes at $\sim 1000^\circ\text{C}$ for several days¹⁰⁰ or by heating oxides or carbonates of metals (or in the case of Ba_2ZnS_3 , BaZnO_2)¹⁰¹ under hydrogen sulphide or carbon disulphide atmospheres at $\sim 1000^\circ\text{C}$ for ~ 24 hours.¹⁰²

Table 1.12 Unit cell parameters of the compounds Ba_2MS_3 (M = Mn, Hg, Cd, and Fe, Co, Zn). Standard deviations for Ba_2ZnS_3 were not reported. a - Volumes calculated as not quoted

M	Mn ¹⁰³	Cd ¹⁰⁴	Hg ¹⁰⁵	Fe ⁹⁸	Co ¹⁰⁶	Zn ¹⁰¹
a (Å)	8.814(5)	8.9145(6)	8.93(1)	12.087(5)	12.000(1)	12.05
b (Å)	4.302(2)	4.3356(2)	4.35(7)	4.246(2)	4.205(2)	4.21
c (Å)	17.048(8)	17.2439(9)	17.25(7)	12.359(5)	12.470(1)	12.65
V (Å ³) ^a	646(1)	666.47(2)	670(1)	634.3(3)	629.24(4)	641.7

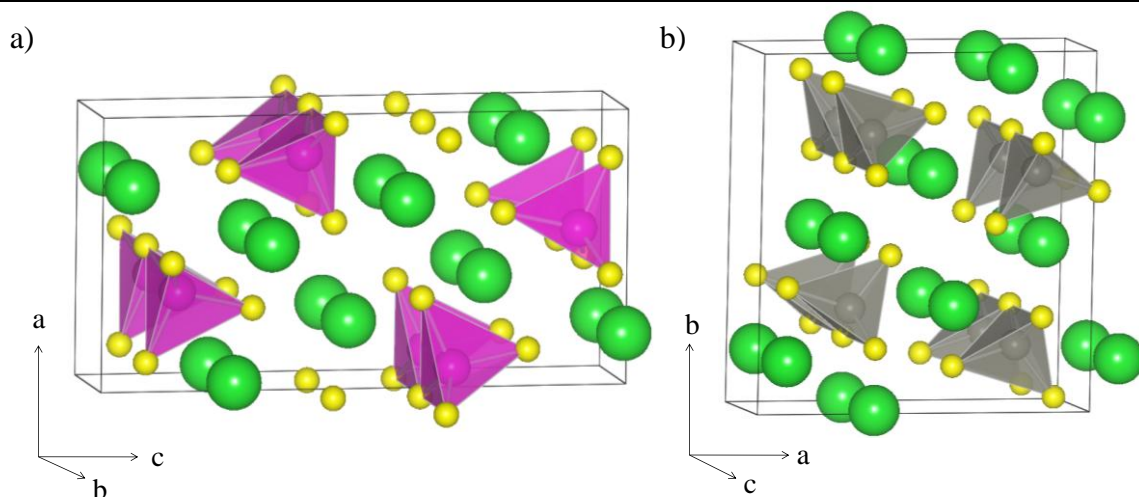


Figure 1.35 Representation of the structure of the compounds Ba_2MS_3 where a) M = Mn, Hg, Cd and b) M = Fe, Co, Zn

An investigation into the magnetic susceptibilities of Ba_2FeS_3 , Ba_2CoS_3 and Ba_2MnS_3 showed broad maxima at 130, 125 and 100 K respectively, features consistent with quasi-one-dimensional antiferromagnetic short-range ordering.¹⁰⁷ Intrachain interactions, J , of -20 , -15 and -12 K (in good agreement with value of $-12.3(5)$ K found in a previous paper on Ba_2MnS_3 and Ba_2MnSe_3)¹⁰³ were found for Ba_2FeS_3 , Ba_2CoS_3 and Ba_2MnS_3 . Long range magnetic ordering was found for all three compounds at 4.2 K due to interchain interactions.¹⁰⁷ The magnetic susceptibility of Ba_2CoS_3 has been reinvestigated and the data again showed a broad peak indicative of

one-dimensional magnetic ordering but also a kink at 46 K, indicative of a transition to long range order, T_N .¹⁰⁶ A more in depth analysis of the structure and properties of Ba_2CoS_3 follows in section 1.6.

Ba_2MnS_3 is insulating with a room temperature resistivity of $10^2 - 10^3 \Omega \text{ cm}$.¹⁰⁸ The resistivity of Ba_2CoS_3 is much lower at $\sim 10^{-1} \Omega \text{ cm}$ and thermopower measurements were indicative of metallic like conduction.¹⁰⁹ Ba_2CoS_3 shows negative magnetoresistance $\sim -1.7\%$ in a 7 T field at 10 K which is higher than that of the only other one dimensional sulphide so far reported to show negative MR ($BaV_{0.8}Ti_{0.2}S_3$ MR $\sim -0.8\%$ in 7 T at 80 K, see section 1.5.2.1).¹⁰⁹

The intra-chain coupling was determined as $-37 \pm 2 \text{ K}$ and the inter-chain coupling J' was estimated to be $\sim 0.9 \text{ K}$.¹¹⁰ A powder neutron diffraction study at 1.5 K showed that the magnetic unit cell is double the crystallographic unit cell along the c axis ($a = 11.971(1) \text{ \AA}$, $b = 12.443(1) \text{ \AA}$, $c = 8.3781(8) \text{ \AA}$).¹¹¹

An investigation into Ba_2FeS_3 suggests limited electron delocalisation. The high resistivity ($10^4 \Omega \text{ cm}$), the effective magnetic moment of $5.29 \mu_B$ and Mössbauer spectroscopy suggest that iron is present as Fe^{2+} .⁶⁸

1.5.5 Conclusion

Some general trends can be seen within this group of compounds and it is possible to see how changing the structure of a compound can be used to affect the properties.

All of the Pt^{2+}/Pd^{2+} (d^8) containing compounds show the expected square planar arrangement and they show chains similar to $PdCl_2$ type units.¹¹²

Iron shows a preference for tetrahedral geometry in both the 2+ and 3+ oxidation state and many of these tetrahedral compounds show structures based on that of SiS_2 ,¹¹³ see figure 1.36, including $A_3Fe_2S_4$ and $AFeS_2$. The compounds A_2CoS_2 , A_2MnS_2 and Na_2ZnS_2 also show structures related to this.

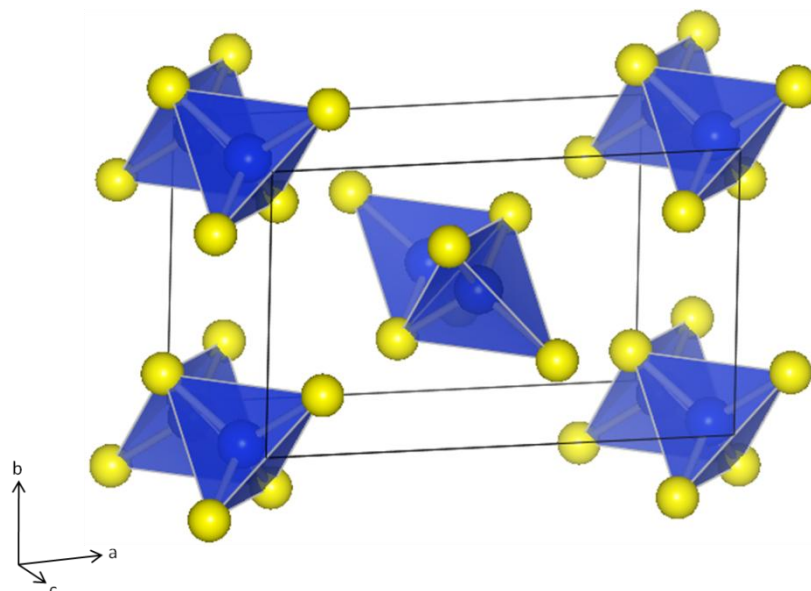


Figure 1.36 Structure of SiS_2 showing edge linked tetrahedra seen in many one dimensional sulphides

As expected from the strong interactions between transition metals and sulphur all of the compounds with $S = \frac{1}{2}$ transition metals show anti-ferromagnetic coupling as a result of indirect metal-metal exchange mediated by the sulphur atoms. The only exception is the paramagnetic CsFeS_2 and this magnetic behaviour is due to the alternating Fe-Fe bond lengths.

Comparing the properties of AFeS_2 ($A = \text{Na, K, Rb}$) and K_2MnS_2 is interesting as both iron and manganese are present as d^5 metal centres in these structurally related compounds. They all have edge linked TMS_4 tetrahedra and are all $S = \frac{1}{2}$ one-dimensional anti-ferromagnets. In AFeS_2 the iron is formally trivalent but there is considerable delocalisation due to short Fe-Fe bonds of around 2.6 - 2.7 Å. In K_2MnS_2 the bonds are longer at around 3.2 Å and there is less delocalisation resulting in higher magnetic susceptibility.

There are also many examples of compounds that have not been fully characterised that could provide interesting information about structure property relationships. For example K_2MnS_2 and Na_2ZnS_2 are isostructural compounds containing Mn^{2+} (d^5) and Zn^{2+} (d^{10}) respectively. K_2MnS_2 has been characterised and shows the expected antiferromagnetic interactions but Na_2ZnS_2 , which would be expected to be diamagnetic, is as yet uncharacterised.

Another example for comparison is BaFe_2S_4 and the series $\text{A}_3\text{Fe}_2\text{S}_4$ ($A = \text{Na, K, Rb, Cs, Tl}$) which have iron in oxidation state 3+ and 2.5+ respectively and could provide an

interesting study into the effect this difference has on the properties of these structurally similar compounds. So far no properties have been reported for BaFe_2S_4 and only limited studies on the series $\text{A}_3\text{Fe}_2\text{S}_4$ ($\text{A} = \text{Na}, \text{K}, \text{Rb}, \text{Cs}, \text{Tl}$) have been carried out.

A full study on the compound K_2CoS_2 could provide an interesting study into the difference in properties between edge linked tetrahedra and the corner linked tetrahedra shown in the compound Ba_2CoS_3 as both compounds contain Co^{2+} and are anti-ferromagnetic.

One-dimensional materials in general provide excellent examples of compounds that can be used to study the relationship between structure and properties and the wide variety of sulphides presented here show that further research into this area could provide valuable information. In addition one-dimensional sulphides form materials with a diverse range of useful properties.

1.6 Ba_2CoS_3

Ba_2CoS_3 was first synthesised by Hong and Steinfink in a 1972 investigation into the phases formed in the Ba-Fe-S system.⁹⁸ The structure was reported as isostructural with Ba_2FeS_3 and crystallised in the orthorhombic space group $Pnma$ with $a = 11.87\text{\AA}$, $b = 4.20\text{\AA}$ and $c = 12.30\text{\AA}$ (no standard deviations quoted). This is also isostructural with the previously prepared Ba_2ZnS_3 ⁹⁸ and K_2CuCl_3 ¹¹⁴ and structurally similar to Ba_2MnS_3 (see section 1.2.4.12 for a full description).¹⁰³ Nakayama *et al.*¹⁰⁰ investigated the magnetic susceptibilities of Ba_2CoS_3 along with Ba_2FeS_3 and Ba_2MnS_3 . All three compounds showed features consistent with quasi-one-dimensional anti-ferromagnetic short-range ordering.

The structure of Ba_2CoS_3 was first fully described by Baikie *et al.*¹⁰⁶ by PXRD and Headspith *et al.*¹¹¹ by neutron diffraction. It was described as the first compound containing one-dimensional corner sharing Co^{2+} tetrahedra; shown in figure 1.35b. The unit cell parameters from PXRD were slightly different to those previously reported with $a = 12.000(1)\text{\AA}$, $b = 12.470(1)\text{\AA}$ and $c = 4.205(2)\text{\AA}$. Room temperature neutron diffraction gave parameters of $a = 11.994(2)\text{\AA}$, $b = 12.472(2)\text{\AA}$ and $c = 4.201(1)\text{\AA}$. For these refinements and the work presented here a different setting of the $Pnma$ space

group has been used. Here the b and c axes have been swapped to give the *Pnam* setting with the c as the short axes.

The corner linked distorted CoS_4 tetrahedra run in chains along the c axis. The tetrahedra are stretched along the chains with Co-S bond length along the chain of 2.427(2) Å compared to 2.330(3) Å and 2.317(3) Å for the terminal Co-S bonds. The intra-chain Co-Co distance is 4.2010(7) whilst the inter-chain distances are 6.182(10) Å and 6.5807(10) Å. The Ba^{2+} ions are present in two crystallographically different sites.

A full study into Ba_2CoS_3 has been performed to fully investigate the structure and physical properties and included EXAFS, XANES, *ab initio* calculations and a microscopic investigation into the origin of the antiferromagnetic coupling.¹¹⁰ By comparing the Co-K edge XANES spectra of Ba_2CoS_3 with standards of known geometry (figure 1.36) it is clear that cobalt is in a tetrahedral environment. The slight difference between Ba_2CoS_3 and the tetrahedral standard $\text{CoBr}_2(\text{PPh}_3)_2$ at 7708.6 eV is due to the sulphur ligands and has previously been observed in Ni^{2+} complexes.¹¹⁵

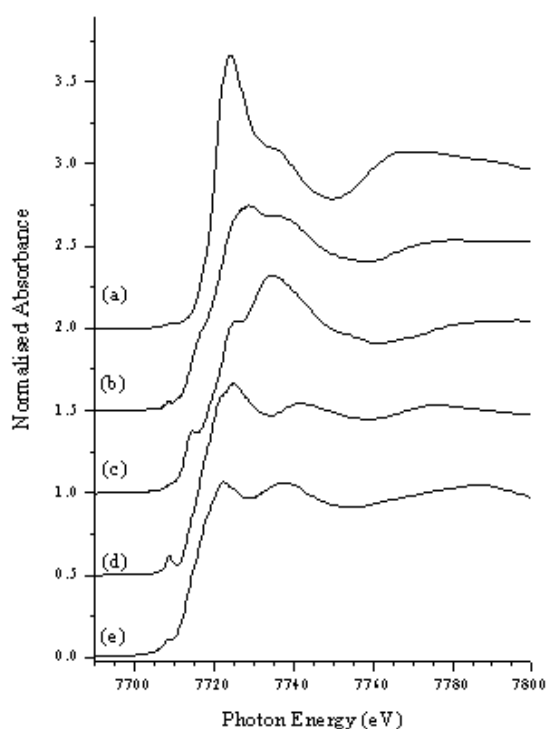
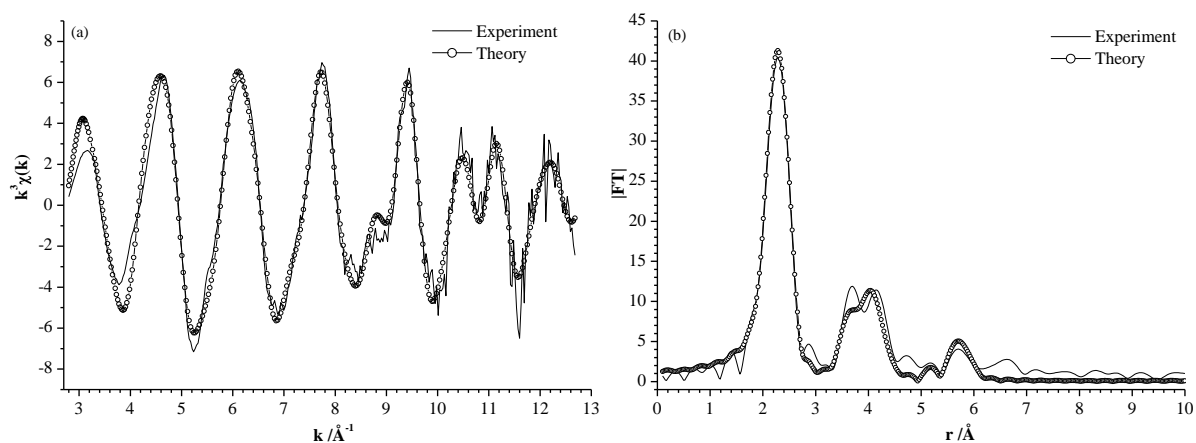


Figure 1.36 Co-K edge XANES spectra of (a) octahedral $[\text{Co}(\text{acac})_2 \cdot \text{H}_2\text{O}]_2$,¹¹⁶ (b) square based pyramidal $[\text{Co}(\text{salen})]_2$,¹¹⁷ (c) square planar Co-3,5-*t*-Bu-cysalen,¹¹⁸ (d) tetrahedral $\text{CoBr}_2(\text{PPh}_3)_2$ ¹¹⁹ and (e) Ba_2CoS_3

An EXAFS study was then performed to investigate the local environment of the Co^{2+} . Table 1.13 shows the refined parameters for the inter-atomic distances and figure 1.37 shows the EXAFS and Fourier transform.

Table 1.13 Summary of refined Co-K edge EXAFS parameters for Ba_2CoS_3 ¹¹⁰

Bond	$r/\text{\AA}$	$\sigma^2/\text{\AA}^2$
Co-S (x4)	2.341(4)	0.0149(6)
Co-Ba (x3)	3.553(11)	0.0224(16)
Co-Ba (x4)	3.873(17)	0.0224(16)
Co-Co (x2)	4.090(12)	0.0119(39)
Co-Ba (x4)	5.554(15)	0.0170(29)
Er = -8.6(5)	R = 26.12%	FI = 0.30

**Figure 1.37** Co-K edge EXAFS (a) and Fourier transform (b) for Ba_2CoS_3 ¹¹⁰

The distances agree very closely with the PXRD data up to at least 5.5 \AA from the Co atoms.

The magnetic susceptibility was investigated and showed a broad peak when plotted against T. This is shown in figure 1.38 and is indicative of one-dimensional magnetic ordering.

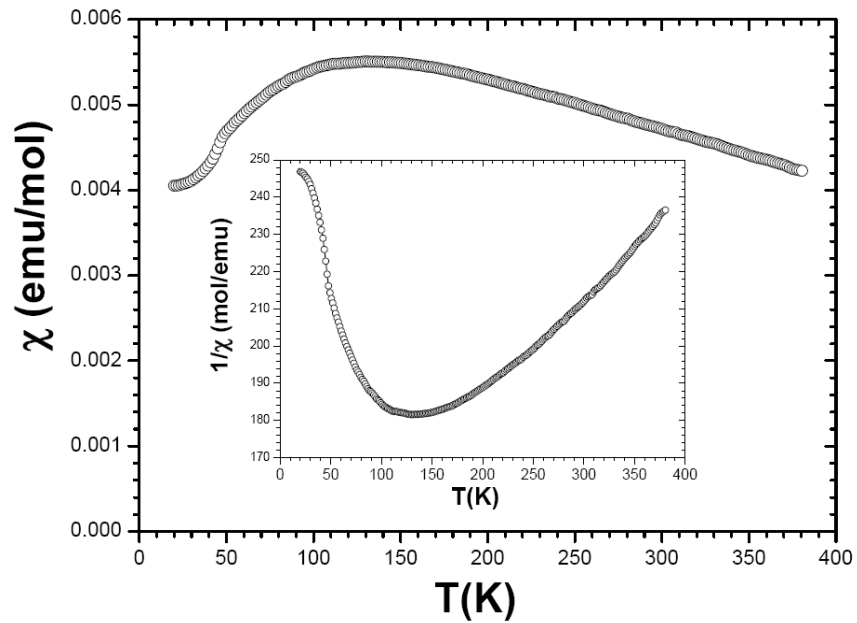


Figure 1.38 Variation of magnetic susceptibility with temperature for Ba_2CoS_3

Further investigation into the properties of Ba_2CoS_3 showed that it exhibited negative magnetoresistance as well as metallic-like features.¹⁰⁹ The resistivity, thermopower and low temperature magnetic susceptibility were all measured. The resistivity (ρ) measured was much lower than that seen for the structurally similar Ba_2MnS_3 ($\sim 10^{-1} \Omega\text{m}$ for Ba_2CoS_3 compared to $\sim 10^2 - 10^3 \Omega\text{m}$ for Ba_2MnS_3). A plot of resistivity versus temperature is shown as the inset on figure 1.39 with the decreasing trend with temperature not significant enough to suggest any semiconducting behaviour but due to defects. The plot of thermopower (S) versus temperature, seen in figure 1.39, is linear in the region $50 \text{ K} \leq T \leq 300 \text{ K}$ and this is indicative of metallic like conduction confirming the resistivity data.

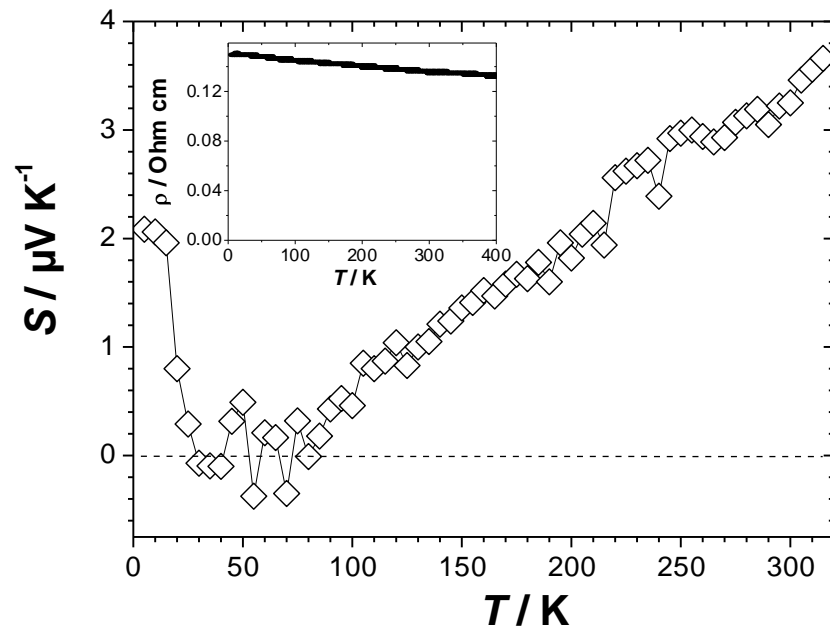


Figure 1.39 Variation of Seebeck coefficient with temperature for Ba_2CoS_3 and inset, variation of resistivity with temperature

The upturn of the Seebeck coefficient seen at $\sim 50\text{K}$ is indicative of an antiferromagnetic transition, T_N and, although the previous studies had shown some antiferromagnetic interactions, this was the first evidence of a transition point. To confirm this, the low temperature susceptibility was re-investigated and the data, shown in figure 1.40, shows a kink at 46 K, again indicative of a T_N , this is exemplified in the plot of the first derivative shown in the inset of figure 1.40.

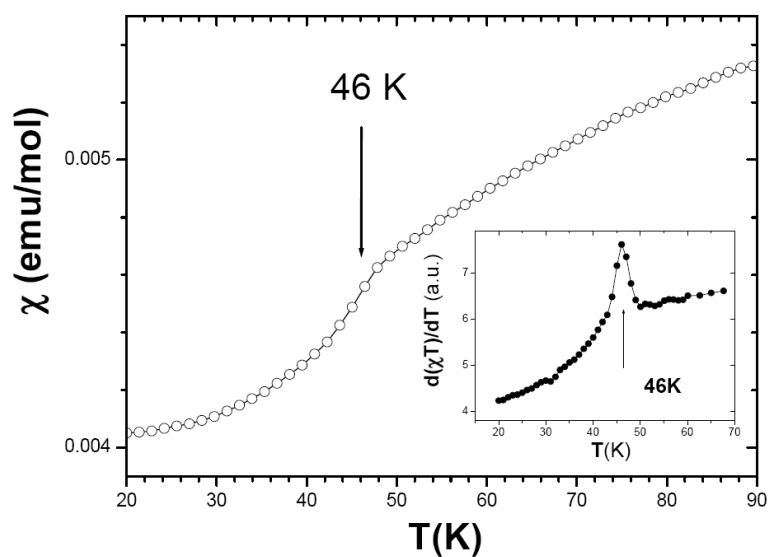


Figure 1.40 Plot showing temperature dependence of susceptibility with feature at 46 K. The inset shows the temperature dependence of the derivative of χT showing the change at 46 K more clearly

Measurements of magnetoresistivity (MR) versus temperature are shown in figure 1.41 and show that Ba_2CoS_3 shows negative MR $\sim -1.7\%$ in a 7 T field at 10 K, a value higher than the only other one dimensional sulphide known to date to show negative MR; $\text{BaV}_{0.8}\text{Ti}_{0.2}\text{S}_3$, which shows $\sim -0.8\%$ in 7 T at 80 K.⁴⁶

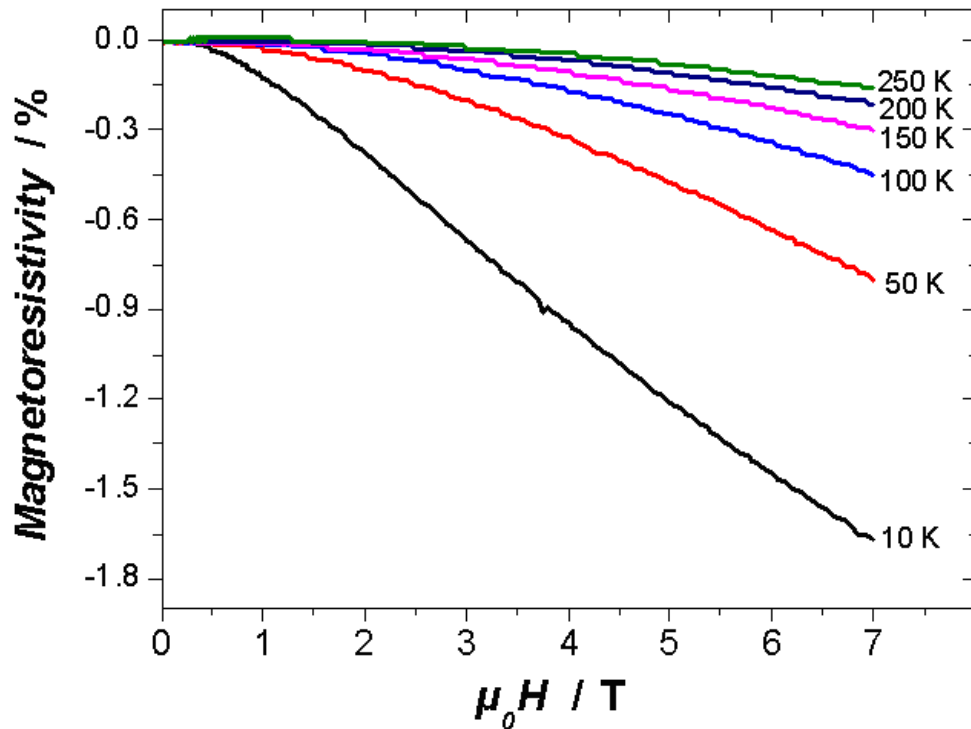


Figure 1.41 Plot of magnetoresistivity against field strength at different temperatures for Ba_2CoS_3

The origin of the MR in Ba_2CoS_3 is not known but spin polarisation has been ruled out by non linear plots of MR versus M^2 and the MR cannot be fully associated with the onset of long range order (LRO) as it changes gradually with temperature and there is not a sudden change at ~ 46 K.

The *ab initio* study, based on data from PXRD, calculated that Co^{2+} is in a distorted tetrahedral environment for which the point group is not T_d but a C_s subgroup. The lowering of symmetry causes the lifting of the degeneracy of the orbitals and the subsequent orbital splitting is quite large (figure 1.42). The ground state was calculated to be high spin, $S = 3/2$ state with $L = 0$.

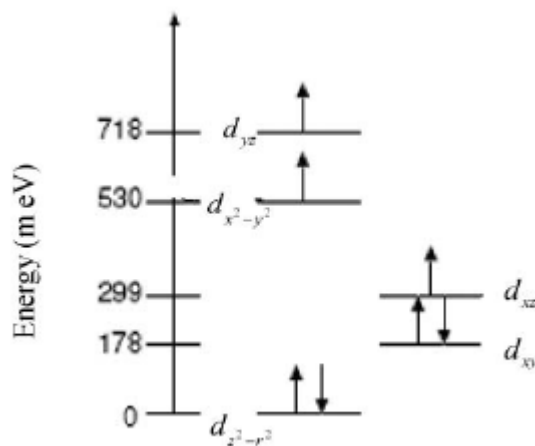


Figure 1.42 Orbital diagram for the ground state of Co^{2+} in a heavily distorted tetrahedral environment

Calculations into the microscopic origin of the intrachain antiferromagnetic coupling between Co^{2+} cations revealed that it is due to the spin flip mechanism mediated by the sulphur orbitals and not *via* direct exchange between the 3d orbitals. There are four different terms which can flip the spins, all of which result in antiferromagnetic ordering. Figure 1.43 shows a schematic of the spin flip mechanism.

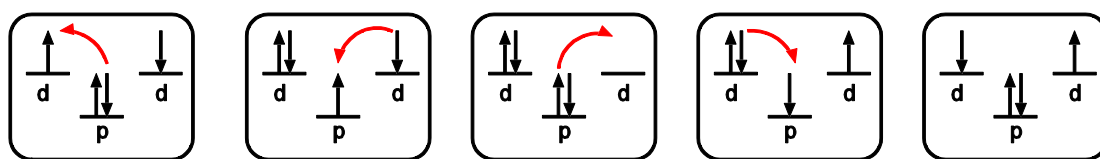


Figure 1.43 The spin flip mechanism between the d orbitals on Co^{2+} and p orbitals on S^{2-}

The intra-chain coupling was determined by analyses of the χ versus T plot and determined that Ba_2CoS_3 is a Heisenberg system with a J value of -37 ± 2 K and $g \approx 2.36 \pm 0.01$. From this the inter-chain coupling J' was also estimated to be ~ 0.9 K¹²⁰ and the ratio of J'/J found is indicative of a quasi one-dimensional system.

The powder neutron diffraction (PND) study performed by Headsith *et al.*¹¹¹ investigated the long range magnetic order (see section 1.1.6) by comparing a PND pattern recorded at 200 K with the pattern produced at 1.5 K, i.e. above and below the T_N . The extra peaks seen at low temperature were used to determine an anti-ferromagnetic unit cell characterised by $a_{\text{mag}} = a_{\text{cryst}}$, $b_{\text{mag}} = b_{\text{cryst}}$ and $c_{\text{mag}} = 2c_{\text{cryst}}$ and which shown in figure 1.44. The Co^{2+} cations are anti-ferromagnetically ordered along [100] with a magnetic moment of $1.97(4) \mu_B$ per cation.

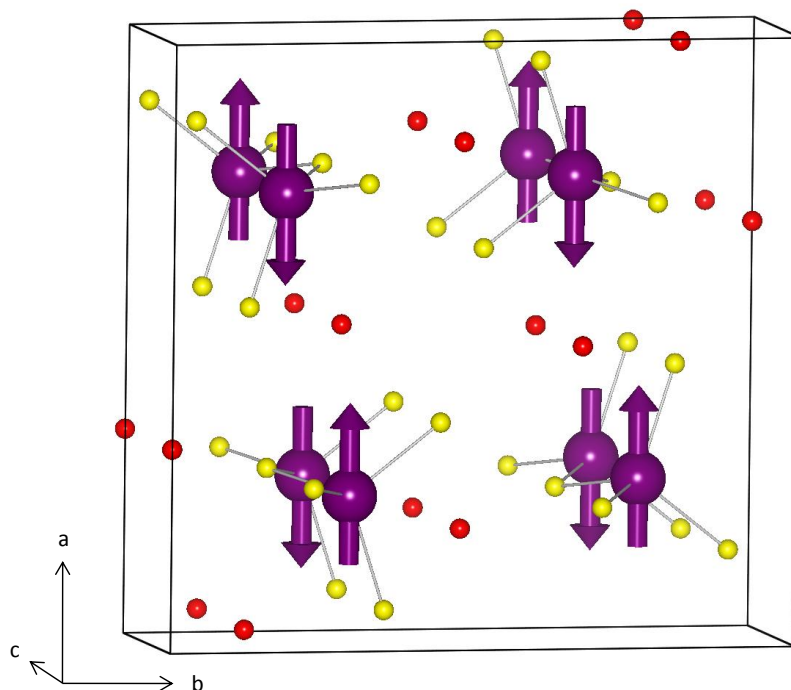


Figure 1.44 Ba_2CoS_3 magnetic unit cell. The arrows represent the direction of the spins on the Co^{2+} cations

Each Co^{2+} is also ferromagnetically aligned with four cations in neighbouring chains and antiferromagnetically with two others; this can be seen in figure 1.44. Interestingly the low angle area at which the extra peaks are seen at 1.5 K showed some more diffuse peaks at higher T and this is possibly an indication of short-range magnetic ordering.

1.7 Project Aims and Outline

The aim of this work was to synthesise and investigate some new one-dimensional sulphides based on Ba_2CoS_3 . In order to prepare new one-dimensional sulphides and explore further the unusual properties of Ba_2CoS_3 , cationic substitutions have been carried out on both the barium and cobalt site to form solid solutions. Chapter 2 outlines the experimental techniques that have been used in this work.

Chapter 3 details the investigation into the series $\text{Ba}_2\text{Co}_{1-x}\text{Zn}_x\text{S}_3$. Chapter 4 describes the series $\text{Ba}_2\text{Co}_{1-x}\text{Fe}_x\text{S}_3$ and chapter 5 the work done starting with Ba_2ZnS_3 to form the series $\text{Ba}_2\text{Zn}_{1-x}\text{TM}_x\text{S}_3$ with TM = Cr, Ni, Mn and Fe.

Chapter 6 focuses on the investigations performed by substituting barium for other metals in both aliovalent and isovalent substitutions.

2.0 Experimental Techniques

2.1 Synthesis and characterisation

The synthesis of all of the products in this work is achieved *via* a solid-gas reaction between powdered metals, metal oxides or carbonates, and a CS₂-N₂ gas stream in a tubular furnace. Carbon disulphide (CS₂) is a liquid with high vapour pressure and as such can be carried by a nitrogen gas flow through the tubular furnace. A diagram of the apparatus used for these reactions is shown below in figure 2.1a. Nitrogen gas is first passed through a Dreschel bottle containing concentrated sulphuric acid, to remove moisture, and then through one containing CS₂. A bypass system is in place so that pure nitrogen can be passed through the tube before the reaction to eliminate any trace of air from the system, then CS₂ can be passed through the tube to carry out the preparation of sulphides, then pure nitrogen can be flown to eliminate any residue of toxic CS₂ after the reaction is completed. Stoichiometric amounts of the starting reagents are intimately mixed by grinding in a pestle and mortar before being placed in a carbon boat at the centre of the tube. At the opposite end of the quartz tube is a Dreschel bottle containing paraffin oil, which prevents air from entering the system and acts as a scrubber to remove residual CS₂. The furnace is programmed to heat up to a set point at a given rate, remain there and then cool down, again at a given rate. A typical reaction involves flowing nitrogen through the system for 15 minutes to remove any air, then allowing CS₂ to flow. The furnace is then heated to 1000°C at a rate of 100°C/h and held at that temperature for 20 hours. Subsequently the system is slow cooled at a rate of 100°C/hour and, when at room temperature, pure nitrogen is flowed to remove residual CS₂ from the system.

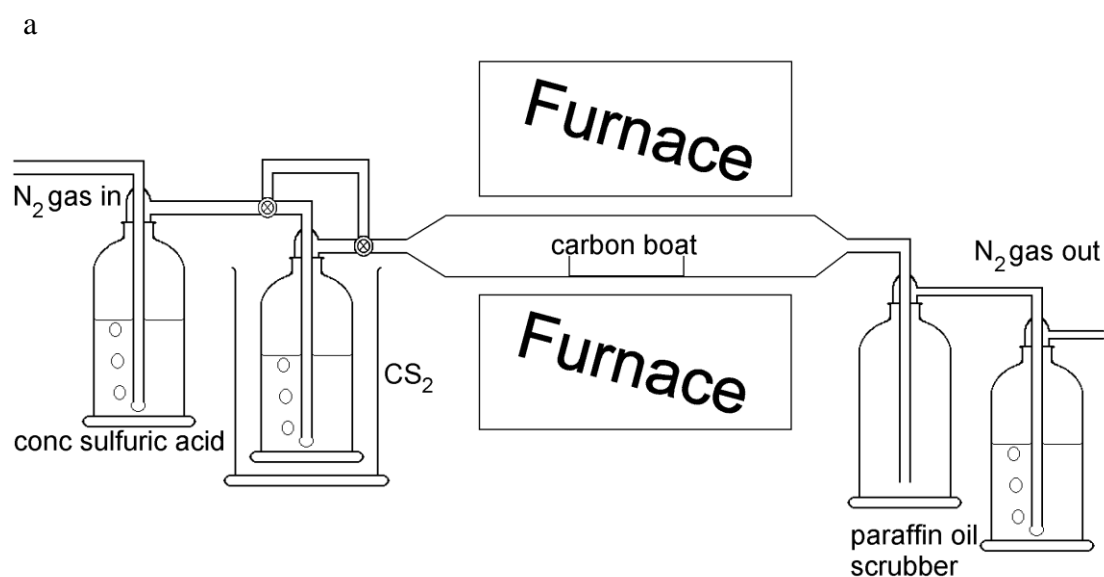


Figure 2.1 a) Diagram of the apparatus used for reactions of solids with CS_2 vapour. b) Tubular furnace used in sulphuration reactions

There are problems associated with this method including the toxicity of CS_2 , the long heating periods required and the carbon deposits left on the product by the dissociation of CS_2 . All synthesis of sulphides were carried out using quartz glass tubes with which some sulphides react, this problem has been partially overcome in this work by first coating the quartz glass tubes with carbon. This is achieved by using the same setup as used for the sulphuration reactions but replacing CS_2 with either hexane or acetone and heating for approximately 3 hours at 700°C . This results in a thin layer of carbon

forming on the inside of the glass tube which acts as a protective layer and is repeated occasionally to ensure continuous protection.

All the samples in this work series were analysed using PXRD, see following section for theoretical background to diffraction. Initially search match software supplied with the D5000 diffractometer was used to determine the purity of the samples. Rietveld refinements were then performed using the software GSAS in conjunction with EXPGUI.^{121,122} The structure of Ba_2CoS_3 was chosen as the starting model for the refinements against diffraction data for all $\text{Ba}_2\text{Co}_{1-x}\text{TM}_x\text{S}_3$ samples with TM included on the Co site. The fractional occupancies were set to those expected from the stoichiometry of the starting materials.¹⁰⁶ Small impurities of BaS and Ba_2SiS_4 (due to reaction of BaS with the SiO_2 of the glass tube) were found in some samples and could not be eliminated upon further heating. The amount of Ba_2SiS_4 formed could be limited but not eliminated by using carbon coated tubes as discussed in the Experimental section (2.1). No corresponding impurities containing cobalt or other transition metals were seen in the PXRD data. The phase fraction, zero point, cell parameters, atomic position parameters (with the atomic positions of cobalt and the appropriate transition metal were constrained to be equal), background (a linear interpolation function) and peak profile (~3 terms of the pseudo-Voigt) were all refined.

PXRD was carried out on all samples on a Siemens D5000 diffractometer with $\text{Cu K}\alpha$ radiation. Powder neutron diffraction data were collected for selected compounds at the Polaris diffractometer at the ISIS pulsed spallation source, Rutherford Appleton laboratory, UK. Approximately 5g of samples were used, and placed in a vanadium can and data collection was performed at room temperature or 5 K for approximately 4 hours.

The Co- and Zn- K-edge X-ray absorption spectra (see section 2.2.5 for theoretical details) were collected from samples diluted in BN in transmission mode at ~80 K on station 9.3 of the Daresbury Laboratory SRS (2 GeV ~200 mA) using a Si(220) double crystal monochromator.

The physical properties of the materials were analysed by collaborators Laboratoire CRISMAT, ENSICAEN, the theoretical details can be found in section 2.3.2. Magnetic susceptibility measurements were made using a SQUID magnetometer over the range 5-300 K using a 2 T external field (zero-field cooled). The resistivity of the samples was measured using a PPMS device and the four point probe method over the temperature

range 5-300 K and magnetoresistance measurements were also carried out using this device over the magnetic field range 0-7 T at 5-300 K.

2.2 Structural Characterisation

2.2.1 Crystallography

2.2.1.1 Symmetry

A crystalline solid consists of a 3-D array of atoms arranged in an ordered lattice and this lattice can be described using symmetry concepts.¹²³⁻¹²⁶

2.2.1.2 Symmetry Operations

A symmetry operation is a geometric movement, which, after it has been completed, leaves an object unchanged. There are two kinds of symmetry operations important to solid-state chemistry. Firstly, point symmetry operations, in which at least one point remains unaltered; secondly translation symmetry, which involves movement along an axis. The five point symmetry elements are listed below along with the commonly used notation;

Inversion ($\bar{1}$) – Each point is projected through an inversion centre and so creates an equivalent point through the other side,

Rotation (n) – Each point is rotated anticlockwise around an axis by an angle of $360^\circ/n$, where, for a lattice, n can be 1, 2, 3, 4 or 6 and the element is simply noted by the integer number.

Reflection (m) – All points are reflected through a mirror plane, creating new points equidistant from the mirror.

Rotoinversion (\bar{n}) – Each point is first subjected to a rotation (as described above) and then an inversion through a point located on the rotation axis. This element is given the symbol \bar{n} with n as the integer relating to the rotation. This symmetry element is sometimes referred to as an improper rotation axis.

Rotoreflexion (\tilde{n}) – A rotation followed by reflection in a mirror plane which is perpendicular to the rotation axis, this is given the symbol \tilde{n} , again with n as the integer relating to the rotation. This element is rarely used as each one is equivalent to an alternative rotoinversion axis, i.e. $\tilde{1} = \bar{2}$, $\tilde{2} = \bar{1}$, $\tilde{3} = \bar{6}$, $\tilde{4} = \bar{4}$, $\tilde{6} = \bar{3}$.

There are a further two symmetry operations when including translation elements;

Rototranslation (n_m) – Also known as a screw axis this involves a rotation of $360^\circ/n$ followed by a translation parallel to the rotation axis. Given the symbol n_m where n refers to the rotation, m is an integer and the translation is over a distance of m/n . E.g. a 6_3 axis involves a rotation of 60° followed by a translation of $3/6$ ($1/2$) of the length of the unit cell (see definition below) along the rotation axis.

Reflectotranslation – This operation is a reflection followed by a translation parallel to the mirror plane and there are three different possible combinations depending on the translation, they are more commonly referred to as glide planes. Those labelled a , b and c refer to a translation along those respective axes of $1/2$ the unit cell. An n or diagonal glide refers to a diagonal translation of $1/2$ across one face or through the body of the unit cell and a d or diamond glide involves the same motion across $1/4$ of the unit cell.¹²⁵

2.2.1.3 Unit Cell

The unit cell is a repeatable unit containing one or more atoms. When stacked in three-dimensions the unit cell describes the bulk arrangement of atoms in the crystal. It is defined by the vectors and angles of its edges (figure 2.2) and is quite often the smallest repeatable unit within the lattice.

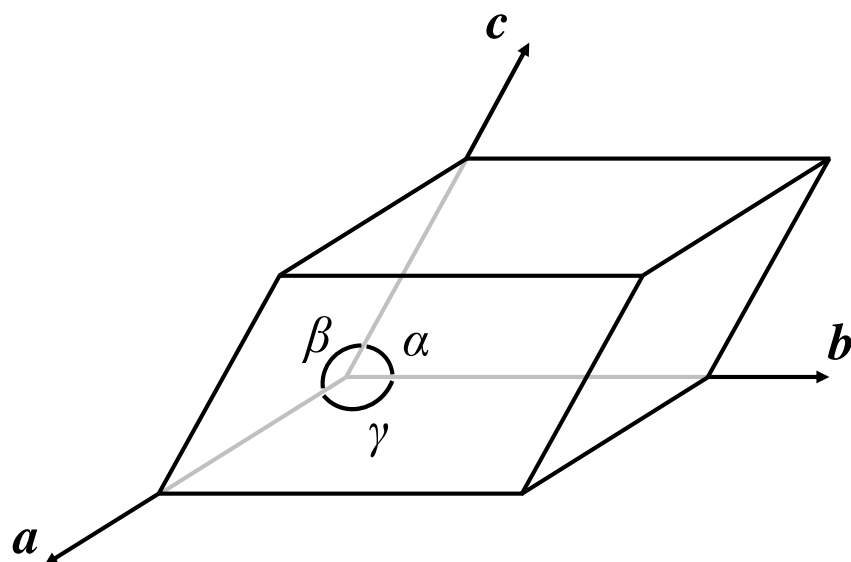


Figure 2.2 The vectors, *a*, *b*, *c*, and angles α , β , and γ which define a unit cell

By translating this unit cell one unit along its axes without reorientation the entire 3-D lattice can be built up and there are seven possible crystal systems depending on the dimensions of the unit cell (table 2.1). Although the dimensions of the unit cell are usually sufficient to describe it, a more accurate description depends on the symmetry of the cell. The unit cell is usually, therefore, chosen to highlight the symmetry of the system (right hand column of table 2.1).

Table 2.1 The seven crystal systems based on the unit cell parameters and symmetry requirements¹²⁵

Crystal System	Unit cell	Symmetry requirements
Triclinic	$\alpha \neq \beta \neq \gamma \neq 90^\circ$ $a \neq b \neq c$	none
Monoclinic	$\alpha = \gamma = 90^\circ, \beta \neq 90^\circ$ $a \neq b \neq c$	One two-fold axis or one symmetry plane
Orthorhombic	$\alpha = \beta = \gamma = 90$ $a \neq b \neq c$	Any combination of three mutually perpendicular two-fold axes or planes of symmetry
Trigonal/rhombohedral	$\alpha = \beta = \gamma \neq 90^\circ$ $a = b = c$	One three-fold axis
Hexagonal	$\alpha = \beta = 90^\circ, \gamma = 120^\circ$ $a = b \neq c$	One six-fold axis or one six-fold improper axis
Tetragonal	$\alpha = \beta = \gamma = 90^\circ$ $a = b \neq c$	One four-fold axis or one four-fold improper axis
Cubic	$\alpha = \beta = \gamma = 90^\circ$ $a = b = c$	Four three-fold axes along the body diagonals

These crystal systems describe all the possible shapes of a unit cell but it is also necessary to include points within the unit cell. In a crystalline material these points may be atoms or groups of atoms, each of which has identical surroundings. The arrangement of these points is referred to as the lattice and there are four different types of lattice arrangement (figure 2.3): the primitive lattice, denoted P, contains only one lattice point, typically represented as a unit cell with a lattice point on each corner, the body centred, I, a primitive lattice with an additional point in the centre, the all face centred, F, a primitive lattice with one point at the centre of each face and the face centred, A, (or B or C) a primitive lattice with two points at the centre of opposite faces (on the *bc* face for A-centred, the *ac* face for B-centred and the *ab* face for C-centred). Lattice points at a vertex are shared by eight adjacent unit cells, at a face by two; points at the centre of a unit cell are not shared.

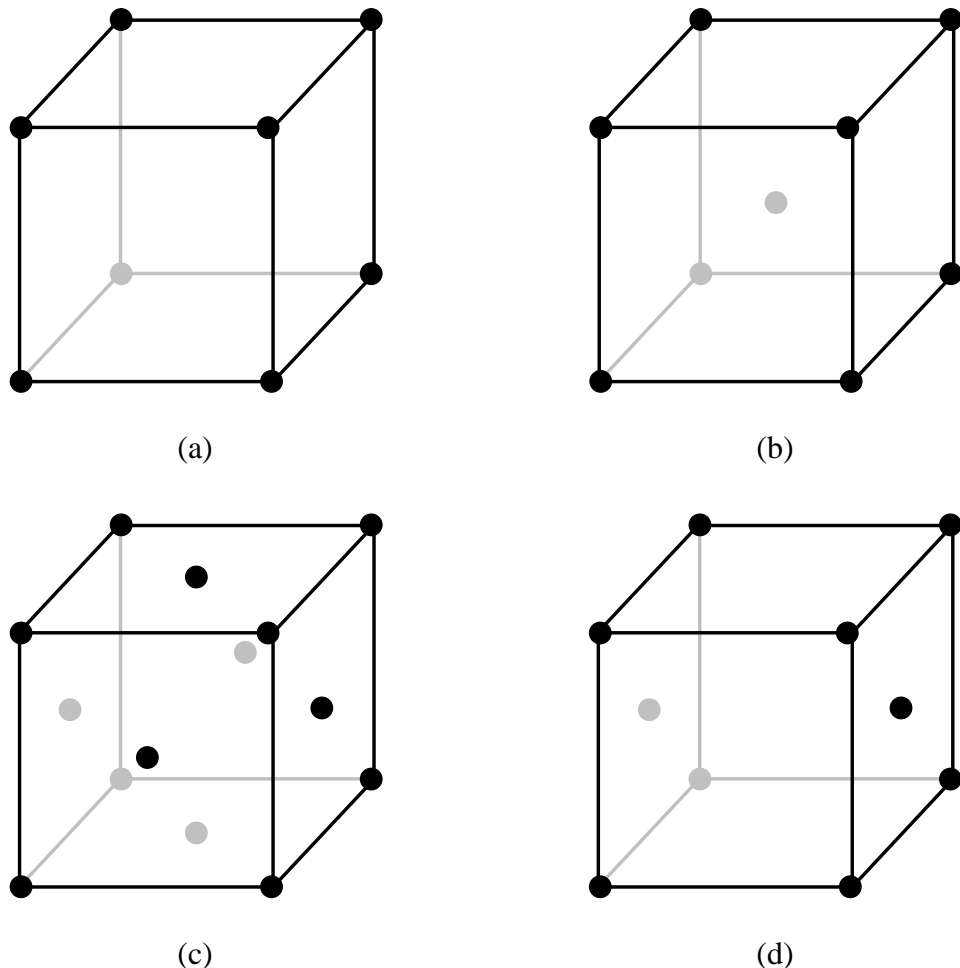


Figure 2.3 The four lattice types a) Primitive b) body centred c) all-face centred d) face centred

By combining these four lattice types with the seven crystal systems (and the restrictions placed upon them by symmetry elements they must contain) 14 possible 3-D space filling lattices result, known as the Bravais lattices (table 2.2).

Table 2.2 The 14 Bravais lattices

Crystal system	Lattice symbol
Triclinic	<i>aP</i>
Monoclinic primitive	<i>mP</i>
Monoclinic centred	<i>mC</i>
Orthorhombic primitive	<i>oP</i>
Orthorhombic C-face-centred	<i>oC</i>
Orthorhombic body-centred	<i>oI</i>
Orthorhombic face-centred	<i>oF</i>
Tetragonal primitive	<i>tP</i>
Tetragonal body-centred	<i>tI</i>
Trigonal (Rhombohedral)	<i>hR</i>
Hexagonal primitive	<i>hP</i>
Cubic primitive	<i>cP</i>
Cubic body-centred	<i>cI</i>
Cubic face-centred	<i>cF</i>

By combining the 14 Bravais lattices with the point group symmetry discussed above 32 possible point groups for three dimensional lattices are generated. By further combining the 32 point groups with the translational symmetry operations there are 230 possible space groups to which all crystalline solids must belong. These space groups are numbered and given a unique symbol to identify any possible crystalline solid. The symbol of each space group consists of the lattice type, P, F, I, A, B, C or R (for a primitive rhombohedral) followed by the notation for up to three of the most significant symmetry elements (i.e. those which may also lead to others being present), e.g. space group number 62, *Pnma*, common in this work, consists of a primitive lattice with a diagonal glide plane, *n*, a mirror plane, *m*, and an *a* glide plane all perpendicular to one another.

2.2.1.4 Lattice Notations

In order to describe the crystal structure of a material completely it is necessary to include the atomic positions of the atoms within the unit cell. The simplest way to do this is by taking one lattice point as the origin and using coordinates along the x , y and z axes of the unit cell, e.g. a point described as 101 is one unit along the a axis and one unit along the c axis from the origin (000). These coordinates are assigned the letters u , v and w and the values can also be negative, in which case they are written as \bar{u} , \bar{v} and \bar{w} . By combining this information with the space group it is necessary only to define the positions of a few atoms, known as the asymmetric unit, with the others generated by the symmetry of the space group.

The notation used to describe atomic positions can also be used to describe directions and planes within a unit cell. Miller indices are used to define the lattice planes and correspond to the reciprocal of the point at which a plane intersects the unit cell on each edge. Each Miller plane is represented by the letters h , k and l in round brackets. For example the (120) plane intercepts the a axis at 1, the b axis at $1/2$ and does not intercept the c axis. The values are reduced to the lowest set of integers if necessary. Miller planes are of high importance in X-ray diffraction, as described below. Some further examples of Miller planes and indices are shown in figure 2.4.

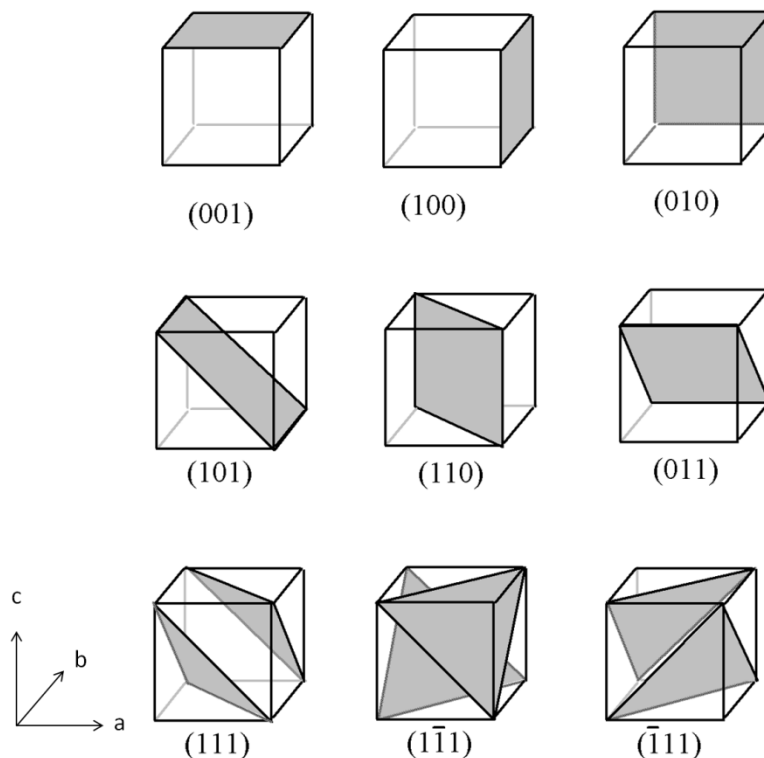


Figure 2.4 Some examples of Miller planes, negative values are again represented by a bar over the number

2.2.1.5 Diffraction

When radiation interacts with matter it can be scattered in one of two ways; if the energy of the reflected beam is different from that of the incident beam it is known as inelastic scattering and can result in a complex reflected beam which can be difficult or impossible to interpret. If however there is no change in energy the interaction results in elastic, coherent scattering and information can be obtained about the matter with which the radiation is interacting. A particular kind of coherent scattering known as diffraction results when the wavelength of the radiation is similar to the spacing of the gaps within the matter. For studying crystalline solids X-rays are therefore commonly used in diffraction experiments as they have a wavelength around 0.5-1.8 Å; similar to the interatomic distances in a solid. The most common and one of the simplest ways to describe the interaction is using Bragg's definition in which waves interfere after partially reflecting from a crystalline solid, figure 2.5.

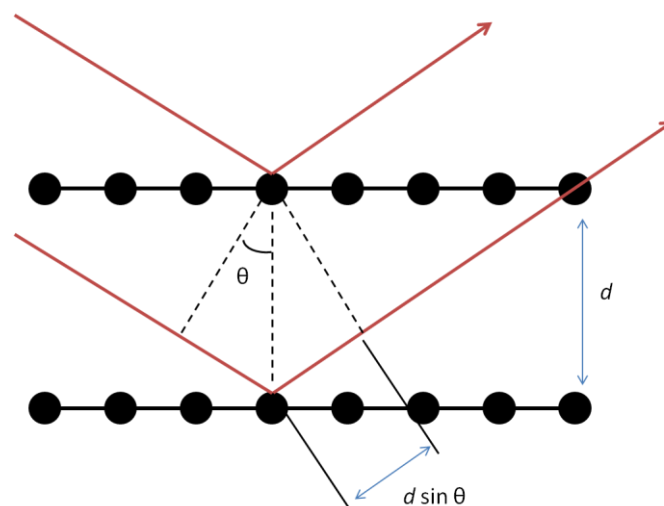


Figure 2.5 Schematic diagram illustrating Bragg's diffraction. Black spheres represent atoms on crystallographic planes, d is the spacing between those planes and θ is the angle between the planes and the incident radiation

Each family of lattice planes can be treated as a semi-transparent mirror, reflecting some X-rays and allowing others to pass through. If two incoming waves are reflected by subsequent layers of the crystal they will interfere with one another after the reflection. If the distance, d , between the layers and the angle of reflection, θ , is such that the two waves remain in phase after the reflection they will interfere constructively. This is achieved if the difference in the paths travelled by the two waves is equal to an integer number of wavelengths of the radiation and is represented mathematically by Bragg's law;

where λ is the wavelength of the X-rays and n is an integer.¹²⁷ If the two waves are no longer in phase after the reflection they will interfere destructively. Bragg's law applies when $\lambda \leq 2d$.

For any given crystal there will be a large number of crystallographic planes, the Miller planes, that can diffract the X-rays in this way and the interaction of the X-rays with these planes gives rise to the characteristic pattern of maxima and minima known as the diffraction pattern. In order to produce a good diffraction pattern it is necessary to study the diffraction of as many of the Miller planes as possible and this can be done, according to Bragg's law, by varying either the wavelength or the angle of the incident radiation. For laboratory experiments it is more practical to vary the angle by simply rotating the sample in a constant wavelength X-ray beam. By detecting the angle of the maxima produced, 2θ , the value of the spacing between planes, d , can be calculated. In order to analyse the pattern produced it is necessary to detect the maxima at all angles simultaneously. By using a sample consisting of a powder, i.e. containing small crystals randomly oriented to one another, all possible diffracting planes are presented to the beam at one time and cones of diffracted X-rays are formed by the interactions. By placing a moving detector at 2θ to the sample the diffracted X-rays can be detected. This can speed up the time required to collect information about a crystal but can also make analysis of the information more complex. In this work all diffraction experiments performed used powder X-ray diffraction (PXRD).

The position of the peaks in a diffraction pattern is indicative of the unit cell size and symmetry and a process called 'indexing' assigns Miller planes to all the diffraction peaks in a pattern, this is commonly done using a computer program. This information is then used along with the Bragg's equation to calculate the unit cell parameters. In systems where $\alpha = \beta = \gamma = 90^\circ$ the equation is relatively simple. For example, the equation for orthorhombic systems is:

$$\frac{1}{d^2} = \frac{h^2}{a^2} + \frac{k^2}{b^2} + \frac{l^2}{c^2}$$

and the equation for the cubic system is even simpler:

$$\frac{1}{d^2} = \frac{h^2 + k^2 + l^2}{a^2}$$

The variation in intensity of the peaks is caused by the complex interactions that occur as atoms in the unit cell scatter the X-rays and this is discussed in section 2.2.4 along with other factors affecting the intensity.

2.2.2 Powder X-ray Diffraction (PXRD)

Powder X-ray Diffraction is an analytical technique used to determine information about the crystal structure and chemical make up of a solid. The information is obtained from the diffraction pattern produced when a beam of X-rays hits a crystalline powder and is diffracted by the atoms in the structure.

2.2.2.1 X-ray Generation

X-radiation is electromagnetic radiation with a wavelength in the 0.1-100 Å range. In a diffractometer X-rays are generated by firing electrons from a high voltage system (typically tens to hundreds of kilovolts) at a metal target. A schematic representation of a typical X-ray tube for X-ray generation in an ordinary diffractometer is shown in figure 2.6.

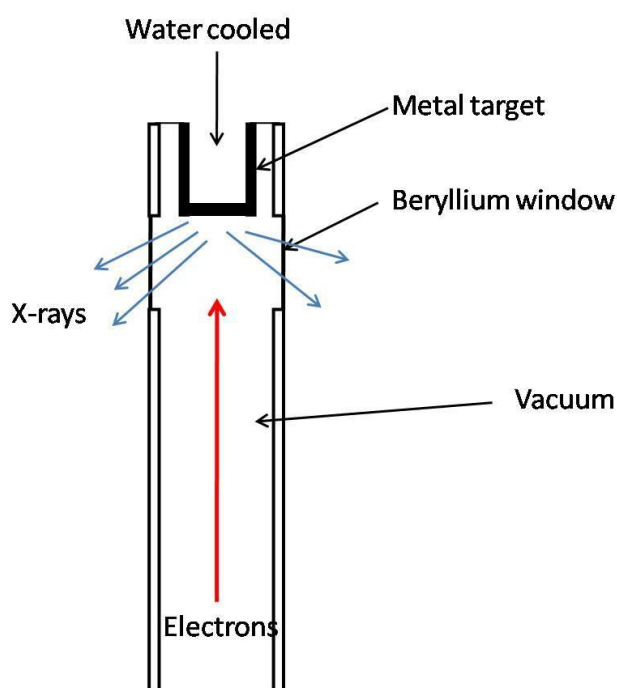


Figure 2.6 Schematic diagram of an X-ray generating tube

The interaction of the electrons with the metal target produces X-rays in two ways. The first results in continuous wavelength X-ray radiation and is caused by the sudden slowing of the electrons as they encounter the metal, this is known as Bremsstrahlung (from German meaning braking radiation). The second kind produces narrow range wavelength X-rays with the wavelength dependent on the metal used for the target. When electrons impact upon the metal target with sufficient energy, called the excitation potential, they can dislodge an electron from the inner shell of the metal atom and, as electrons from higher shells fall in energy to occupy the now vacant inner shell, a photon of X-ray energy is emitted. This photon will have a specific wavelength depending on the energy gap between the two orbital energy levels and so characteristic spectral lines are produced for different metals. Multiple lines are produced as multiple orbitals can be involved and each orbital will produce two lines; one for each electron spin. The emission spectra for the two most commonly used metals, copper and molybdenum, are shown in figure 2.7.

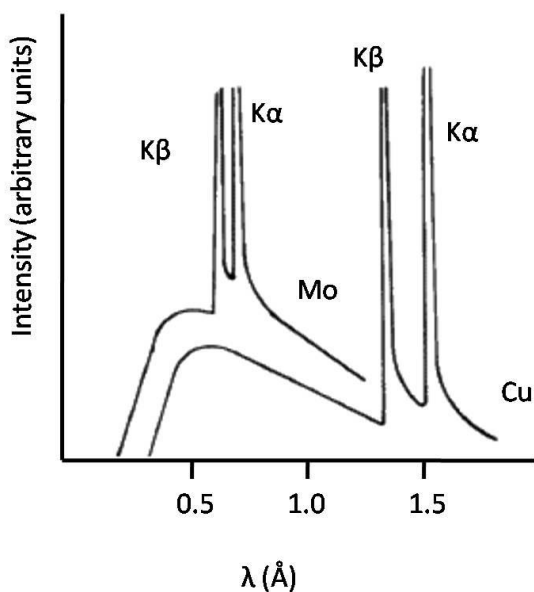


Figure 2.7 X-ray emission spectra of Copper and Molybdenum

The lines produced are named after the electron removed, i.e. K for a 1s electron, L for a 2s electron and so on. The subscript α indicates that the electron goes down one energy level, β for two; as both lines are produced by electrons falling into the same energy level both of these events occur at the same time. The most intense of the wavelengths produced is normally the $K\alpha$ and this can be selected by a monochromator and targeted at the sample. The monochromator usually consists of a single crystal of

silicon or germanium cut along one face with the diffraction from this face selecting single wavelength radiation. The energy levels for a typical atom are shown in figure 2.8.

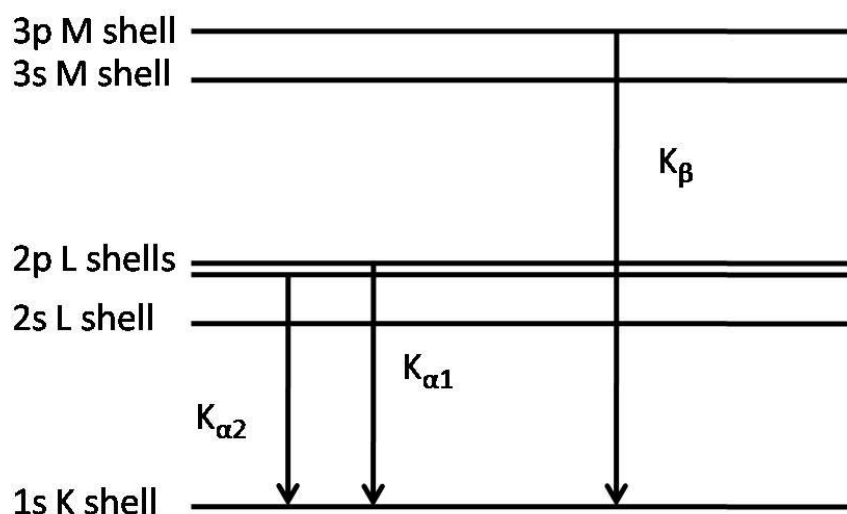


Figure 2.8 Representation of the energy levels and changes involved in an X-ray emission

As mentioned previously the different spin states in each shell give rise to two spectral lines the $K_{\alpha 1}$ and $K_{\alpha 2}$, and this splitting is only observable in a diffraction pattern at high angle. It is useful to remove the K_{β} radiation line and this can be done by placing a piece of metal in front of the target. The choice of this metal is dependent on the metal in the target, for example nickel is used in conjunction with a copper target. It is also desirable to have a beam of parallel X-rays and so a device known as a collimator is used. A Söller collimator consists of a piece of lead with tiny holes, which only allow X-rays parallel to the holes to pass through. Whilst this produces a parallel beam of X-rays it also reduces the intensity of the X-rays reaching a sample.

The characteristic nature of the K_{α} X-radiation means that the metal chosen for the target can be changed to vary the wavelength of the X-rays emitted; the atomic number of the metal used is proportional to the square root of the frequency produced. For PXRD the most common metals used are copper and molybdenum, which produce primary emission lines of 1.54 Å and 0.71 Å respectively.

X-rays can also be produced in a synchrotron and this produces a more intense, less divergent beam which is useful for smaller sample sizes and for specialist uses such as X-ray Absorption Spectroscopy discussed in section 2.2.5.

Synchrotrons are cyclic particle accelerators which use both magnetic and electric fields to accelerate particles. Most commonly they consist of straight line sections where the particles are accelerated by an electric field, linked with curved areas which contain magnets which force the particles around the corners. This magnetic field keeps the particles on a regular circular path so they can be accelerated to higher energies at each revolution by the carefully controlled electric field. As the particles are forced around a corner by the magnets they lose energy, emitted in the form of electromagnetic radiation at a tangent to the circular path of the beam and this radiation can cover a broad range of energies from infrared to X-rays. Initially this loss of energy was a by-product of synchrotrons that were designed to produce high energy particles but many synchrotrons are now specifically designed to utilise the electromagnetic radiation produced.

Figure 2.9 shows the typical arrangement of such a synchrotron. A stream of electrons is produced by heating a metal cathode in a vacuum, and these electrons, which typically have energies of around 50-100 keV, are then accelerated further to around 100 MeV in a linear accelerator (linac) before being injected into a booster ring. The booster ring consists of two straight sections connected by two semicircular regions and accelerates the electrons up to energies of 3 GeV by using radiofrequency. At this point the electrons are injected into the storage ring.

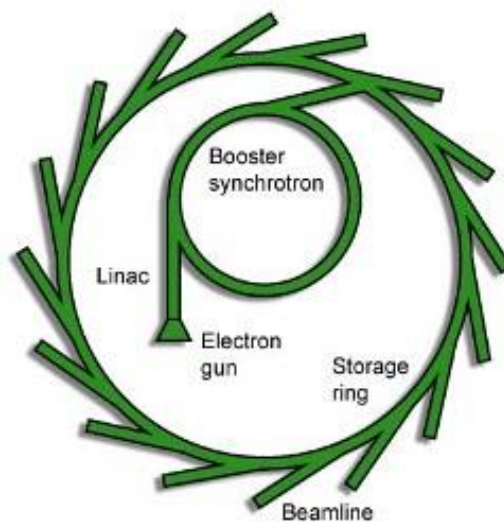


Figure 2.9 Representation of the components of a synchrotron

The storage ring consists of multiple straight line sections and bending magnets and components known as ‘insertion devices’. These are split into two types known as wigglers and undulators both of which consist of arrays of magnets designed to

maximise the energy output from bending of the beam. At the peak of each oscillation a cone of energy is emitted (figure 2.10). Wigglers generally have magnets arranged in a so-called Halbach array (figure 2.11), and produce high energy but broader spectrum energy than undulators. Undulators (figure 2.10), produce a smaller oscillation amplitude in the electron beam and as such the energy emitted from each oscillation can interfere with that from other oscillations leading to constructive interference and therefore intense and narrow band X-rays.

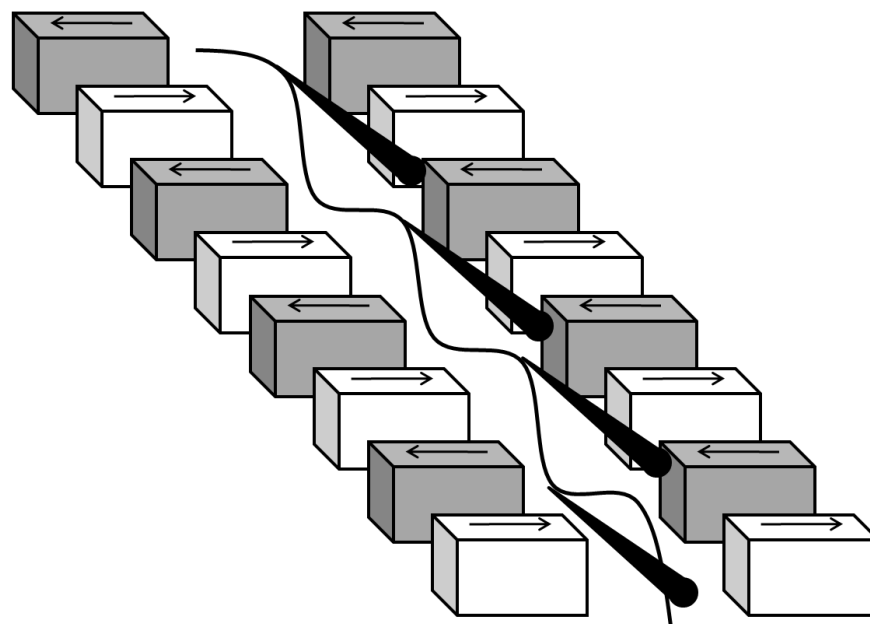


Figure 2.10 Undulator, showing the cones of energy emitted at each oscillation, these can constructively interfere to produce high intensity energy

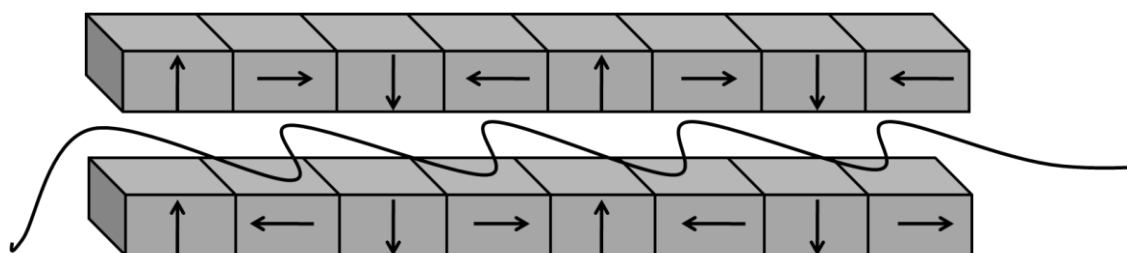


Figure 2.11 Wiggler showing the Halbach array, an arrangement of magnets designed to produce maximum angular change and hence maximum energy output

At each bending magnet or insertion device the electromagnetic energy emitted is produced at a tangent to the beam and is directed down a beamline. Each beamline may

be designed differently depending on what the electromagnetic radiation is to be used for but will typically contain a monochromator and some focusing optics.

2.2.2.2 Diffractometer

It is possible to perform X-ray diffraction in either transmission or reflection mode; in this work all PXRD was carried out in reflection mode using a Siemens D5000 and using the Bragg-Brentano geometry. This geometry rotates both the sample and the detector and is shown in figure 2.12. The X-ray source, sample centre and detector are all at points on the circumference of an imaginary circle known as the focusing circle. The sample is rotated θ degrees whilst the detector is rotated 2θ degrees and this ensures that the sample remains at a tangent to the focusing circle.

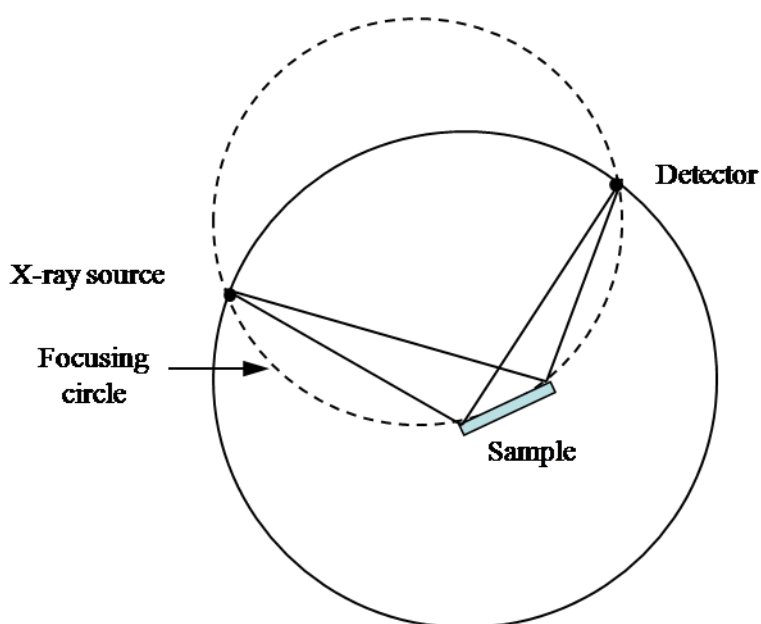


Figure 2.12 Schematic diagram of the focusing circle in a diffractometer

2.2.2.3 X-ray Detection

Generally X-rays can be detected in a number of ways such as photographic plates or Geiger counters but for PXRD the most commonly used are based on scintillation detectors, which exploit the property of scintillation whereby a material emits light when impacted by ionizing radiation. A photomultiplier tube is then used to measure the

emission from the scintillator and convert this to an electrical signal. This signal is then recorded for data analysis.

2.2.3 Neutron Powder Diffraction (NPD)

Neutron powder diffraction is based on similar concepts to PXRD, utilising the diffraction of neutrons as opposed to X-rays; there are, however, significant differences. The absorption cross section of most materials is lower for neutrons than for X-rays and as such neutrons can penetrate further into a sample; up to centimetre scales as opposed to ~0.5mm for X-rays. Neutrons can, therefore, probe the bulk of a material but larger sample volumes are required for analysis. Neutrons interact with the nucleus of an atom, X-rays with the electron cloud. Neutrons do not show the same dependence on atomic mass for scattering cross section as X-rays, allowing for some nearby atoms to be easily distinguished in neutron analysis that could not be using X-ray diffraction. For example the neutron scattering lengths differ significantly for the neighbouring transition metals Mn, Fe and Co (−3.73 fm, 9.45 fm and 2.5 fm respectively) allowing for the atoms to be distinguished when solid solutions containing these atoms are investigated using neutron diffraction. A further advantage of this is that light elements diffract as well as heavier elements so allowing for the detection of light atoms even in samples containing many heavy atoms. The scattering length is independent of the diffraction angle allowing for more accurate analysis of the unit cell parameters as high quality data are acquired across the whole 2θ range.

Another major difference is that neutrons have a magnetic moment of $1.9132 \mu_B$ and can therefore interact with the magnetic moment of unpaired electrons, via the dipole-dipole interaction. Unlike the nuclear scattering this is angle dependent but it allows for studying the magnetic structure of materials.

Neutrons can be produced in two ways and the method of production determines the type of experiment that can be performed. The first method is *via* the nuclear fission of ^{235}U which gives neutrons with around 5 MeV of kinetic energy; these neutrons are used in constant wavelength experiments using a setup analogous to a standard powder X-ray diffraction experiment.

The second method of producing neutrons is *via* a technique called ‘spallation’ and this type of source is used for ‘time-of-flight’ (t-o-f) neutron diffraction. Spallation works by

bombarding a material with high energy particles leading to the emission of a large number of nucleons. To produce neutrons, protons are accelerated to around 800 MeV and sent in pulses to a target, often tungsten, uranium or lead. The target emits neutrons of a range of wavelengths, i.e. a 'white' beam. A range of wavelengths can then be roughly selected by passing the beam through a 'chopper', a rotating disc of neutron absorbing material with an opening cut into it. Changing the speed of rotation allows for selecting the wavelength range required. In this type of experiment the detector does not move through a 2θ range, rather a fixed detector bank is used, which measures all angles at once. All wavelengths of neutrons impinge on the sample at once and all possible reflections occur. The time taken from the neutrons hitting the sample to reaching the detector is used to calculate the wavelength of the neutrons and this is then used in the Bragg equation. For time-of-flight experiments the Bragg Law;

is modified to become;

where m = mass of a neutron, L = flight path. The detectors are located such that $L\sin\theta$ is a constant.

The resolution of a time-of-flight diffractometer is dependent on the flight path length and detector angle, with a long flight path and angle of $\theta = 90^\circ$ providing the best resolution. However a range of detectors is needed to provide higher d -spacing data. The entire 2θ range is collected with every pulse of neutrons, approximately once every 20 ms, and the scans are then aggregated to improve the signal/noise ratio. The disadvantages of t-o-f are that the corrections for incident intensity, absorption, extinction coefficient, and detector efficiency have to be applied and the peak shape is highly asymmetrical. However, with modern computer power these problems are relatively easily overcome.

In both cases the neutrons produced are often too high in energy to be used immediately in diffraction experiments and are first sent through one or more moderators, this is often H_2O , D_2O , liquid methane or liquid helium and simply slows the neutrons down. For constant wavelength neutron sources a monochromator is also used and both types use collimators to improve the resolution of the diffraction pattern. Neutron diffraction

experiments are accurate enough to provide lattice constants accurate to a few hundredths of an angstrom.

Samples are typically placed into vanadium cans as vanadium has an almost zero scattering length in neutrons.

Neutrons have a magnetic moment and as such can interact with unpaired electrons in materials, allowing for characterisation of the magnetic structure of materials. Constructive interference occurs between neutrons reflected by unpaired electrons possessing the same spin. This allows for the characterisation of both ferromagnetic and antiferromagnetic materials but because the scattering is caused by the large electron cloud the intensity of the magnetic diffraction peaks decreases at higher angles. For ferromagnetic materials (figure 2.13) constructive interference occurs between adjacent crystallographic planes and so results in increased intensity at the 2θ position of these planes.

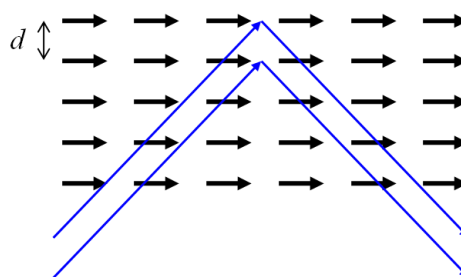


Figure 2.13 Magnetic scattering in a ferromagnetic material

For antiferromagnetic materials the spins on adjacent planes are antiparallel and so there is no constructive interference, this instead occurs for every other plane (figure 2.14) i.e. when $n\lambda = 4d \sin \theta$. This effectively shows up as a separate ‘magnetic unit cell’ in a diffraction pattern and so antiferromagnetic materials show extra peaks in diffraction patterns. For both ferromagnetic and antiferromagnetic materials magnetic scattering leads to increased intensity in structural peaks of the diffraction pattern.

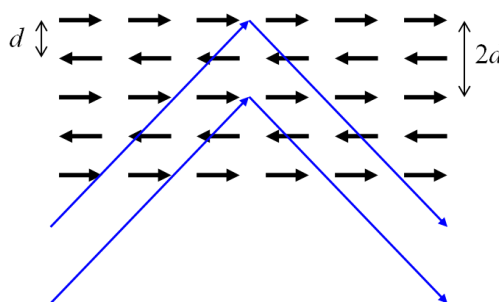


Figure 2.14 Magnetic scattering in an antiferromagnetic material

To detect neutrons a scintillator can be used, often made from ZnS or alternatively a detector containing ^3He can be used. This utilises the production of gamma radiation when ^3He is hit by a neutron and converts to ^4He .

The neutron diffraction experiments carried out in this work were all performed on the Polaris beamline at the ISIS pulsed neutron and muon source at the Rutherford Appleton Laboratory. The neutrons at ISIS are produced from a tungsten target and pulsed in 200 μs bursts of up to 200 μA . Three detection banks were used simultaneously to cover a broad range of d-spacing with good resolution with the details shown in table 2.3.

Table 2.3 Details of the three detection banks at Polaris beamline used in this work

Position	Low angle	90 degrees	Back scattering
Type	^3He gas tubes	ZnS scintillation	^3He gas tubes
No. of detectors	80	216	58
2θ range	28-42°	85-95°	130-160°
Resolution ($\Delta d/d$)	1×10^{-2}	7×10^{-3}	5×10^{-3}
d-range (Å)	0.5-8.15	0.3-4.1	0.2-3.2

2.2.4 Rietveld Refinement

Traditionally structure solution from PXRD data is very challenging. In most cases a powder pattern must be compared to a pattern calculated from an initial model. This is done mathematically by using the Rietveld method^{128,129} and involves incrementally changing the parameters which influence the intensity and position of the peaks until the model matches the experimental pattern as closely as possible. The value which is being minimised is called the ‘least squares residual’ and is defined by the equation;

where y_{io} and y_{ic} are the observed and calculated intensities at point i and w_i , the weighting, is equal to $1/y_{io}$.

The intensity at any point in the diffraction pattern is due to a combination of factors including those from the crystal structure itself, those arising from the diffraction and instrumental effects and is determined by the following equation;

where K represents the Miller indices hkl (section 2.2.1.4)

The scale factor, s , is simply a number which ensures that the calculated and measured intensities are on the same scale.

L_K is a factor which contains the Lorentz, polarisation and multiplicity factors.

The incident X-ray beam, produced by a laboratory diffractometer is generally unpolarised but can be partially polarised by the crystallites in a sample, reducing the intensity of the detected X-rays; this can be corrected for by the polarisation factor;

–

In addition the Lorentz factor can be added to this polarisation term to account for the fact that Bragg reflections in reality occur over a smaller range than the ideal. This gives a modified version of the polarisation factor;

–

The multiplicity factor takes into account the fact that multiple diffraction planes can contribute to the intensity as the diffracted X-rays can overlap. For example in a cubic system the 100, 010 and 001 all contribute to the diffraction pattern at the same point.¹³⁰

Φ is a function to describe the profile of each reflection and is a combination of both instrument and specimen factors. In PXRD the Gaussian, Lorentzian and pseudo-Voigt profiles are the most common with values affecting the full-width-at-half-maximum (FWHM) varied in the refinement process. The Pseudo-Voigt profile function is a mixture of the Gaussian and Lorentzian profiles and the proportion of the two can be varied.¹³⁰

For neutron time-of-flight experiments the peak shape is markedly different and is more asymmetrical with a sharp leading edge and a long tail. This is intrinsic in the method as the initial neutron pulse does not produce neutrons of a symmetrical distribution. The function used to describe time-of-flight peak profiles in this work was a combination of pseudo-Voigt with two exponentials with the rise and fall of these exponentials fixed to values obtained from measuring a standard.

Preferred orientation, P_K , is a phenomenon which usually occurs with flat, plate like materials. In these materials it is common for each crystallite to align and this gives enhanced intensity for the orientations parallel to the surface. This is less of a problem in neutron diffraction due to the type of sample holder and the increased penetration of the neutron beam.

The structure factor, F_K , is governed by the value for the atomic scattering factor, f , and the position and thermal motion of all the atoms present. Each element of the periodic table has a characteristic scattering factor, f , which is determined by the number of electrons it has; the amplitude of scattering is increased as the number of electrons increases.

The position of the atoms in the unit cell is combined with the scattering factors to give scattering vectors for each atom in the unit cell. These vectors are then summed over the j th atom to give the structure factor F_K :

where N is the site occupancy

x , y , and z are the atomic positions

h , k , and l are the miller indices

and $M_j = 8\pi^2 \sin^2\theta/\lambda^2$ with $\langle u^2 \rangle$ the root mean square of the thermal displacement of the atom.

It is important to note here how the scattering factor influences the intensity and causes differences in X-ray and neutron diffraction. X-rays are scattered by the electron cloud, approximately 10^4 times larger than the nucleus which diffracts neutrons. The scattering factor is related (via Fourier Transform) to the distribution of the scattering density. For

X-rays the scattering factor decreases with 2θ but for neutrons this is not the case and the nuclear scattering factor is essentially constant. The scattering length b_j does not vary systematically with atomic number, Z , and can be negative (which implies a phase change in the neutrons of 180°).

The absorption coefficient, A , is a measure of how much of the X-ray beam is absorbed by the material being studied and reduces the intensity of all peaks, it is not usually angle dependent although in some special cases more complex corrections are required.

The background function, y_{bi} , is used to account for the intensity contributed by the sample holder and any amorphous material in the sample. The background function can be an interpolation function, manually described or a multi-term function and adds intensity at any given point.

2.2.4.1 Criteria of Fit

It is necessary to determine if a refinement is progressing and to ensure that the global minimum in the difference between the model and data is being reached rather than a local 'false' minimum. This can be done using a variety of measures of criteria of fit. R_{wp} is mathematically more meaningful than others as the numerator is the least squares residual being minimised:

R_p is a slight modification:

where w_i is a weighting factor, y_{io} and y_{ic} are the observed and calculated intensity. The values for both R factors should be minimised.

χ^2 is also a useful criterion of fit;

where N is the number of observations and P is the number of parameters. For a correct refinement χ^2 should approach 1.¹³⁰

Visual evaluation of the progress of the refinement is fundamental. In general for Rietveld refinement it is important to have a good initial model with fairly accurate unit cell parameters and an 'instrument file' is often used to provide good starting values for the peak profile, Lorentz and polarisation factors and the peak profile function.

2.2.5 X-ray Absorption Spectroscopy

X-ray absorption spectroscopy (XAS) is a technique used to determine the oxidation state and local structure of an atom and is based on the photoelectric effect whereby electrons are emitted by atoms when they absorb electromagnetic radiation of high enough energy. A beam of monochromatic X-rays is targeted at a material and the energy of the X-rays is gradually increased whilst the incident and transmitted X-ray intensity is recorded. When X-rays provide sufficient energy to remove an electron from the atom a large, sharp increase is recorded in the absorption. Multiple steps or edges occur for each atom as electrons from different shells are removed and each element has characteristic values for the absorption energy of these edges. A typical plot of energy versus absorption for an element is shown in figure 2.15.

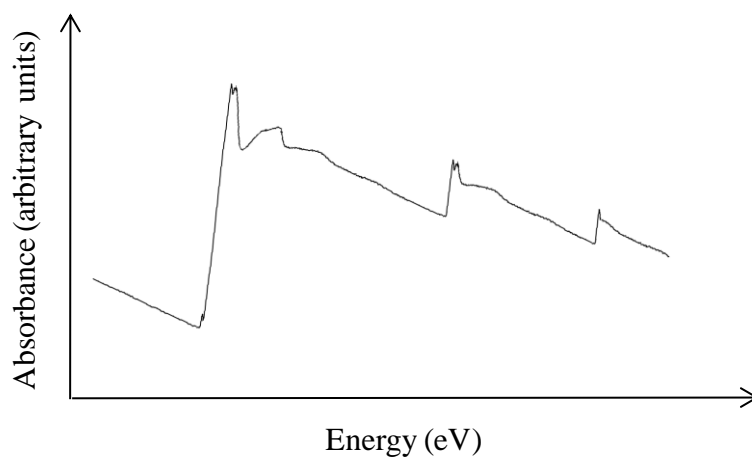


Figure 2.15 Absorption spectrum of an element showing multiple absorption edges

The absorption is quantified by using the absorption coefficient, μ , defined using the following equation;

$$\mu = \frac{I_0 - I}{I_0 x}$$

where x is the thickness of the sample, I_0 is the intensity of the incident radiation and I_t the transmitted radiation. Equation 1 can be rearranged to give the transmitted radiation;

A synchrotron source of X-rays is used as this provides high intensity X-radiation. The wavelength of the incident beam is then swept across a range, chosen to include the absorption edge of one of the elements in the sample and a spectrum of energy versus absorption is produced. This spectrum can be broken down into two components known as the X-ray Absorption Near Edge Structure (XANES) and Extended X-ray Absorption Fine Structure (EXAFS) and these regions are shown in figure 2.16.

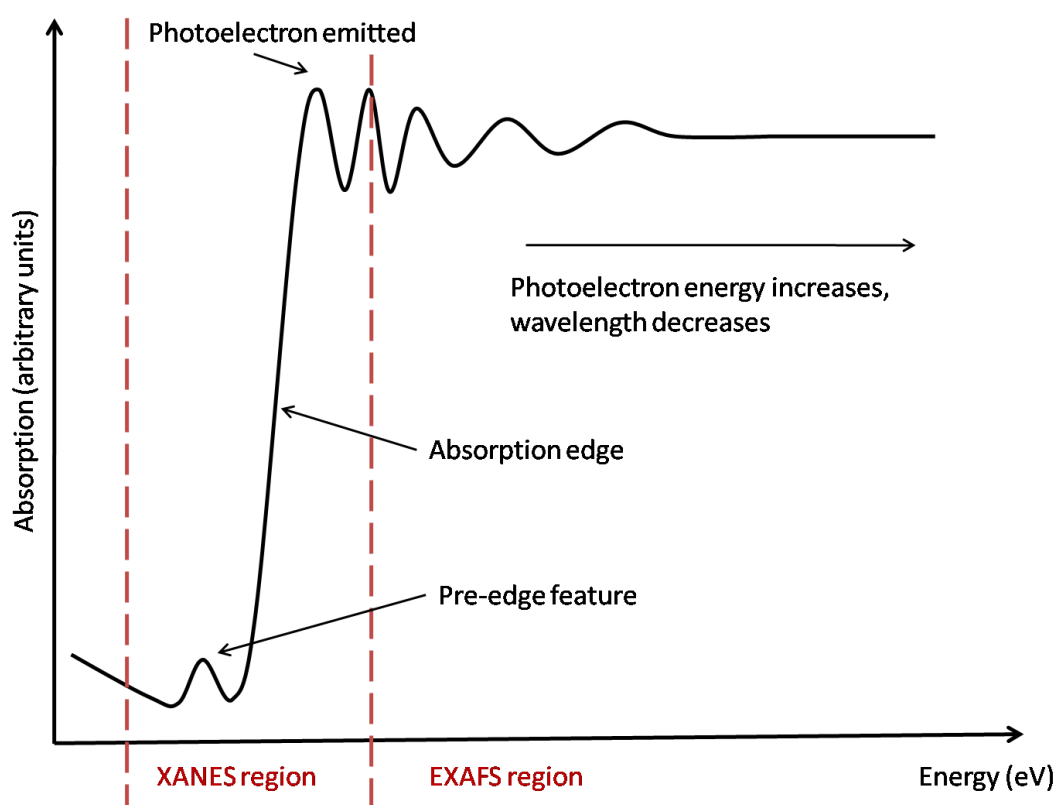


Figure 2.16 Schematic diagram of an XAS spectrum showing different regions

These two regions give different but complimentary information. The XANES region provides information about the oxidation state and coordination geometry of the atom and the EXAFS region provides information about the distance and number of atoms in the surroundings. The XANES pre-edge feature is due to s-d transitions and, depending on allowed transitions, provides information about the geometry around the atom.

The absorption edge is due to s-p transitions and its position on the energy axis provides information about the oxidation state of the atom. The absorption edges for atoms in different oxidation states are tabulated for comparison or a standard may be analysed together with the samples.

The EXAFS region is an interference pattern produced by the emitted photoelectron. The photoelectron ejected upon impact by the X-ray energy has energy equivalent to the energy of the absorbed X-ray minus the binding energy, i.e. the energy required to move the electron from its orbit to the continuum. The emitted photoelectron interacts with the surrounding atoms in a wave like fashion, turning them into point scatterers. This emitted and scattered photoelectron can then interfere with the forward propagating X-ray energy and produces a modulation of the absorption spectrum. This is seen in the region around 15eV after the absorption edge. The modulation is altered by the distance and nature of the point scatterers, i.e. the atoms surrounding the excited atom. The frequency of the interference pattern is related to the atomic distance, a short distance producing shorter oscillations. The intensity of the peaks provides information about how many atoms are surrounding the excited atom and the disorder in the atomic distances, the Debye Waller factor. Information on the nature of the surrounding atoms is also contained in the EXAFS region, the frequency has a phase shift which gives some information and the intensity of the peaks is generally higher for larger atoms. In addition the pattern of the change of relative peak intensities with energy also gives information.

The absorption spectra can be collected in either transmission or fluorescence mode. For this work transmission mode was used and the experimental set-up is shown in figure 2.17.

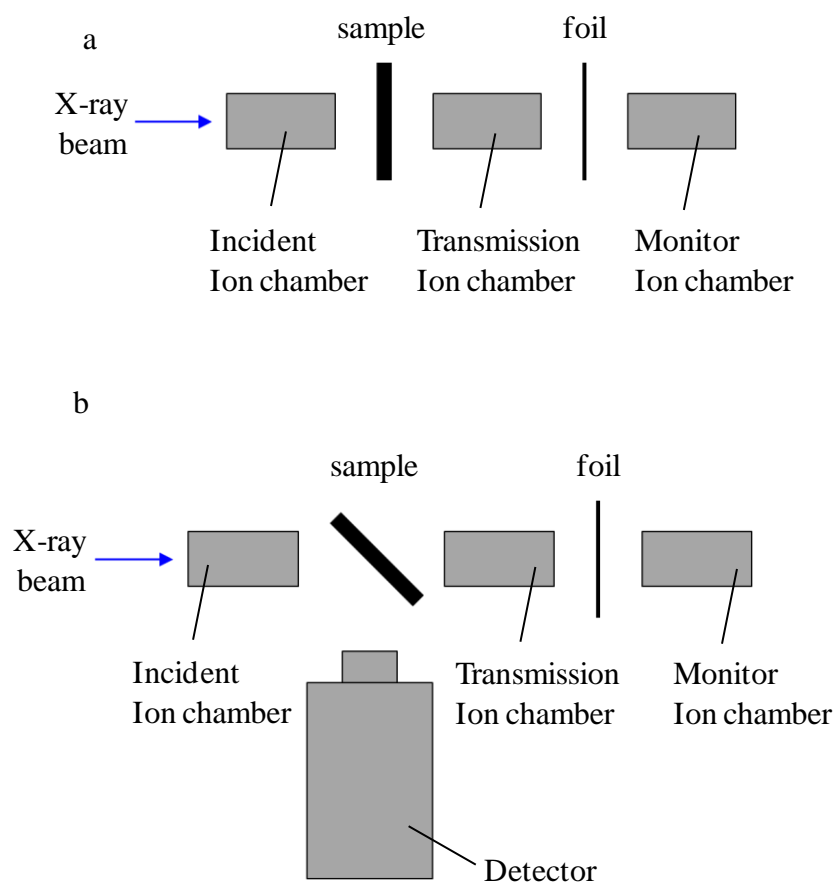


Figure 2.17 Standard experimental set-ups for XAS a) transmission mode b) fluorescence mode

In both cases the X-ray beam is first passed through an incident ion chamber to record the intensity of the incident X-ray beam and then impinges upon the sample. In fluorescence mode the sample is rotated 45° to the beam and only the emission is detected. In transmission mode an ion chamber after the sample is used to detect the transmitted radiation. It is possible to place a foil of a material with a known spectrum after the transmission ion chamber followed by a further detector to allow for calibration against a standard.

In this work three parameters have been used to describe the fitting of the EXAFS data. E_f is a single refined parameter to reflect differences in the theoretical and experimental Fermi levels.

The R factor which is a measure of the absolute misfit between data and theory

And the Fit Index

$$FI = \sum_i [(\chi^T - \chi^E)k^3]^2$$

2.3 Physical Characterisation

2.3.1 Magnetic Measurements

Magnetic susceptibility measurements were carried out using a Superconducting Quantum Interference Device (SQUID). Such devices are able to measure a magnetic field down to 5×10^{-18} T with very low noise. A SQUID is based upon a Josephson junction, (figure 2.18), which is a ring of superconducting material separated by a ‘weak link’, i.e. an area of lower current density; commonly a thin layer of insulator.

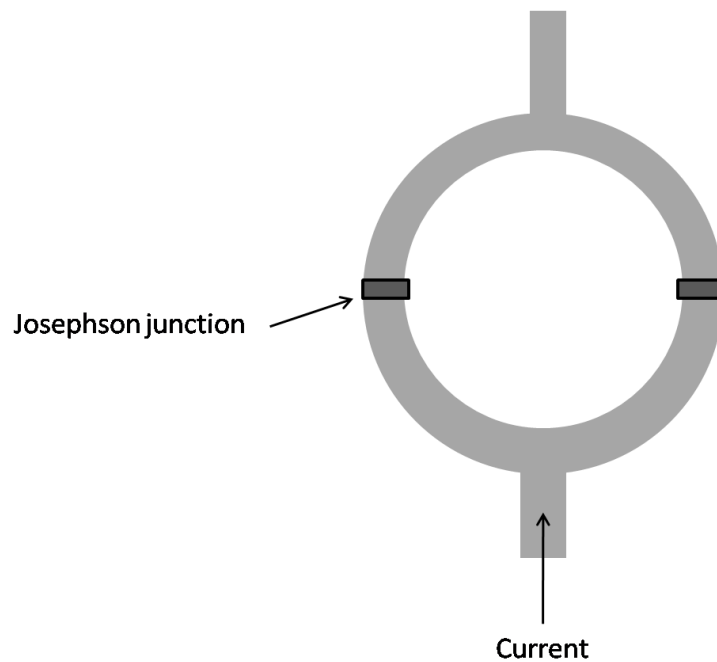


Figure 2.18 Josephson junction as used in a SQUID

Below a critical current, I_c , the Cooper pairs formed in the superconducting material can tunnel through the insulator. With

$$I_c = 2I_j \cos(\pi\Phi/\Phi_0)$$

where I_j is a constant dependent on the geometry of the junction, Φ is the flux within the superconducting ring and ϕ_0 is the quantised flux, equal to $h/2e$ (h = Planck's constant, e = charge on an electron) or $2 \times 10^{-15} \text{ Tm}^2$. Any changes in external field are compensated for by the superconducting current so that the total flux is always an integer of ϕ_0 . In this way, external flux causes changes in the maximum current that the loop can carry and this is measurable as a voltage across the junction. As the sample is introduced into the system its magnetic field affects the maximum current and this effect is proportional to the magnetisation of the sample. The temperature and external field strength can both be varied to measure the effect these factors have on the magnetisation of the sample. For this work the field-cooled magnetisation was generally measured at 2 T and over the range 5-300 K. The measurements were carried out by Antoine Maignan at ENSICAEN.

2.3.2 Transport Measurements

Transport measurements were carried out using a Quantum Design Physical Properties Measurement System (PPMS). This device allows for the measurement of a wide variety of physical properties over a wide temperature range. For this work the resistivity was determined using the 'four-probe method'. The polycrystalline sample is pressed into a pellet then cut into a rectangular shape to which four electrodes are attached using indium contacts. The arrangement is pictured in Figure 2.19. The current is passed across 1-2 and the voltage measured across 3-4.

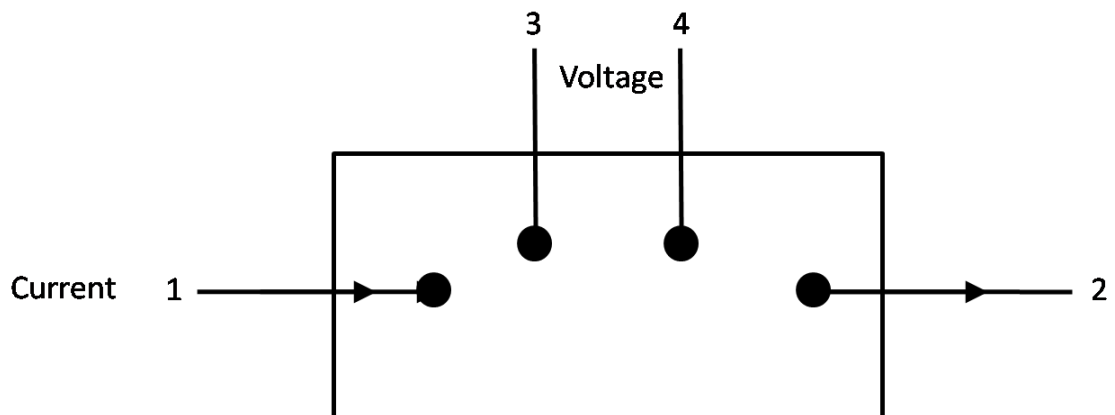


Figure 2.19 Arrangement of contacts on a sample for measuring resistivity data

The sample is then placed into the PPMS device (figure 2.20) and the temperature, magnetic field and other factors can be varied during the resistance measurements, allowing for measurements of the magnetoresistance.

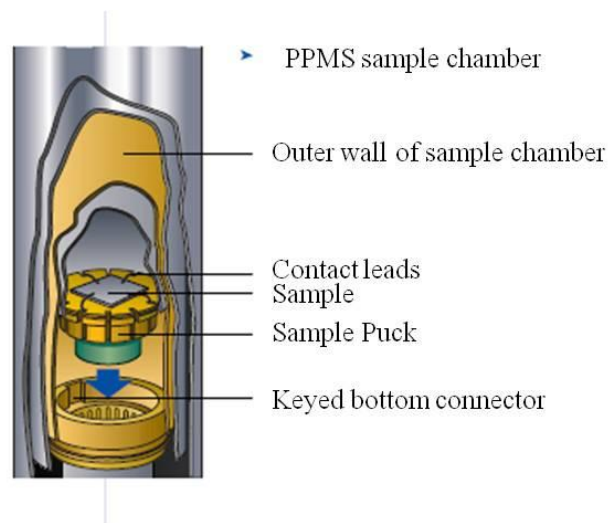


Figure 2.20 Representation of the sample environment in a PPMS device

The resistance of the material is then calculated using the equation;

—

and the resistivity, which is an intrinsic property of the material, can then be calculated using the equation;

—

where A is the cross sectional area and l is the length of the material.

The magnetoresistance (MR) of the material can be measured across a temperature range either by cooling the material gradually and measuring the resistance with and without an external field or by letting the material reach a set temperature and gradually varying the magnetic field whilst measuring the resistance. The latter method has been used predominantly in this work as it provided results with less background noise. The magnetoresistance is then expressed as percentage using the equation;

—————

where $\rho(H)$ is the resistivity in applied field and $\rho(0)$ the resistivity in the absence of a field.

For this work the resistivity was measured using the four-probe technique over the range 5-300 K with magnetoresistance measurements carried out over the range 0-7 T. The measurements were performed by Vincent Hardy at ENSICAEN.

Analysis of the magnetic and transport measurements was performed to determine the properties of the materials and is described in the Results sections of the Experimental chapters (3-6).

3.0 Ba₂Co_{1-x}Zn_xS₃

3.1 Synthesis and Characterisation

The synthesis of the ternary sulphides Ba₂Co_{1-x}Zn_xS₃ (x = 0.1, 0.2, 0.25, 0.4, 0.5, 0.6, 0.75, 0.8) was achieved *via* a solid-gas reaction as discussed in the Experimental section 2.1. Stoichiometric mixtures of barium carbonate (99%) cobalt (99.8%) and zinc oxide (99.8%) were reacted with carbon disulphide (99%) for 24 hours at 1000°C.

3.2 Results and Discussion

3.2.1 Powder X-ray Diffraction (PXRD)

A typical refinement is shown in figure 3.1 with the atomic positions, thermal parameters and occupancies for Ba₂Co_{0.75}Zn_{0.25}S₃ shown in table 3.1, all other refinements are included in Appendix 1. The unit cell parameters and fitting parameters (R_p, R_{wp} and χ^2) for all of the samples are shown in table 3.2.

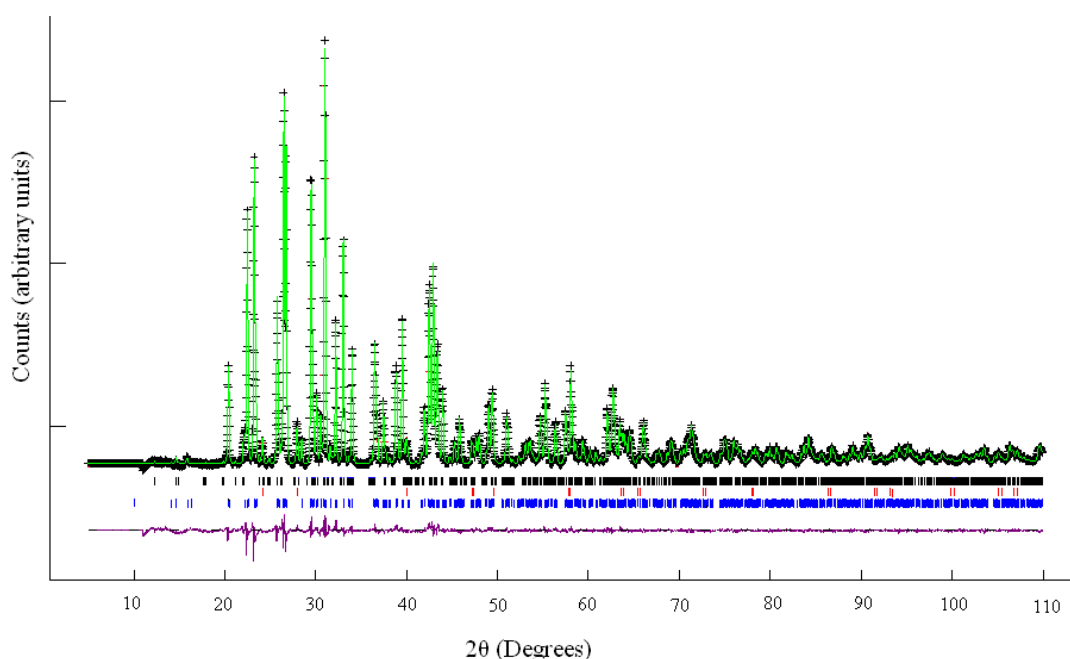


Figure 3.1 Rietveld refinement against X-ray diffraction data for Ba₂Co_{0.75}Zn_{0.25}S₃: Black line (observed), green line (calculated) and purple line (difference). Blue tick marks correspond to Ba₂Co_{0.75}Zn_{0.25}S₃ red to BaS and black to Ba₂SiS₄

Table 3.1 Refined atomic coordinates, thermal parameters and occupancies for $\text{Ba}_2\text{Co}_{0.75}\text{Zn}_{0.25}\text{S}_3$

Atom	x	y	z	U	F
Ba1	0.82711(8)	0.48114(8)	0.25	0.0067(4)	1
Ba2	0.48840(9)	0.67370(9)	0.25	0.0075(4)	1
Co	0.7461(2)	0.1967(2)	0.25	0.0067(4)	0.75
Zn	0.7461(2)	0.1967(2)	0.25	0.0067(4)	0.25
S1	0.8659(3)	0.0528(3)	0.25	0.0002(7)	1
S2	0.5593(3)	0.1407(3)	0.25	0.0002(7)	1
S3	0.2255(3)	0.7097(3)	0.25	0.0002(7)	1

Although the effective ionic radius for Zn^{2+} is slightly larger (0.60 Å in tetrahedral coordination) than that of Co^{2+} (0.58 Å in tetrahedral coordination)¹³¹ in PXRD analysis the unit cell parameters a, b and c do not show the linear variation expected from Vegard's Law. The overall unit cell volume, however, does generally increase as the amount of zinc present increases.

Table 3.2 Unit cell parameters and fitting parameters from PXRD data for the series $\text{Ba}_2\text{Co}_{1-x}\text{Zn}_x\text{S}_3$ ($x = 0.1, 0.2, 0.25, 0.4, 0.5, 0.6, 0.75, 0.8$)

x	0.1	0.2	0.25	0.4	0.5	0.6	0.75	0.8
a (Å)	12.0104(6)	12.0065(9)	11.9991(2)	12.0086(9)	11.9957(2)	12.0091(8)	12.0035(3)	12.0057(5)
b (Å)	12.4952(6)	12.5103(9)	12.5055(2)	12.5349(9)	12.5349(3)	12.5619(8)	12.5693(4)	12.5772(5)
c (Å)	4.2082(2)	4.2085(3)	4.20647(5)	4.2099(3)	4.2059(1)	4.2101(3)	4.2099(1)	4.2086(2)
V (Å ³)	631.53(7)	632.13(2)	631.20(2)	633.70(1)	632.42(3)	635.13(9)	635.17(4)	635.49(6)
R_p (%)	12.15	7.76	3.04	7.24	4.96	11.58	6.61	10.24
R_{wp} (%)	14.85	9.68	4.43	9.98	5.90	14.03	8.28	12.50
χ^2	1.53	2.18	4.39	1.99	1.44	1.34	2.52	1.48

3.2.2 Neutron Powder Diffraction (NPD)

Neutron diffraction data were collected for the samples $\text{Ba}_2\text{Co}_{1-x}\text{Zn}_x\text{S}_3$ with $x = 0.1, 0.25, 0.5, 0.6, 0.75$ on the Polaris beamline at ISIS, all measurements were carried out at room temperature except for the sample $\text{Ba}_2\text{Co}_{0.5}\text{Zn}_{0.5}\text{S}_3$ which was measured at ~ 5 K. Three detection banks were used (low angle, 90 degrees and backscattering) and all three histograms produced were analysed simultaneously using Rietveld refinement with the software GSAS in conjunction with EXPGUI.^{121,122}

The structure of Ba_2CoS_3 was chosen as the starting model with Zn and Co located on the same site and the fractional occupancies set initially to the values dictated by the stoichiometry of the starting material. The scale, cell parameters, atomic positions (with the atomic positions of Zn and Co constrained to be equal) and peak profile (~ 5 terms) were all refined. Analysis showed that impurities of BaS and/or Ba_2SiS_4 are present in the samples and there is some evidence for a poorly crystalline impurity seen in the broad peaks seen at 1.226 Å, 2.097 Å and 3.434 Å (in d-spacing) in some of the neutron diffraction patterns. This poorly crystalline impurity could contain the excess transition metal resulting from the formation of Ba-containing impurities.

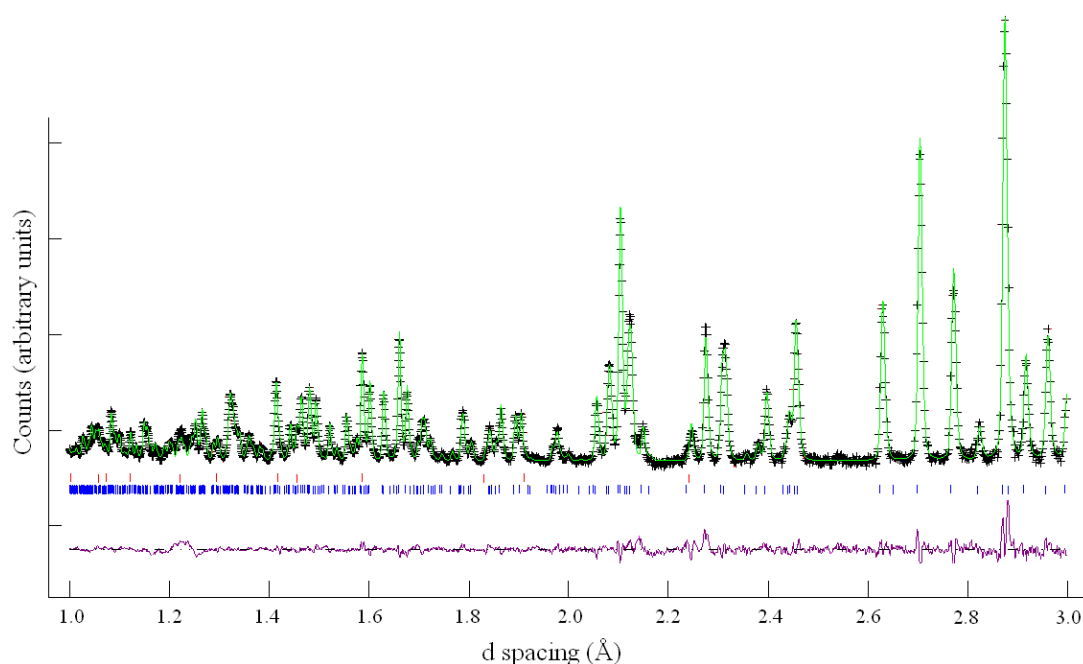


Figure 3.2 Rietveld refinement against neutron diffraction data for $\text{Ba}_2\text{Co}_{0.75}\text{Zn}_{0.25}\text{S}_3$: Black line (observed), green line (calculated) and purple line (difference). Blue tick marks correspond to $\text{Ba}_2\text{Co}_{0.75}\text{Zn}_{0.25}\text{S}_3$ and red to BaS

An example of a refinement is shown in figure 3.2 with the atomic positions, thermal parameters and occupancies for $\text{Ba}_2\text{Co}_{0.75}\text{Zn}_{0.25}\text{S}_3$ shown in table 3.3 with all other

refinements in Appendix 2. A summary of the unit cell parameters for all the samples along with the residual fit parameters is shown in table 3.4.

Table 3.3 Refined atomic coordinates, thermal parameters and occupancies for $\text{Ba}_2\text{Co}_{0.75}\text{Zn}_{0.25}\text{S}_3$ from neutron diffraction data

Atom	x	y	z	U	F
Ba1	0.8285(1)	0.4808(1)	0.25	0.0090(3)	1
Ba2	0.4882(1)	0.6730(1)	0.25	0.0057(2)	1
Co	0.7488(2)	0.1984(2)	0.25	0.0030(4)	0.75
Zn	0.7488(2)	0.1984(2)	0.25	0.0030(4)	0.25
S1	0.8649(2)	0.0526(2)	0.25	0.0129(6)	1
S2	0.5612(2)	0.1410(2)	0.25	0.0036(4)	1
S3	0.2279(2)	0.7111(2)	0.25	0.0029(4)	1

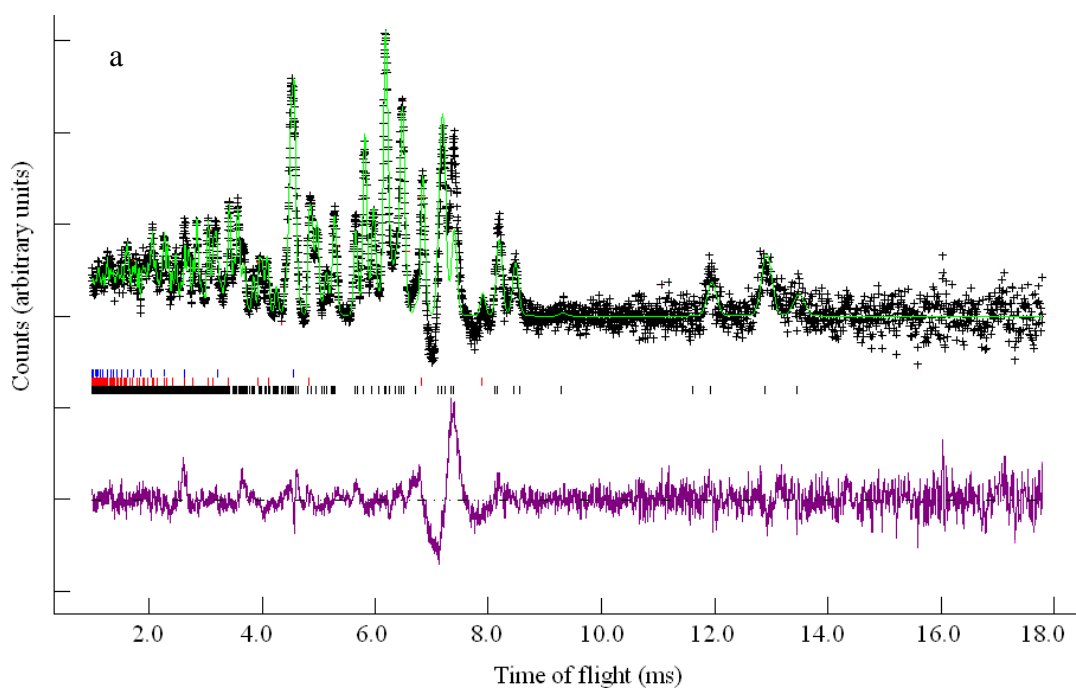
In agreement with results from Rietveld refinement against the PXRD data the unit cell parameters do not show the linear variation expected from Vegard's Law but the overall unit cell volume does increase as the amount of zinc increases.

The diffraction pattern of $\text{Ba}_2\text{Co}_{0.5}\text{Zn}_{0.5}\text{S}_3$ was collected at ~5 K to determine the possible existence of a transition to three-dimensional magnetic order in analogy to Ba_2CoS_3 , which shows such a transition at $T_N = 46$ K. The absence of additional diffraction peaks at high d space in the pattern collected at 5 K showed that no magnetic transition is present in $\text{Ba}_2\text{Co}_{0.5}\text{Zn}_{0.5}\text{S}_3$.

The neutron patterns collected at 273 K and 5 K do not show any difference which may indicate the presence of a superstructure (figure 3.3).

Table 3.4 Summary of lattice parameters and residual fit parameters from neutron data for $\text{Ba}_2\text{Co}_{1-x}\text{Zn}_x\text{S}_3$

x	0^{III}	0.1	0.25	0.5	0.6	0.75
a (Å)	11.994(2)	11.9975(5)	11.9987(3)	11.9756(4)	11.9946(5)	11.9980(2)
b (Å)	12.472(2)	12.4843(6)	12.5033(3)	12.5013(5)	12.5458(5)	12.5601(3)
c (Å)	4.201(1)	4.2059(2)	4.2067(1)	4.1965(2)	4.2067(2)	4.20844(8)
V (Å ³)	628.5(3)	629.96(7)	631.10(4)	628.26(5)	633.03(6)	634.20(3)
R_p	5.14	4.18	3.18	2.42	6.01	3.64
R_{wp}	4.03	2.58	2.30	1.45	2.93	2.12
χ^2	5.06	2.66	3.94	3.94	3.11	3.07



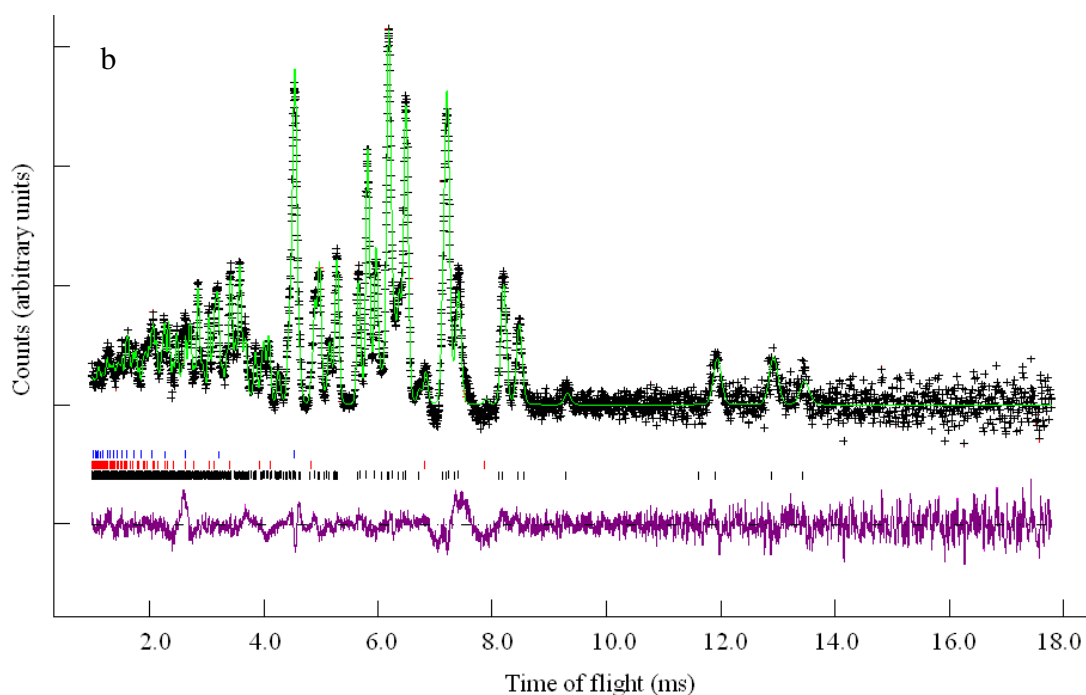


Figure 3.3 Rietveld refinement against neutron diffraction data for **a)** $\text{Ba}_2\text{Co}_{0.5}\text{Zn}_{0.5}\text{S}_3$ measured at 5 K and **b)** $\text{Ba}_2\text{Co}_{0.5}\text{Zn}_{0.5}\text{S}_3$ measured at 273 K: Black line (observed), green line (calculated) and purple line (difference). Blue tick marks correspond to $\text{Ba}_2\text{Co}_{0.5}\text{Zn}_{0.5}\text{S}_3$, blue to V and red to BaS. Data out to high d-spacing ($\sim 8 \text{ \AA}$) shows no additional peaks for the low temperature data. The broad peaks at 2.2, 3.8, and 7.7 ms are due to poorly crystalline impurities

Some selected bond lengths and angles from the refinement against PXRD and neutron diffraction data for the samples $\text{Ba}_2\text{Co}_{1-x}\text{Zn}_x\text{S}_3$ ($x = 0.25, 0.5, 0.75$) are shown in tables 3.5 and 3.6 respectively and figure 3.4 shows the labelling of the sulphur atoms around the transition metal.

As the amount of zinc in the samples increases the (S(3)-TM-S(3)) angle tends to decrease whilst the others remain approximately unchanged. The TM-S(3) bond length increases as the zinc content increases whilst the other TM-S bond lengths remain the same (within error values).

Table 3.5 Selected bond lengths and angles from refinement against PXRD data for $\text{Ba}_2\text{Co}_{1-x}\text{Zn}_x\text{S}_3$

x	0.25	0.5	0.75
Bond Lengths (Å)			
TM-S(1)	2.31(3)	2.32(3)	2.35(3)
TM-S(2)	2.33(3)	2.32(3)	2.32(3)
TM-S(3) × 2	2.430(15)	2.45(2)	2.46(2)
TM-TM interchain	4.2064(10)	4.2059(10)	4.2099(10)
TM-TM intrachain	6.60(3), 6.14(3)	6.61(3), 6.14(3)	6.63(3), 6.14(3)
Angles (°)			
S(1)-TM-S(2) × 1	110.7(3)	110.7(3)	110.4(3)
S(1)-TM-S(3) × 2	106.4(3)	106.7(3)	105.7(3)
S(2)-TM-S(3) × 2	106.7(3)	107.2(3)	108.7(3)
S(3)-TM-S(3) × 1	119.85(15)	118.40(15)	117.5(2)

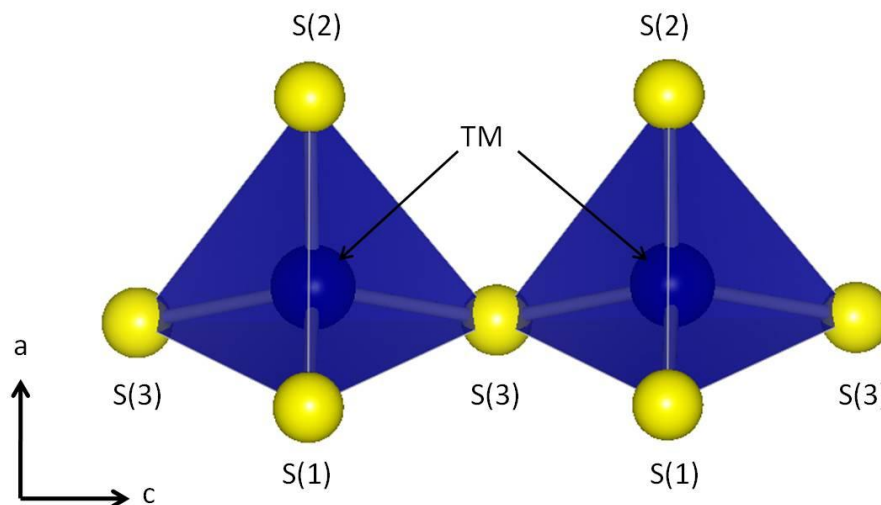


Figure 3.4 The distorted tetrahedral environment around the transition metal showing the three sulphur atoms around each tetrahedral metal centre

Table 3.6 Selected bond lengths and angles from refinement against NPD data for $\text{Ba}_2\text{Co}_{1-x}\text{Zn}_x\text{S}_3$

x	0.25	0.5	0.75
Bond Lengths (Å)			
TM-S(1)	2.29(3)	2.30(3)	2.31(3)
TM-S(2)	2.37(3)	2.38(3)	2.36(3)
TM-S(3)	2.403(14)	2.424(15)	2.43(2)
TM-TM interchain	4.2054(10)	4.2018(10)	4.2020(10)
TM-TM intrachain	6.59(3), 6.13(3)	6.60(3), 6.14(3)	6.61(3), 6.13(3)
Angles (°)			
S(1)-TM-S(2)	109.6(2)	110.0(2)	109.9(2)
S(1)-TM-S(3)	107.8(3)	108.5(3)	108.0(3)
S(2)-TM-S(3)	104.5(3)	104.7(3)	105.7(3)
S(3)-TM-S(3)	122.08(12)	120.18(12)	119.49(13)

The values generally show good consistency between PXRD and neutron refinements. Neutron diffraction results tend to indicate slightly shorter bond lengths compared with PXRD except for the Co-S(2) bond, which runs along the a axis, which is longer from neutron diffraction results. This is reflected in the bond angles around the transition metal with the angles found in neutron diffraction higher along the chain (S(3)-TM-S(3)) and between the S(3) and S(1) atoms and the angles between S(2) and S(1) and S(2) and S(3) lower than in the PXRD results.

3.2.3 X-ray Absorption Spectroscopy (XAS)

The first step taken in the data analysis was averaging of the multiple spectra collected for each sample, followed by calibrating the absorption edge of the samples against the metal foils used as standards. A background subtraction was then performed using the program PAXAS,¹³² the intensity was then normalised before XANES analysis was performed.

To prepare the EXAFS data for analysis the post edge data were first extracted i.e. the ‘atomic component’ (the part of the spectrum free atoms would contribute) was removed, using a 5 or 6 order polynomial or spline using the program PYSPLINES.¹³³ The extracted data, now in the form of normalised intensity plotted against k space (\AA^{-1}) were then weighted, to ensure that low intensity, high energy data are properly accounted for, by multiplying each data point by k^3 . The data produced were then analysed using the program EXCURV 98.¹³⁴ A model containing the type and number of atoms surrounding the central atom as well as their distance from the central atom is compared to the data and a refinement of this model carried out. A Fourier transform (FT) is used to provide a plot of distance from the central atom against intensity for visual comparison.

3.2.3.1 XANES

The Co-K-edge XANES spectrum of Ba_2CoS_3 has been studied and is consistent with a distorted tetrahedral environment.¹¹⁰ A comparison of this spectrum with the spectra collected for the series $\text{Ba}_2\text{Co}_{1-x}\text{Zn}_x\text{S}_3$ ($x = 0.25, 0.5, 0.75$) confirms that the tetrahedral environment is maintained upon substitution of Zn for Co (figure 3.4).

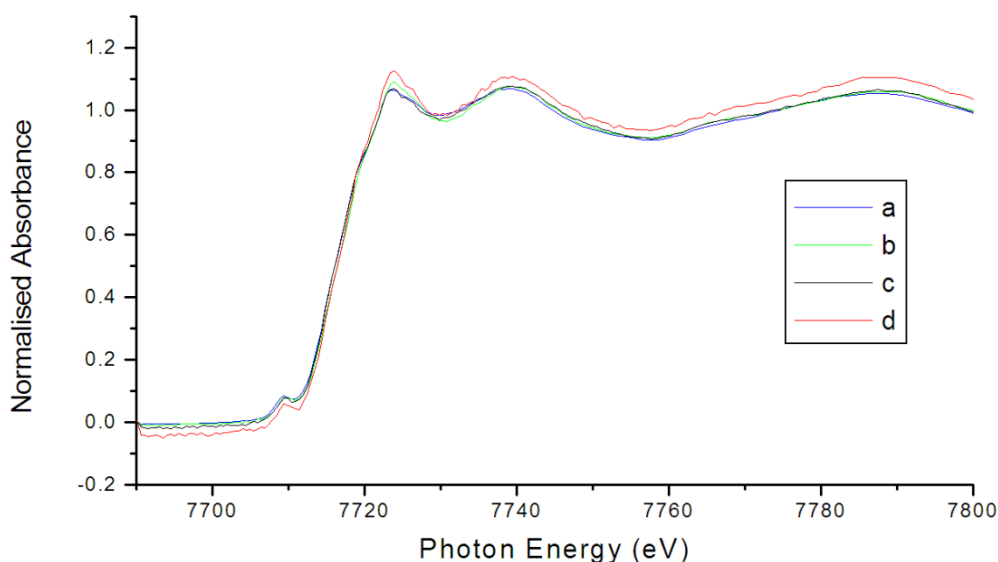


Figure 3.4 Co-K-edge XANES spectra of a) Ba_2CoS_3 b) $\text{Ba}_2\text{Co}_{0.75}\text{Zn}_{0.25}\text{S}_3$ c) $\text{Ba}_2\text{Co}_{0.5}\text{Zn}_{0.5}\text{S}_3$ d) $\text{Ba}_2\text{Co}_{0.25}\text{Zn}_{0.75}\text{S}_3$

The pre-edge feature seen at around 7710 eV can be used to characterise 1s-3d transitions and is more intense for environments with no centre of symmetry. The presence of a shoulder on the edge itself is caused by 1s-4p transitions and is generally indicative of square planar materials or square based pyramidal centres. The XANES spectra for all the materials studied show relatively intense pre-edge features but no shoulder and as such are consistent with a tetrahedral environment.

The Zn-K-edge of Ba_2ZnS_3 has not previously been studied. As zinc is present in $\text{Ba}_2\text{Co}_{1-x}\text{Zn}_x\text{S}_3$ as $\text{Zn}^{2+} d^{10}$ there can be no 1s-4p transition so no pre-edge feature is expected. A comparison of the XANES spectra for Ba_2ZnS_3 and zinc sulphide, ZnS, shows that the pre-edge and edge areas are the same confirming that the structure is consistent with a tetrahedral environment for the Zn, figure 3.5. The differences in the patterns seen after the edge (i.e. the EXFAS region) are due to the different environments of the zinc atoms beyond the first shell.

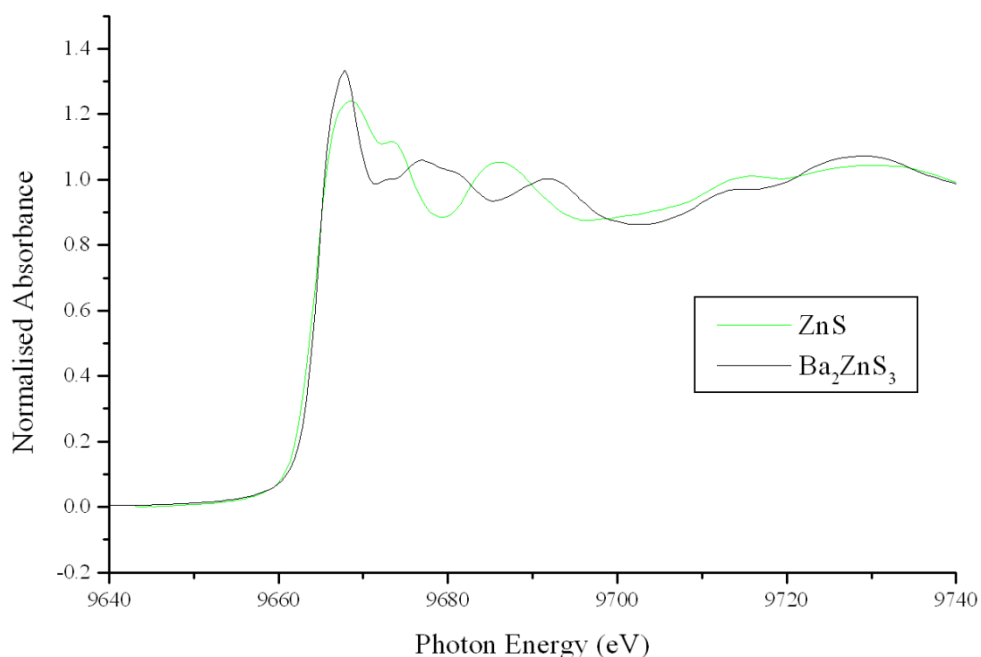


Figure 3.5 Zn-K-edge XANES spectra of ZnS and Ba_2ZnS_3

Comparing the compounds in the series $\text{Ba}_2\text{Co}_{1-x}\text{Zn}_x\text{S}_3$ with the XANES spectra for Ba_2ZnS_3 shows that this structure is maintained throughout, see figure 3.6.

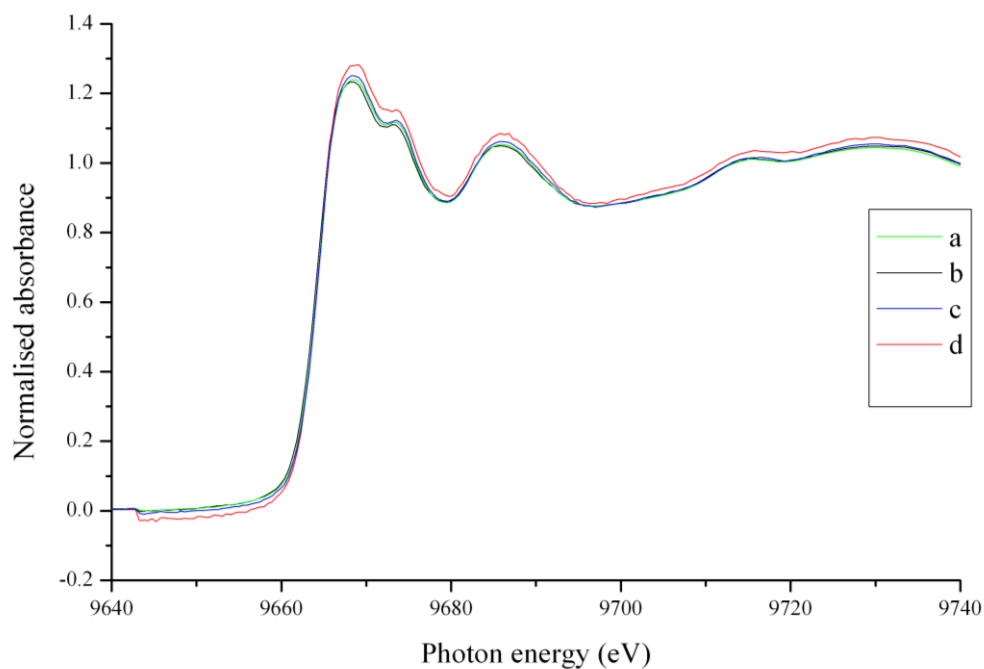


Figure 3.6 Zn-K-edge XANES spectra of a) Ba_2ZnS_3 b) $\text{Ba}_2\text{Co}_{0.25}\text{Zn}_{0.75}\text{S}_3$ c) $\text{Ba}_2\text{Co}_{0.5}\text{Zn}_{0.5}\text{S}_3$ d) $\text{Ba}_2\text{Co}_{0.75}\text{Zn}_{0.25}\text{S}_3$

3.2.3.2 EXAFS

For the analysis of EXAFS data the local environment of the transition metal (TM) was initially set using the parameters obtained from a previous study of the EXAFS data for Ba_2CoS_3 and from PXRD data.¹¹⁰ The analysis was initially performed modelling five shells. The first TM-S shell in the Fourier transform (FT) was set as a single shell of four sulphur atoms at a radius of 2.35 Å. The next significant shell is made up of a mixture of seven TM-Ba interactions, three at 3.5 Å and four at 3.8 Å, followed by two TM-TM interactions at 4.1 Å. The final shell in the FT to be fitted was that at about 5.7 Å resulting from another TM-Ba shell. Figure 3.7 shows a representation of these interactions.

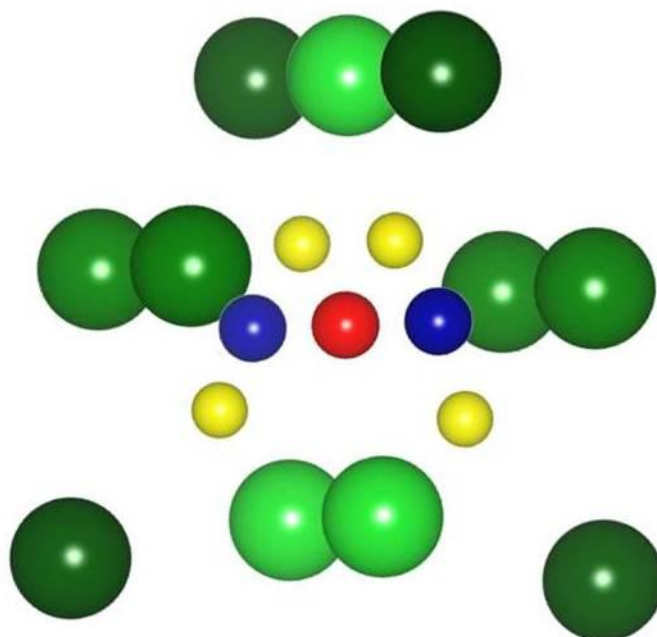


Figure 3.7 Representation of the atoms modelled in EXAFS analysis. The red atom represents the central transition metal atom with the two neighbouring transition metals in blue and the sulphur shown in yellow. The three different barium environments are shown in green with darker green representing the barium atoms further from the transition metal

The distances and the Debye-Waller factors were refined. The Debye-Waller factor is a measure of the variation in atomic distances and accounts for the molecular, structural and thermal disorder of a sample. The results for the Co-K-edge are shown in figures 3.8-3.11 and the results of the refinements are shown in table 3.5. The results for the Zn-K-edge are shown graphically in figures 3.12-3.15 and the results of the refinements are shown in table 3.6.

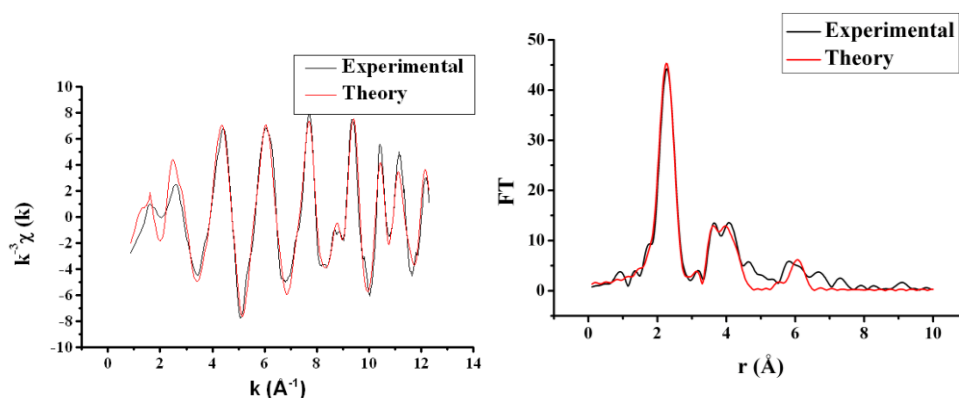


Figure 3.8 Co-K-edge EXAFS and Fourier Transform for Ba_2CoS_3

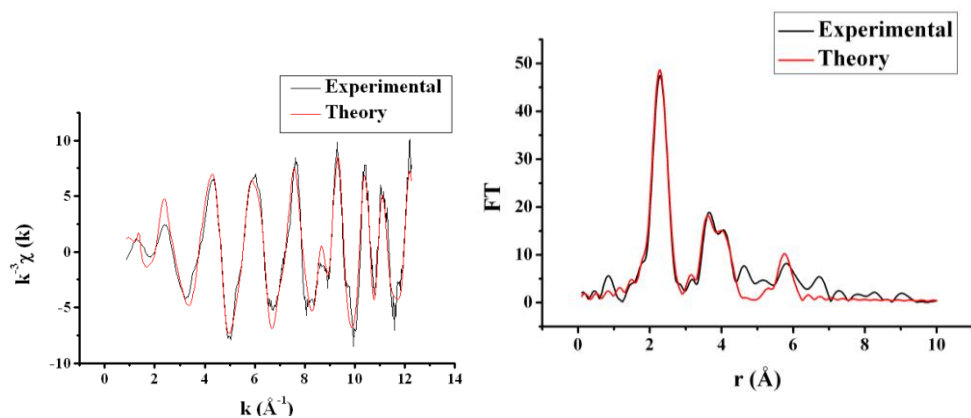


Figure 3.9 Co-K-edge EXAFS and Fourier Transform for $\text{Ba}_2\text{Co}_{0.75}\text{Zn}_{0.25}\text{S}_3$

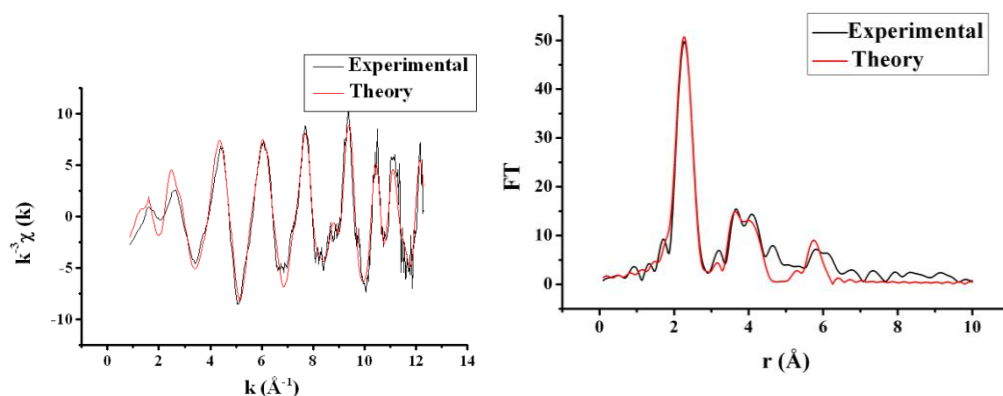


Figure 3.10 Co-K-edge EXAFS and Fourier Transform for $\text{Ba}_2\text{Co}_{0.5}\text{Zn}_{0.5}\text{S}_3$

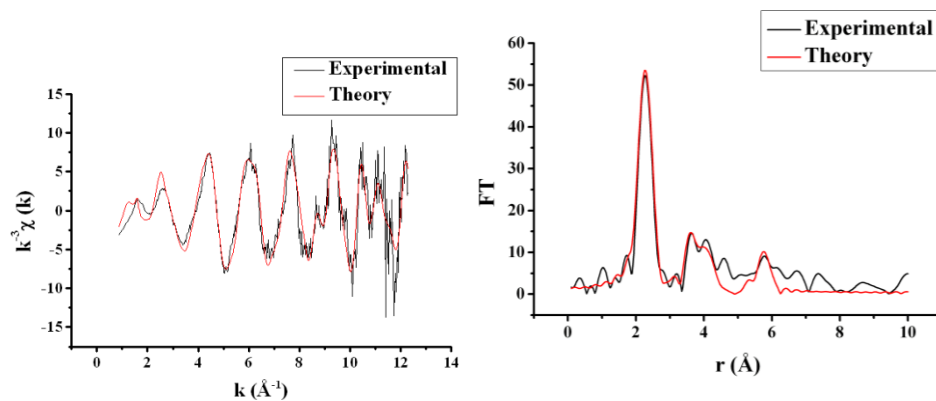


Figure 3.11 Co-K-edge EXAFS and Fourier Transform for $\text{Ba}_2\text{Co}_{0.25}\text{Zn}_{0.75}\text{S}_3$

Table 3.5 Summary of refined Co-K-edge EXAFS parameters

Bond	Ba_2CoS_3		$\text{Ba}_2\text{Co}_{0.75}\text{Zn}_{0.25}\text{S}_3$		$\text{Ba}_2\text{Co}_{0.5}\text{Zn}_{0.5}\text{S}_3$		$\text{Ba}_2\text{Co}_{0.25}\text{Zn}_{0.75}\text{S}_3$	
	r (Å)	$2\sigma^2$ (Å ²)	r (Å)	$2\sigma^2$ (Å ²)	r (Å)	$2\sigma^2$ (Å ²)	r (Å)	$2\sigma^2$ (Å ²)
Co-S (4)	2.334(3)	0.0138(6)	2.343(3)	0.0123(7)	2.334(4)	0.0117(7)	2.336(5)	0.0108(9)
Co-Ba (3)	3.533(7)	0.0167(18)	3.538(6)	0.0113(1)	3.537(8)	0.0133(14)	3.526(12)	0.0136(22)
Co-Ba (4)	3.865(21)	0.0275(99)	3.841(25)	0.0248(12)	3.851(40)	0.0379(18)	3.830(65)	0.0407(29)
Co-Co (2)	4.090(16)	0.0071(24)	4.081(22)	0.0077(43)	4.100(13)	0.0064(25)	4.084(19)	0.0072(40)
Co-Ba (4)	5.573(10)	0.0129(19)	5.579(8)	0.0081(14)	5.587(10)	0.0093(18)	5.605(14)	0.0082(25)
E_f	-9.2(3)		-5.9(4)		-9.3(4)		-9.2(6)	
R	25.2%		27.3%		30.6%		39.3%	
FI	0.25		0.33		0.41		0.86	

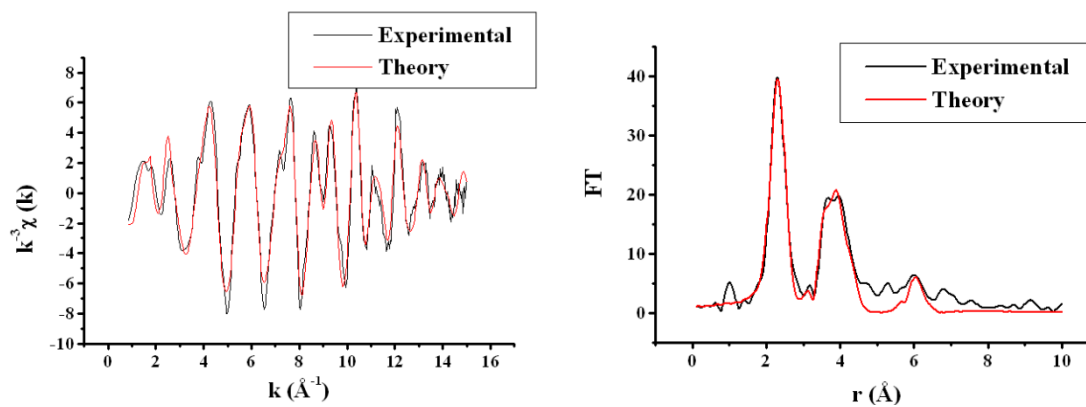


Figure 3.12 Zn-K-edge EXAFS and Fourier Transform for Ba_2ZnS_3

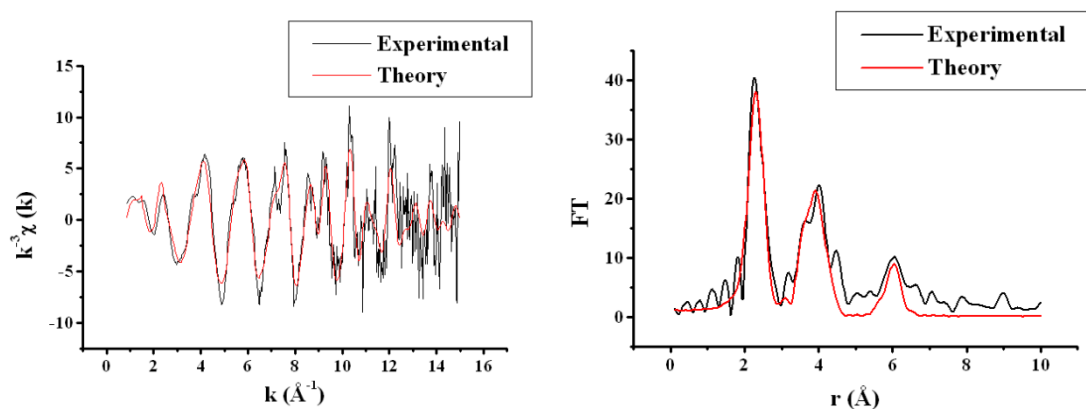


Figure 3.13 Zn-K-edge EXAFS and Fourier Transform for $\text{Ba}_2\text{Co}_{0.75}\text{Zn}_{0.25}\text{S}_3$

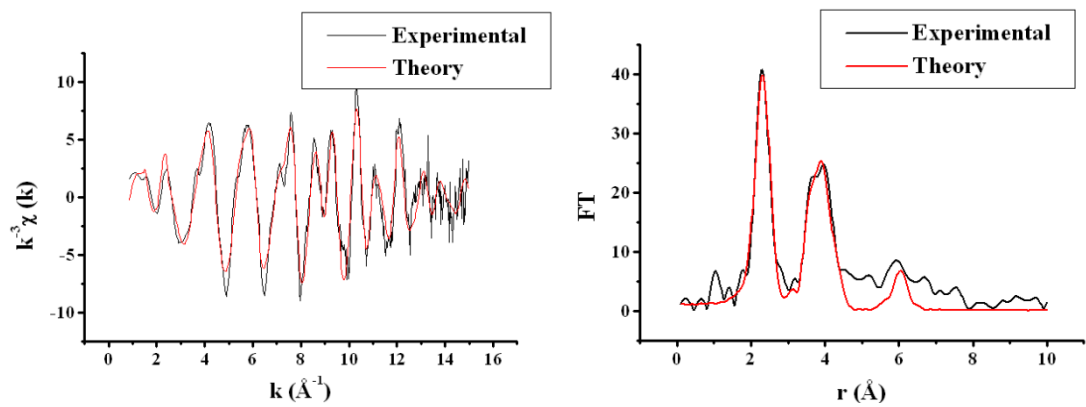


Figure 3.14 Zn-K-edge EXAFS and Fourier Transform for $\text{Ba}_2\text{Co}_{0.5}\text{Zn}_{0.5}\text{S}_3$

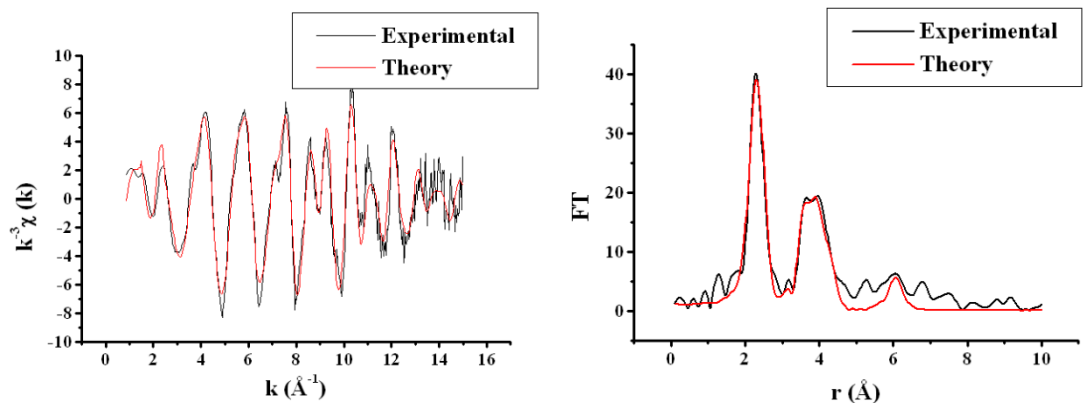


Figure 3.15 Zn-K-edge EXAFS and Fourier Transform for $\text{Ba}_2\text{Co}_{0.25}\text{Zn}_{0.75}\text{S}_3$

Table 3.6 Summary of refined Zn-K-edge EXAFS parameters

Bond	$\text{Ba}_2\text{Co}_{0.75}\text{Zn}_{0.25}\text{S}_3$		$\text{Ba}_2\text{Co}_{0.5}\text{Zn}_{0.5}\text{S}_3$		$\text{Ba}_2\text{Co}_{0.25}\text{Zn}_{0.75}\text{S}_3$		Ba_2ZnS_3	
	r (Å)	$2\sigma^2$ (Å ²)	r (Å)	$2\sigma^2$ (Å ²)	r (Å)	$2\sigma^2$ (Å ²)	r (Å)	$2\sigma^2$ (Å ²)
Zn-S (4)	2.360(8)	0.016(2)	2.366(4)	0.0148(8)	2.366(4)	0.0150(7)	2.367(3)	0.0153(6)
Zn-Ba (3)	3.525(15)	0.017(3)	3.528(8)	0.0158(17)	3.533(7)	0.0157(14)	3.533(6)	0.0164(13)
Zn-Ba (4)	3.829(25)	0.020(5)	3.814(8)	0.0140(13)	3.809(8)	0.0170(17)	3.808(6)	0.0157(12)
Zn-Zn (2)	4.070(21)	0.009(4)	4.122(24)	0.0163(49)	4.137(20)	0.0164(42)	4.130(19)	0.0179(41)
Zn-Ba (4)	5.903(17)	0.010(3)	5.903(14)	0.0130(24)	5.917(15)	0.0148(27)	5.912(11)	0.0140(19)
E_f	-7.3(7)		-7.9(4)		-7.9(4)		-11.3(3)	
R	49.6%		36.3%		32.7%		28.1%	
FI	1.05		0.44		0.36		0.25	

The high quality of the data allowed for two further shells, both transition metal to sulphur interactions, to be modelled with some success. The first shell occurs as four TM-S interactions at 4.8 Å and the second as three TM-S interactions at 5.0 Å. Although the fitting of the models with seven shells improves the R values it is not a statistically significant improvement enabling any firm conclusions to be drawn. The results for the Co-K-edge are shown graphically in figures 3.16-3.19 and the results of the refinements are shown in table 3.7 and the results for the Zn-K-edge are shown graphically in figures 3.20-3.23 with the results of the refinements shown in table 3.8.

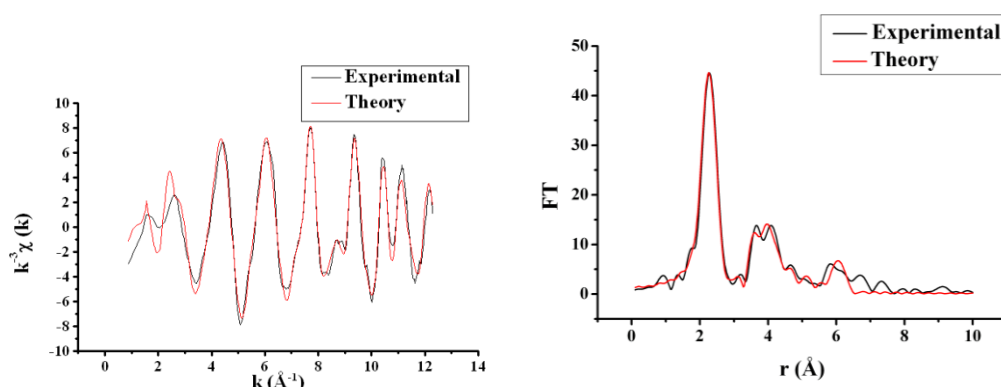


Figure 3.16 Co-K-edge EXAFS and Fourier Transform for Ba_2CoS_3

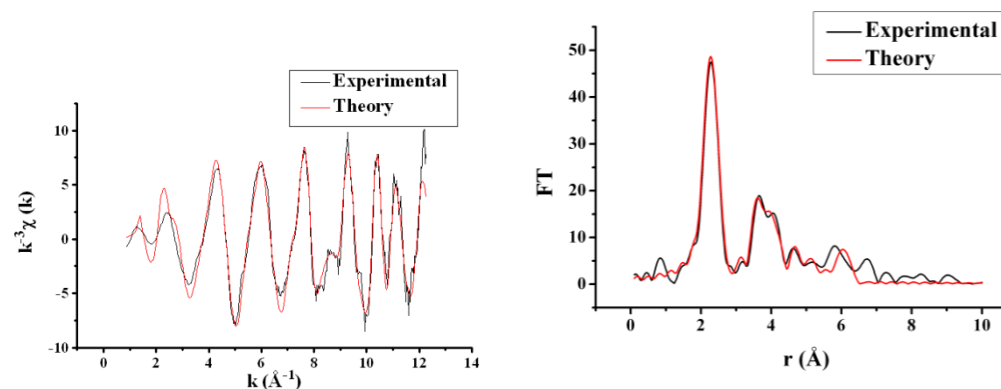


Figure 3.17 Co-K-edge EXAFS and Fourier Transform for $\text{Ba}_2\text{Co}_{0.75}\text{Zn}_{0.25}\text{S}_3$

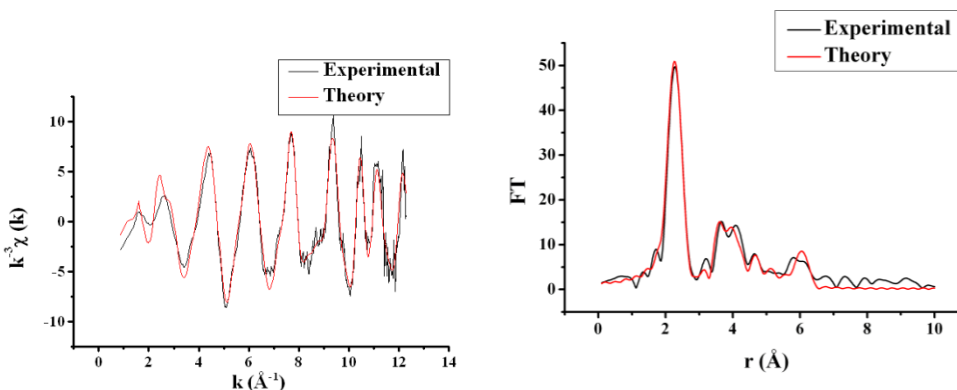


Figure 3.18 Co-K-edge EXAFS and Fourier Transform for $\text{Ba}_2\text{Co}_{0.5}\text{Zn}_{0.5}\text{S}_3$

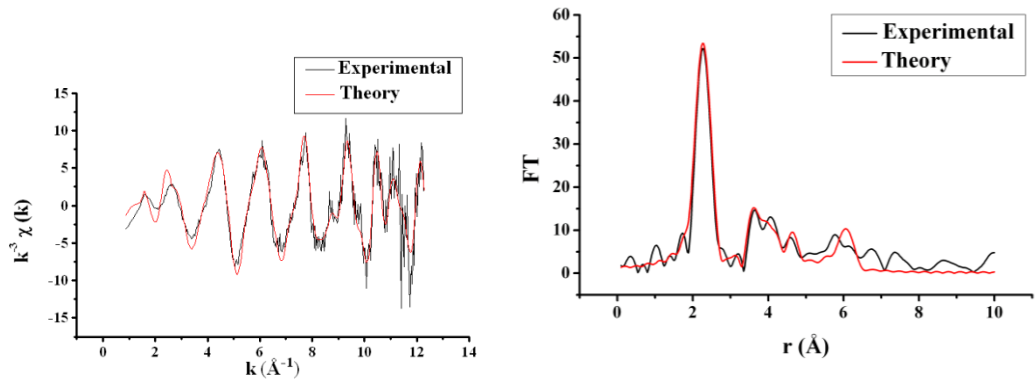


Figure 3.19 Co-K-edge EXAFS and Fourier Transform for $\text{Ba}_2\text{Co}_{0.25}\text{Zn}_{0.75}\text{S}_3$

Table 3.7 Summary of refined Co-K-edge EXAFS parameters

Bond	Ba ₂ CoS ₃		Ba ₂ Co _{0.75} Zn _{0.25} S ₃		Ba ₂ Co _{0.5} Zn _{0.5} S ₃		Ba ₂ Co _{0.25} Zn _{0.75} S ₃	
	r (Å)	2σ ² (Å ²)	r (Å)	2σ ² (Å ²)	r (Å)	2σ ² (Å ²)	r (Å)	2σ ² (Å ²)
Co-S (4)	2.332(3)	0.0138(5)	2.347(3)	0.0124(6)	2.335(3)	0.0116(7)	2.336(5)	0.0108(9)
Co-Ba (3)	3.528(6)	0.0152(11)	3.543(7)	0.0109(15)	3.536(7)	0.0129(12)	3.525(12)	0.0133(21)
Co-Ba (4)	3.851(27)	0.0415(121)	3.824(20)	0.0214(92)	3.842(40)	0.0411(179)	3.811(56)	0.0345(234)
Co-Co (2)	4.101(7)	0.0068(15)	4.088(27)	0.0133(84)	4.104(11)	0.0074(26)	4.088(24)	0.0098(65)
Co-S (4)	4.781(12)	0.0146(40)	4.785(19)	0.0108(41)	4.785(21)	0.0099(42)	4.766(28)	0.0065(53)
Co-S (3)	5.054(33)	0.0168(80)	5.051(34)	0.0131(83)	5.039(41)	0.0138(99)	5.000(45)	0.0076(95)
Co-Ba (4)	5.572(10)	0.0135(20)	5.587(8)	0.0085(15)	5.591(10)	0.0096(19)	5.606(13)	0.0070(23)
E _f	-9.0(3)		-6.5(4)		-9.5(4)		-9.3(6)	
R	22.3%		24.7%		27.8%		37.8%	
FI	0.20		0.27		0.34		0.77	

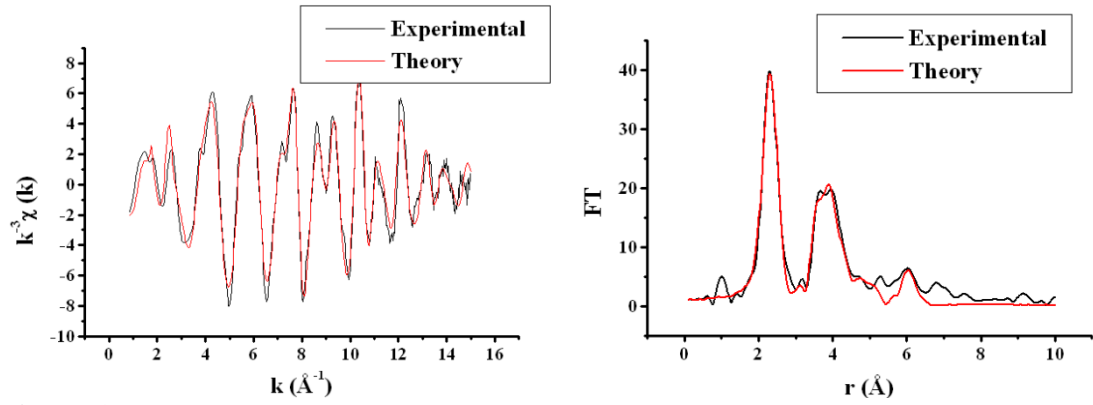


Figure 3.20 Zn-K-edge EXAFS and Fourier Transform for Ba_2ZnS_3

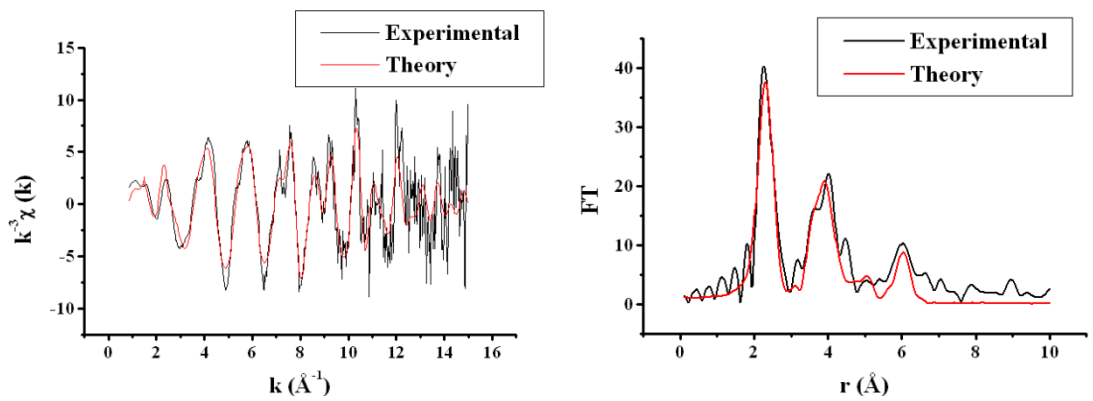


Figure 3.21 Zn-K-edge EXAFS and Fourier Transform for $\text{Ba}_2\text{Co}_{0.75}\text{Zn}_{0.25}\text{S}_3$

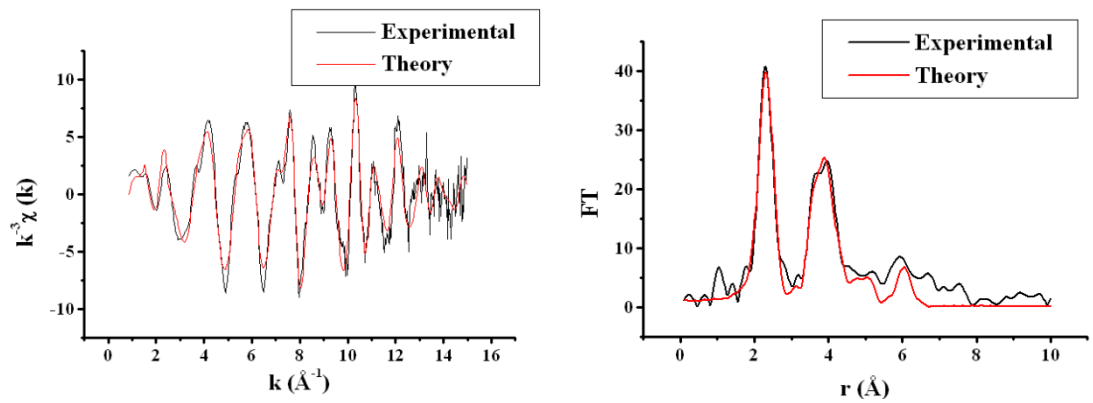


Figure 3.22 Zn-K-edge EXAFS and Fourier Transform for $\text{Ba}_2\text{Co}_{0.5}\text{Zn}_{0.5}\text{S}_3$

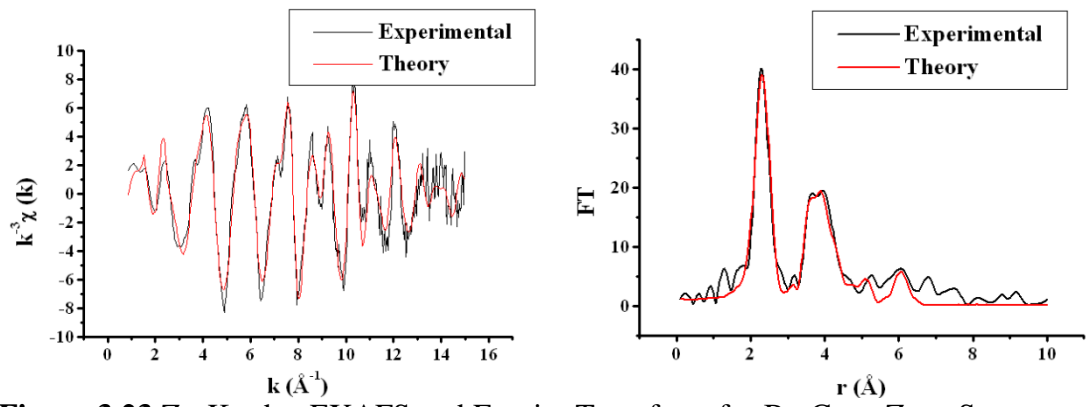


Figure 3.23 Zn-K-edge EXAFS and Fourier Transform for $\text{Ba}_2\text{Co}_{0.25}\text{Zn}_{0.75}\text{S}_3$

Table 3.8 Summary of refined Zn-K-edge EXAFS parameters

Bond	$\text{Ba}_2\text{Co}_{0.75}\text{Zn}_{0.25}\text{S}_3$		$\text{Ba}_2\text{Co}_{0.5}\text{Zn}_{0.5}\text{S}_3$		$\text{Ba}_2\text{Co}_{0.25}\text{Zn}_{0.75}\text{S}_3$		Ba_2ZnS_3	
	r (Å)	$2\sigma^2$ (Å ²)	r (Å)	$2\sigma^2$ (Å ²)	r (Å)	$2\sigma^2$ (Å ²)	r (Å)	$2\sigma^2$ (Å ²)
Zn-S (4)	2.365(7)	0.016(2)	2.367(4)	0.0148(8)	2.368(3)	0.0151(7)	2.366(3)	0.0152(6)
Zn-Ba (3)	3.526(18)	0.018(4)	3.529(8)	0.0157(16)	3.535(7)	0.0157(14)	3.533(6)	0.0163(12)
Zn-Ba (4)	3.829(17)	0.016(3)	3.816(8)	0.0141(12)	3.809(8)	0.0172(17)	3.807(6)	0.0157(11)
Zn-Zn (2)	4.076(63)	0.021(15)	4.121(23)	0.0164(47)	4.137(19)	0.0160(38)	4.128(18)	0.0179(37)
Zn-S (4)	4.784(66)	0.023(18)	4.804(30)	0.0196(82)	4.826(37)	0.0256(111)	4.805(20)	0.0189(54)
Zn-S (3)	5.085(47)	0.012(10)	5.106(25)	0.0109(55)	5.121(23)	0.0114(47)	5.106(26)	0.0157(59)
Zn-Ba (4)	5.907(16)	0.010(3)	5.905(13)	0.0131(23)	5.919(14)	0.0147(24)	5.908(10)	0.0142(19)
E_f	-7.9(7)		-8.2(4)		-8.2(3)		-11.2(2)	
R	48.0%		34.0%		31.2%		26.1%	
FI	1.02		0.39		0.34		0.22	

In the Co-K-edge EXAFS the interactions at 3.8 Å and 4.1 Å are shown in the FT as peaks of different height whereas in the Zn-K-edge data the two peaks are equal. As this is seen in the data for Ba₂CoS₃ and Ba₂ZnS₃ as well as for the substituted compounds this can be assigned to a difference caused by the excited atom rather than any structural difference in the samples.

The bond lengths from the EXAFS data are slightly lower than those from the PXRD and NPD refinement results but this is expected as the EXAFS experiments were carried out at low temperature. The agreement between both the Co- and Zn- K-edge EXAFS and XANES data with the X-ray and neutron diffraction data out to 5.5 Å confirms the structure of Ba₂CoS₃ and Ba₂ZnS₃ is maintained with throughout the Ba₂Co_{1-x}Zn_xS₃ solid solution.

3.2.4 Transition Electron Microscopy (TEM)

Ba₂Co_{0.75}Zn_{0.25}S₃ was examined by TEM by O. Lebedev (ENSICAEN) and indexed with the space group *Pnam* and showed unit cell parameters: $a = 11.994(2)$ Å, $b = 12.472(2)$ Å, $c = 4.201(1)$ Å. The ED patterns shown in figure 3.24 do not exhibit any signature of ordering, superstructure or visible distortion. EDX measurements to determine the elemental composition were carried out, with four measurements taken and these show good correspondence with the nominal composition, see table 3.9.

Table 3.9 Elemental analysis results from EDX

Atom %	Ba	S	Co	Zn
1	36.18	47.80	12.83	3.19
2	33.60	50.83	12.50	3.08
3	34.49	51.24	11.01	3.25
4	35.65	48.68	13.07	2.60
Expected	33.33	50	12.5	4.17

Therefore, based on all TEM measurements it can be concluded that the Zn is randomly and homogeneously distributed on the Co position in the $\text{Ba}_2\text{Co}_{0.75}\text{Zn}_{0.25}\text{S}_3$ solid solution.

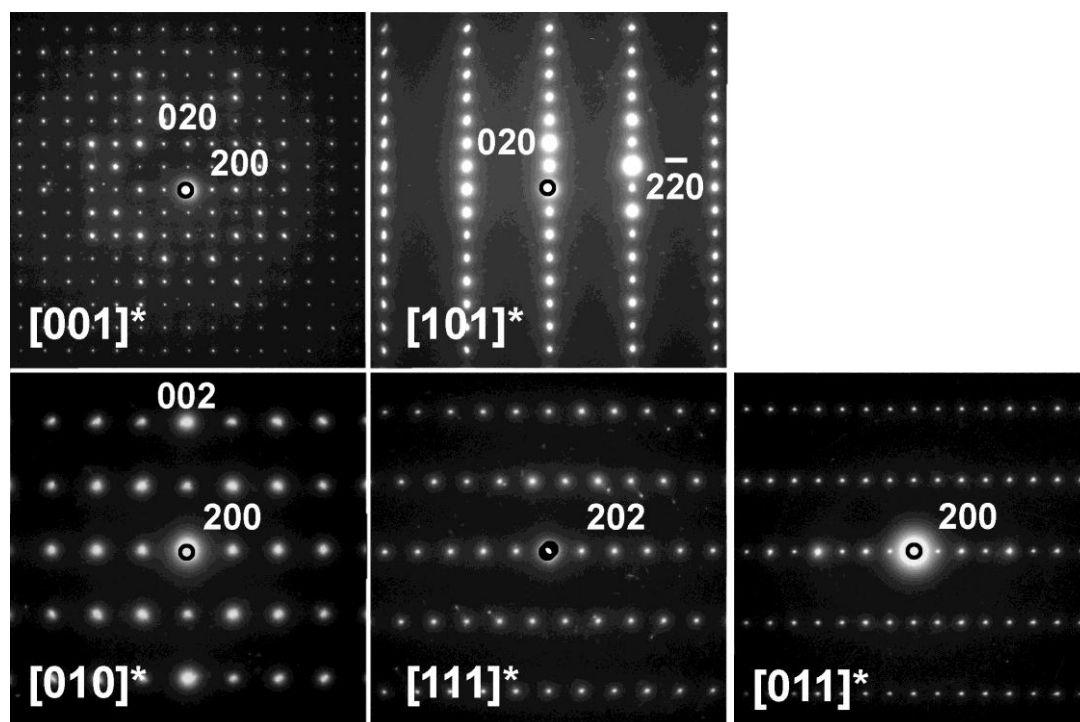


Figure 3.24 TEM images of $\text{Ba}_2\text{Co}_{0.75}\text{Zn}_{0.25}\text{S}_3$ (image along 100 axis not provided)

3.3 Physical Properties

3.3.1 Magnetic Susceptibility

The susceptibility and inverse susceptibility plots of the series are shown in figures 3.25 and 3.26 respectively. At temperatures above 200 K all of the samples show a linear dependence of inverse susceptibility on temperature indicative of paramagnetic behaviour.

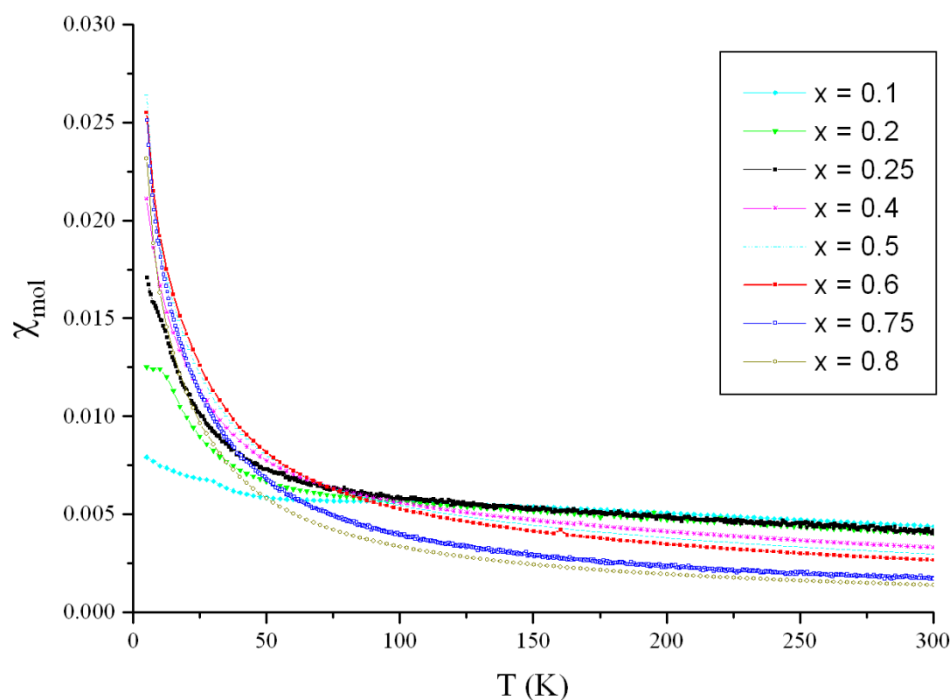


Figure 3.25 Susceptibility curves for $\text{Ba}_2\text{Co}_{1-x}\text{Zn}_x\text{S}_3$ ($x = 0.1, 0.2, 0.25, 0.4, 0.5, 0.6, 0.75$ and 0.8)

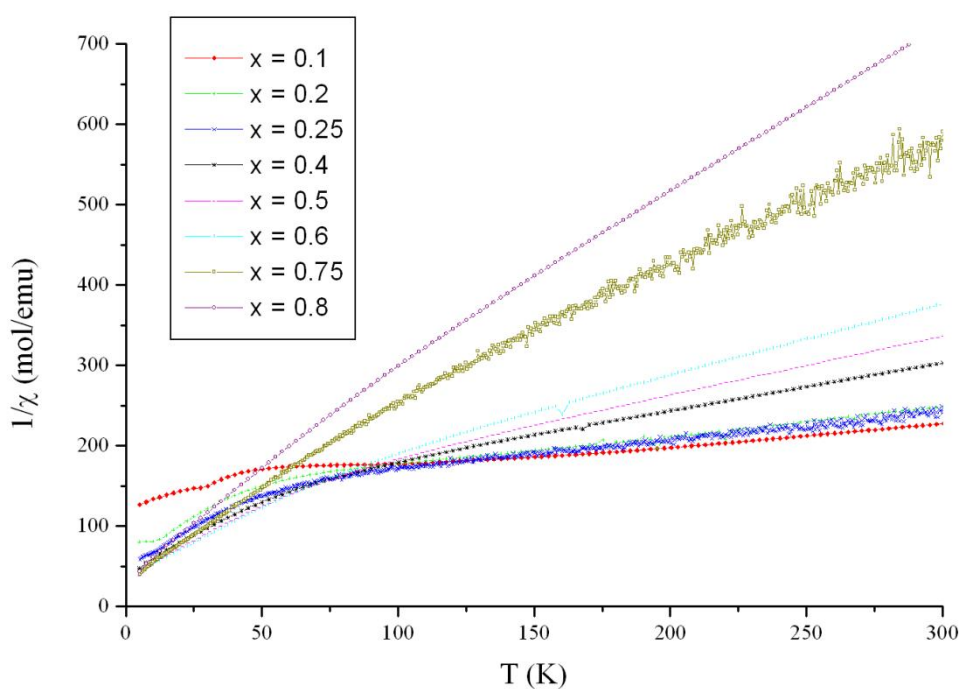


Figure 3.26 Inverse susceptibility plots for $\text{Ba}_2\text{Co}_{1-x}\text{Zn}_x\text{S}_3$ ($x = 0.1, 0.2, 0.25, 0.4, 0.5, 0.6, 0.75$ and 0.8)

The substitution of zinc into the Ba_2CoS_3 system is expected to break up the antiferromagnetic interaction between the Co^{2+} centres and change the system from a 1-

D antiferromagnet into a paramagnetic system and for samples with $x \geq 0.4$ the curves show purely paramagnetic behaviour. For samples with $x < 0.4$ some antiferromagnetic interactions are still present, shown by deviations from the low temperature data and the intercept in the plots of inverse susceptibility not at the origin (figure 3.27 and 3.28).

In the susceptibility plot for Ba_2CoS_3 an upturn in the data was detected around 46 K and has been attributed, with the use of low temperature NPD data, to the onset of long-range order, i.e. the formation of a 3-d ferromagnetic phase. There are also slight kinks in the data for the substituted compounds $\text{Ba}_2\text{Co}_{1-x}\text{Zn}_x\text{S}_3$ ($x = 0.1, 0.2, 0.25$) occurring at ~ 33 K for $\text{Ba}_2\text{Co}_{0.9}\text{Zn}_{0.1}\text{S}_3$, ~ 17.5 K for $\text{Ba}_2\text{Co}_{0.8}\text{Zn}_{0.2}\text{S}_3$ and ~ 16 K for $\text{Ba}_2\text{Co}_{0.75}\text{Zn}_{0.25}\text{S}_3$ which may indicate the formation of long-range order, figure 3.28. The kinks occur at lower temperatures as the value of x is increased suggesting that Zn is partially disrupting the formation of the 3-d phase.

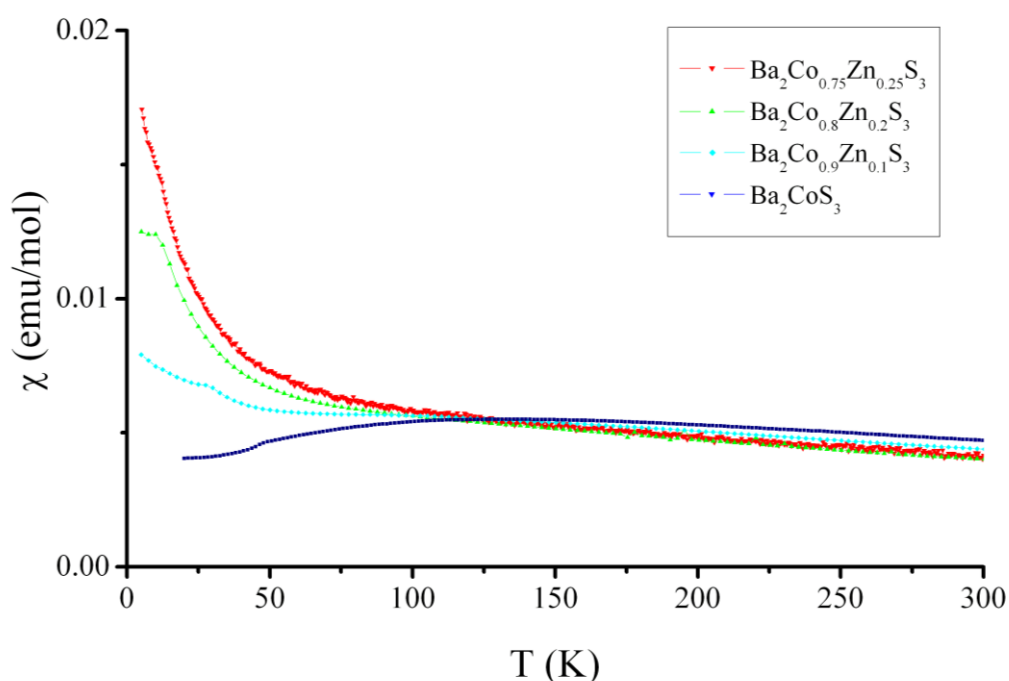


Figure 3.27 Susceptibility curves for $\text{Ba}_2\text{Co}_{1-x}\text{Zn}_x\text{S}_3$ ($x = 0.1, 0.2, 0.25$) and Ba_2CoS_3

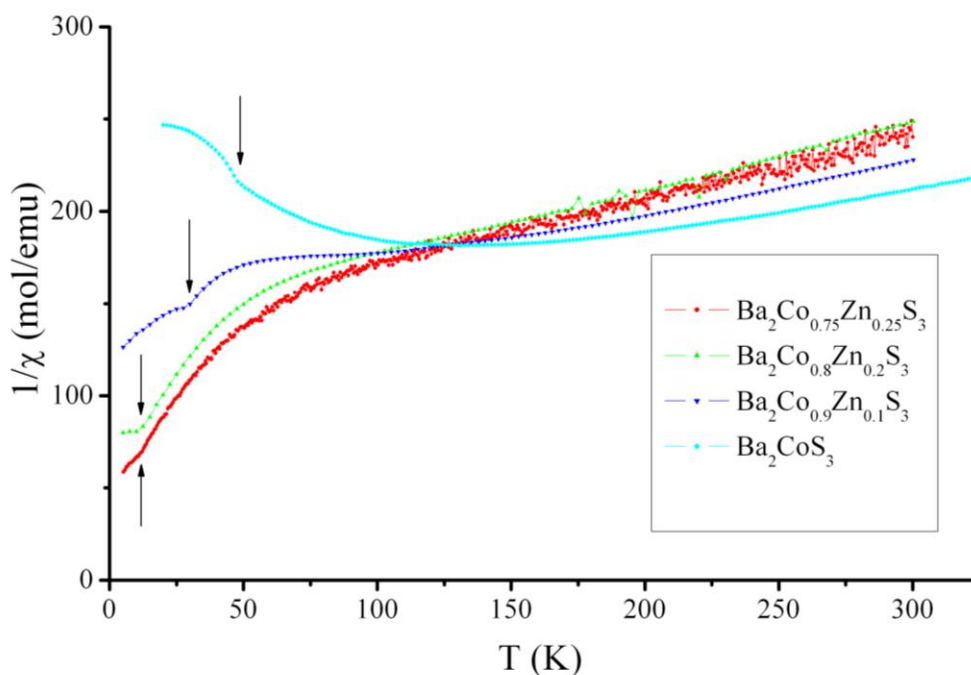


Figure 3.28 Inverse susceptibility curves for $\text{Ba}_2\text{Co}_{1-x}\text{Zn}_x\text{S}_3$ ($x = 0.1, 0.2,$ and 0.25) and Ba_2CoS_3 showing kinks in the data possibly indicating transition to 3-dimensional order

The Curie constants and effective magnetic moments have been calculated from the linear part of the plots between 200 and 300 K (fig 3.29) using the relationship;

$$-\quad -\quad -$$

Where χ is the susceptibility, C the Curie constant and θ the Weiss constant (calculated from extrapolation of the linear part of the plots to the intercept on the x axis). The effective magnetic moment, μ_{eff} , can then be calculated using the relationship;

$$\text{---}$$

For the case of paramagnetic materials $\chi_m T = C$ hence;

$$-$$

and values of C obtained from linear fitting of the plots can therefore be used to estimate μ_{eff} . The linear fit for each of the susceptibility plots are shown in Appendix 2.

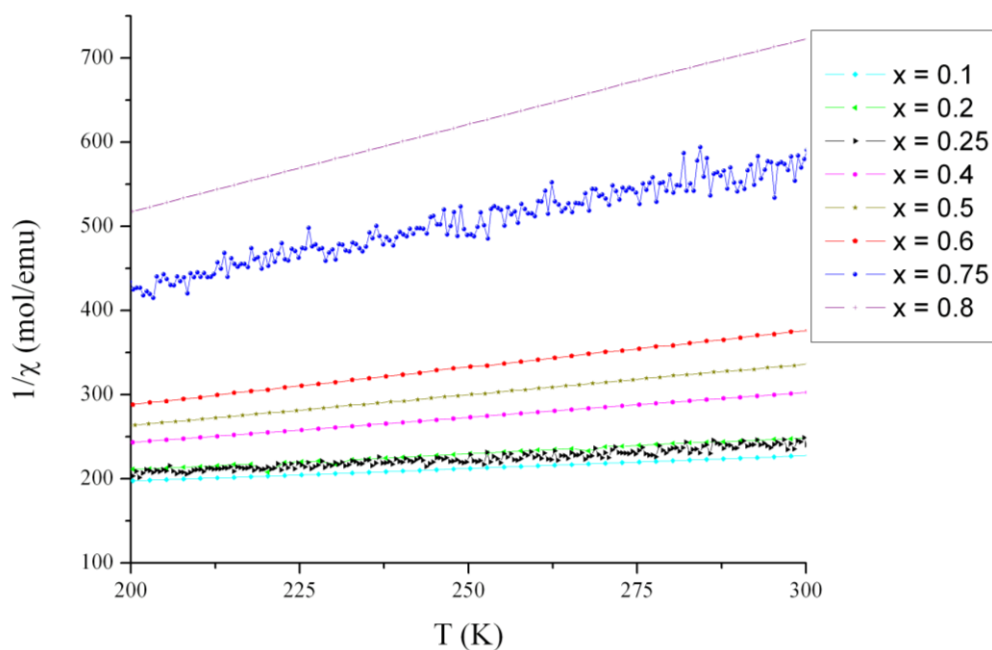


Figure 3.29 Linear part of inverse susceptibility plots for $\text{Ba}_2\text{Co}_{1-x}\text{Zn}_x\text{S}_3$ ($x = 0.1, 0.2, 0.25, 0.4, 0.5, 0.6, 0.75$ and 0.8)

Despite the antiferromagnetic interactions present in samples with $x < 0.4$, above 200 K these interactions are very weak and as such the Curie-Weiss law can still be used to provide reasonable estimates of the values of μ_{eff} . The values for Curie constant, Weiss constant and μ_{eff} obtained are tabulated in table 3.9. The Curie constant shows the expected decrease with increased substitution as Co^{2+} , d^7 , $S = 3/2$ (due to distorted tetrahedral environment)¹¹⁰ is replaced by Zn^{2+} , d^{10} , $S = 0$ (figure 3.29).

Table 3.9 Summary of Weiss temperature, Curie constants and effective magnetic moments for compounds in the series $\text{Ba}_2\text{Co}_{1-x}\text{Zn}_x\text{S}_3$ ($x = 0.1, 0.2, 0.25, 0.4, 0.5, 0.6, 0.75, 0.8$)

x	θ (K)	C ($\text{emu}\cdot\text{mol}^{-1}\text{K}$)	μ_{eff} (μ_{B})	μ_{eff} per ion (μ_{B})
0.1	-452(2)	3.30(1)	5.14(4)	5.42(4)
0.2	-366(3)	2.86(3)	4.78(2)	5.35(3)
0.25	-365(2)	2.67(4)	4.62(2)	5.34(4)
0.4	-206(3)	1.67(3)	3.66(5)	4.72(2)
0.5	-162(2)	1.37(2)	3.31(1)	4.68(2)
0.6	-125(3)	1.13(3)	3.00(2)	4.75(4)
0.75	-69(3)	0.63(5)	2.23(5)	4.49(1)
0.8	-8(2)	0.49(1)	1.97(3)	4.42(3)

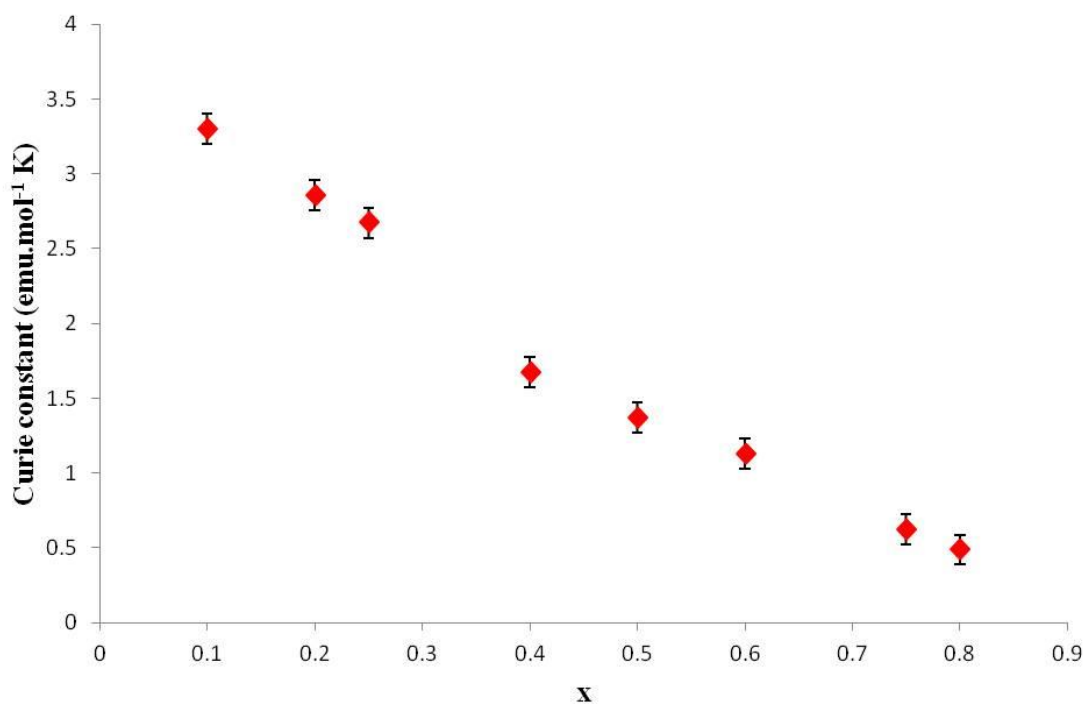


Figure 3.29 Plot of Curie constant against x for $\text{Ba}_2\text{Co}_{1-x}\text{Zn}_x\text{S}_3$ ($x = 0.1, 0.2, 0.25, 0.4, 0.5, 0.6, 0.75, 0.8$)

The literature values of the μ_{eff} for Co^{2+} in a tetrahedral environment surrounded by oxygen are 3.94-4.54 μ_{B} ¹³⁵ and for Ba_2CoS_3 ($\text{Co}^{2+} S = 3/2$) the value has been previously calculated as 4.6 μ_{B} .¹¹⁰ Theoretical values for the series have been calculated using the latter value in the equation

with x for $\text{Ba}_2\text{Co}_{1-x}\text{Zn}_x\text{S}_3$

The theoretical values show good agreement for $x \geq 0.4$ where the presence of zinc has destroyed the antiferromagnetic interaction (Figure 3.30). The value of the effective magnetic moment per ion is also fairly consistent throughout the series.

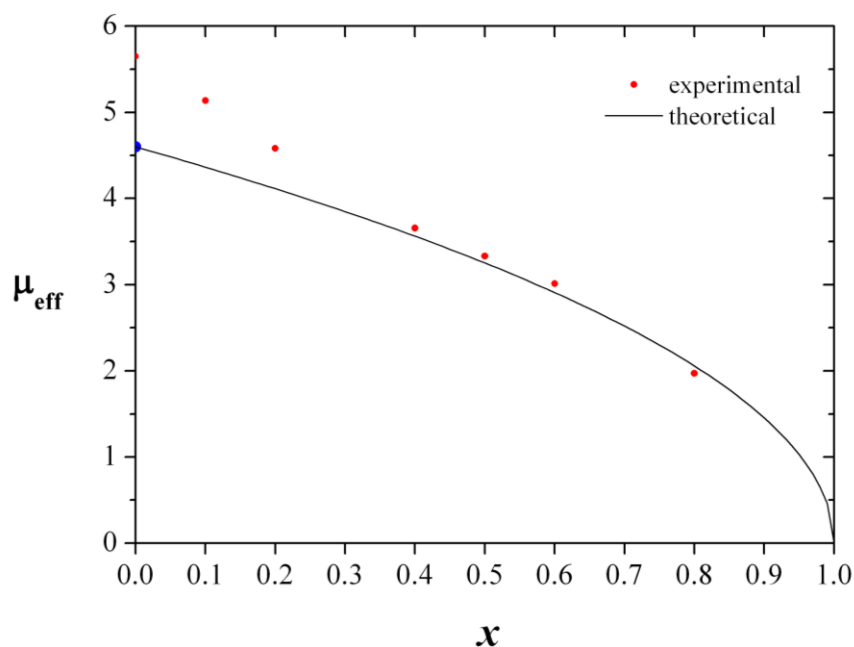


Figure 3.30 Theoretical and experimental values of μ_{eff} for $\text{Ba}_2\text{Co}_{1-x}\text{Zn}_x\text{S}_3$ ($x = 0.1, 0.2, 0.25, 0.4, 0.5, 0.6, 0.75$ and 0.8) showing good correlation for $x \geq 0.4$

Although the significance of the Weiss constant in this series is limited due to the absence of long-range order it does show an increase (approaching zero) as x increases (Figure 3.31) and the zinc disrupts the formation of any antiferromagnetic phase.

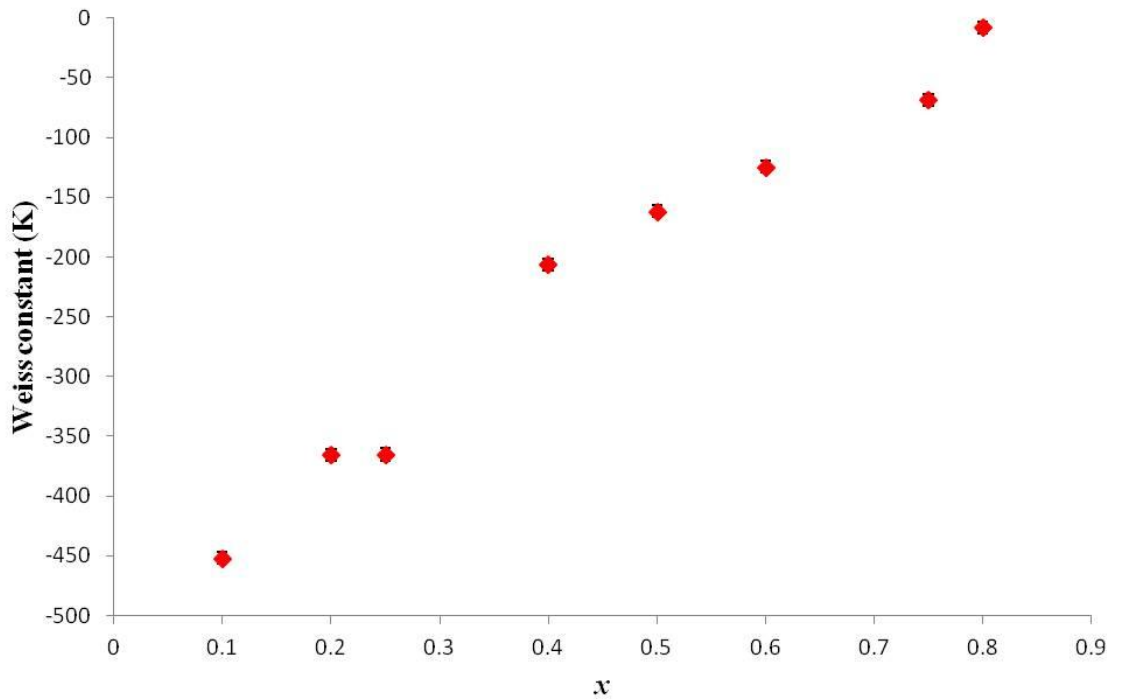


Figure 3.31 Plot of Weiss constant against x for $\text{Ba}_2\text{Co}_{1-x}\text{Zn}_x\text{S}_3$ ($x = 0.1, 0.2, 0.25, 0.4, 0.5, 0.6, 0.75, 0.8$)

The field-cooled susceptibility has also been measured for $\text{Ba}_2\text{Co}_{1-x}\text{Zn}_x\text{S}_3$ ($x = 0.1, 0.2, 0.25, 0.4, 0.5, 0.6, 0.75, 0.8$) and shows no difference from the zero-field-cooled data (figure 3.32). Any difference in the field cooled and zero-field cooled magnetisation indicates a spin-glass system may be present. In some one-dimensional spin glass systems (disordered materials exhibiting high magnetic frustration) inter-chain interactions at low temperature lead to remanant magnetisation and magnetoresistance.¹³⁶

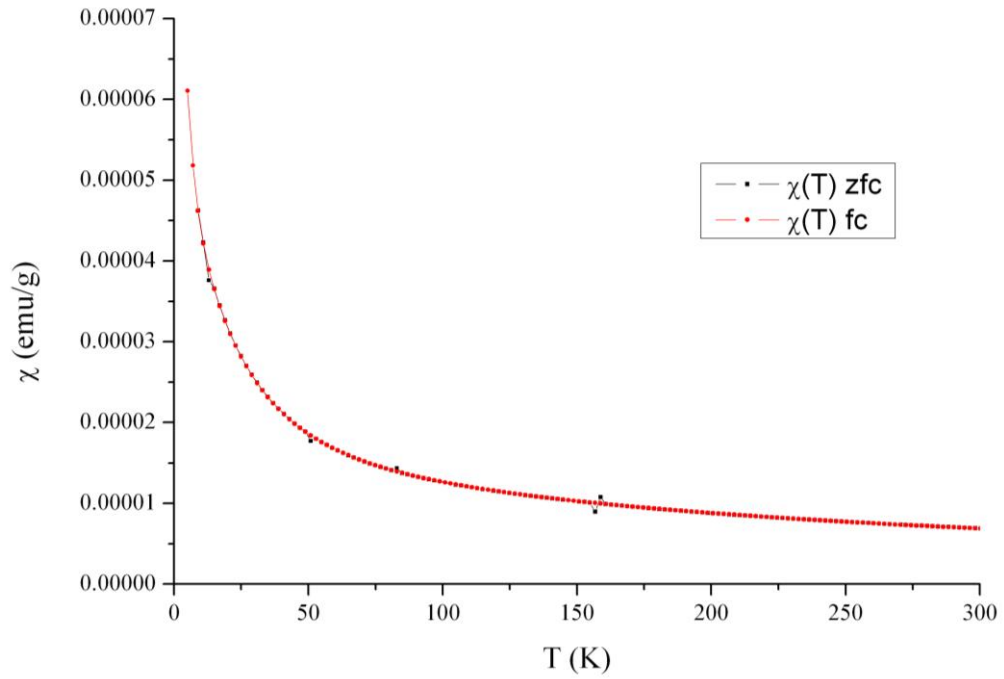


Figure 3.32 Field cooled and zero field cooled susceptibility for $\text{Ba}_2\text{Co}_{0.5}\text{Zn}_{0.5}\text{S}_3$, external field strength 0.1T

3.3.2 Transport Properties

All the samples are semiconductors, indicated by the increase in resistivity as the temperature is reduced as well as the values for the resistivity which fall well within the range expected for semiconductors and are much higher than that of Ba_2CoS_3 ($10^{-1} \Omega \text{ cm}$), considered a bad metal (figure 3.33).

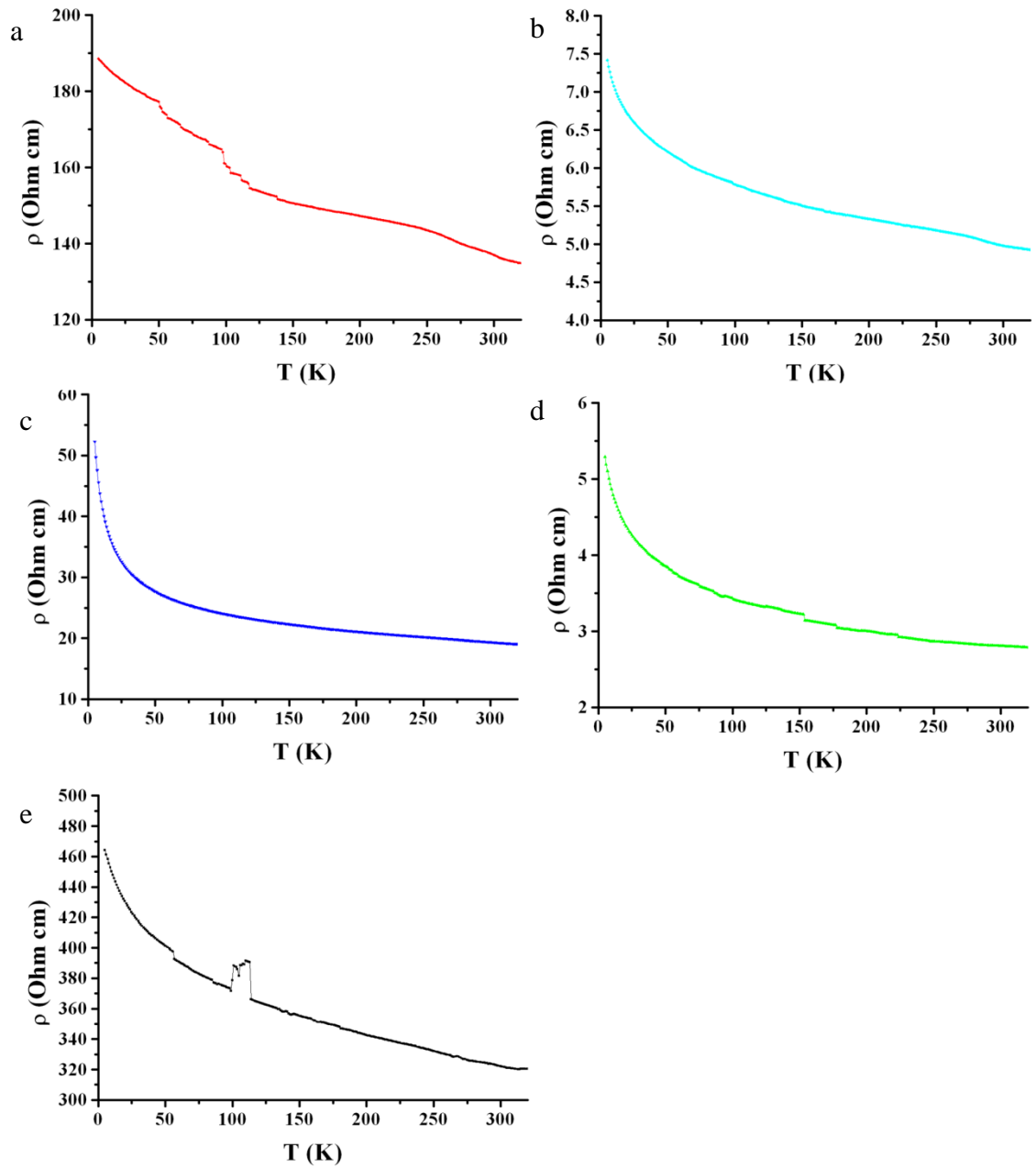


Figure 3.33 Resistivity of the series $\text{Ba}_2\text{Co}_{1-x}\text{Zn}_x\text{S}_3$ a) $\text{Ba}_2\text{Co}_{0.9}\text{Zn}_{0.1}\text{S}_3$ b) $\text{Ba}_2\text{Co}_{0.75}\text{Zn}_{0.25}\text{S}_3$ c) $\text{Ba}_2\text{Co}_{0.5}\text{Zn}_{0.5}\text{S}_3$ d) $\text{Ba}_2\text{Co}_{0.4}\text{Zn}_{0.6}\text{S}_3$ e) $\text{Ba}_2\text{Co}_{0.25}\text{Zn}_{0.75}\text{S}_3$

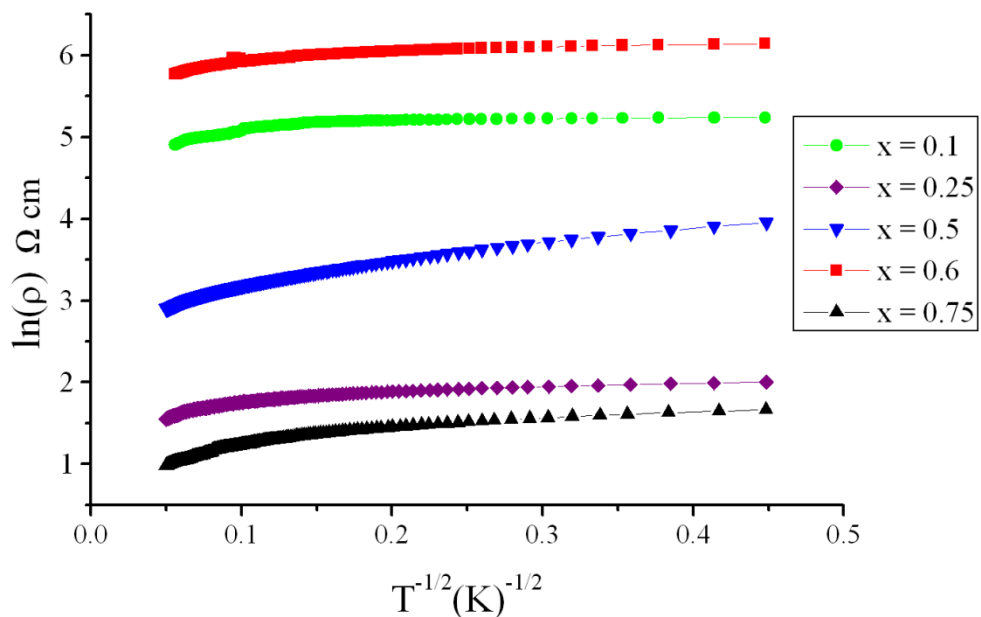
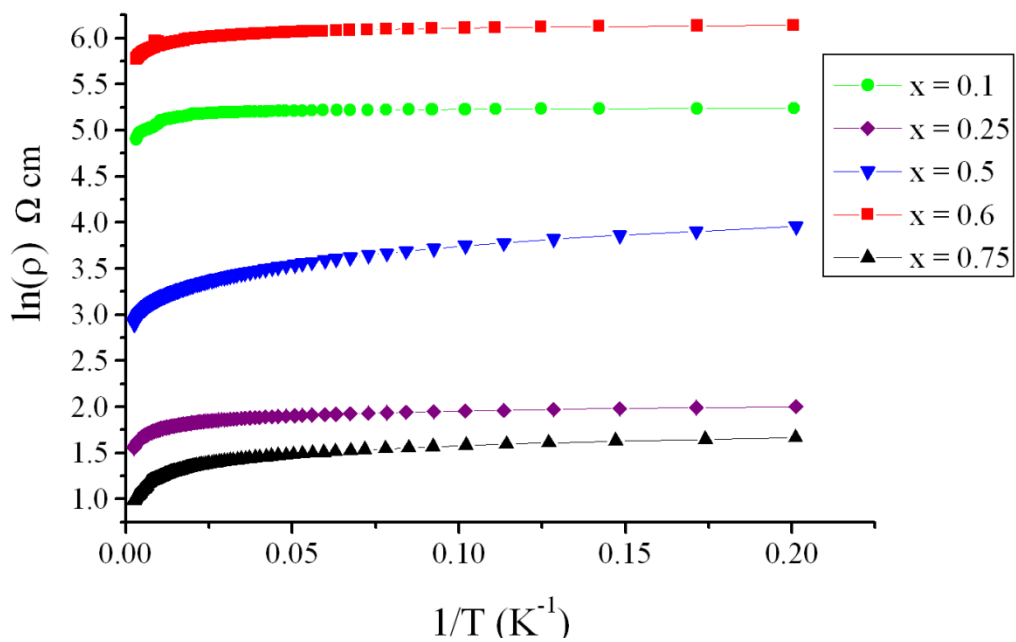
To determine the dimensionality of the conduction the resistivity data have been analysed using the variable range hopping model based on the equation;

—

Where ρ is the resistivity, T the temperature, T_0 the activation temperature and n the dimension of the conductance with;

where k_B is the Boltzmann constant, $N(E_F)$ is the density of states and ξ is the localisation length.

Plots of $\ln(\rho)$ against $1/T^{1/n+1}$, with $n = 0.1$ and 3 , figure 3.34, show that the method of conduction is three dimensional as plots of $1/T^{1/4}$ (i.e. $n = 3$) against $\ln(\rho)$ yield straight lines (figure 3.34c).



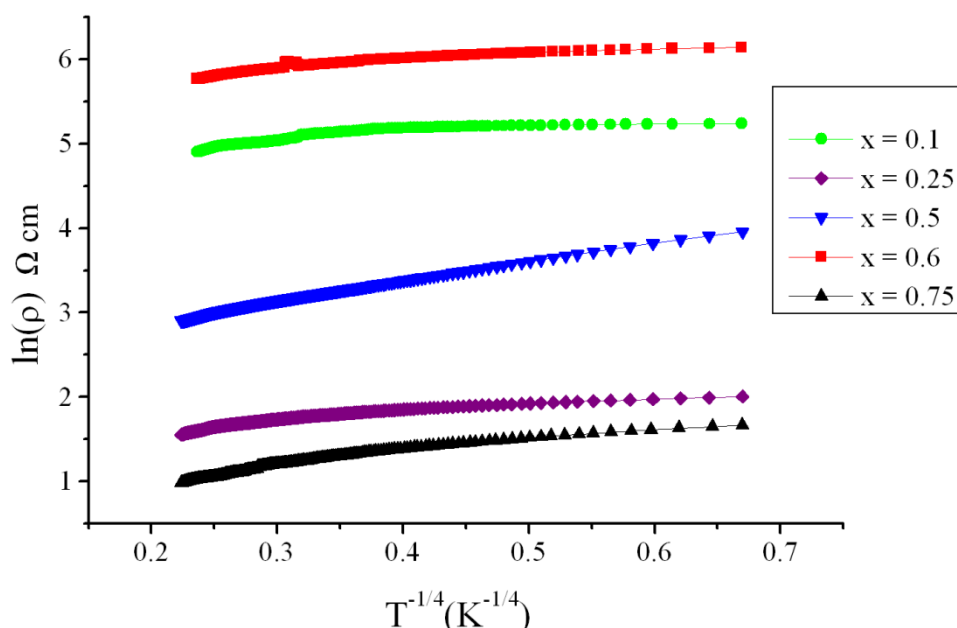


Figure 3.34 a) Arrhenius plot of resistivity data for $\text{Ba}_2\text{Co}_{1-x}\text{Zn}_x\text{S}_3$ ($x = 0.1, 0.25, 0.5, 0.6, 0.75$) **b)** plot of $\ln(\rho)$ against $T^{-1/2}$ linear dependence would be expected in the case of 1-d conductivity **c)** plot showing the linear dependence of $\ln(\rho)$ against $T^{-1/4}$ indicating 3-d conductivity

The linear parts of the plots of $\ln(\rho)$ against $T^{-1/4}$ (5-40 K) have been used to determine the parameters ρ_0 and T_0 , table 3.10.

Table 3.10 Values for ρ_0 and T_0 obtained from linear fitting of plot of $\ln(\rho)$ against $T^{-1/4}$ over the range 5-40 K for $\text{Ba}_2\text{Co}_{1-x}\text{Zn}_x\text{S}_3$ ($x = 0.1, 0.25, 0.5, 0.6, 0.75$)

x	ρ_0 (Ω cm)	T_0 (K)
0.1	1.63(2)	2030(5)
0.25	0.48(4)	5880(8)
0.5	0.92(6)	22020(7)
0.6	1.76(2)	5090(1)
0.75	-0.04(1)	10840(6)

There is no trend connected to the Zn content in the $\text{Ba}_2\text{Co}_{1-x}\text{Zn}_x\text{S}_3$ series in the values of the resistivity or the parameters ρ_0 and T_0 . However it is worth noting that only a very small amount of zinc is sufficient to change Ba_2CoS_3 from a metallic-like conductor to a semiconductor.

The resistivity was also measured in the presence of an external magnetic field to determine the magnetoresistance.

The resistivity of the samples $\text{Ba}_2\text{Co}_{1-x}\text{Zn}_x\text{S}_3$ ($x = 0.1, 0.25, 0.5, 0.6, 0.75$) was measured at 5 K in a field from 0-7 T, and the difference between the resistivity, ρ , at $H = 0$ and in the presence of an external field, H , analysed using the relationship $\rho_H/(\rho_{H=0})$, figure 3.35.

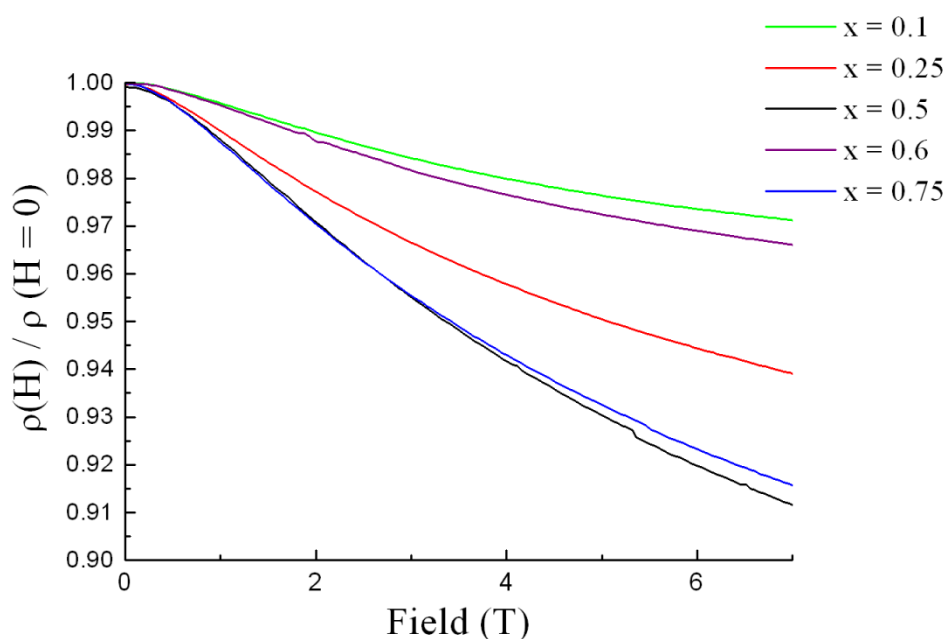


Figure 3.35 Isothermal resistivity curves for $\text{Ba}_2\text{Co}_{1-x}\text{Zn}_x\text{S}_3$ ($x = 0.1, 0.25, 0.5, 0.6, 0.75$) measured at 5 K

All the samples measured initially show increased magnetoresistance over Ba_2CoS_3 ($\sim -1.7\%$ at 5 K, 7 T) reaching a maximum value of $\sim -9\%$ for $\text{Ba}_2\text{Co}_{0.5}\text{Zn}_{0.5}\text{S}_3$, table 3.11.

Table 3.11 Magnetoresistance for $\text{Ba}_2\text{Co}_{1-x}\text{Zn}_x\text{S}_3$ ($x = 0.1, 0.25, 0.5, 0.6, 0.75$) at 5 K, 7 T

x	MR (%)
0.1	3
0.25	6
0.5	9
0.6	3.5
0.75	8.5

As with the resistivity there is no trend associated with the magnetoresistance in relation to the amount of zinc present and there is also none between the values of resistivity, ρ , and the magnetoresistance. Since no clear dependency on the stoichiometry could be found two further samples of $\text{Ba}_2\text{Co}_{0.75}\text{Zn}_{0.25}\text{S}_3$ and $\text{Ba}_2\text{Co}_{0.4}\text{Zn}_{0.6}\text{S}_3$ were analysed. The magnetoresistance of the two samples is shown in figure 3.36.

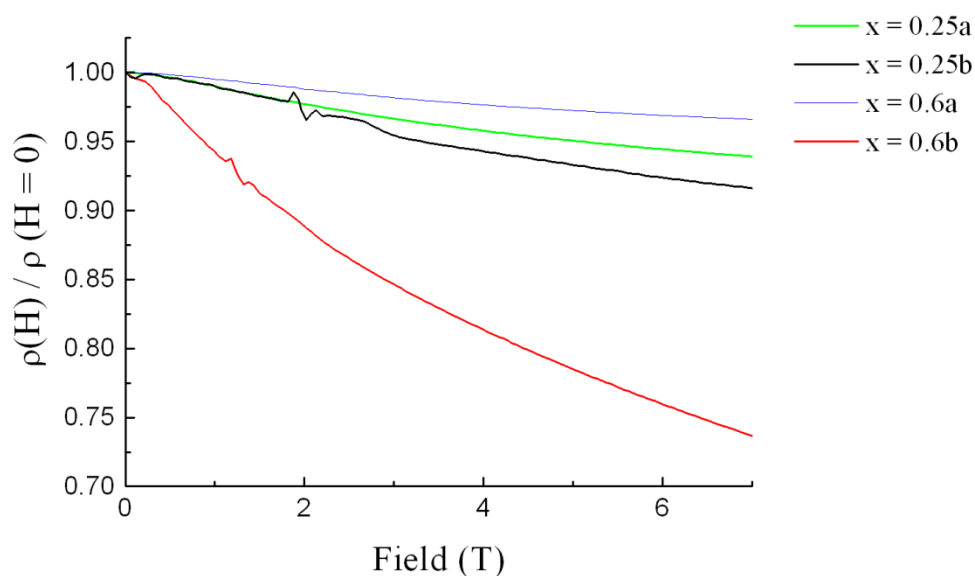


Figure 3.36 Isothermal resistivity curves showing a comparison between two samples of $\text{Ba}_2\text{Co}_{0.75}\text{Zn}_{0.25}\text{S}_3$ and two samples of $\text{Ba}_2\text{Co}_{0.4}\text{Zn}_{0.6}\text{S}_3$ measured at 5 K

The magnetoresistance for the second sample of $\text{Ba}_2\text{Co}_{0.4}\text{Zn}_{0.6}\text{S}_3$ ($\text{Ba}_2\text{Co}_{0.4}\text{Zn}_{0.6}\text{S}_3$ b in figure 3.36) shows the largest value of any sample with $\text{MR} > -25\%$ in a 7 T field at 5 K, a 7 fold increase on the value for the first sample measured. The difference between

the two $x = 0.25$ samples is smaller but still significant. The discrepancies between the magnetoresistance seen for samples of the same stoichiometry suggest that the origin of the magnetoresistance in $\text{Ba}_2\text{Co}_{1-x}\text{Zn}_x\text{S}_3$ may not be due to electronic factors, but more to extrinsic parameters such as particle size and the conditions of sample preparation. Another factor that may influence the magnetoresistance may be the sulphur stoichiometry which is difficult to control during synthesis and also hard to determine accurately. To explore this hypothesis further it would be necessary to measure compounds with strictly controlled stoichiometry and particle size and identify possible trends. The gradual increase of the magnetoresistance with temperature and field strength also excludes any structural or electronic transitions as the origin of this phenomenon in $\text{Ba}_2\text{Co}_{1-x}\text{Zn}_x\text{S}_3$.

3.3.3 Conclusion

The series $\text{Ba}_2\text{Co}_{1-x}\text{Zn}_x\text{S}_3$ ($x = 0.1, 0.2, 0.25, 0.4, 0.5, 0.6, 0.75, 0.8$) has been successfully synthesised and its structural properties analysed using PXRD, NPD, XAS and TEM. Results from all these techniques are in agreement to confirm that the series forms a solid solution with zinc and cobalt randomly distributed across the same crystallographic site and that the one-dimensional structure of the two end members, Ba_2CoS_3 and Ba_2ZnS_3 , is maintained.

Analysis of the physical properties of the $\text{Ba}_2\text{Co}_{1-x}\text{Zn}_x\text{S}_3$ series shows that the compounds are paramagnetic with some 1-D antiferromagnetic interactions at low temperature for samples with zinc content $x < 0.4$ and a possible transition to 3-D order although this has not been confirmed. Resistivity measurements show that all the compounds are semiconductors with 3-D variable-range-hopping as the method of conduction. All the materials show significant magnetoresistance up to a maximum of $\sim -25\%$ for $\text{Ba}_2\text{Co}_{0.4}\text{Zn}_{0.6}\text{S}_3$ although the cause of this phenomenon is as yet unknown.

4.0 Ba₂Co_{1-x}Fe_xS₃

4.1 Synthesis and Characterisation

The synthesis of the ternary sulphides Ba₂Co_{1-x}Fe_xS₃ ($x = 0.25, 0.5, 0.75$) was performed *via* a solid-gas reaction as discussed in the Experimental section 2.1. Stoichiometric mixtures of barium carbonate (99%) cobalt (99.8%) and iron (99.8%) were reacted with carbon disulphide (99%) for 24 hours at 1000°C. The synthesis of Ba₂FeS₃ was also attempted from a stoichiometric mixture of the solids, ground and heated in a nitrogen atmosphere to 1200°C for 24 hours.

4.2 Results and Discussion

4.2.1 Powder X-ray Diffraction (PXRD)

The diffraction patterns for Ba₂Co_{1-x}Fe_xS₃ with $x = 0.5$ and 0.75 showed a Ba₂CoS₃ phase along with large amounts of BaS and various Ba_xFe_yS_z phases. There are a large number of Ba_xFe_yS_z phases reported in the literature (see section 1.5) and Ba₂FeS₃ has not been reported as a single phase; as such it is not surprising that synthesising this solid solution presents difficulties. In order to explore an alternative route to synthesise the solid solutions an attempt was made to synthesise Ba₂FeS₃ from the elements using a conventional solid-state technique; however this was also unsuccessful and resulted in a mixture of BaS and a variety of Ba_xFe_yS_z phases. Ba₂Co_{0.75}Fe_{0.25}S₃ contained fewer impurities compared to all other compositions attempted and Rietveld refinement was performed using the GSAS software in conjunction with EXPGUI.^{121,122} An impurity of ~10% BaS was found and upon further heating this was reduced to ~5%. No corresponding impurities containing Fe or Co were seen in the PXRD data. The phase fraction, zero point, cell parameters, atomic position parameters (with the atomic positions of Fe and Co constrained to be equal), thermal parameters, background (a linear interpolation function), and peak profile (~3 terms of the pseudo-Voigt) were all refined.

The refinement is shown in figure 4.1 with the atomic positions and thermal parameters for Ba₂Co_{0.75}Fe_{0.25}S₃ shown in table 4.1. The unit cell parameters refined to $a = 12.0134(6)$ Å, $b = 12.4512(6)$ Å, $c = 4.2124(2)$ Å and volume = $630.09(7)$ Å³ with

fitting parameters of $R_p = 9.09\%$, $R_{wp} = 11.18\%$, $\chi^2 = 1.49$. As the effective ionic radius for Fe^{2+} is larger (0.63 \AA in tetrahedral coordination) than that of Co^{2+} (0.58 \AA in tetrahedral coordination)¹³¹ the unit cell parameters show the increase expected from Ba_2CoS_3 .

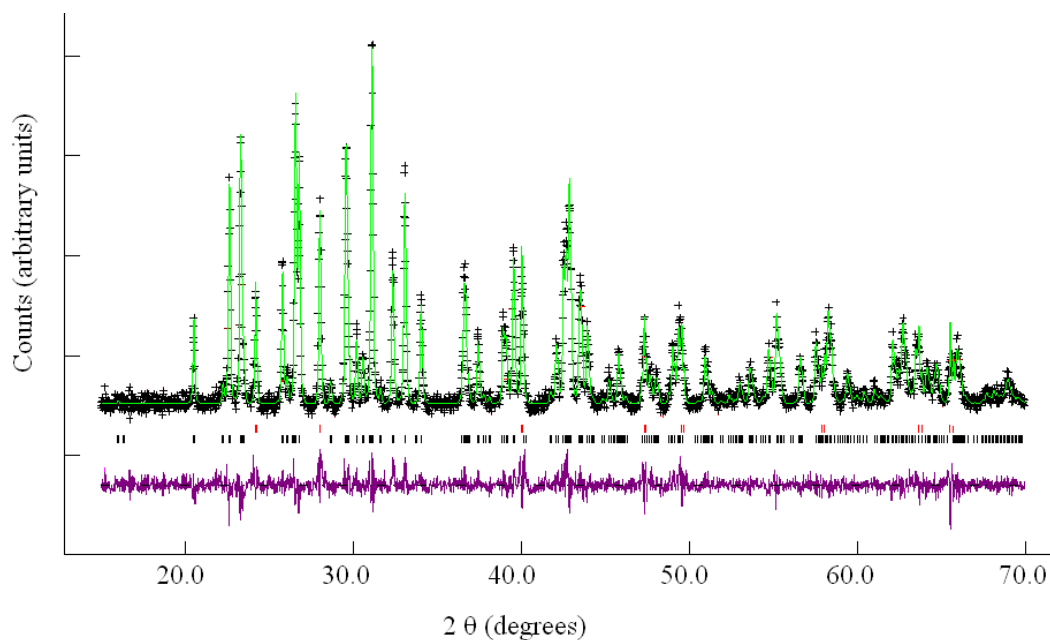


Figure 4.1 Rietveld refinement against X-ray diffraction data for $\text{Ba}_2\text{Co}_{0.75}\text{Fe}_{0.25}\text{S}_3$: Black line (observed), green line (calculated) and purple line (difference). Black tick marks correspond to $\text{Ba}_2\text{Co}_{0.75}\text{Fe}_{0.25}\text{S}_3$ and red to BaS

Table 4.1 Refined atomic coordinates and thermal parameters for $\text{Ba}_2\text{Co}_{0.75}\text{Fe}_{0.25}\text{S}_3$

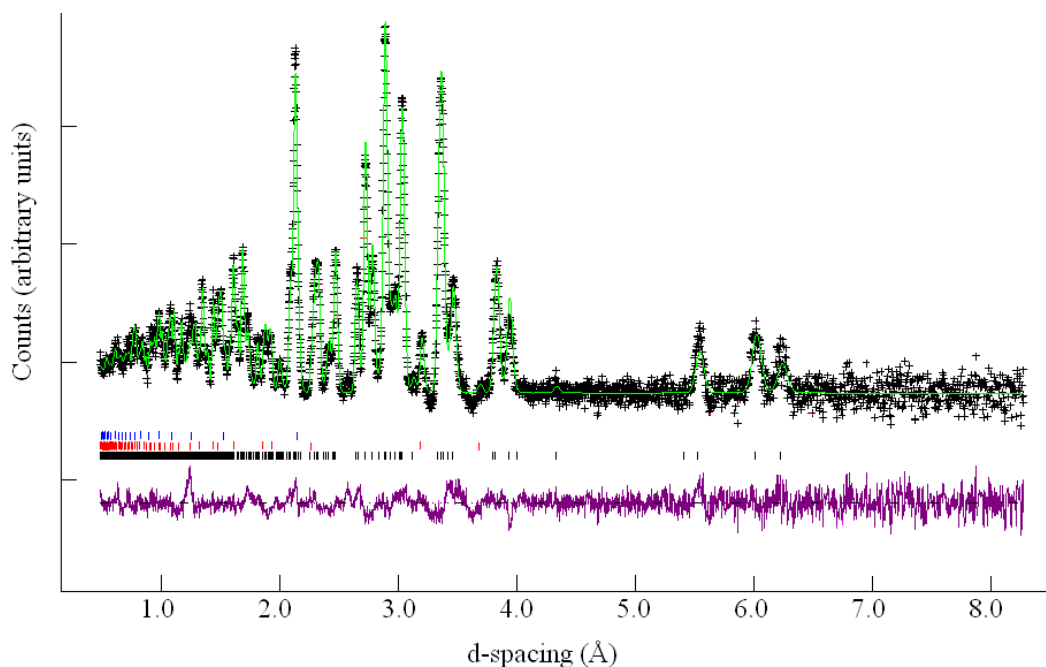
Atom	x	y	z	U	F
Ba1	0.8281(4)	0.4799(4)	0.25	0.25(2)	1
Ba2	0.4888(4)	0.6733(4)	0.25	0.32(2)	1
Co	0.7451(9)	0.1984(8)	0.25	0.09(4)	0.75
Fe	0.7451(9)	0.1984(8)	0.25	0.09(4)	0.25
S1	0.8665(13)	0.0510(12)	0.25	0.18(6)	1
S2	0.5584(12)	0.1400(14)	0.25	0.20(6)	1
S3	0.2240(12)	0.7099(13)	0.25	0.11(6)	1

4.2.2 Neutron Powder Diffraction (NPD)

Neutron diffraction data were collected for the sample $\text{Ba}_2\text{Co}_{0.75}\text{Fe}_{0.25}\text{S}_3$ on the Polaris beamline at ISIS at room temperature. Three detection banks were used and all three histograms produced were analysed simultaneously using Rietveld refinement with the software GSAS in conjunction with EXPGUI.^{121,122}

The structure of Ba_2CoS_3 was chosen as the starting model with Fe and Co located on the same site and the fractional occupancies set initially to the values dictated by the stoichiometry of the starting material. The scale, cell parameters, atomic positions (with the atomic positions of Fe and Co constrained to be equal), and peak profile (~5 terms) were all refined. Analysis showed that an impurity of ~2 % BaS is present in the sample and there is some evidence for a poorly crystalline impurity in the broad peaks seen at 1.226 Å, 2.097 Å and 3.434 Å (in d-spacing) in the neutron diffraction patterns. This poorly crystalline impurity could contain the excess transition metal resulting from the formation of Ba-containing impurities.

The three refinements of are shown in figure 4.2 with the atomic positions, thermal parameters and occupancies shown in table 4.2.



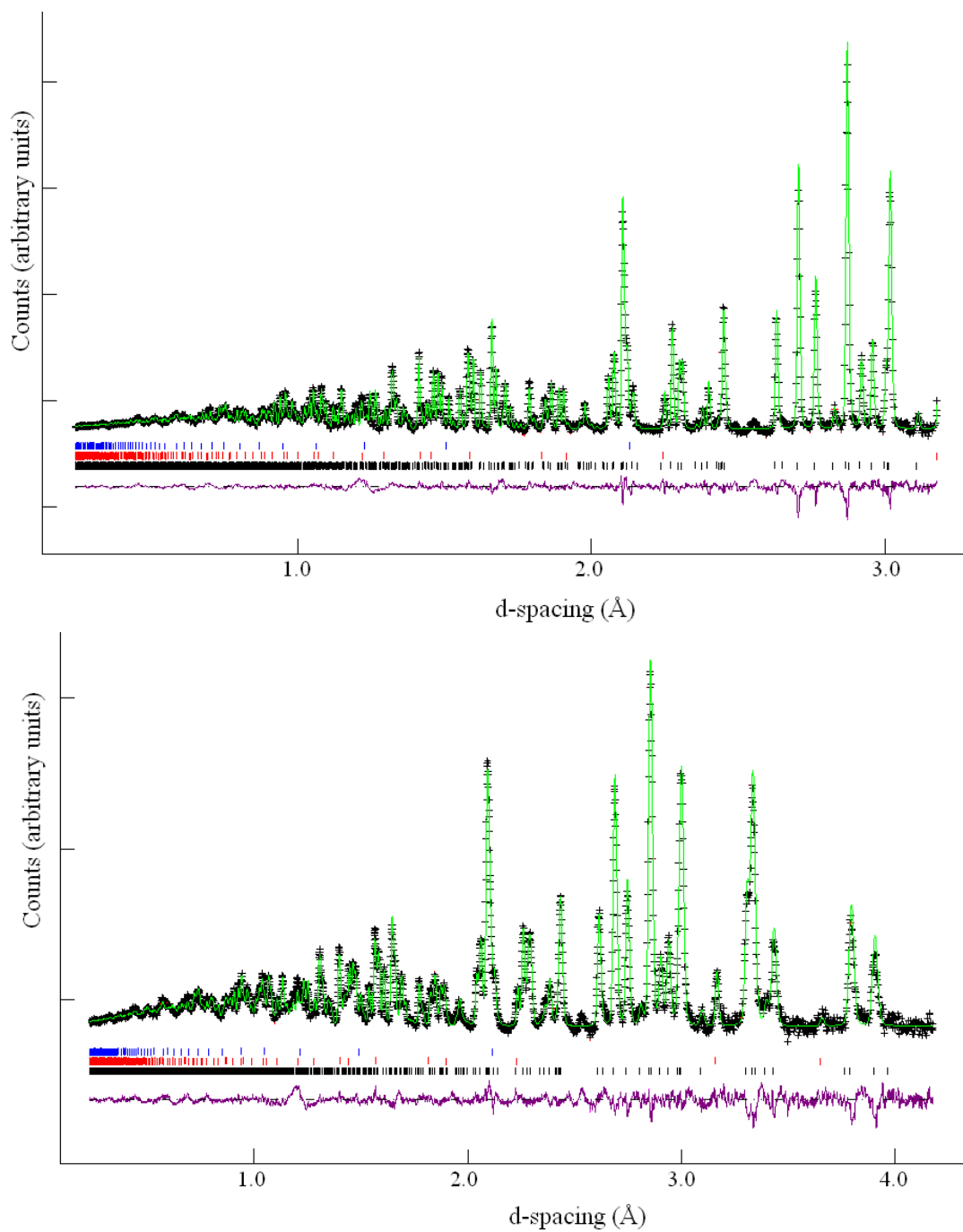


Figure 4.2 Rietveld refinement against neutron diffraction data for $\text{Ba}_2\text{Co}_{0.75}\text{Fe}_{0.25}\text{S}_3$: Black line (observed), green line (calculated) and purple line (difference). Blue tick marks correspond to vanadium, black to $\text{Ba}_2\text{Co}_{0.75}\text{Fe}_{0.25}\text{S}_3$ and red to BaS

Table 4.2 Refined atomic coordinates, thermal parameters and occupancies for $\text{Ba}_2\text{Co}_{0.75}\text{Fe}_{0.25}\text{S}_3$ from neutron diffraction data

Atom	x	y	z	U	F
Ba1	0.8284(1)	0.4800(1)	0.25	0.0092(2)	1
Ba2	0.48827(1)	0.6721(1)	0.25	0.0053(2)	1
Co	0.7484(1)	0.1980(1)	0.25	0.0026(3)	0.75
Fe	0.7484(1)	0.1980(1)	0.25	0.0026(3)	0.25
S1	0.8654(2)	0.0530(2)	0.25	0.0096(5)	1
S2	0.5609(2)	0.1405(2)	0.25	0.0052(4)	1
S3	0.2281(2)	0.7116(1)	0.25	0.0007(3)	1

The unit cell parameters refined to $a = 12.0173(3) \text{ \AA}$, $b = 12.4543(3) \text{ \AA}$, $c = 4.2152(1) \text{ \AA}$ and volume = $630.87(4) \text{ \AA}^3$ with excellent fitting parameters of $R_p = 2.95$, $R_{wp} = 1.99$, $\chi^2 = 4.32$. In agreement with results from Rietveld refinement against the PXRD data the unit cell parameters show the increase expected from Ba_2CoS_3 .

4.2.3 X-ray Absorption Spectroscopy (XAS)

The Co and Fe K-edge X-ray absorption spectra were collected in transmission mode at $\sim 80 \text{ K}$ from samples diluted in BN on station 9.3 of the Daresbury Laboratory SRS (2 GeV $\sim 200 \text{ mA}$) using a Si(111) double crystal monochromator.

The first step taken in the data analysis was averaging the multiple spectra collected for the sample, followed by calibrating the absorption edge of each sample against the metal foils used as standards. A background subtraction was performed using the program PAXAS,¹³² the intensity was then normalised before XANES analysis was performed.

To prepare the EXAFS data for analysis the post edge data were first extracted i.e. the 'atomic component' (the part of the spectrum to which free atoms would contribute) was removed, using a 5 or 6 order polynomial or spline using the program

PYSPLINES.¹³³ The extracted data are in the form of normalised intensity plotted against k ($k = \text{reciprocal space, } \text{\AA}^{-1}$) and were then weighted, to ensure that low intensity, high energy data were properly accounted for, by multiplying each data point by k^3 . The data produced were then analysed using the program EXCURV 98.¹³⁴ A model containing the type and number of atoms surrounding the central atom as well as their distance from the central atom is compared to the data and a refinement of this model carried out. A Fourier transform (FT) is used to provide a plot of distance from the central atom against intensity for visual comparison.

4.2.3.1 XANES

The Co-K-edge XANES spectrum of Ba_2CoS_3 has been studied and is consistent with a distorted tetrahedral environment.¹¹⁰ A comparison of this spectrum with the spectra collected for $\text{Ba}_2\text{Co}_{0.75}\text{Fe}_{0.25}\text{S}_3$ confirms that this tetrahedral environment is maintained upon substitution of Fe for Co and that Co shows oxidation state +2 (figure 4.3). There is a slight change in the edge position but it is not significant enough to indicate any change in oxidation state for Co in $\text{Ba}_2\text{Co}_{0.75}\text{Fe}_{0.25}\text{S}_3$.

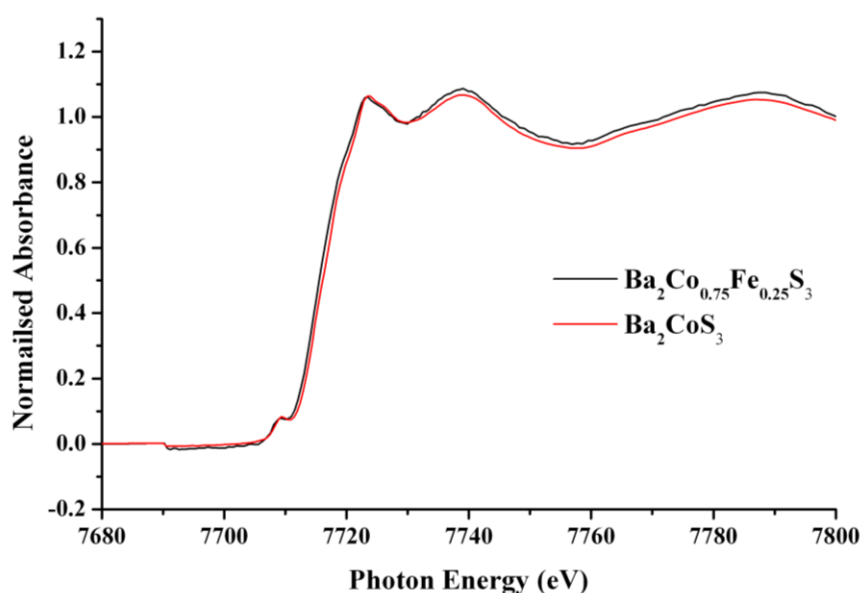


Figure 4.3 Co-K-edge XANES spectra of Ba_2CoS_3 and $\text{Ba}_2\text{Co}_{0.75}\text{Fe}_{0.25}\text{S}_3$

The pre-edge feature seen at around 7710 eV can be used to characterise 1s-3d transitions and is more intense for environments with no centre of symmetry. The

presence of a shoulder on the edge itself is caused by 1s-4p transitions and is generally indicative of square planar materials or square based pyramidal centres. The XANES spectrum for $\text{Ba}_2\text{Co}_{0.75}\text{Fe}_{0.25}\text{S}_3$ shows a relatively intense pre-edge feature but no shoulder and as such is consistent with a tetrahedral environment.

4.2.3.2 EXAFS

For the analysis of EXAFS data the local environment of the transition metal (TM) was initially set using the parameters obtained from a previous study of the EXAFS data for Ba_2CoS_3 and from PXRD data.¹¹⁰ The analysis was performed modelling five shells. The first TM-S shell in the Fourier transform (FT) was set as a single shell of four sulphur atoms at a radius of 2.35 Å. The next significant shell is made up of a mixture of seven TM-Ba interactions, three at 3.5 Å and four at 3.8 Å, followed by two TM-TM interactions at 4.1 Å. The final shell in the FT to be fitted was that at about 5.7 Å resulting from another TM-Ba shell. The distances and the Debye-Waller factors were refined. The Debye-Waller factor is a measure of the variation in atomic distances and accounts for the structural and thermal disorder of a sample. The EXAFS and Fourier Transform for the Co-K-edge are shown in figure 4.4 and the results of the refinement are shown in table 4.3. The Fe-K-edge data were not of sufficient quality to be able to fit beyond the first shell (since the amount of iron in the sample is relatively small the absorption is poor; any increase in the amount of sample in the beamline simply leads to increased absorption by the larger barium atoms) and will not be presented here.

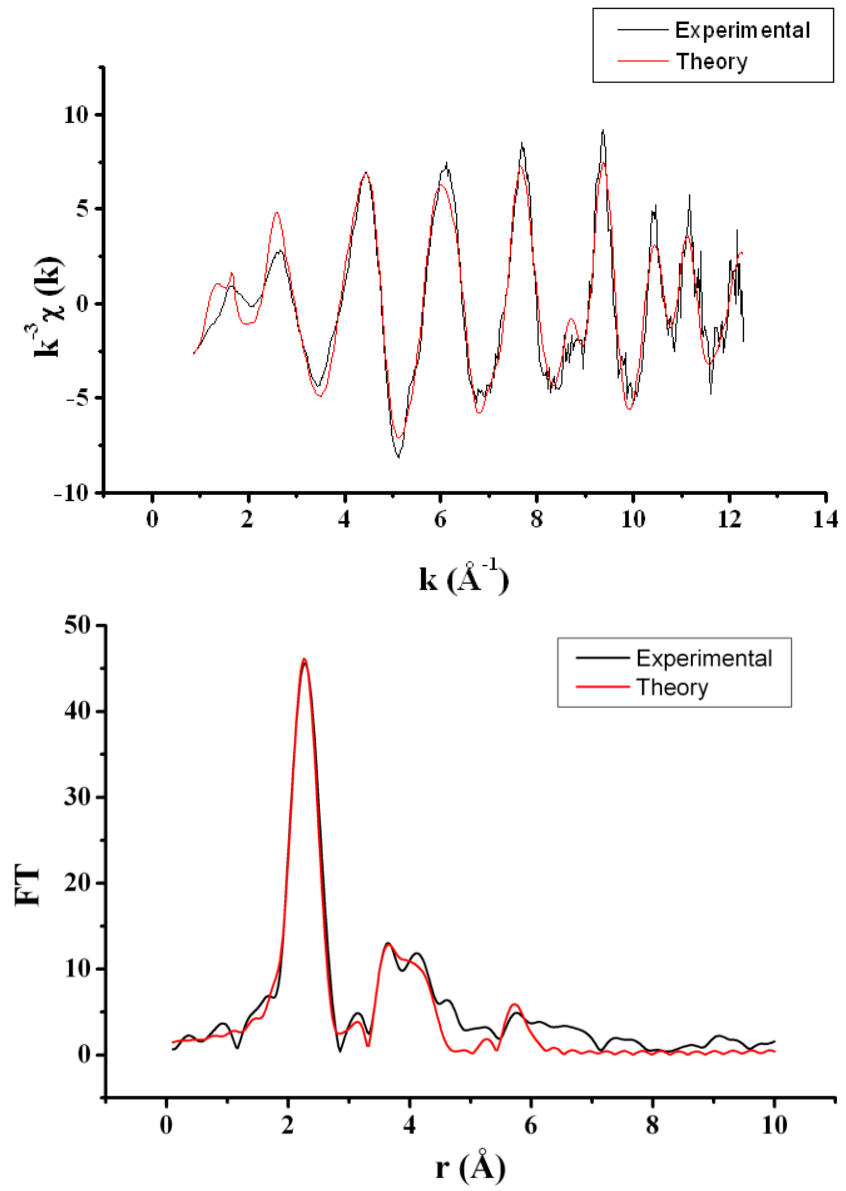


Figure 4.4 Co-K-edge a) EXAFS and b) Fourier Transform for $\text{Ba}_2\text{Co}_{0.75}\text{Fe}_{0.25}\text{S}_3$

Table 4.3 Summary of refined Co-K-edge EXAFS parameters for $\text{Ba}_2\text{Co}_{0.75}\text{Fe}_{0.25}\text{S}_3$

Bond	r (Å)	$2\sigma^2$ (Å ²)
Co-S (4)	2.335(3)	0.0135(7)
Co-Ba (3)	3.533(7)	0.0156(13)
Co-Ba (4)	3.847(50)	0.0572(23)
Co-Co (2)	4.126(8)	0.0079(18)
Co-Ba (4)	5.577(15)	0.0155(30)
$E_f = -9.9(3)$	$R = 27.2\%$	$FI = 0.32$

The agreement between the Co-K-edge EXAFS and XANES data with the X-ray and neutron diffraction data out to 5.5 Å confirms the structure of Ba_2CoS_3 is maintained in the compound $\text{Ba}_2\text{Co}_{0.75}\text{Fe}_{0.25}\text{S}_3$.

4.2.4 Physical Properties

4.2.4.1 Transport Properties

The resistivity of $\text{Ba}_2\text{Co}_{0.75}\text{Fe}_{0.25}\text{S}_3$ was measured using the four point probe method over the temperature range 5-300 K (figure 4.5). The room temperature resistivity is $\sim 30 \Omega\text{cm}$ and increases as the temperature is reduced. This trend and the relatively high value of the resistivity are both indicative of semiconducting behaviour.

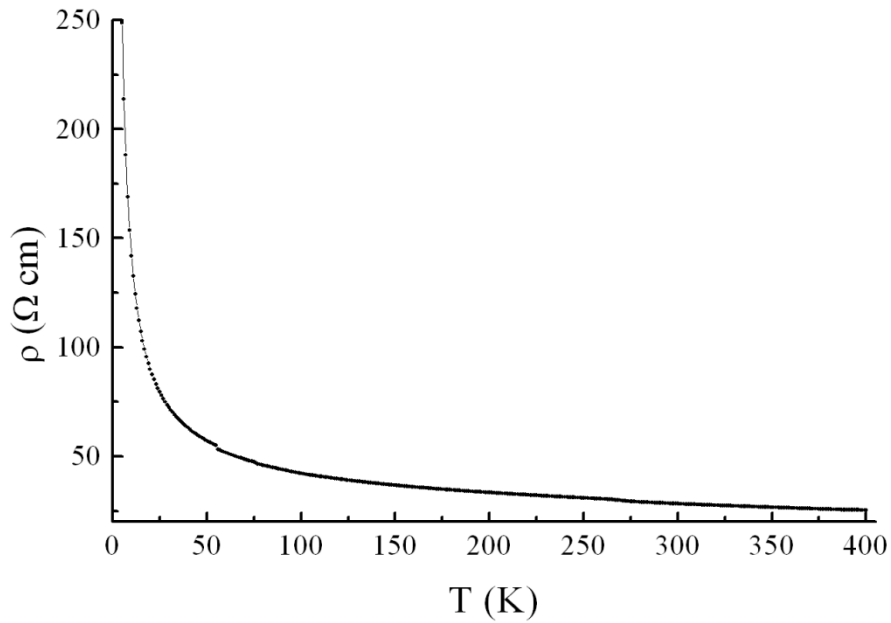


Figure 4.5 Plot of resistivity versus temperature for of $\text{Ba}_2\text{Co}_{0.75}\text{Fe}_{0.25}\text{S}_3$

The resistivity data have been analysed using the variable range hopping model, based on the equation;

—

Where ρ is the resistivity, T the temperature, T_0 the activation temperature and n the dimension of the conductance and;

—————

Where k_B is the Boltzmann constant, $N(E_F)$ is the density of states and ξ is the localisation length.

Plots of $\ln(\rho)$ against $1/T^{1/n+1}$, with $n = 0$ and 3 (figure 4.6) show that the method of conduction is three dimensional as plots of $1/T^{1/4}$ (i.e. $n = 3$) against $\ln(\rho)$ yield straight lines (figure 4.6b).

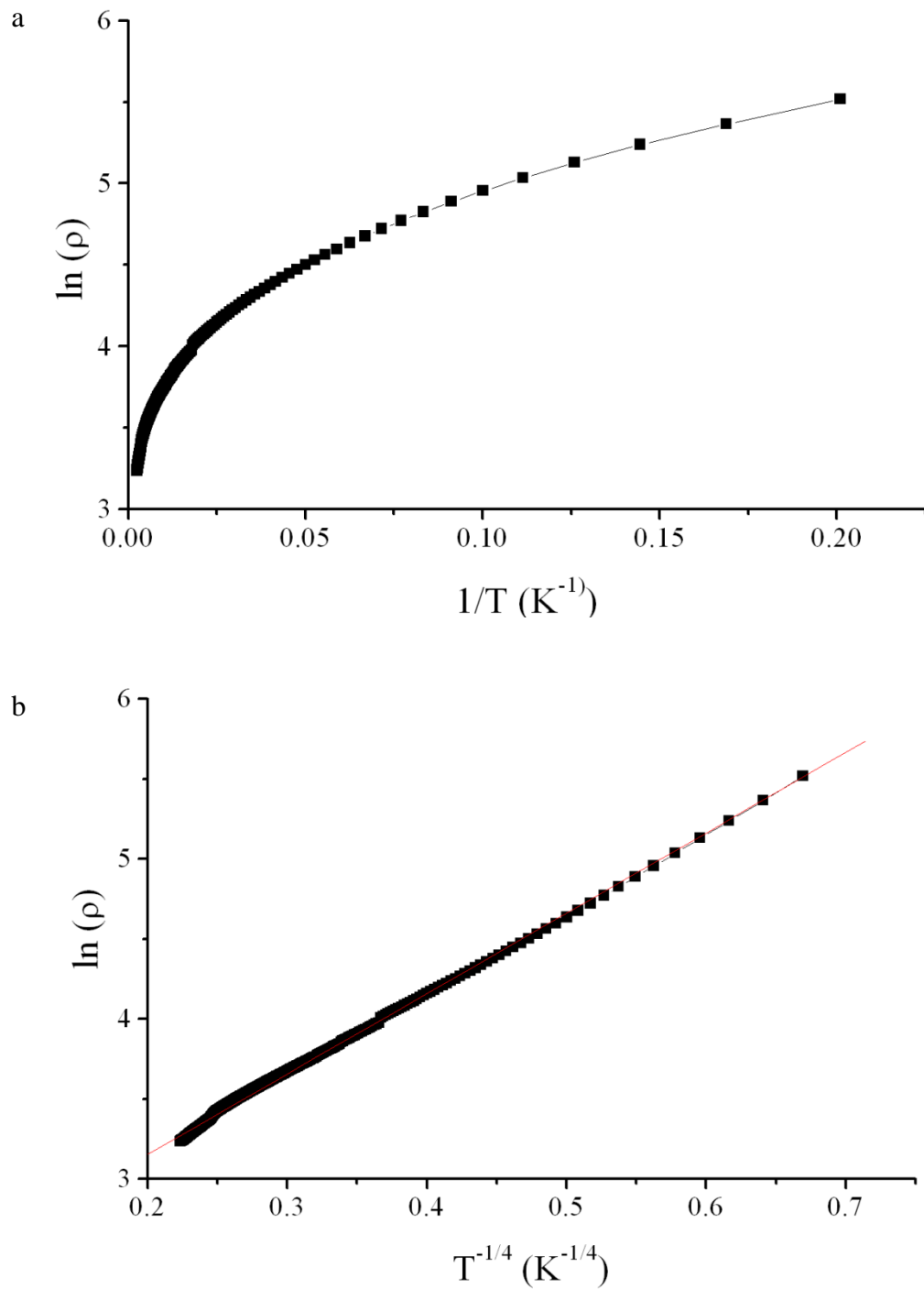


Figure 4.6 a) Arrhenius plot of resistivity data for $\text{Ba}_2\text{Co}_{0.75}\text{Fe}_{0.25}\text{S}_3$ b) plot showing the linear dependency of $\ln(\rho)$ against $T^{-1/4}$ indicating 3-D conductivity

Analysis of the linear section of the plot of $\ln(\rho)$ against $T^{-1/4}$ gives values of $\rho_0 = 8.58$ and $T_0 = 1.50$.

4.2.5 Conclusion

The compound $\text{Ba}_2\text{Co}_{0.75}\text{Fe}_{0.25}\text{S}_3$ was the only one from the series $\text{Ba}_2\text{Co}_{1-x}\text{Fe}_x\text{S}_3$ that could be prepared with relatively small amount of impurities. It was analysed using PXRD, NPD, XAS and TEM and maintains the same structure as Ba_2CoS_3 . However the resistivity is much higher than that of Ba_2CoS_3 and it shows semiconducting behaviour, i.e. the partial replacement of Fe for Co causes loss of metallic-like features. It is the first time that a compound from the Ba_2CoS_3 - Ba_2FeS_3 solid solution has been prepared.

5.0 $\text{Ba}_2\text{Zn}_{1-x}\text{M}_x\text{S}_3$ (M = Fe, Mn, Cr, Ni)

5.1 Synthesis and Characterisation

The synthesis of the ternary sulphides $\text{Ba}_2\text{Zn}_{1-x}\text{TM}_x\text{S}_3$ (TM = Fe, Mn, Cr, Ni, $x = 0.25, 0.5, 0.75$), was performed *via* a solid-gas reaction as discussed in the Experimental section 2.1. Stoichiometric mixtures of barium carbonate (99%), zinc oxide (99.8%), iron powder (99%), manganese carbonate (98%), chromium powder (99.9%) and nickel carbonate (99.5%) were reacted with carbon disulphide (99%) for 24 hours at 1000°C. The samples were then initially characterised using powder X-ray diffraction, carried out on all samples on a Siemens D5000 diffractometer with Cu $K\alpha$ radiation, and if impurities were present the heating process was repeated until, if possible, high purity samples (~95%) were obtained; these were then further characterised using neutron diffraction. Powder neutron diffraction data were collected for selected compounds at the Polaris diffractometer at the ISIS pulsed spallation source, Rutherford Appleton Laboratory, UK. Approximately 5g of samples were used, and placed in a vanadium can and data collection was performed at room temperature or 5 K for approximately 4 hours. Magnetic susceptibility measurements were then performed on selected samples using a SQUID magnetometer over the range 5-300 K using a 2 T external field (zero-field cooled). The resistivity of the samples was measured using a PPMS device and the four point probe method over the temperature range 5-300 K and magnetoresistance measurements were also carried out using this device over the magnetic field range 0-7 T at 5-300 K.

5.2 Results and Discussion

5.2.1 Powder X-ray Diffraction (PXRD)

Due to time and instrument constraints, data collection for powder X-ray diffraction for these materials was only performed for short times (~2 hours) to confirm the purity of the samples which were then further analysed using neutron diffraction experiments. Because of these short collection times the data quality is lower and therefore high values for fitting parameters are seen. Not all of the samples could be successfully synthesised, as explained in the following sections and small impurities of BaS and

Ba₂SiS₄ (due to reaction of BaS with the SiO₂ of the glass tube) were found in some samples and could not be eliminated. Rietveld refinements were then performed using the software GSAS in conjunction with EXPGUI.^{121,122} For these materials the occupancies and atomic thermal parameters (set to 0.005) were not refined.

5.2.1.1 Ba₂Zn_{1-x}Fe_xS₃ (x = 0.25, 0.5, 0.75)

Analysis of the unit cell parameters from Rietveld refinement shows no significant change in the overall unit cell volume when substituting the larger Fe²⁺ (0.63 Å for tetrahedral coordination) for Zn²⁺ (0.60 Å for tetrahedral coordination). The *c* axis, i.e. along the length of the TMS₄ chains, increases as does the *a* axis whilst the *b* axis decreases in size (table 6.1). Further discussion of the unit cell parameters and atomic positions is contained in section 5.3.2.1. An impurity of 2-4 % BaS was found in the samples although no corresponding impurities containing Zn or TM were seen in the PXRD data. An example refinement is shown in figure 5.1 with the corresponding refined atomic coordinates in table 5.2; all other refinements are in Appendix 4.

Table 5.1 Unit cell parameters and fitting parameters for Ba₂Zn_{1-x}Fe_xS₃

x	0.25	0.5	0.75
<i>a</i> (Å)	12.0243(6)	12.0410(7)	12.0544(7)
<i>b</i> (Å)	12.5609(6)	12.5155(7)	12.4797(7)
<i>c</i> (Å)	4.2190(2)	4.2295(2)	4.2400(3)
<i>V</i> (Å ³)	637.22(7)	637.38(2)	637.85(5)
<i>R_p</i> (%)	17.58	15.75	13.13
<i>R_{wp}</i> (%)	13.80	12.64	15.84
χ ²	2.52	2.03	1.90

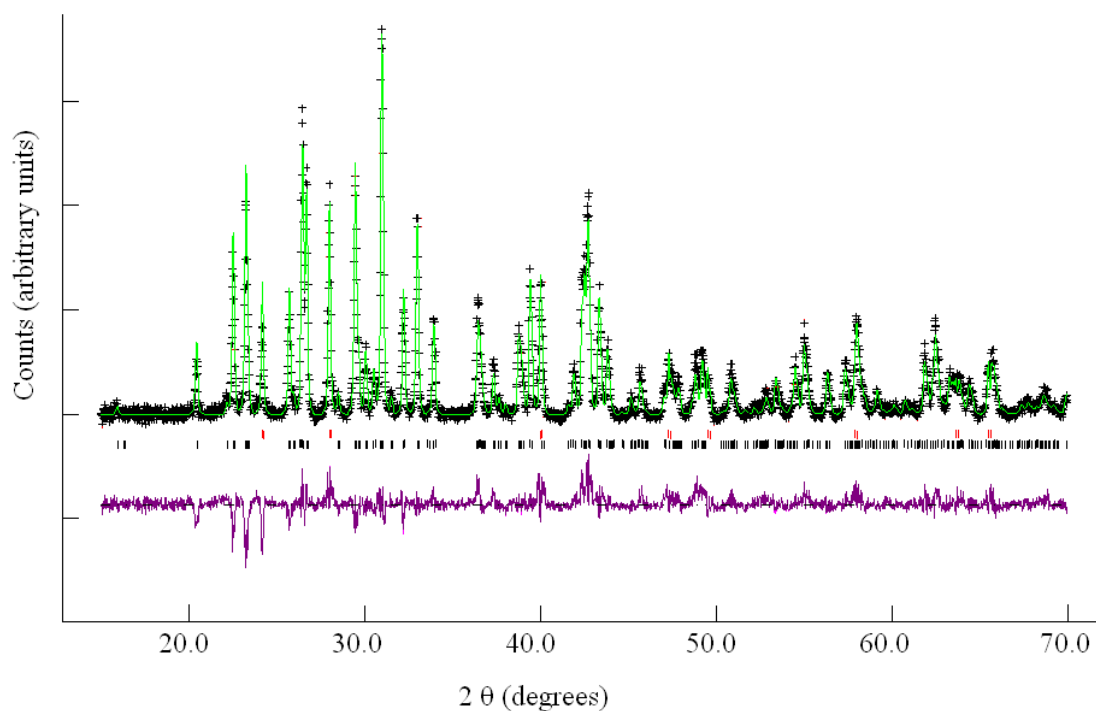


Figure 5.1 Rietveld refinement against X-ray diffraction data for $\text{Ba}_2\text{Zn}_{0.5}\text{Fe}_{0.5}\text{S}_3$: Black line (observed), green line (calculated) and purple line (difference). Black tick marks correspond to $\text{Ba}_2\text{Zn}_{0.5}\text{Fe}_{0.5}\text{S}_3$ and red to BaS

Table 5.2 Refined atomic coordinates for $\text{Ba}_2\text{Zn}_{0.5}\text{Fe}_{0.5}\text{S}_3$

Atom	x	y	z	F
Ba1	0.8260(4)	0.4816(4)	0.25	1
Ba2	0.4888(3)	0.6744(3)	0.25	1
Zn	0.7447(7)	0.1969(6)	0.25	0.5
Fe	0.7447(7)	0.1969(6)	0.25	0.5
S1	0.8653(12)	0.0500(11)	0.25	1
S2	0.5585(11)	0.1390(13)	0.25	1
S3	0.2236(10)	0.7054(11)	0.25	1

5.2.1.2 Ba₂Zn_{1-x}Mn_xS₃ (x = 0.25, 0.5, 0.75)

Whilst Ba₂MnS₃ forms the K₂AgI₃-type structure, Ba₂ZnS₃ has previously only been shown to form the K₂CuCl₃-type structure¹³⁷ (a description of the two structures can be found in section 1.5.4.12) similarly to Ba₂CoS₃. However, previous attempts to form a Ba₂Co_{1-x}Mn_xS₃ solid solution resulted in a mixture of Ba₂CoS₃ and Ba₂MnS₃. Analysis of the PXRD data revealed that for the samples Ba₂Zn_{1-x}Mn_xS₃ (x = 0.25, 0.5) the majority phase formed is of the K₂AgI₃-type structure (i.e. Ba₂MnS₃) with some Ba₂SiS₄ impurity (5-7%) present although no corresponding impurities containing Zn or TM were seen in the PXRD data. For Ba₂Zn_{0.25}Mn_{0.75}S₃ a mixture of phases was found including a Ba₂CoS₃ type and Ba₂MnS₃ type, and further heating did not result in a single phase product. The unit cell parameters of the x = 0.25 and x = 0.50 samples increase as the larger Mn²⁺ (0.66 Å for tetrahedral coordination) is substituted for Zn²⁺ (0.60 Å for tetrahedral coordination). The unit cell parameters of Ba₂Zn_{1-x}Mn_xS₃ (x = 0.25, 0.5) are shown in table 5.3 and an example refinement is shown in figure 5.2 with the corresponding refined atomic coordinates in table 5.4; the other refinement is in Appendix 5.

Table 5.3 Unit cell parameters and fitting parameters for Ba₂Zn_{1-x}Mn_xS₃

x	0.25	0.5
<i>a</i> (Å)	8.7897(5)	8.7982(5)
<i>b</i> (Å)	4.2641(3)	4.2767(2)
<i>c</i> (Å)	17.039(1)	17.0556(9)
<i>V</i> (Å ³)	638.63(2)	641.76(5)
<i>R_p</i> (%)	13.30	13.32
<i>R_{wp}</i> (%)	16.52	17.06
χ^2	1.89	1.73

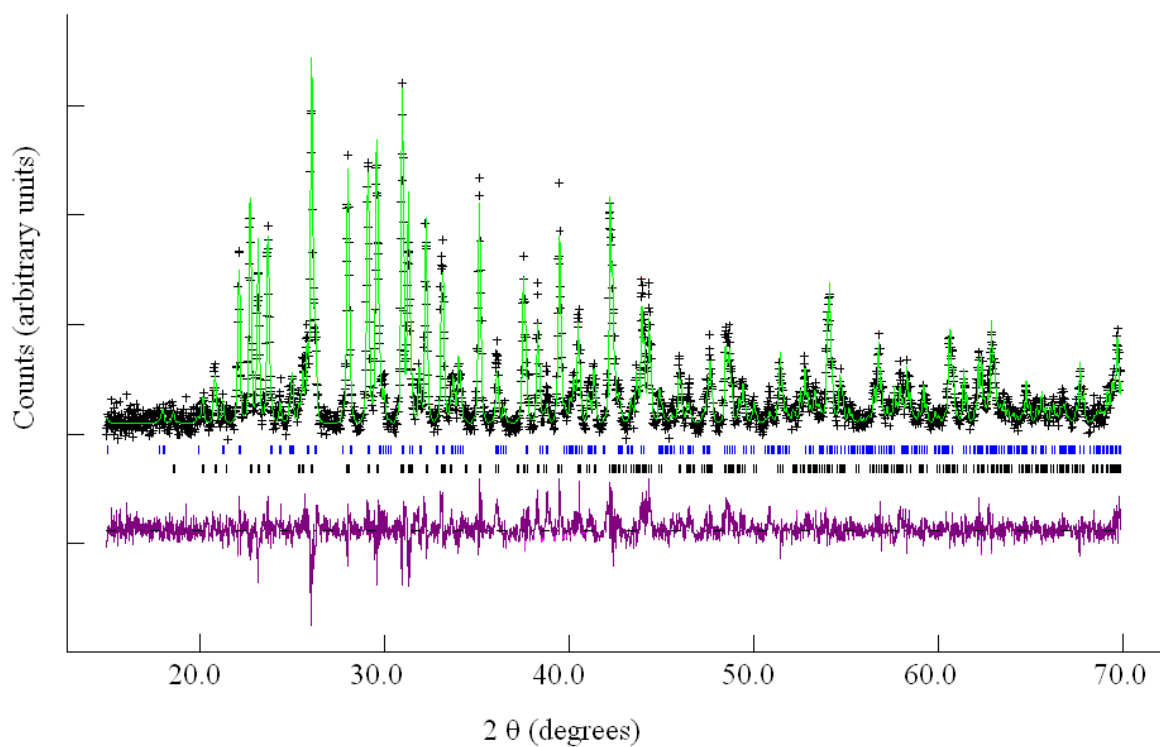


Figure 5.2 Rietveld refinement against X-ray diffraction data for $\text{Ba}_2\text{Zn}_{0.5}\text{Mn}_{0.5}\text{S}_3$: Black line (observed), green line (calculated) and purple line (difference). Black tick marks correspond to $\text{Ba}_2\text{Zn}_{0.5}\text{Mn}_{0.5}\text{S}_3$ black to Ba_2SiS_4

Table 5.4 Refined atomic coordinates for $\text{Ba}_2\text{Zn}_{0.5}\text{Mn}_{0.5}\text{S}_3$

Atom	x	y	z	F
Ba1	0.4166(7)	0.25	0.7129(4)	1
Ba2	0.2569(8)	0.25	0.458194)	1
Zn	0.375(1)	0.25	0.1322(8)	0.5
Mn	0.375(1)	0.25	0.1322(8)	0.5
S1	0.317(2)	0.25	0.277(2)	1
S2	0.133(3)	0.25	0.082(2)	1
S3	1.007(2)	0.25	0.598(1)	1

5.2.1.3 Ba₂Zn_{1-x}Cr_xS₃ (x = 0.25, 0.5, 0.75)

Of these samples only Ba₂Zn_{0.75}Cr_{0.25}S₃ could be made as a relatively pure phase with large amounts of impurities (BaS, ZnS and various CrS_x phases) found for the other samples. Rietveld refinement against the data for Ba₂Zn_{0.75}Cr_{0.25}S₃ gives unit cell parameters $a = 12.008(1) \text{ \AA}$, $b = 12.601(1) \text{ \AA}$, $c = 4.2111(3) \text{ \AA}$ and a volume = $637.2(1) \text{ \AA}^3$ with fitting parameters $R_p = 18.22$, $R_{wp} = 13.95$, $\chi^2 = 2.26$. An impurity of 8% Ba₂SiS₄ was found. The refinement is shown in figure 5.3 with the refined atomic coordinates shown in table 5.5.

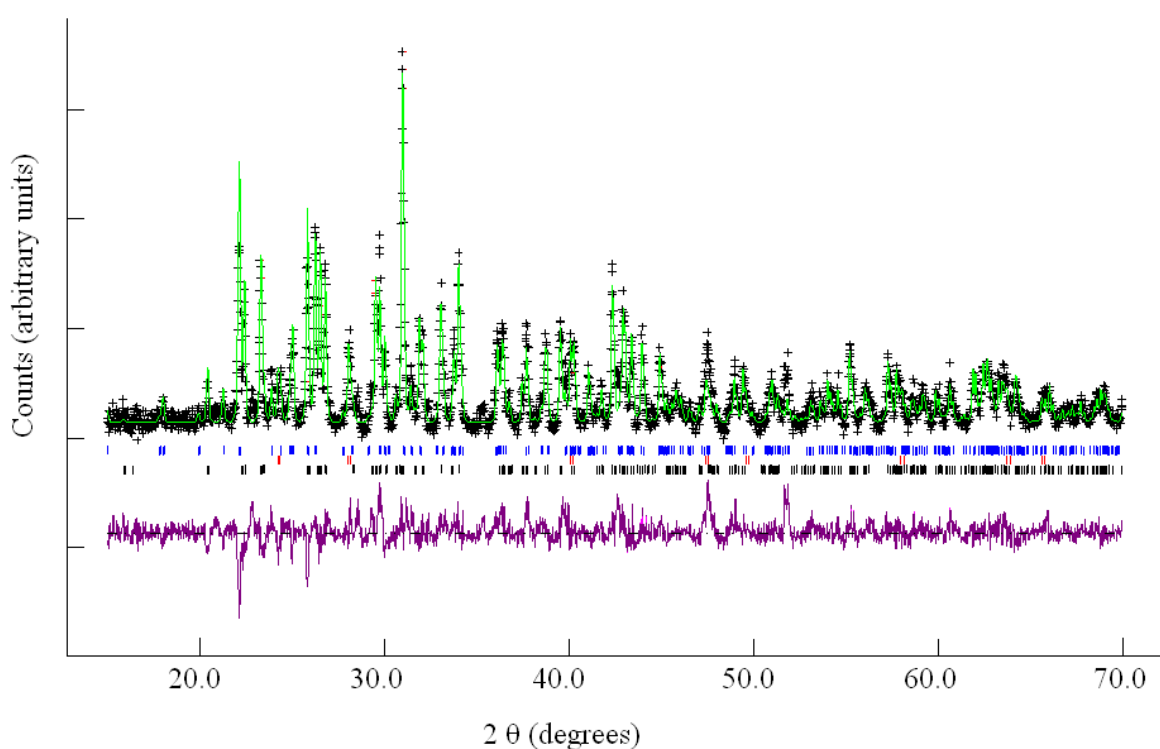


Figure 5.3 Rietveld refinement against X-ray diffraction data for Ba₂Zn_{0.75}Cr_{0.25}S₃: Black line (observed), green line (calculated) and purple line (difference). Blue tick marks correspond to Ba₂Zn_{0.75}Cr_{0.25}S₃ black to Ba₂SiS₄ and red to BaS

Table 5.5 Refined atomic coordinates for $\text{Ba}_2\text{Zn}_{0.75}\text{Cr}_{0.25}\text{S}_3$

Atom	x	y	z	F
Ba1	0.8282(7)	0.4828(9)	0.25	1
Ba2	0.4875(9)	0.6747(8)	0.25	1
Zn	0.742(3)	0.198(2)	0.25	0.75
Cr	0.742(3)	0.198(2)	0.25	0.25
S1	0.866(3)	0.057(4)	0.25	1
S2	0.565(4)	0.142(4)	0.25	1
S3	0.222(4)	0.712(4)	0.25	1

5.2.1.4 $\text{Ba}_2\text{Zn}_{1-x}\text{Ni}_x\text{S}_3$ ($x = 0.25, 0.5, 0.75$)

Of these samples only $\text{Ba}_2\text{Zn}_{0.75}\text{Ni}_{0.25}\text{S}_3$ could be made as a relatively pure phase with large amounts of impurities (BaS, ZnS and various other unidentified impurities) found for the other samples. The unit cell parameters for $\text{Ba}_2\text{Zn}_{0.75}\text{Ni}_{0.25}\text{S}_3$ found were $a = 12.0102(6)$ Å, $b = 12.571(6)$ Å, $c = 4.2171(2)$ Å and a volume = $636.71(7)$ Å³. An impurity of 7% Ba_2SiS_4 was found. The refinement is shown in figure 5.4 with the refined atomic coordinates and fitting parameters shown in table 5.6. $R_p = 9.55$, $R_{wp} = 11.63$, $\chi^2 = 1.37$.

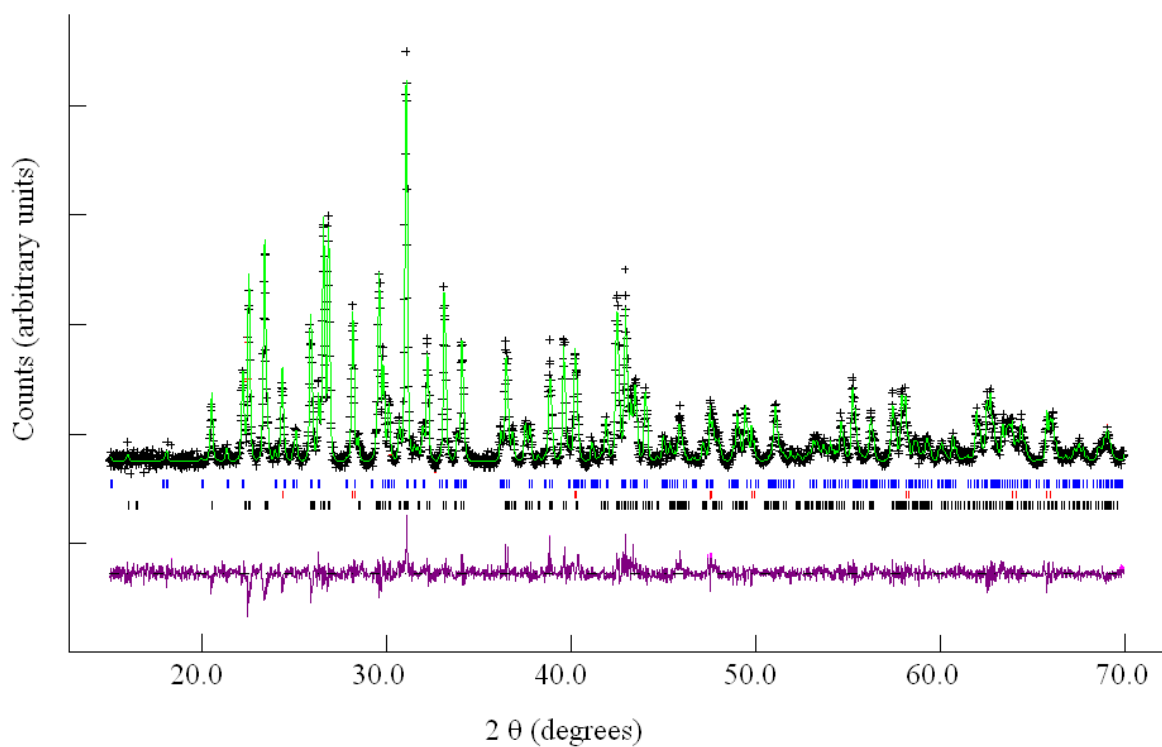


Figure 5.4 Rietveld refinement against X-ray diffraction data for $\text{Ba}_2\text{Zn}_{0.75}\text{Ni}_{0.25}\text{S}_3$: Black line (observed), green line (calculated) and purple line (difference). Blue tick marks correspond to $\text{Ba}_2\text{Zn}_{0.75}\text{Ni}_{0.25}\text{S}_3$ black to Ba_2SiS_4 and red to BaS

Table 5.6 Refined atomic coordinates for $\text{Ba}_2\text{Zn}_{0.75}\text{Ni}_{0.25}\text{S}_3$

Atom	x	y	z	F
Ba1	0.8262(4)	0.4822(4)	0.25	1
Ba2	0.4879(4)	0.6744(4)	0.25	1
Zn	0.7460(7)	0.1975(7)	0.25	0.75
Ni	0.7460(7)	0.1975(7)	0.25	0.25
S1	0.864(1)	0.048(1)	0.25	1
S2	0.559(1)	0.142(2)	0.25	1
S3	0.226(1)	0.708(1)	0.25	1

5.2.2 Neutron Powder Diffraction (NPD)

Neutron diffraction data were collected on the Polaris beamline at ISIS for the samples $\text{Ba}_2\text{Zn}_{1-x}\text{Fe}_x\text{S}_3$ ($x = 0.25, 0.5, 0.75$), $\text{Ba}_2\text{Zn}_{1-x}\text{Mn}_x\text{S}_3$ ($x = 0.25, 0.5$) and $\text{Ba}_2\text{Zn}_{0.75}\text{Cr}_{0.25}\text{S}_3$ at room temperature and at ~ 5 K and for $\text{Ba}_2\text{Zn}_{0.75}\text{Ni}_{0.25}\text{S}_3$ at room temperature only. Three detection banks were used and all three histograms produced were analysed simultaneously using Rietveld refinement with the software GSAS in conjunction with EXPGUI.^{121,122}

For $\text{Ba}_2\text{Zn}_{1-x}\text{TM}_x\text{S}_3$ with $\text{TM} = \text{Fe}, \text{Cr}$ and Ni the structure of Ba_2CoS_3 was chosen as the starting model and for $\text{Ba}_2\text{Zn}_{1-x}\text{Mn}_x\text{S}_3$ the structure of Ba_2MnS_3 was used, in both cases Zn and TM were located on the same site and the fractional occupancies set initially to the values dictated by the stoichiometry of the starting material. The scale, cell parameters, atomic positions (with the atomic positions of Zn and Co constrained to be equal), occupancies (with the combined occupancy of Zn and TM constrained to equal one), thermal parameters and peak profile (~ 5 terms) were all refined. Analysis showed that impurities of BaS and/or Ba_2SiS_4 are present in the samples and there is some evidence for a poorly crystalline impurity seen in the broad peaks seen at 1.226 Å, 2.097 Å and 3.434 Å (in d-spacing) in some of the neutron diffraction patterns. This poorly crystalline impurity could contain the excess transition metal resulting from the formation of Ba-containing impurities.

5.2.2.1 $\text{Ba}_2\text{Zn}_{1-x}\text{Fe}_x\text{S}_3$ ($x = 0.25, 0.5, 0.75$)

The unit cell parameters from the Rietveld refinements for both room temperature and low temperature data show an overall increase in the unit cell volume as expected when substituting the larger Fe^{2+} (0.63 Å for tetrahedral coordination) for Zn^{2+} (0.60 Å for tetrahedral coordination) and there is excellent consistency between the room temperature and 5 K data with slightly smaller unit cell parameters and lower thermal parameters at low temperature (table 5.7 and 5.8), as expected. As seen in the PXRD data the c axis, i.e. along the length of the TMS_4 chains, increases as does the a axis whilst the b axis decreases in size. This variation in the a and b axes has the effect of making the interchain distances more uniform.

Table 5.7 Unit cell parameters from Rietveld refinement against neutron diffraction data at room temperature

x	a (Å)	b (Å)	c (Å)	Volume (Å ³)
0.25	12.0156(2)	12.5436(2)	4.21925(6)	635.92(2)
0.5	12.0366(2)	12.5065(2)	4.2311(1)	636.94(2)
0.75	12.0560(4)	12.4700(5)	4.2385(1)	637.21(5)

Table 5.8 Unit cell parameters from Rietveld refinement against neutron diffraction data at 5 K

x	a (Å)	b (Å)	c (Å)	Volume (Å ³)
0.25	11.9951(2)	12.5251(2)	4.20945(7)	632.43(3)
0.5	12.0121(2)	12.4832(2)	4.21982(8)	632.76(3)
0.75	12.0329(4)	12.4466(5)	4.2255(2)	632.85(5)

Analysis of the bond lengths shows that the increase in the length of the a parameter is determined by the bond angle rather than the bond length. The bond lengths for the transition metal to the sulphur along the a axis actually decrease slightly from 2.44(2) Å for Ba₂Zn_{0.75}Fe_{0.25}S₃ to 2.43(1) Å for Ba₂Zn_{0.5}Fe_{0.5}S₃ and 2.42(3) Å for Ba₂Zn_{0.25}Fe_{0.75}S₃ whilst the TM-S-TM angle increases from 119° to 120° and 121° for the same compounds. The other TM-S bond lengths increase and the tetrahedra effectively become more regular as the amount of iron increases. The atomic positions, thermal parameters, occupancies and fitting parameters for Ba₂Zn_{1-x}Fe_xS₃ ($x = 0.25, 0.5, 0.75$) are shown in tables 5.8-5.13. The occupancies all fall within reasonable limits of those expected and show that despite the presence of crystalline impurities containing barium and possible poorly crystalline impurities containing transition metal(s) the stoichiometry remains similar to that expected from the starting materials. Comparing the low and high temperature data does not show any extra peaks which may indicate an antiferromagnetic unit cell or enhancement of any peaks which may indicate a ferromagnetic unit cell. An example refinement is shown in figure 5.5 with all other refinements in Appendix 6.

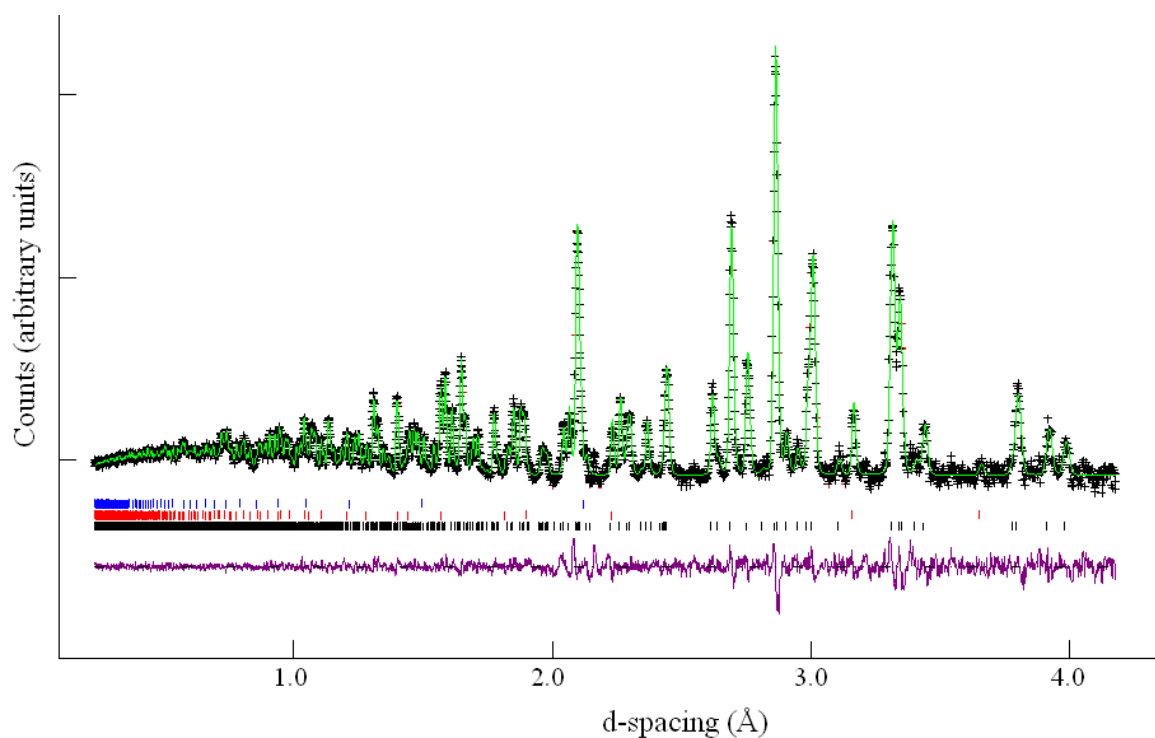


Figure 5.5 Rietveld refinement against neutron diffraction data for $\text{Ba}_2\text{Zn}_{0.5}\text{Fe}_{0.5}\text{S}_3$ at 5 K: Black line (observed), green line (calculated) and purple line (difference). Black tick marks correspond to $\text{Ba}_2\text{Zn}_{0.5}\text{Fe}_{0.5}\text{S}_3$ blue to Ba_2Si_4 and red to BaS

Table 5.8 Refined atomic coordinates, thermal parameters and occupancies for $\text{Ba}_2\text{Zn}_{0.75}\text{Fe}_{0.25}\text{S}_3$ from neutron diffraction data at room temperature

Atom	x	y	z	U	F
Ba1	0.82695(8)	0.48241(8)	0.25	0.0091(1)	1
Ba2	0.48895(8)	0.67416(8)	0.25	0.0060(2)	1
Zn	0.74590(8)	0.19825(6)	0.25	0.0078(1)	0.75
Fe	0.74596(8)	0.19827(6)	0.25	0.0078(1)	0.25
S1	0.8656(1)	0.0527(1)	0.25	0.0095(3)	1
S2	0.5591(1)	0.1414(2)	0.25	0.0074(3)	1
S3	0.2247(1)	0.7082(1)	0.25	0.0057(1)	1
$R_p = 5.84\%$		$R_{wp} = 2.61\%$		$\chi^2 = 3.60$	

Table 5.9 Refined atomic coordinates, thermal parameters and occupancies for $\text{Ba}_2\text{Zn}_{0.75}\text{Fe}_{0.25}\text{S}_3$ from neutron diffraction data at 5 K

Atom	x	y	z	U	F
Ba1	0.82649(9)	0.48276(8)	0.25	0.0015(1)	1
Ba2	0.48900(8)	0.67375(8)	0.25	0.0005(1)	1
Zn	0.74624(9)	0.19832(7)	0.25	0.0022(1)	0.75
Fe	0.74624(9)	0.19832(7)	0.25	0.0022(1)	0.25
S1	0.8657(1)	0.0527(1)	0.25	0.0019(3)	1
S2	0.5579(1)	0.1416(2)	0.25	0.0035(3)	1
S3	0.2244(1)	0.7072(1)	0.25	0.0014(2)	1
$R_p = 2.20\%$			$R_{wp} = 0.99\%$	$\chi^2 = 1.72$	

Table 5.10 Refined atomic coordinates, thermal parameters and occupancies for $\text{Ba}_2\text{Zn}_{0.5}\text{Fe}_{0.5}\text{S}_3$ from neutron diffraction data at room temperature

Atom	x	y	z	U	F
Ba1	0.82697(8)	0.48167(7)	0.25	0.0077(2)	1
Ba2	0.48904(8)	0.67411(7)	0.25	0.0056(1)	1
Zn	0.74548(7)	0.19823(5)	0.25	0.0093(1)	0.5
Fe	0.74548(7)	0.19823(5)	0.25	0.0077(1)	0.5
S1	0.8661(1)	0.0525(1)	0.25	0.0072(3)	1
S2	0.5595(1)	0.1407(1)	0.25	0.0057(3)	1
S3	0.2248(1)	0.7095(1)	0.25	0.0058(3)	1
$R_p = 5.34\%$			$R_{wp} = 2.15\%$	$\chi^2 = 2.41$	

Table 5.11 Refined atomic coordinates, thermal parameters and occupancies for $\text{Ba}_2\text{Zn}_{0.5}\text{Fe}_{0.5}\text{S}_3$ from neutron diffraction data at 5 K

Atom	x	y	z	U	F
Ba1	0.82679(9)	0.48205(8)	0.25	0.0016(1)	1
Ba2	0.48889(9)	0.67352(8)	0.25	0.0016(2)	1
Zn	0.74589(8)	0.19870(6)	0.25	0.0013(1)	0.5
Fe	0.74589(8)	0.19870(6)	0.25	0.0013(1)	0.5
S1	0.8655(1)	0.0526(1)	0.25	0.0023(3)	1
S2	0.5585(1)	0.1410(2)	0.25	0.0027(3)	1
S3	0.2247(1)	0.7086(1)	0.25	0.0017(3)	1
$R_p = 1.93\%$		$R_{wp} = 0.84\%$		$\chi^2 = 1.21$	

Table 5.12 Refined atomic coordinates, thermal parameters and occupancies for $\text{Ba}_2\text{Zn}_{0.25}\text{Fe}_{0.75}\text{S}_3$ from neutron diffraction data at room temperature

Atom	x	y	z	U	F
Ba1	0.8292(2)	0.4809(2)	0.25	0.0092(5)	1
Ba2	0.4892(2)	0.6702(2)	0.25	0.0064(4)	1
Zn	0.7475(2)	0.1971(1)	0.25	0.0065(3)	0.25
Fe	0.7475(2)	0.1971(1)	0.25	0.0065(3)	0.75
S1	0.8665(3)	0.0502(3)	0.25	0.0024(3)	1
S2	0.5590(3)	0.1418(4)	0.25	0.0024(3)	1
S3	0.2313(3)	0.7103(3)	0.25	0.0024(3)	1
$R_p = 4.88\%$		$R_{wp} = 2.74\%$		$\chi^2 = 5.71$	

Table 5.13 Refined atomic coordinates, thermal parameters and occupancies for $\text{Ba}_2\text{Zn}_{0.25}\text{Fe}_{0.75}\text{S}_3$ from neutron diffraction data at 5 K

Atom	x	y	z	U	F
Ba1	0.8275(2)	0.4818(2)	0.25	0.0015(3)	1
Ba2	0.4887(2)	0.6710(2)	0.25	0.0009(3)	1
Zn	0.7473(2)	0.1982(1)	0.25	0.007(2)	0.25
Fe	0.7473(2)	0.1982(1)	0.25	0.0002(2)	0.75
S1	0.8663(4)	0.0498(3)	0.25	0.001	1
S2	0.5585(3)	0.1419(4)	0.25	0.001	1
S3	0.2284(3)	0.7087(3)	0.25	0.001	1
$R_p = 2.31\%$		$R_{wp} = 1.16\%$		$\chi^2 = 2.46$	

5.2.2.2 $\text{Ba}_2\text{Zn}_{1-x}\text{Mn}_x\text{S}_3$ ($x = 0.25, 0.5$)

Analysis of the unit cell parameters from Rietveld refinement against the data for $\text{Ba}_2\text{Zn}_{1-x}\text{Mn}_x\text{S}_3$ ($x = 0.25, 0.5$) show that an increase in all parameters occurs as the amount of Mn is increased and this is expected as Mn^{2+} (0.66 Å for tetrahedral coordination) has a larger effective ionic radius than Zn^{2+} (0.60 Å for tetrahedral coordination) (table 5.14 and 5.15). The TM-S bond lengths all increase as the amount of manganese present increases and analysis of the angles in the TMS_4 tetrahedra suggest a slight lessening of the distortion as the amount of manganese increases. An example refinement is shown in figure 5.6 with the atomic coordinates shown in tables 5.14-5.19 with all other refinements shown in Appendix 7.

Table 5.14 Unit cell parameters from Rietveld refinement against neutron diffraction data at room temperature

x	a (Å)	b (Å)	c (Å)	Volume (Å ³)
0.25	8.7846(2)	4.2619(1)	17.0295(4)	637.58(2)
0.5	8.79475(8)	4.27619(4)	17.0480(2)	641.14(1)

Table 5.15 Unit cell parameters from Rietveld refinement against neutron diffraction data at 5 K

x	a (Å)	b (Å)	c (Å)	Volume (Å ³)
0.25	8.7636(2)	4.2515(1)	16.9948(4)	633.20(2)
0.5	8.7764(2)	4.2680(1)	17.0170(4)	637.42(3)

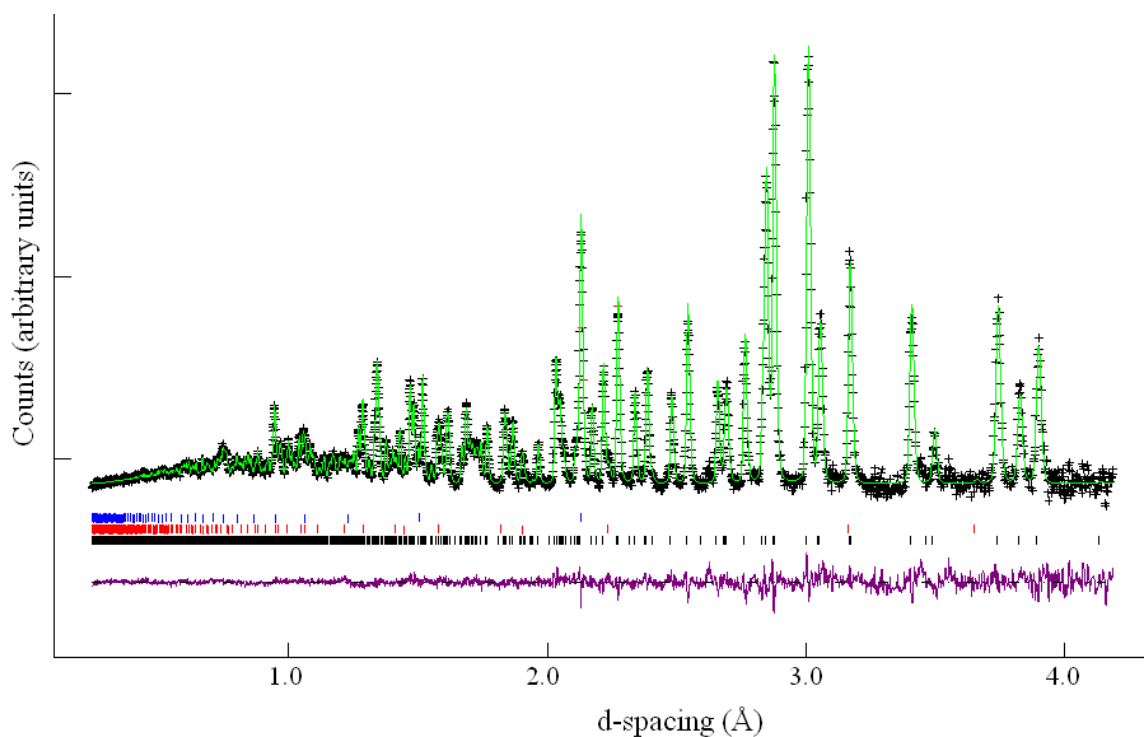


Figure 5.6 Rietveld refinement against neutron diffraction data for Ba₂Zn_{0.5}Mn_{0.5}S₃ at 5 K: Black line (observed), green line (calculated) and purple line (difference). Black tick marks correspond to Ba₂Zn_{0.5}Mn_{0.5}S₃ black to Ba₂SiS₄ and red to BaS

Table 5.16 Refined atomic coordinates, thermal parameters and occupancies for $\text{Ba}_2\text{Zn}_{0.75}\text{Mn}_{0.25}\text{S}_3$ from neutron diffraction data at room temperature

Atom	x	y	z	U	F
Ba1	0.4197(2)	0.25	0.7138(1)	0.0087(3)	1
Ba2	0.2551(2)	0.25	0.4562(1)	0.0098(4)	1
Zn	0.3668(3)	0.25	0.1365(2)	0.0081(5)	0.75
Mn	0.3668(3)	0.25	0.1365(2)	0.0081(5)	0.25
S1	0.3209(4)	0.25	0.2707(2)	0.0079(3)	1
S2	0.1273(4)	0.25	0.0726(2)	0.0079(3)	1
S3	1.0023(5)	0.25	0.6036(2)	0.0079(3)	1
$R_p = 5.58\%$		$R_{wp} = 3.49\%$		$\chi^2 = 5.96$	

Table 5.17 Refined atomic coordinates, thermal parameters and occupancies for $\text{Ba}_2\text{Zn}_{0.75}\text{Mn}_{0.25}\text{S}_3$ from neutron diffraction data at 5 K

Atom	x	y	z	U	F
Ba1	0.4205(2)	0.25	0.7141(1)	0.0015(2)	1
Ba2	0.2554(2)	0.25	0.4565(1)	0.0011(2)	1
Zn	0.3643(3)	0.25	0.1352(1)	0.0009(3)	0.75
Mn	0.3643(3)	0.25	0.1352(1)	0.0009(3)	0.25
S1	0.3194(3)	0.25	0.2714(2)	0.0021(2)	1
S2	0.1244(4)	0.25	0.0725(2)	0.0021(2)	1
S3	1.0048(4)	0.25	0.6032(2)	0.0021(2)	1
$R_p = 2.14\%$		$R_{wp} = 1.19\%$		$\chi^2 = 2.53$	

Table 5.18 Refined atomic coordinates, thermal parameters and occupancies for Ba₂Zn_{0.5}Mn_{0.5}S₃ from neutron diffraction data at room temperature

Atom	x	y	z	U	F
Ba1	0.41887(9)	0.25	0.71359(4)	0.0068(2)	1
Ba2	0.25746(9)	0.25	0.45600(4)	0.0090(2)	1
Zn	0.3530(4)	0.25	0.1356(2)	0.0034(5)	0.5
Fe	0.3530(4)	0.25	0.1356(2)	0.0036(5)	0.5
S1	0.3189(1)	0.25	0.27156(7)	0.0050(2)	1
S2	0.1277(1)	0.25	0.07246(8)	0.0050(2)	1
S3	1.0044(1)	0.25	0.60108(7)	0.0050(3)	1
$R_p = 3.43\%$		$R_{wp} = 1.69\%$		$\chi^2 = 1.11$	

Table 5.19 Refined atomic coordinates, thermal parameters and occupancies for Ba₂Zn_{0.5}Mn_{0.5}S₃ from neutron diffraction data at 5 K

Atom	x	y	z	U	F
Ba1	0.4194(2)	0.25	0.7141(1)	0.0006(2)	1
Ba2	0.2578(1)	0.25	0.4562(1)	0.0010(2)	1
Zn	0.3584(6)	0.25	0.1364(3)	0.0010(5)	0.5
Mn	0.3584(5)	0.25	0.1364(3)	0.0010(5)	0.5
S1	0.3195(3)	0.25	0.2715(1)	0.0023(3)	1
S2	0.1261(2)	0.25	0.0723(1)	0.0009(3)	1
S3	1.0019(3)	0.25	0.6007(1)	0.0052(4)	1
$R_p = 1.78\%$		$R_{wp} = 0.79\%$		$\chi^2 = 1.03$	

5.2.2.3 Ba₂Zn_{0.75}Cr_{0.25}S₃

It is very unusual for Cr²⁺ (d⁴) to be present in tetrahedral coordination and as such neutron diffraction is a very valuable tool to ensure that chromium is indeed present in the sample. Analysis of the occupancies for this sample, particularly in the low temperature study where the data are of better quality, suggests that this is the case (table 5.21). The unit cell parameters are very similar to those for Ba₂ZnS₃ and although there is no literature value for the atomic radius of Cr²⁺ in a tetrahedral environment there is some evidence that it does exist, can be formed in highly reducing environments and has a similar ionic radius to Zn²⁺.^{138,139} Most commonly in reported cases of tetrahedral Cr²⁺ it is reported in distorted tetrahedral environments and analysis of the bond lengths and angles from neutron diffraction data in this work suggest that Cr²⁺ is in a distorted tetrahedral environment comparable to that of Ba₂CoS₃. Comparison between PND data at room and low temperature does not suggest the presence of any magnetic or crystal superstructure. An example refinement is shown in figure 5.7 with the atomic coordinates shown in tables 5.21-5.22 with all other refinements shown in Appendix 8.

Table 5.20 Unit cell parameters from Rietveld refinement against neutron diffraction for Ba₂Zn_{0.75}Cr_{0.25}S₃ at room temperature and 5 K

	a (Å)	b (Å)	c (Å)	Volume (Å ³)
Room T	12.0152(3)	12.6018(3)	4.2129(1)	637.88(3)
5 K	11.9883(3)	12.5758(3)	4.2002(1)	633.23(3)

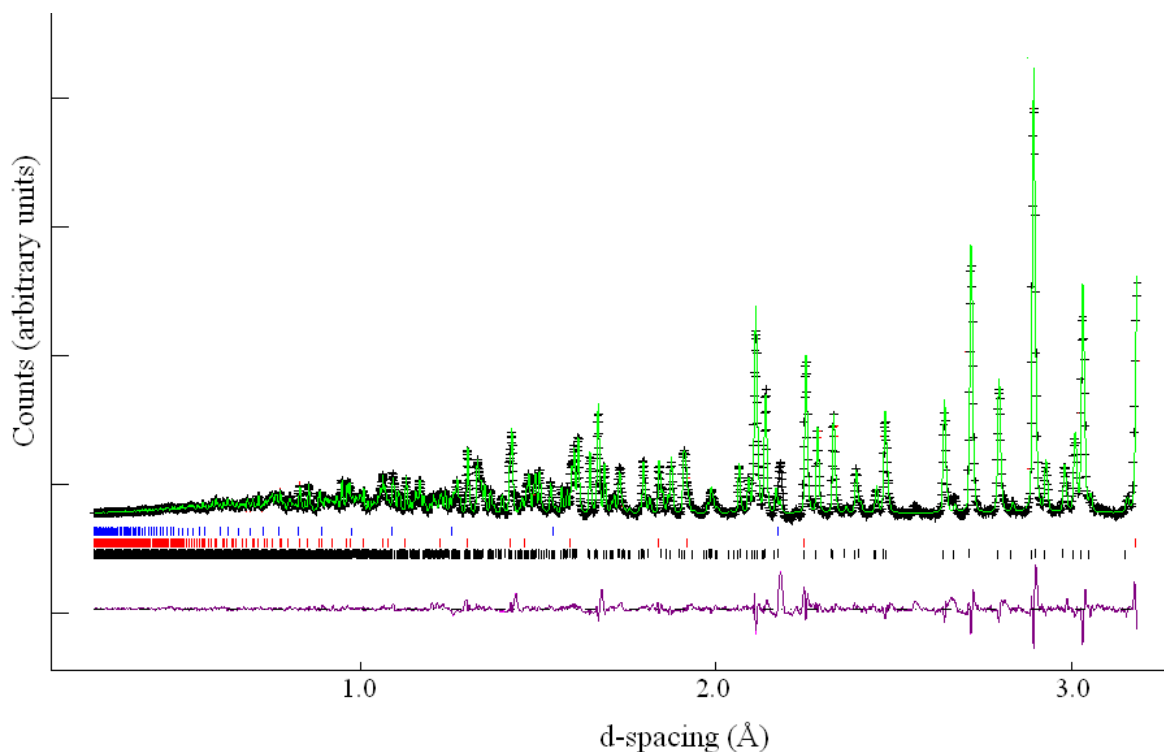


Figure 5.7 Rietveld refinement against neutron diffraction data for $\text{Ba}_2\text{Zn}_{0.75}\text{Cr}_{0.25}\text{S}_3$ at 5 K: Black line (observed), green line (calculated) and purple line (difference). Black tick marks correspond to $\text{Ba}_2\text{Zn}_{0.75}\text{Cr}_{0.25}\text{S}_3$ black to Ba_2SiS_4 and red to BaS

Table 5.21 Refined atomic coordinates, thermal parameters and occupancies for $\text{Ba}_2\text{Zn}_{0.75}\text{Cr}_{0.25}\text{S}_3$ from neutron diffraction data at room temperature

Atom	x	y	z	U	F
Ba1	0.8281(1)	0.4830(1)	0.25	0.0101(3)	1
Ba2	0.4892(1)	0.6728(1)	0.25	0.0093(3)	1
Zn	0.7463(1)	0.1972(1)	0.25	0.0057(3)	0.75
Cr	0.7463(1)	0.1972(1)	0.25	0.0135(6)	0.25
S1	0.8657(2)	0.05231(2)	0.25	0.0135(6)	1
S2	0.5564(2)	0.1406(2)	0.25	0.0103(5)	1
S3	0.2258(2)	0.7062(2)	0.25	0.0116(6)	1
$R_p = 5.47\%$		$R_{wp} = 3.03\%$		$\chi^2 = 4.42$	

Table 5.22 Refined atomic coordinates, thermal parameters and occupancies for Ba₂Zn_{0.75}Cr_{0.25}S₃ from neutron diffraction data at 5 K

Atom	x	y	z	U	F
Ba1	0.8271(1)	0.4833(1)	0.25	0.0013(2)	1
Ba2	0.4884(1)	0.6729(1)	0.25	0.0020(2)	1
Zn	0.7464(1)	0.1979(1)	0.25	0.0021(2)	0.75
Cr	0.7464(1)	0.1979(1)	0.25	0.0022(4)	0.25
S1	0.8651(2)	0.0519(2)	0.25	0.0023(4)	1
S2	0.5564(2)	0.1413(3)	0.25	0.0036(4)	1
S3	0.2254(2)	0.7070(2)	0.25	0.0036(4)	1
R _p = 2.21%		R _{wp} = 1.09%		χ ² = 2.01	

5.2.2.4 Ba₂Zn_{0.75}Ni_{0.25}S₃

Rietveld refinement against the neutron diffraction data gives unit cell parameters of $a = 12.0049(3)$ Å, $b = 12.5658(4)$ Å, $c = 4.2166(1)$ Å and a volume = $636.07(4)$ Å³ which is very similar to that obtained from PXRD. The refinement against bank 2 is shown in figure 5.8 with the atomic coordinates and fitting parameters in table 5.23 and the other banks shown in Appendix 9. The fraction of nickel in the sample refines to a lower value than that expected from the stoichiometry of the starting material suggesting that there is a low limit of the amount of nickel which can be incorporated into the Ba₂ZnS₃ structure although further experiments would be required to confirm this. However, no nickel containing impurity has been identified. Although it is unusual for Ni²⁺ d⁸ to form tetrahedral complexes it does occur with ligands low in the spectrochemical series such as S²⁻ and with bulky ligands, as in this case where the rest of the crystal is effectively the ligand.

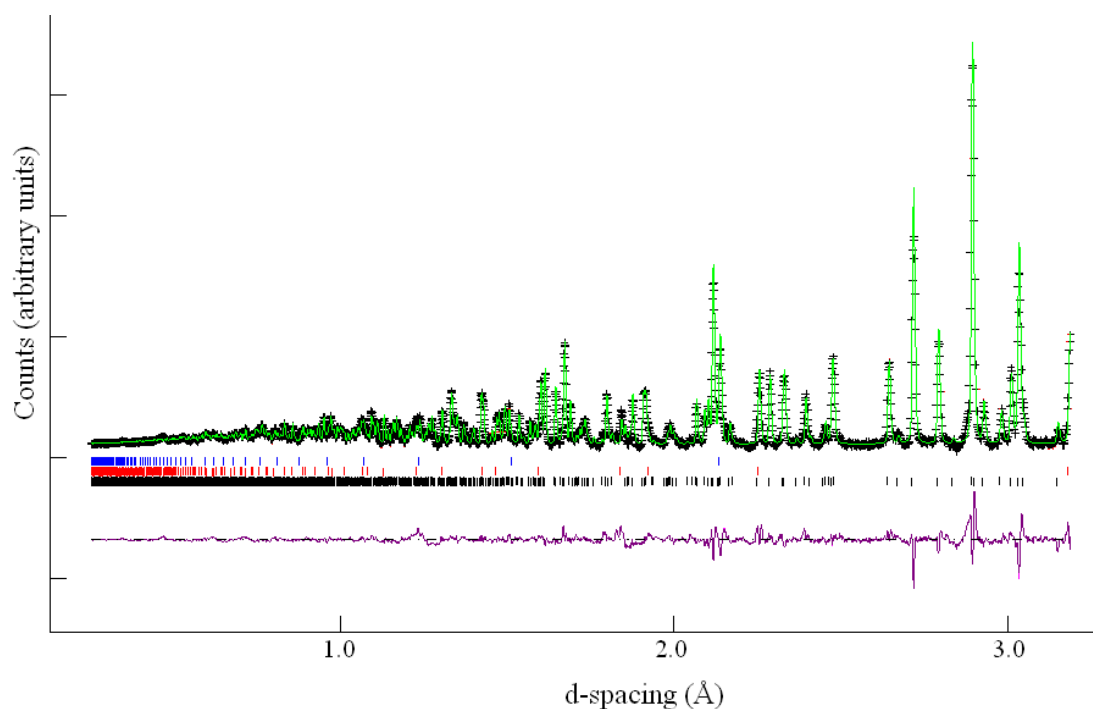


Figure 5.7 Rietveld refinement against neutron diffraction data for $\text{Ba}_2\text{Zn}_{0.75}\text{Ni}_{0.25}\text{S}_3$ at 5 K: Black line (observed), green line (calculated) and purple line (difference). Black tick marks correspond to $\text{Ba}_2\text{Zn}_{0.75}\text{Ni}_{0.25}\text{S}_3$ black to Ba_2Si_4 and red to BaS

Table 5.23 Refined atomic coordinates, thermal parameters and occupancies for $\text{Ba}_2\text{Zn}_{0.75}\text{Ni}_{0.25}\text{S}_3$ from neutron diffraction data at room temperature

Atom	x	y	z	U	F
Ba1	0.8289(1)	0.4832(1)	0.25	0.0092(3)	1
Ba2	0.4894(2)	0.6735(2)	0.25	0.0063(3)	1
Zn	0.7477(2)	0.1979(1)	0.25	0.0076(3)	0.75
Ni	0.7477(2)	0.1979(1)	0.25	0.0076(3)	0.25
S1	0.8670(3)	0.0496(3)	0.25	0.0099(7)	1
S2	0.5591(3)	0.1418(3)	0.25	0.0107(7)	1
S3	0.2280(3)	0.7076(3)	0.25	0.0076(3)	1
$R_p = 5.73\%$		$R_{wp} = 3.36\%$		$\chi^2 = 7.52$	

5.2.3 Physical Properties

5.2.3.1 Magnetic Susceptibility

The susceptibility of $\text{Ba}_2\text{Zn}_{0.5}\text{Fe}_{0.5}\text{S}_3$ was measured using a SQUID magnetometer over the range 5-300 K using a 3 T external field (zero-field cooled). The inverse susceptibility plot is shown in figure 5.8. At temperatures above 200 K it shows the linear dependency of inverse susceptibility on temperature indicative of paramagnetic behaviour. Analysis of the straight line part of the data, from 200-300 K, using the method described in the section 3.3.2 gives values for the Curie constant of $2.38 \text{ emu}\cdot\text{mol}^{-1} \text{ K}$ and a Weiss constant of -211 K with a μ_{eff} of $4.36 \mu_{\text{B}}$. These values are all consistent with the presence of high spin Fe^{2+} in a tetrahedral environment.

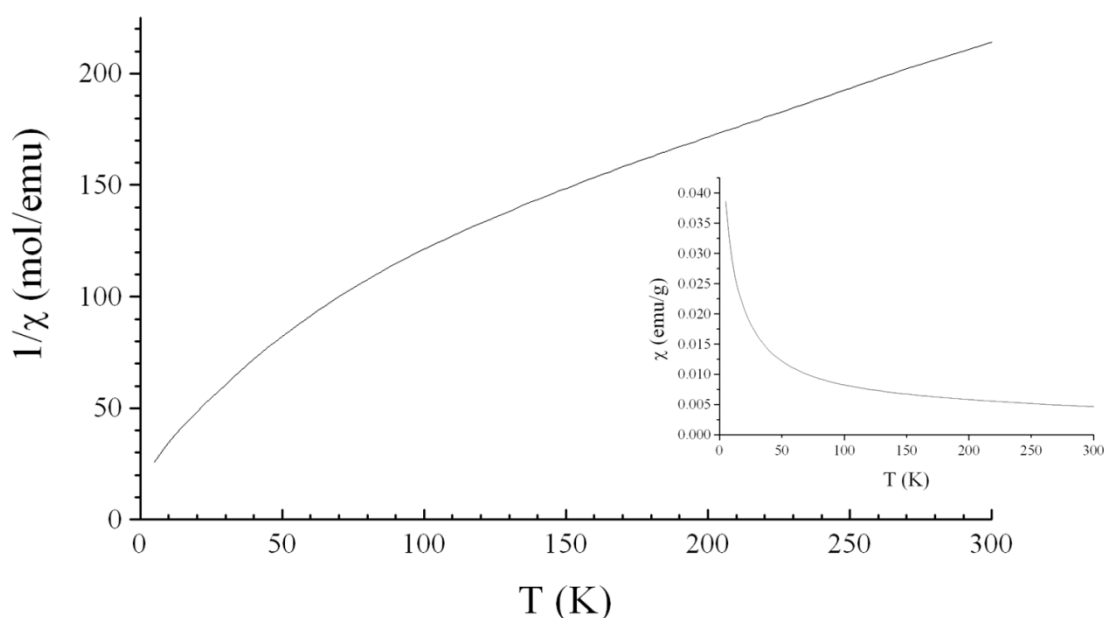


Figure 5.8 Inverse susceptibility plot of $\text{Ba}_2\text{Zn}_{0.5}\text{Fe}_{0.5}\text{S}_3$ with susceptibility versus temperature shown in insert

5.2.3.2 Transport Properties

The magnetoresistance of two $\text{Ba}_2\text{Zn}_{0.75}\text{Cr}_{0.25}\text{S}_3$ and $\text{Ba}_2\text{Zn}_{0.5}\text{Mn}_{0.5}\text{S}_3$ has been measured and provides further evidence of an extrinsic contribution to the magnetoresistance in these materials. $\text{Ba}_2\text{Zn}_{0.5}\text{Mn}_{0.5}\text{S}_3$ shows a magnetoresistance of around -3% at 5 K (figure 5.9) and $\text{Ba}_2\text{Zn}_{0.75}\text{Cr}_{0.25}\text{S}_3$ shows an even higher value of around 10% (figure 5.10). These compounds have very different electronic structures to that found in Ba_2CoS_3 and show high and unexpected values of MR.

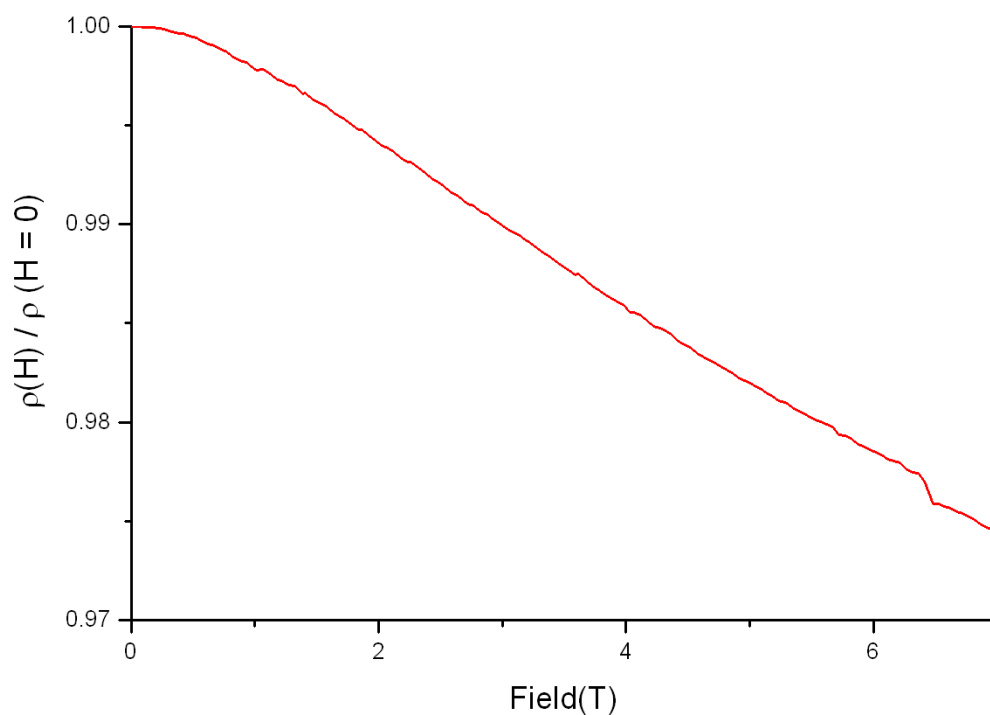


Figure 5.9 Isothermal resistivity curve of $\text{Ba}_2\text{Zn}_{0.5}\text{Mn}_{0.5}\text{S}_3$ measured at 5 K

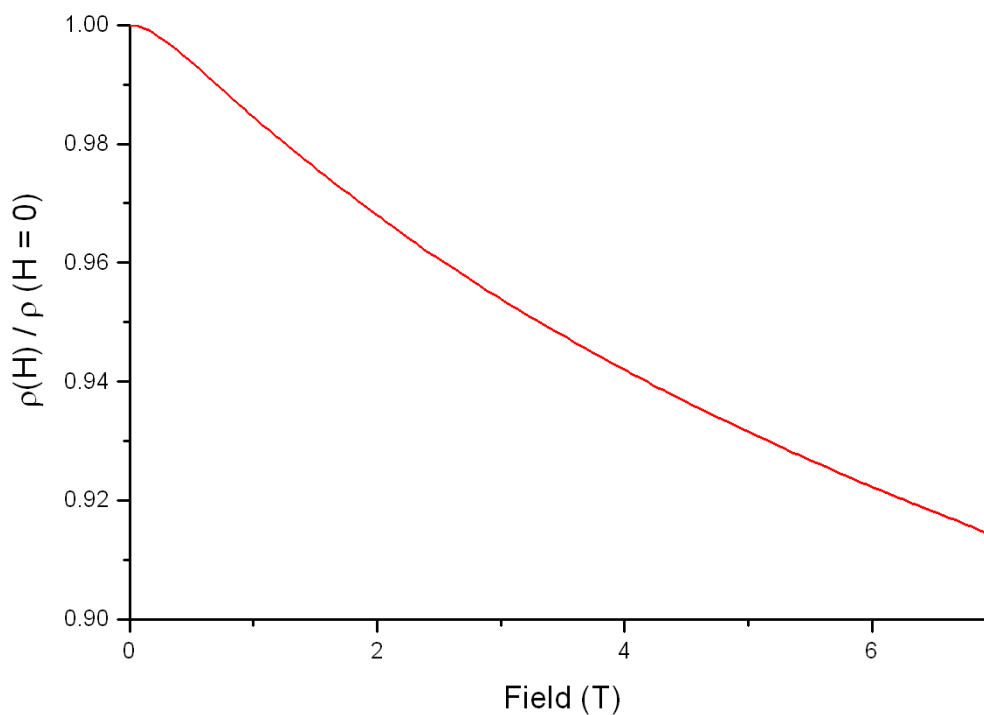


Figure 5.10 Isothermal resistivity curve of $\text{Ba}_2\text{Zn}_{0.5}\text{Cr}_{0.5}\text{S}_3$ measured at 5 K

5.2.4 Conclusions

A wide range of new one-dimensional sulphides, with general formula $\text{Ba}_2\text{Zn}_{1-x}\text{TM}_x\text{S}_3$ have been synthesised. A full solid solution for $\text{Ba}_2\text{Zn}_{1-x}\text{Fe}_x\text{S}_3$ has been prepared where this did not prove possible for $\text{Ba}_2\text{Co}_{1-x}\text{Fe}_x\text{S}_3$. The series $\text{Ba}_2\text{Zn}_{1-x}\text{Mn}_x\text{S}_3$ showed a Ba_2MnS_3 type structure, previously not seen for the Ba_2ZnS_3 . $\text{Ba}_2\text{Zn}_{1-x}\text{TM}_x\text{S}_3$ with $\text{TM} = \text{Ni}$ and $x = 0.25$ and $\text{Ba}_2\text{Zn}_{1-x}\text{TM}_x\text{S}_3$ with $\text{TM} = \text{Cr}$ and $x = 0.25, 0.50$ were also prepared. The $\text{Ba}_2\text{Zn}_{1-x}\text{Cr}_x\text{S}_3$ samples seem to contain Cr^{2+} in a distorted tetrahedral environment. These factors all point to an increased flexibility of zinc over cobalt in forming these materials. A limited analysis has been performed on some of the physical properties of the materials in these series which shows that they exhibit significant levels of magnetoresistance which requires further investigation.

6.0 Ba_{2-y}A_yCoS₃ (A = Ca, Mg, Sr, K)

6.1 Synthesis and Characterisation

As well as substituting other transition metals for cobalt attempts were also made to perform isovalent and aliovalent substitutions on the barium site. Initially isovalent substitutions were tried using other group 2 elements magnesium, calcium, and strontium. After this an aliovalent substitution was tried using potassium which has a similar ionic radius (1.46 Å, 7 coordinate, 1⁺) to barium (1.38 Å, 7 coordinate, 2⁺) to try to induce some mixed valency in the cobalt.¹³¹ The synthesis of the ternary sulphides Ba_{2-y}A_yCoS₃ (A = Ca, Mg, Sr, K) was performed *via* a solid-gas reaction as discussed in the Experimental section 2.1. Stoichiometric mixtures of barium carbonate (99%) cobalt (99.8%) and carbonates of calcium (99%), magnesium (98%), strontium (98%) or potassium (99.8%) were reacted with carbon disulphide (99%) for 24 hours at 1000°C. PXRD was carried out on all samples and powder neutron diffraction data were then collected for Ba_{1.9}K_{0.1}CoS₃ at room temperature for approximately 4 hours.

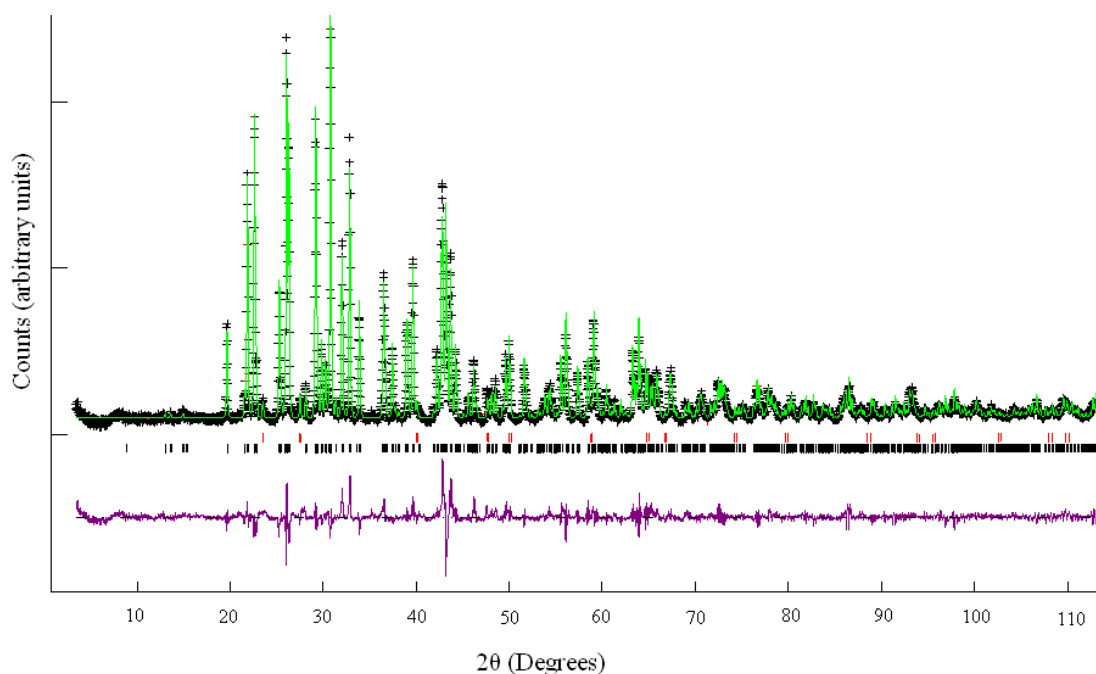
6.3 Results and Discussion

6.1.1 Powder X-ray Diffraction (PXRD)

The only sample that could be successfully synthesised was Ba_{1.9}K_{0.1}CoS₃. A small impurity of BaS was found (~1%) in the samples and could not be eliminated upon further heating. By comparison, the PXRD pattern showed that Ba_{1.9}K_{0.1}CoS₃ maintains the one-dimensional structure of Ba₂CoS₃. Rietveld refinements were then performed and the phase fraction, zero point, cell parameters, atomic position parameters, background (a linear interpolation function) and peak profile (~3 terms of the pseudo-Voigt) were all refined. It was not possible to refine the occupancies or atomic thermal parameters. The refinement is shown in figure 6.1 with the refined atomic coordinates in table 6.1, the unit cell parameters refined to a = 12.0033(2) Å, b = 12.4801(2) Å, and c = 4.20166(6) Å, volume = 629.42(2) Å³ with fitting parameters $\chi^2 = 7.74$, Rp = 5.66% and Rwp = 7.57%.

Table 6.1 Refined atomic coordinates for Ba_{1.9}K_{0.1}CoS₃ from PXRD data

Atom	x	y	z	U	F
Ba1	0.8277(2)	0.4798(2)	0.25	0.0097(4)	1
Ba2	0.4886(2)	0.6726(2)	0.25	0.0064(3)	1
Co	0.7494(4)	0.1996(3)	0.25	0.0059(6)	1
S1	0.8651(3)	0.0541(3)	0.25	0.0123(8)	1
S2	0.5617(2)	0.1407(3)	0.25	0.0047(6)	1
S3	0.2263(3)	0.7122(2)	0.25	0.0034(5)	1

**Figure 6.1** Rietveld refinement against X-ray diffraction data for Ba_{1.9}K_{0.1}CoS₃: Black line (observed), green line (calculated) and purple line (difference). Black tick marks correspond to Ba_{1.9}K_{0.1}CoS₃ and red to BaS

6.1.2 Neutron Powder Diffraction (NPD)

Neutron diffraction data were collected on the Polaris beamline at ISIS at room temperature. Three detection banks were used and all three histograms produced were analysed simultaneously using Rietveld refinement with the software GSAS in conjunction with EXPGUI.^{121,122}

The structure of Ba₂CoS₃ was chosen as the starting model and the phase fraction, zero point, cell parameters, atomic position parameters background (a linear interpolation function) peak profile (~3 terms of the pseudo-Voigt), occupancies and atomic thermal parameters were all refined. It was not possible to refine the occupancy of potassium as it is potentially present across two crystallographic sites in only a small amount and barium and potassium have relatively similar scattering lengths (5.07 fm and 3.67 fm respectively).¹⁴⁰ It was also decided not to include potassium on the barium site for the refinements for the same reasons. Analysis showed that a small impurity of BaS is present (~1%) in the sample and there is some evidence for a poorly crystalline impurity seen in the broad peaks seen at 1.226 Å, 2.097 Å and 3.434 Å (in d-spacing). This poorly crystalline impurity could contain the excess transition metal resulting from the formation of Ba-containing impurities. The unit cell parameters refine to a = 11.9989(4) Å, b = 12.4751(4) Å, c = 4.1992(1) Å and volume = 628.56(5) Å³ and the atomic coordinates, occupancies, thermal parameters and fitting parameters are shown in table 6.2 with the refinement from bank shown in figure 6.2 and the other banks shown in Appendix 10.

Table 6.2 Refined atomic coordinates, thermal parameters and occupancies for Ba_{1.9}K_{0.1}CoS₃ from neutron diffraction data at room temperature

Atom	x	y	z	U	F
Ba1	0.8277(2)	0.4798(2)	0.25	0.0097(4)	1
Ba2	0.4886(2)	0.6726(2)	0.25	0.0064(3)	1
Co	0.7494(4)	0.1996(3)	0.25	0.0059(6)	1
S1	0.8651(3)	0.0541(3)	0.25	0.0123(8)	1
S2	0.5617(2)	0.1407(3)	0.25	0.0047(6)	1
S3	0.2263(3)	0.7122(2)	0.25	0.0034(5)	1
R _p = 2.98%		R _{wp} = 1.45%		χ ² = 0.83	

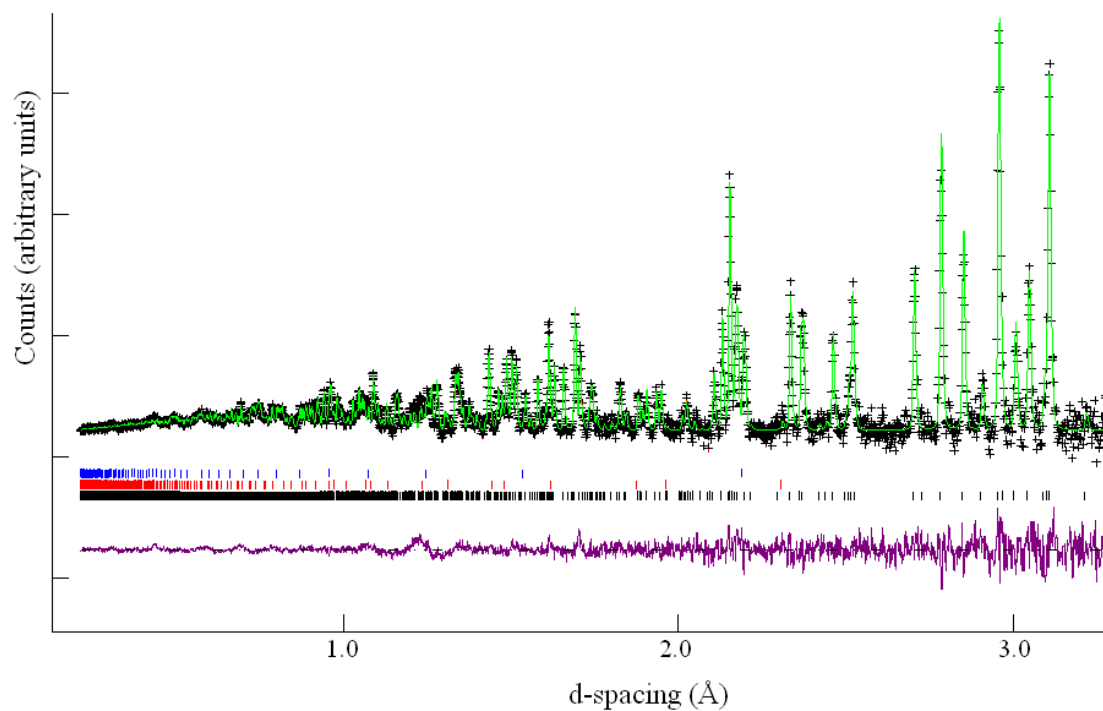


Figure 6.2 Rietveld refinement against neutron diffraction data for $\text{Ba}_{1.9}\text{K}_{0.1}\text{CoS}_3$: Black line (observed), green line (calculated) and purple line (difference). Black tick marks correspond to $\text{Ba}_{1.9}\text{K}_{0.1}\text{CoS}_3$ red to BaS and blue to BaS

7.0 Overall Conclusions

The synthesis of a variety of compounds based on Ba_2CoS_3 has been successfully achieved and investigations into their properties carried out.

A complete solid solution has been found for $\text{Ba}_2\text{Co}_{1-x}\text{Zn}_x\text{S}_3$ and the properties studied. X-ray, neutron diffraction, EXAFS and TEM studies have shown that the zinc and cobalt are randomly distributed throughout the materials. This random distribution of the zinc and cobalt throughout the materials is important to note as not all materials show this, for example in the series $(2\text{ZnX})_x(\text{CuInX}_2)_{1-x}$ with $\text{X} = \text{S}, \text{Se}, \text{Te}$ the zinc is shown to be non-statistically distributed in the materials.¹⁴¹ The distribution of the non-magnetic zinc throughout the material will clearly have an effect on the properties. Substitution of zinc for cobalt in Ba_2CoS_3 suppresses the metallic-like behaviour in favour of a semiconducting behaviour with variable range hopping as the method of conduction. Substitution of zinc for cobalt in Ba_2CoS_3 also suppresses one dimensional anti-ferromagnetism in favour of paramagnetic behaviour, with a Zn content above 40% shown to eliminate any residual antiferromagnetic behaviour. All the members of the series show significant values for magnetoresistance with a maximum value of $\sim -25\%$ for $\text{Ba}_2\text{Co}_{0.4}\text{Zn}_{0.6}\text{S}_3$. The origin of the magnetoresistance is currently unknown although it is suspected that the phenomenon is due partially to extrinsic factors such as grain size, grain contact and density.

The gradual decrease of MR with temperature along with studies into the low temperature neutron diffraction data excludes any structural or electronic transitions as the origin of this phenomenon in $\text{Ba}_2\text{Co}_{1-x}\text{Zn}_x\text{S}_3$ as it is in the vast majority of magnetoresistive materials. In addition the analysis of the susceptibility comparing field-cooled and non field-cooled measurements has shown that the materials do not exhibit spin-glass behaviour as in some magnetoresistive materials. There are a number of materials which exhibit extrinsic magnetoresistance, many of which are either thin films or nano particles. The ability to alter the amount of magnetoresistance in a material by altering the bulk structure has been observed in a variety of doped lanthanum manganites.¹⁴² In $\text{La}_{0.7}\text{Ca}_{0.3}\text{MnO}_3$ and also Fe_3O_4 the magnetoresistance of the materials is enhanced by the introduction of scattering interfaces by forming them into thin films.¹⁴³ As described in the introduction magnetoresistance in the manganites is accompanied by a metal-insulator transition and is due to double exchange. Forming

them into thin films adds an element of tunnelling magnetoresistance at the grain boundaries augmenting the double exchange type magnetoresistance within the grains. The tunnelling magnetoresistance is shown by anomalies in the measurements of resistance versus applied magnetic field at low temperature. In the manganites the extent of magnetoresistance can also be altered by altering the sintering conditions.¹⁴⁴ A similar effect has also been seen in chromium oxide which exhibits increased magnetoresistance as a polycrystalline material with the inter-granular resistance playing an important part. Extrinsic magnetoresistance has so far mostly been ascribed to surface interactions in spin polarised materials (or 'half metals') and there are two theories about the effects occurring at the surface which leads to the magnetoresistance, either spin dependent scattering or tunnelling magnetoresistance.

Within the $\text{Ba}_2\text{Co}_{1-x}\text{Fe}_x\text{S}_3$ series, only the compound $\text{Ba}_2\text{Co}_{0.75}\text{Fe}_{0.25}\text{S}_3$ has been successfully synthesised and attempts to increase the amount of iron in the compound were not successful. Substitution of Fe for Co in Ba_2CoS_3 leads to loss of metallic-like behaviour in favour of semiconducting behaviour and as with the $\text{Ba}_2\text{Co}_{1-x}\text{Zn}_x\text{S}_3$ series the conduction is shown to be *via* variable range hopping. As discussed in the introduction there are a wide variety of known one-dimensional sulfides containing iron, and the end member Ba_2FeS_3 is also known. Although it is the first time that a compound from the Ba_2CoS_3 - Ba_2FeS_3 solid solution has been prepared it is somewhat surprising that only low levels of substitution could be achieved for $\text{Ba}_2\text{Co}_{1-x}\text{Fe}_x\text{S}_3$. Alternative synthesis techniques such as using binary sulfide starting materials may be able to increase this and in other materials high temperature sintering has been seen to increase the stability of solid solutions.¹⁴⁵

Ba_2ZnS_3 was also used as starting point and a large number of compounds in the series $\text{Ba}_2\text{Zn}_{1-x}\text{M}_x\text{S}_3$ ($\text{M} = \text{Fe}, \text{Mn}, \text{Cr}, \text{Ni}$) have also been synthesised. Ba_2ZnS_3 seems to show better structural flexibility than Ba_2CoS_3 considering the large variety of compounds derived *via* partial substitution of zinc. This includes initial investigations which show chromium in tetrahedral coordination to sulfur within the compounds, which is a very unusual configuration for chromium. The structure of the series $\text{Ba}_2\text{Zn}_{1-x}\text{Mn}_x\text{S}_3$ is also unusual as these compounds form the Ba_2MnS_3 type structure, previously not seen for the Ba_2ZnS_3 . Initial investigations into the transport properties of these materials show that they may exhibit low levels of negative magnetoresistance.

Finally, $\text{Ba}_{0.9}\text{K}_{0.1}\text{CoS}_3$ has been synthesised although no investigation into the properties has yet been carried out. Attempts to substitute other metals for barium were not successful.

Previously there has been little work performed on one-dimensional sulfides containing zinc as it generally does not produce many interesting or technologically useful properties due to its d^{10} configuration. This work has shown that by including it along with other transition metals the properties of the original material can be altered not only in the ways expected (i.e. forming paramagnetic materials) but also in unexpected ways, i.e. increasing the negative magnetoresistance. The work has also shown that a wide variety of compounds can be formed within this class of materials and that there is a great deal of flexibility within the structure of Ba_2MS_3 to incorporate different transition metals.

8.0 Further Work

Some of the compounds synthesised have not yet been fully investigated in terms of their physical properties and this would be a first step towards an understanding of the origins of the magnetoresistance in these compounds. In addition, varying the synthetic conditions and analysing the macrostructure of the products to see how this affects the properties would be worthwhile as it would help in understanding the extrinsic properties of the materials that may be giving rise to the magnetoresistance. It is also worth exploring more new compounds by performing further substitutions, for example mercury and rhodium for cobalt/zinc as the compounds Ba_2HgS_3 and Ba_2RhS_3 are known and could therefore be used as end members of new solid solutions. It may also be worthwhile to explore new compositions by performing substitutions on the Ba site, as the preliminary work reported here has shown.

9.0 References

- (1) Martin, D. H. *Magnetism in Solids*; Iliffe Books, 1967.
- (2) Smart, L. E.; Moore, E. A. *Solid State Chemistry: An Introduction*; Chapman and Hall, 1992.
- (3) Dejongh, L. J.; Miedema, A. R. *Advances in Physics* **1974**, *23*, 1-260.
- (4) Carlin, R. L. *J. Chem. Educ.* **1991**, *68*, 361-364.
- (5) Onnes, H. K. *Akad. Van Wetenschappen* **1901**, *14*, 113.
- (6) Poole, C. P.; al., e. *Superconductivity* San Diego, 1998.
- (7) Bardeen, J.; Cooper, L.; Schrieffer, J. R. *Phys. Rev. Lett.* **1957**, *108*, 1175.
- (8) Putilin, S. N.; Antipov, E. V.; Chmainssenn, O.; Mareezio, M. *Nature (London)* **1993**, *362*, 226.
- (9) Thompson, W. *Proc. R. Soc. London* **1857**, *A8*, 546-550.
- (10) Campbell, I. A.; Fert, A.; Jaoul, O. *Journal of Physics Part C Solid State Physics* **1970**, *3*, S95-&.
- (11) Wisniewski, P. *Appl. Phys. Lett.* **2007**, *90*.
- (12) Mott, N. F. *Proc. R. Soc. London, A* **1929**, *124*, 425-442.
- (13) Thompson, S. M. *J. Phys. D: Appl. Phys.* **2008**, *41*.
- (14) Binasch, G.; Grünberg, P.; Saurenbach, F.; Zinn, W. *Phys. Rev. B* **1989**, *39*, 4828-4830.
- (15) Baibich, M. N.; Broto, J. M.; Fert, A.; Vandau, F. N.; Petroff, F.; Eitenne, P.; Creuzet, G.; Friederich, A.; Chazelas, J. *Phys. Rev. Lett.* **1988**, *61*, 2472-2475.
- (16) Xiao, J. Q.; Jiang, J. S.; Chien, C. L. *Phys. Rev. Lett.* **1992**, *68*, 3749-3752.
- (17) Julliere, M. *Phys. Lett. A* **1975**, *54*, 225-226.
- (18) Ikeda, S.; Hayakawa, J.; Ashizawa, Y.; Lee, Y. M.; Miura, K.; Hasegawa, H.; Tsunoda, M.; Matsukura, F.; Ohno, H. *Appl. Phys. Lett.* **2008**, *93*.
- (19) Ramirez, A. P. *J. Phys.: Condens. Matter* **1997**, *9*, 8171-8199.
- (20) Zener, C. *Phys. Rev. A* **1951**, *82*, 403-405.
- (21) Mathur, N. *Nature (London)* **1997**, *390*, 229-&.
- (22) Ramirez, A. P.; Cava, R. J.; Krajewski, J. *Nature (London)* **1997**, *386*, 156-159.
- (23) Gopalakrishnan, J. *Bull. Mater. Sci.* **1981**, *3*, 271-274.
- (24) Sheldrick, W. S.; Wachhold, M. *Angew. Chem., Int. Ed. Engl.* **1997**, *36*, 207-224.
- (25) Kanatzidis, M. G. *Chem. Mater.* **1990**, *2*, 353-363.
- (26) Istomin, S. Y.; Grippa, A. Y.; D'Yachenko, O. G.; Antipov, E. V.; Svensson, G.; Tholence, J. L. *Physica C* **1998**, *300*, 67-70.
- (27) Chianelli, R. R.; Siadati, M. H.; De la Rosa, M. P.; Berhault, G.; Wilcoxon, J. P.; Bearden, R.; Abrams, B. L. *Catalysis Reviews-Science and Engineering* **2006**, *48*, 1-41.
- (28) Boer, K. W. *J. Cryst. Growth* **1982**, *59*, 111-120.
- (29) Pearce, C. I.; Pattrick, R. A. D.; Vaughan, D. J. In *Sulfide Mineralogy and Geochemistry* 2006; Vol. 61, p 127-180.
- (30) de Jongh, L. J.; Miedema, A. R. *Advances in Physics* **2001**, *50*, 947-1170.
- (31) Rouxel, J. *Acc. Chem. Res.* **1992**, *25*, 328-336.
- (32) Bronger, W.; Muller, P. *J. Less Common Met.* **1984**, *100*, 241-247.

- (33) Bronger, W. *Pure Appl. Chem.* **1985**, *57*, 1363-1372.
- (34) Lu, Y.-J.; Ibers, J. A. *Comments Inorg. Chem.* **1993**, *14*, 229-243.
- (35) Mitchell, R. H.; Ross, K. C.; Potter, E. G. *J. Solid State Chem.* **2004**, *177*, 1867-1872.
- (36) Souza, A. M. C.; Neto, S. R. O.; Macedo, C. A. *J. Magn. Magn. Mater.* **2004**, *272*, 521-522.
- (37) Huster, J. Z. *Naturforsch., B: Chem. Sci.* **1980**, *35*, 775-775.
- (38) Kim, S. J.; Bae, H. S.; Yee, K. A.; Choy, J. H.; Kim, D. K.; Hur, N. H. *J. Solid State Chem.* **1995**, *115*, 427-434.
- (39) Gardner, R. A.; Vlasse, M.; Wold, A. *Inorg. Chem.* **1969**, *8*, 2784-2787.
- (40) Ghedira, M.; Chenavas, J.; Sayetat, F.; Marezio, M.; Massenet, O.; Mercier, J. *Acta Crystallogr., Sect. B* **1981**, *37*, 1491-1496.
- (41) Popovic, Z. V.; Mihaly, G.; Kezsmarki, I.; Berger, H.; Forro, L.; Moshchalkov, V. V. *Phys. Rev. B* **2002**, *65*.
- (42) Donohue, P. C.; Weiher, J. F. *J. Solid State Chem.* **1974**, *10*, 142-144.
- (43) Matsuura, K.; Wada, T.; Suzuki, N.; Nakamizo, T.; Ikegawa, S.; Yamauchi, H.; Tanaka, S. *Jpn. J. Appl. Phys., Part 1* **1990**, *29*, L473-L476.
- (44) Yan, J.; Ramanujachary, K. V.; Greenblatt, M. *Mater. Res. Bull.* **1995**, *30*, 463-469.
- (45) Kijima, N.; Morie, K.; Chikazawa, S.; Nishihara, H.; Nagata, S. *J. Solid State Chem.* **1999**, *142*, 57-62.
- (46) Matsuura, K.; Wada, T.; Nakamizo, T.; Yamauchi, H.; Tanaka, S. *Phys. Rev. B* **1991**, *43*, 13118-13123.
- (47) Itti, R.; Wada, T.; Matsuura, K.; Itoh, T.; Ikeda, K.; Yamauchi, H.; Koshizuka, N.; Tanaka, S. *Phys. Rev. B* **1991**, *44*, 2306-2312.
- (48) Wu, Y. D.; Nather, C.; Bensch, W. *J. Solid State Chem.* **2005**, *178*, 1569-1574.
- (49) Lee, C. S.; Kleinke, K. M.; Kleinke, H. *Solid State Sciences* **2005**, *7*, 1049-1054.
- (50) Okai, B.; Takahashi, K.; Saeki, M.; Yoshimoto, J. *Mater. Res. Bull.* **1988**, *23*, 1575-1584.
- (51) Meetsma, A.; Wiegers, G. A.; Deboer, J. L. *Acta Crystallogr., Sect. C* **1993**, *49*, 2060-2062.
- (52) Lelieveld, R.; Ijdo, D. J. W. *Acta Crystallogr., Sect. B* **1978**, *34*, 3348-3349.
- (53) Wiegers, G. A.; Meetsma, A.; Haange, R. J.; Deboer, J. L. *Acta Crystallogr., Sect. C* **1989**, *45*, 847-849.
- (54) Jumas, J. C.; Ribes, M.; Philippot, E.; Maurin, M. *C. R. l'Academie. Sci., Ser. III* **1972**, *275*, 267-272.
- (55) Besrest, F.; Collin, G. *J. Solid State Chem.* **1977**, *21*, 161-170.
- (56) Collin, G.; Laruelle, P. *Bulletin De La Societe Francaise Mineralogie Et De Cristallographie* **1971**, *94*, 113-&.
- (57) Collin, G.; Barthele.E; Gorochov, O. *Comptes Rendus Hebdomadaires Des Seances De L'Academie Des Sciences Serie C* **1973**, *277*, 775-778.
- (58) Plumier, R.; Sougi, M.; Collin, G. *Solid State Commun.* **1974**, *14*, 971-973.
- (59) Huster, J.; Bronger, W. *J. Less Common Met.* **1986**, *119*, 159-165.
- (60) Bronger, W. *Naturwissenschaften* **1965**, *52*, 158.
- (61) Bronger, W.; Kyas, A.; Muller, P. *J. Solid State Chem.* **1987**, *70*, 262-270.
- (62) Welz, D.; Nishi, M. *Phys. Rev. B* **1992**, *45*, 9806-9818.

- (63) Tiwary, S. K.; Vasudevan, S. *Phys. Rev. B* **1997**, *56*, 7812-7814.
- (64) Schmitz, D.; Bronger, W. *Z. Naturforsch., B: Chem. Sci.* **1975**, *30*, 491-493.
- (65) Bronger, W.; Muller, P. *J. Less Common Met.* **1980**, *70*, 253-262.
- (66) Savelsberg, G.; Schafer, H. *Z. Naturforsch., B: Chem. Sci.* **1978**, *33*, 711-713.
- (67) Klepp, K. O.; Bronger, W. *J. Less Common Met.* **1987**, *128*, 65-71.
- (68) Reiff, W. M.; Grey, I. E.; Fan, A.; Eliezer, Z.; Steinfink, H. *J. Solid State Chem.* **1975**, *13*, 32-40.
- (69) Clark, J. R.; Brown, G. E. *Am. Mineral.* **1980**, *65*, 477-482.
- (70) Reissner, M.; Steiner, W.; Wernisch, J.; Boller, H. *Hyperfine Interact.* **2006**, *169*, 1301-1304.
- (71) Anderson, J. S. *J. Chem. Soc., Dalton Trans.* **1973**, 1107-1115.
- (72) Swinnea, J. S.; Steinfink, H. *J. Solid State Chem.* **1980**, *32*, 329-334.
- (73) Onoda, M.; Kato, K. *Acta Crystallogr., Sect. B* **1991**, *47*, 630-634.
- (74) Swinnea, J. S.; Steinfink, H. *J. Solid State Chem.* **1982**, *41*, 114-123.
- (75) Ohtani, T.; Miyoshi, Y.; Fujii, Y.; Koyakumar, T.; Kusano, T.; Minami, K. *Solid State Commun.* **2001**, *120*, 95-99.
- (76) Ohtani, T.; Onoue, S. *Mater. Res. Bull.* **1986**, *21*, 69-76.
- (77) Ohtani, T.; Sano, Y.; Kodama, K.; Onoue, S.; Nishihara, H. *Mater. Res. Bull.* **1993**, *28*, 501-508.
- (78) Garg, A. B.; Vijayakumar, V.; Godwal, B. K.; Ohtani, T.; Martin, B. R.; Hochheimer, H. D. *Solid State Commun.* **2004**, *132*, 731-736.
- (79) Burschka, C. *Z. Naturforsch., B: Chem. Sci.* **1979**, *34*, 396-397.
- (80) Peplinski, Z.; Brown, D. B.; Watt, T.; Hatfield, W. E.; Day, P. *Inorg. Chem.* **1982**, *21*, 1752-1755.
- (81) Whangbo, M. H.; Canadell, E. *Inorg. Chem.* **1990**, *29*, 1395-1397.
- (82) Fukuoka, H.; Miyaki, Y.; Yamanaka, S. *J. Solid State Chem.* **2003**, *176*, 206-212.
- (83) Klepp, K. O. *Z. Naturforsch., B: Chem. Sci.* **1992**, *47*, 201-204.
- (84) Rad, H. D.; Hoppe, R. *Z. Naturforsch., B: Chem. Sci.* **1978**, *33*, 1184-1185.
- (85) Klepp, K. O. *Z. Naturforsch., B: Chem. Sci.* **1985**, *40*, 229-234.
- (86) Bronger, W.; Ruschewitz, U.; Muller, P. *J. Alloys Compd.* **1995**, *218*, 22-27.
- (87) Klepp, K.; Boller, H. *Monatsh. Chem.* **1981**, *112*, 83-89.
- (88) Welz, D.; Deppe, P.; Schaefer, W.; Sabrowsky, H.; Rosenberg, M. *J. Phys. Chem. Solids* **1989**, *50*, 297-308.
- (89) Ensling, J.; Gutlich, P.; Spiering, H.; Klepp, K. *Hyperfine Interact.* **1986**, *28*, 599-602.
- (90) Bronger, W.; Balkhardtdegen, H.; Schmitz, D. *Z. Anorg. Allg. Chem.* **1989**, *574*, 99-106.
- (91) Klepp, K. O.; Bronger, W. *Revue De Chimie Minerale* **1983**, *20*, 682-688.
- (92) Klepp, K. O.; Bronger, W. *J. Less Common Met.* **1984**, *98*, 165-172.
- (93) Bronger, W.; Bomba, C. *J. Less Common Met.* **1990**, *158*, 169-176.
- (94) Bronger, W.; Gunther, O. *J. Less Common Met.* **1972**, *27*, 73-79.
- (95) Bronger, W.; Gunther, O.; Huster, J.; Spangenberg, M. *J. Less Common Met.* **1976**, *50*, 49-55.
- (96) Springborg, M. *Chem. Phys.* **1999**, *246*, 347-361.
- (97) Grey, I. E.; Hong, H.; Steinfink, H. *Inorg. Chem.* **1971**, *10*, 340-343.

- (98) Hong, H. Y.; Steinfink, H. *J. Solid State Chem.* **1972**, *5*, 93-104.
- (99) Shoemaker, C. B. *Z. Kristallogr.* **1973**, *137*, 225-239.
- (100) Nakayama, N.; Kosuge, K.; Kachi, S.; Shinjo, T.; Takada, T. *J. Solid State Chem.* **1980**, *33*, 351-356.
- (101) Schnering, v. H. G.; Hoppe, R. *Z. Anorg. Allg. Chem.* **1961**, *312*, 99-109.
- (102) Harrison, M. R.; Hardy, V.; Maignan, A.; Francesconi, M. G. *Chem. Commun.* **2009**, 2214-2216.
- (103) Grey, I. E.; Steinfink, H. *Inorg. Chem.* **1971**, *10*, 691-696.
- (104) Iglesias, J. E.; Pachali, K. E.; Steinfink, H. *J. Solid State Chem.* **1974**, *9*, 6-14.
- (105) Rad, H. D.; Hoppe, R. *Z. Anorg. Allg. Chem.* **1981**, *483*, 7-17.
- (106) Baikie, T.; Maignan, A.; Francesconi, M. G. *Chem. Commun.* **2004**, 836-837.
- (107) Nakayama, N.; Kosuge, K.; Kachi, S.; Shinjo, T.; Takada, T. *Abstracts of Papers of the American Chemical Society* **1979**, 58-58.
- (108) Greaney, M. A.; Ramanujachary, K. V.; Teweldemedhin, Z.; Greenblatt, M. *J. Solid State Chem.* **1993**, *107*, 554-562.
- (109) Baikie, T.; Hardy, V.; Maignan, A.; Francesconi, M. G. *Chem. Commun.* **2005**, 5077-5079.
- (110) Barnes, A. D. J.; Baikie, T.; Hardy, V.; Lepetit, M. B.; Maignan, A.; Young, N. A.; Francesconi, M. G. *J. Mater. Chem.* **2006**, *16*, 3489-3502.
- (111) Headspith, D. A.; Battle, P. D.; Francesconi, M. G. *J. Solid State Chem.* **2007**, *180*, 2859-2863.
- (112) Wells, A. F. *Z. Kristallogr.* **1938**, *100*, 189-194.
- (113) Peters, J.; Krebs, B. *Acta Crystallogr., Sect. B: Struct. Sci.* **1982**, *38*, 1270-1272.
- (114) Brink, C.; MacGillavry, C. H. *Acta Crystallogr., Sect. A* **1949**, *2*, 158.
- (115) Colpas, G. J.; Maroney, M. J.; Bagyinka, C.; Kumar, M.; Willis, W. S.; Suib, S. L.; Baidya, N.; Mascharak, P. K. *Inorg. Chem.* **1991**, *30*, 920-928.
- (116) Cotton, F. A.; Elder, R. C. *Inorg. Chem.* **1966**, *5*, 423-429.
- (117) Bruckner, S.; Calligaris, M.; Nardin, G.; Randaccio, L. *Acta Crystallogr., Sect. B* **1969**, *25*, 1671-1674.
- (118) Rhodes, B.; Rowling, S.; Tidswell, P.; Woodward, S.; Brown, S. M. *Journal of Molecular Catalysis A: Chemical* **1997**, *116*, 375-384.
- (119) Carlin, R. L.; Chirico, R. D.; Sinn, E.; Mennenga, G.; De Jongh, L. J. *Inorg. Chem.* **1982**, *21*, 2218-2222.
- (120) Oguchi, T. *Phys. Rev.* **1964**, *133*, A1098-A1099.
- (121) Toby, B. H. *J. Appl. Crystallogr.* **2001**, *34*, 210.
- (122) Larson, A. C.; Dreele, R. B. V. Los Alamos National Laboratory Report LAUR, 2004.
- (123) Dinnebier, R. E.; Billinge, S. J. L. *Powder Diffraction: Theory and Practice*; RSC Publishing: Cambridge, 2009.
- (124) Tilley, R. *Crystals and Crystal Structures*; John Wiley & Sons, Ltd: Chichester, 2006.
- (125) Calestani, G. *Advances in Imaging and Electron Physics* **2002**, *123*.
- (126) Weller, M. T. *Inorganic Materials Chemistry*; Oxford University Press: Avon, 1994.
- (127) Bragg, W. H.; Bragg, W. L. *X-Rays and Crystal Structure*; G. Bell and Sons, Ltd, 1915.
- (128) Young, R. A. *The Rietveld Method*; Oxford University Press: New York, 2002.

- (129) Rietveld, H. M. *Acta Crystallogr., Sect. A* **1967**, 22, 151-2.
- (130) *The Rietveld Method*; Oxford University Press: New York, 2002.
- (131) Shannon, R. D.; Prewitt, C. T. *Acta Crystallogr., Sect. B* **1970**, B 26, 1046-&.
- (132) Binsted, N. *PAXAS: EXAFS Analysis Program*, 1988.
- (133) Höllmann, B. *Pyspline*, 1999.
- (134) Binsted, N. *EXCURV98: CCLRC Daresbury Laboratory computer program*, 1998.
- (135) Ardelean, I.; Ilonca, G.; Simon, V.; Filip, S.; Simon, S. *J. Alloys Compd.* **2001**, 326, 121-123.
- (136) Cai, J. W.; Wang, C.; Shen, B. G.; Zhao, J. G.; Zhan, W. S. *Appl. Phys. Lett.* **1997**, 71, 1727-1729.
- (137) Shoemaker, C. B. *Z. Kristallogr.* **1973**, 137, 225-239.
- (138) Angel, R. J.; Gasparik, T.; Finger, L. W. *Am. Mineral.* **1989**, 74, 599-603.
- (139) Tan, X. M.; Kuang, X. Y.; Zhou, K. W. *Solid State Commun.* **2005**, 136, 395-399.
- (140) Sears, V. F. *Neutron News* **1992**, 3, 26-37.
- (141) Schorr, S.; Tover, M.; Sheptyakov, D.; Keller, L.; Geandier, G. *J. Phys. Chem. Solids* **2005**, 66, 1961-1965.
- (142) Singh, A.; Aswal, D. K.; Chowdhury, P.; Padma, N.; Kadam, R. M.; Babu, Y.; Kumar, M. L. J.; Viswanadham, C. S.; Kumar, S.; Gupta, S. K.; Yakhmi, J. V. *Solid State Commun.* **2006**, 138, 430-435.
- (143) Ziese, M.; Srinithiwarawong, C.; Shearwood, C. *J. Phys.: Condens. Matter* **1998**, 10, L659.
- (144) Nossov, A.; Pierre, J.; Strobel, P.; Vassiliev, V.; Slobodin, B.; Vladimirova, E.; Machkaoutsan, V.; Ustinov, V. *J. Magn. Magn. Mater.* **1999**, 196-197, 461-462.
- (145) Harvey, E. J.; Ashbrook, S. E.; Lumpkin, G. R.; Redfern, S. A. T. *J. Mater. Chem.* **2006**, 16, 4665-4674.

10.0 Appendices

10.1 Appendix 1

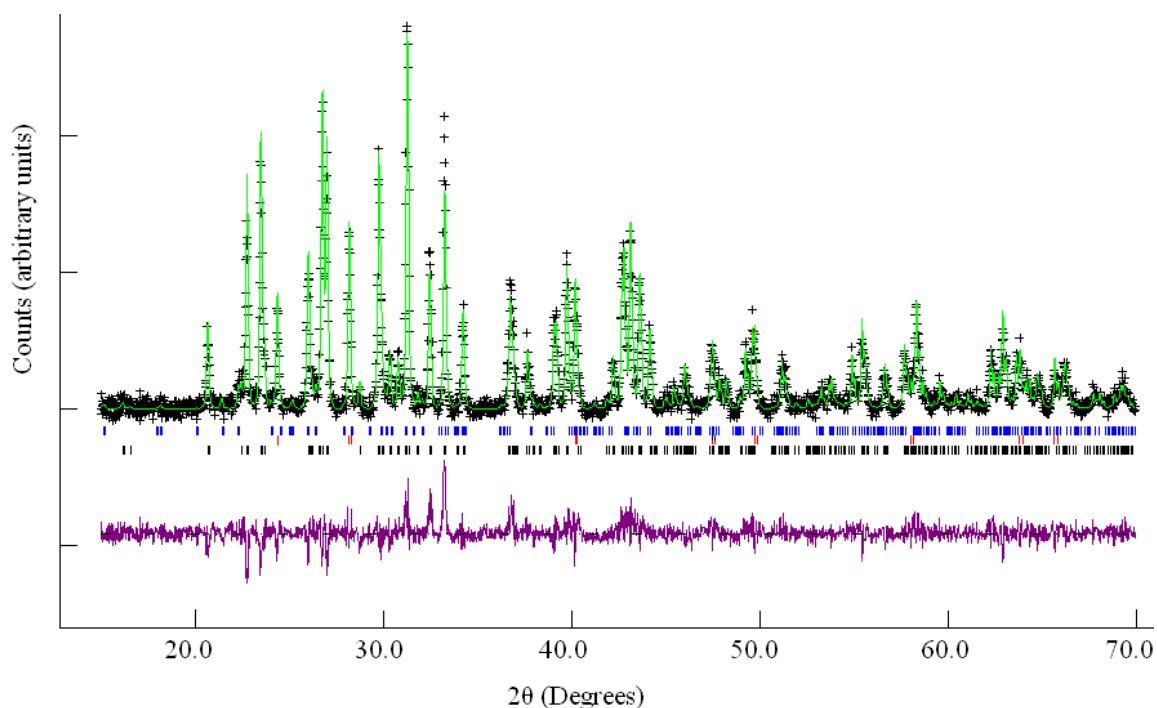


Figure 10.1 Rietveld refinement against X-ray diffraction data for $\text{Ba}_2\text{Co}_{0.9}\text{Zn}_{0.1}\text{S}_3$: Black line (observed), green line (calculated) and purple line (difference). Black tick marks correspond to $\text{Ba}_2\text{Co}_{0.9}\text{Zn}_{0.1}\text{S}_3$, blue to Ba_2SiS_4 and red to BaS

Table 10.1 Atomic positions, thermal parameters and fractional occupancies for $\text{Ba}_2\text{Co}_{0.9}\text{Zn}_{0.1}\text{S}_3$

Atom	x	y	z	U	F
Ba1	0.8281(4)	0.4809(4)	0.25	0.005	1
Ba2	0.4865(4)	0.6739(4)	0.25	0.005	1
Co	0.7465(8)	0.1961(8)	0.25	0.005	0.9
Zn	0.7456(8)	0.1961(8)	0.25	0.005	0.1
S1	0.8659(15)	0.0487(16)	0.25	0.005	1
S2	0.5623(15)	0.1432(17)	0.25	0.005	1
S3	0.2266(15)	0.7137(15)	0.25	0.005	1
$R_p = 13.18$		$R_{wp} = 16.12$		$\chi^2 = 1.99$	

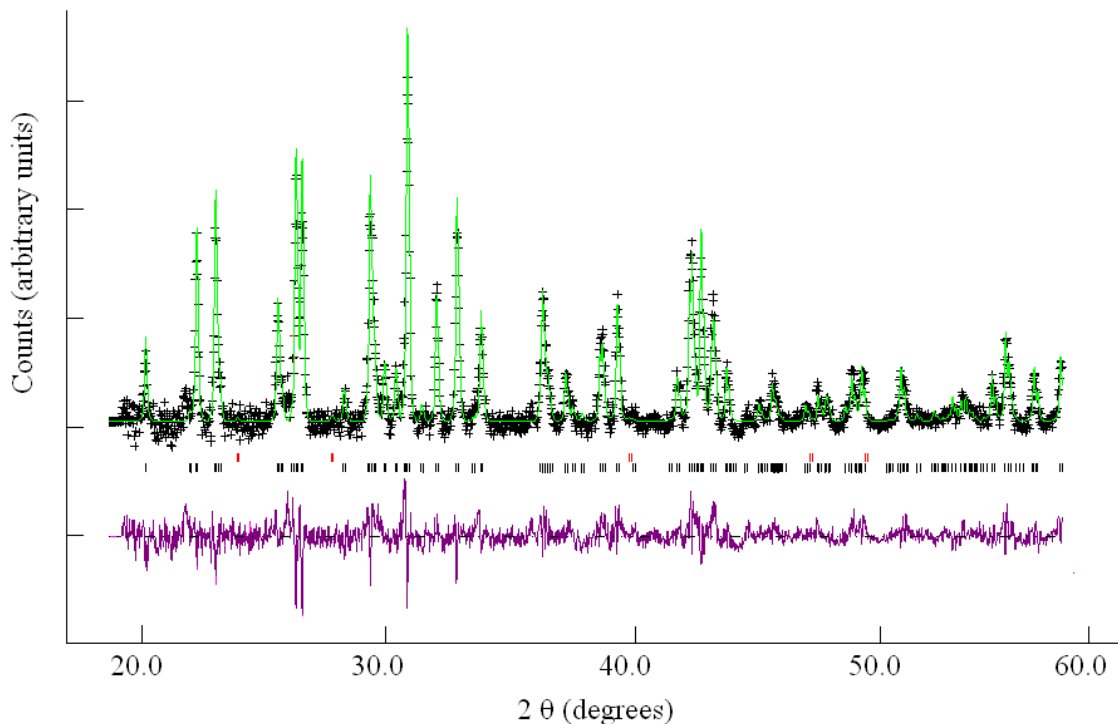


Figure 10.2 Rietveld refinement against X-ray diffraction data for $\text{Ba}_2\text{Co}_{0.8}\text{Zn}_{0.2}\text{S}_3$: Black line (observed), green line (calculated) and purple line (difference). Black tick marks correspond to $\text{Ba}_2\text{Co}_{0.8}\text{Zn}_{0.2}\text{S}_3$ and red to BaS

Table 10.2 Atomic positions, thermal parameters and fractional occupancies for $\text{Ba}_2\text{Co}_{0.8}\text{Zn}_{0.2}\text{S}_3$

Atom	x	y	z	U	F
Ba1	0.8253(7)	0.4812(5)	0.25	0.005	1
Ba2	0.4894(6)	0.6766(6)	0.25	0.005	1
Co	0.7489(1)	0.1983(15)	0.25	0.005	0.8
Zn	0.7489(1)	0.1983(15)	0.25	0.005	0.2
S1	0.8591(14)	0.0563(18)	0.25	0.005	1
S2	0.5600(16)	0.1516(2)	0.25	0.005	1
S3	0.2263(18)	0.7125(3)	0.25	0.005	1
$R_p = 6.53$		$R_{wp} = 7.65$		$\chi^2 = 2.32$	

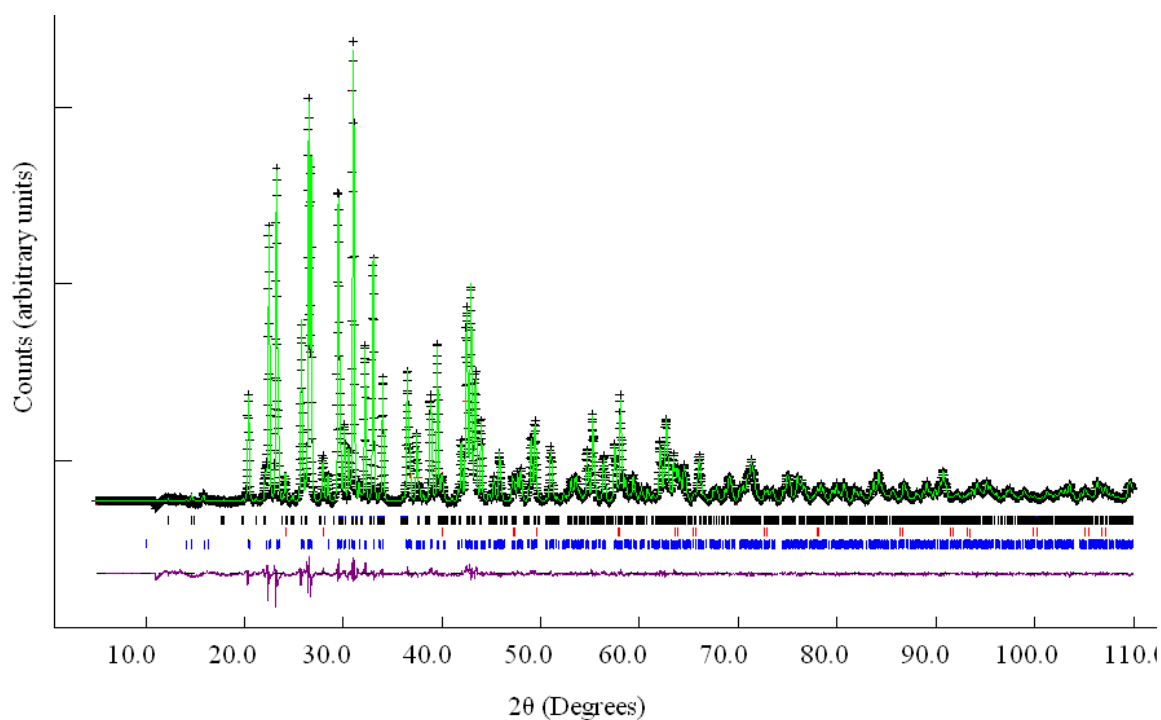


Figure 10.3 Rietveld refinement against X-ray diffraction data for $\text{Ba}_2\text{Co}_{0.75}\text{Zn}_{0.25}\text{S}_3$: Black line (observed), green line (calculated) and purple line (difference). Black tick marks correspond to $\text{Ba}_2\text{Co}_{0.75}\text{Zn}_{0.25}\text{S}_3$, blue to Ba_2Si_4 and red to BaS

Table 10.3 Atomic positions, thermal parameters and fractional occupancies for $\text{Ba}_2\text{Co}_{0.75}\text{Zn}_{0.25}\text{S}_3$

Atom	x	y	z	U	F
Ba1	0.82719(8)	0.48083(7)	0.25	0.005	1
Ba2	0.48860(8)	0.67370(8)	0.25	0.005	1
Co	0.7455(2)	0.1980(2)	0.25	0.005	0.75
Zn	0.7455(2)	0.1980(2)	0.25	0.005	0.25
S1	0.8658(3)	0.0533(3)	0.25	0.005	1
S2	0.5609(3)	0.1407(3)	0.25	0.005	1
S3	0.2247(3)	0.7089(3)	0.25	0.005	1
$R_p = 2.66$		$R_{wp} = 3.55$		$\chi^2 = 3.03$	

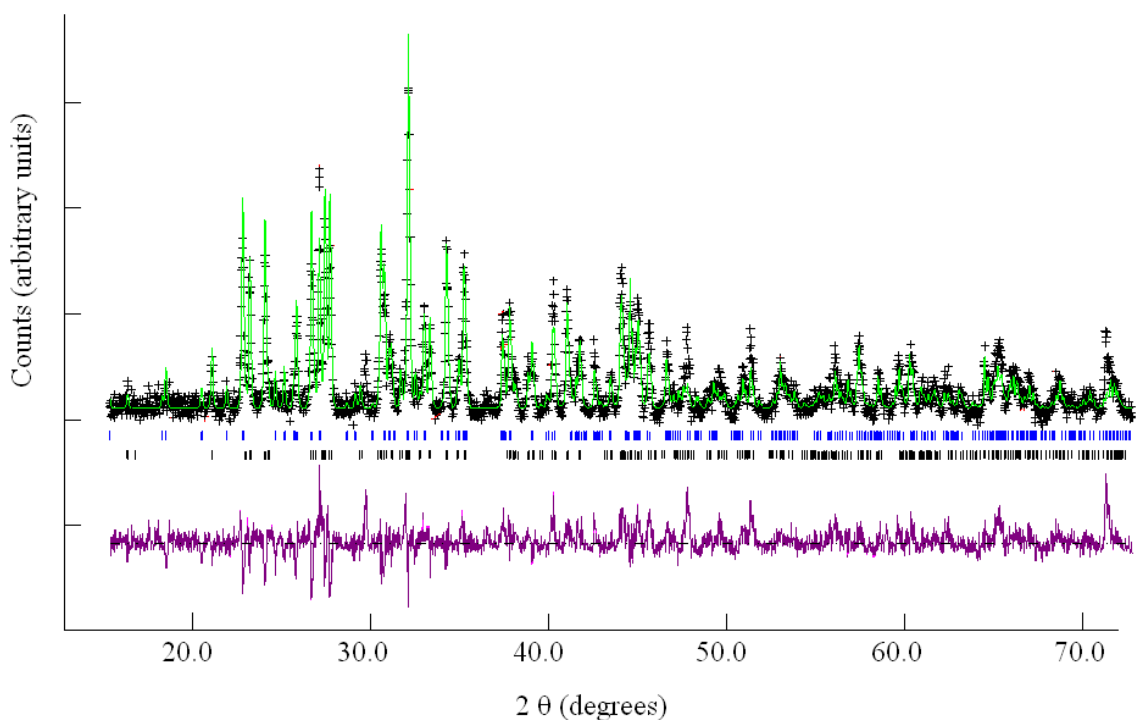


Figure 10.4 Rietveld refinement against X-ray diffraction data for $\text{Ba}_2\text{Co}_{0.6}\text{Zn}_{0.4}\text{S}_3$: Black line (observed), green line (calculated) and purple line (difference). Black tick marks correspond to $\text{Ba}_2\text{Co}_{0.6}\text{Zn}_{0.4}\text{S}_3$ and blue to Ba_2SiS_4

Table 10.4 Atomic positions, thermal parameters and fractional occupancies for $\text{Ba}_2\text{Co}_{0.6}\text{Zn}_{0.4}\text{S}_3$

Atom	x	y	z	U	F
Ba1	0.8257(7)	0.4795(6)	0.25	0.005	1
Ba2	0.4875(8)	0.67373(8)	0.25	0.005	1
Co	0.7455(16)	0.1979(2)	0.25	0.005	0.6
Zn	0.7455(16)	0.1979(2)	0.25	0.005	0.4
S1	0.8611(25)	0.0580(33)	0.25	0.005	1
S2	0.5690(25)	0.1429(18)	0.25	0.005	1
S3	0.2219(29)	0.7086(29)	0.25	0.005	1
$R_p = 13.43$		$R_{wp} = 18.21$		$\chi^2 = 2.01$	

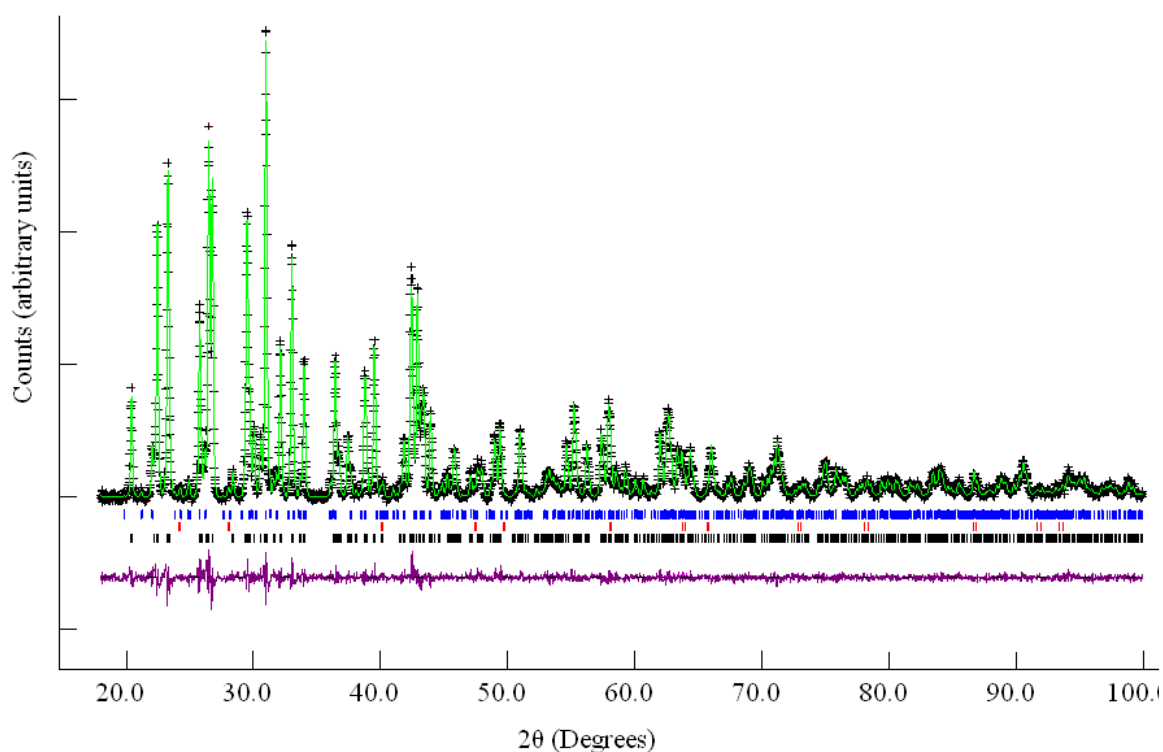


Figure 10.5 Rietveld refinement against X-ray diffraction data for $\text{Ba}_2\text{Co}_{0.5}\text{Zn}_{0.5}\text{S}_3$: Black line (observed), green line (calculated) and purple line (difference). Black tick marks correspond to $\text{Ba}_2\text{Co}_{0.5}\text{Zn}_{0.5}\text{S}_3$, blue to Ba_2SiS_4 and red to BaS

Table 10.5 Atomic positions, thermal parameters and fractional occupancies for $\text{Ba}_2\text{Co}_{0.5}\text{Zn}_{0.5}\text{S}_3$

Atom	x	y	z	U	F
Ba1	0.8272(1)	0.4816(1)	0.25	0.005	1
Ba2	0.4886(1)	0.6734(1)	0.25	0.005	1
Co	0.7455(3)	0.1970(4)	0.25	0.005	0.5
Zn	0.7455(3)	0.1970(4)	0.25	0.005	0.5
S1	0.8663(4)	0.0527(5)	0.25	0.005	1
S2	0.5619(5)	0.1396(6)	0.25	0.005	1
S3	0.2229(5)	0.7076(5)	0.25	0.005	1
$R_p = 4.78$		$R_{wp} = 6.65$		$\chi^2 = 1.47$	

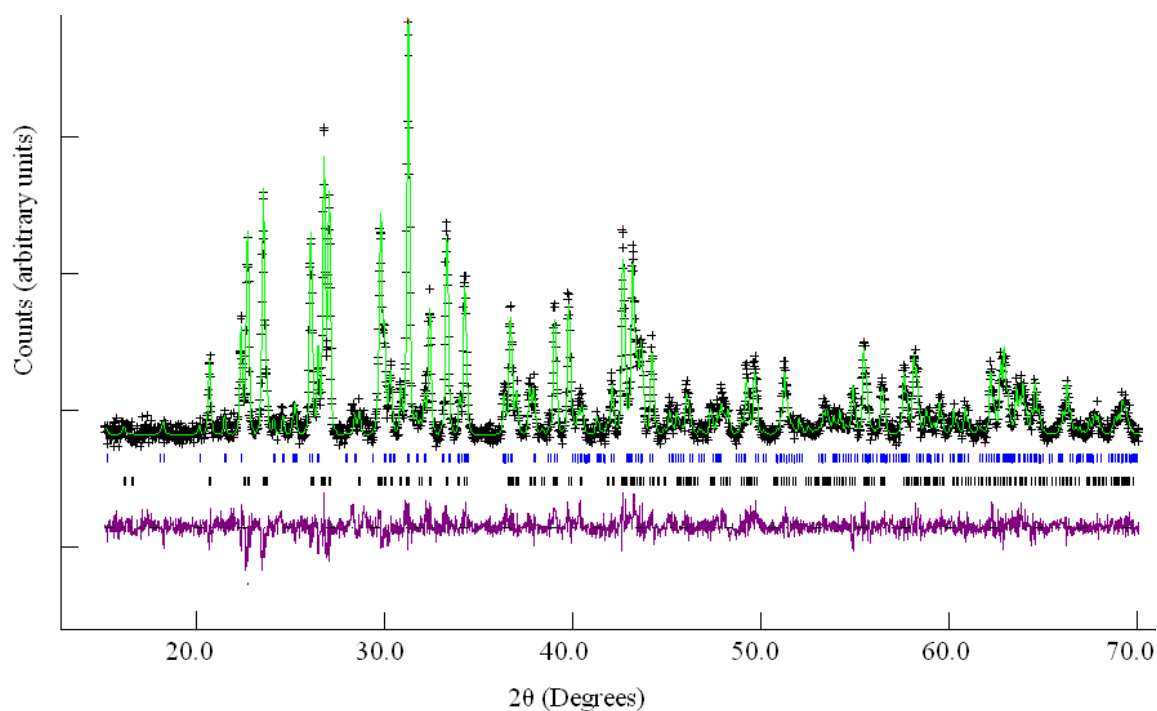


Figure 10.6 Rietveld refinement against X-ray diffraction data for $\text{Ba}_2\text{Co}_{0.4}\text{Zn}_{0.6}\text{S}_3$: Black line (observed), green line (calculated) and purple line (difference). Black tick marks correspond to $\text{Ba}_2\text{Co}_{0.4}\text{Zn}_{0.6}\text{S}_3$, blue to Ba_2Si_4 and red to BaS

Table 10.6 Atomic positions, thermal parameters and fractional occupancies for $\text{Ba}_2\text{Co}_{0.4}\text{Zn}_{0.6}\text{S}_3$

Atom	x	y	z	U	F
Ba1	0.8277(4)	0.4823(4)	0.25	0.005	1
Ba2	0.4874(4)	0.6733(4)	0.25	0.005	1
Co	0.7481(7)	0.1977(9)	0.25	0.005	0.4
Zn	0.7481(7)	0.1977(9)	0.25	0.005	0.6
S1	0.8619(17)	0.0492(16)	0.25	0.005	1
S2	0.5607(14)	0.1391(18)	0.25	0.005	1
S3	0.2254(12)	0.7043(16)	0.25	0.005	1
$R_p = 10.34$		$R_{wp} = 11.78$		$\chi^2 = 1.37$	

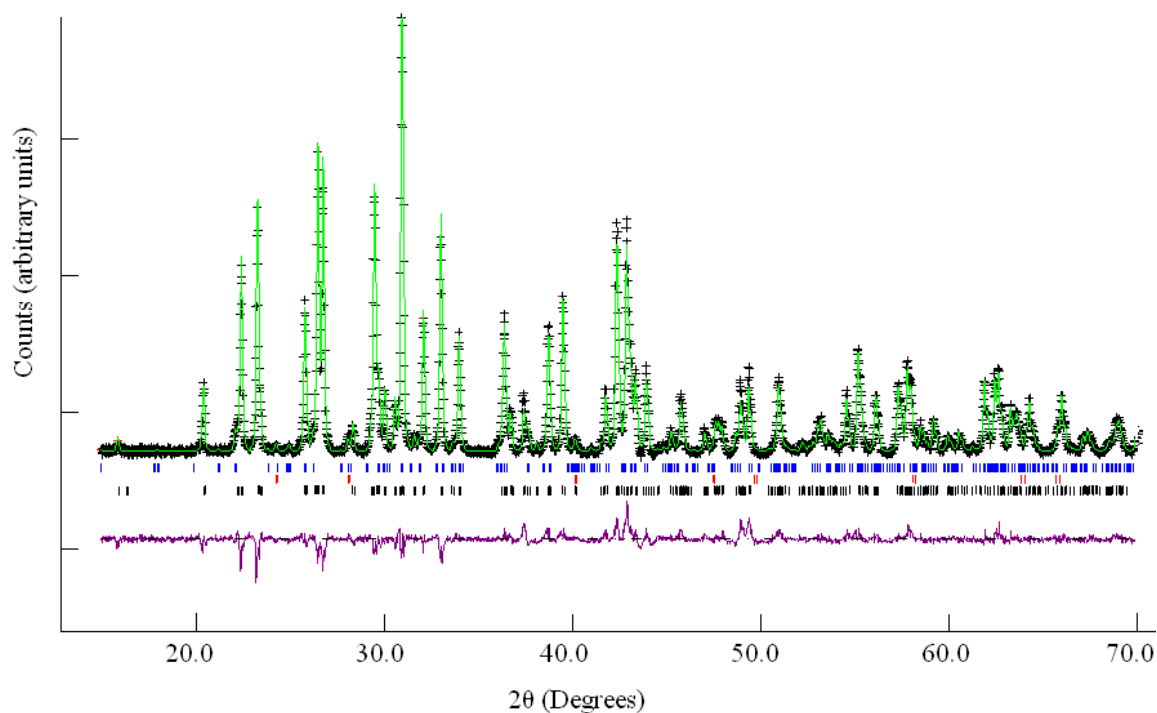


Figure 10.7 Rietveld refinement against X-ray diffraction data for $\text{Ba}_2\text{Co}_{0.25}\text{Zn}_{0.75}\text{S}_3$: Black line (observed), green line (calculated) and purple line (difference). Black tick marks correspond to $\text{Ba}_2\text{Co}_{0.25}\text{Zn}_{0.75}\text{S}_3$, blue to Ba_2Si_4 and red to BaS

Table 10.7 Atomic positions, thermal parameters and fractional occupancies for $\text{Ba}_2\text{Co}_{0.25}\text{Zn}_{0.75}\text{S}_3$

Atom	x	y	z	U	F
Ba1	0.8267(2)	0.4810(3)	0.25	0.005	1
Ba2	0.4889(2)	0.6749(2)	0.25	0.005	1
Co	0.7431(4)	0.1995(2)	0.25	0.005	0.25
Zn	0.7431(4)	0.1995(3)	0.25	0.005	0.75
S1	0.8662(6)	0.0538(7)	0.25	0.005	1
S2	0.5601(8)	0.1414(8)	0.25	0.005	1
S3	0.2212(4)	0.7048(7)	0.25	0.005	1
$R_p = 5.58$		$R_{wp} = 6.99$		$\chi^2 = 2.72$	

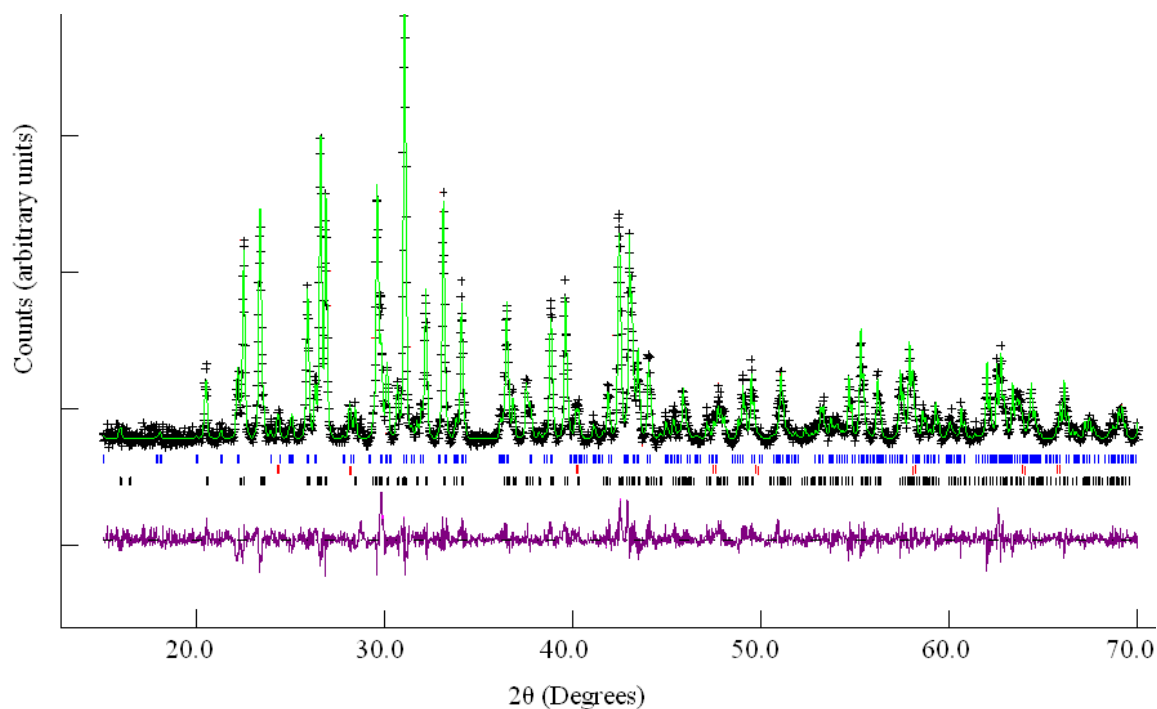
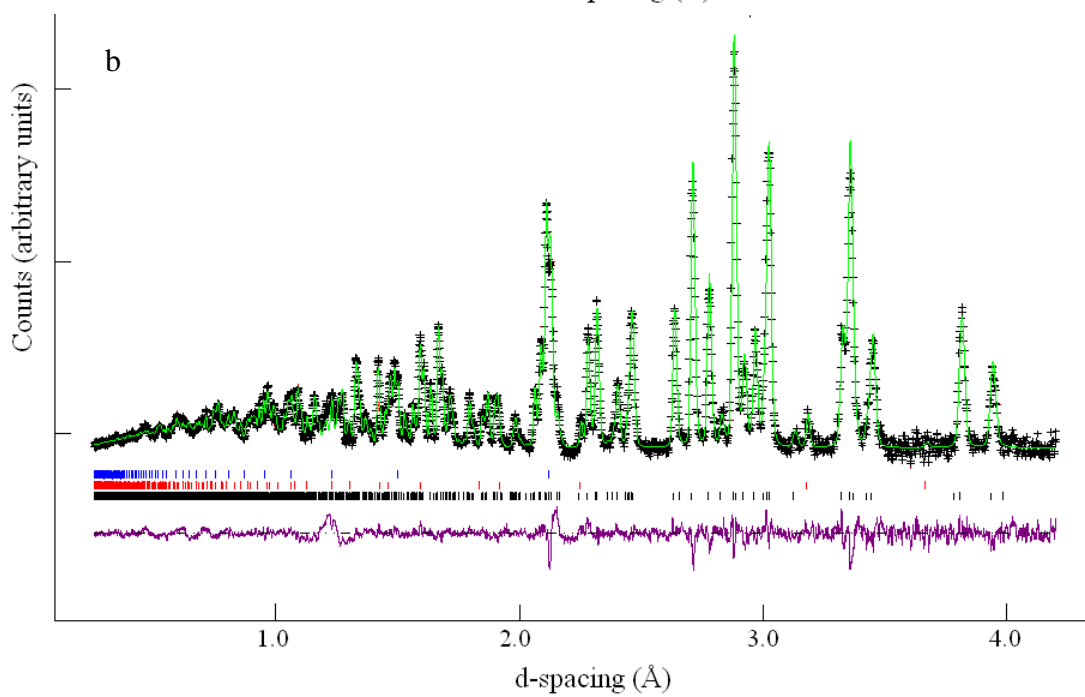
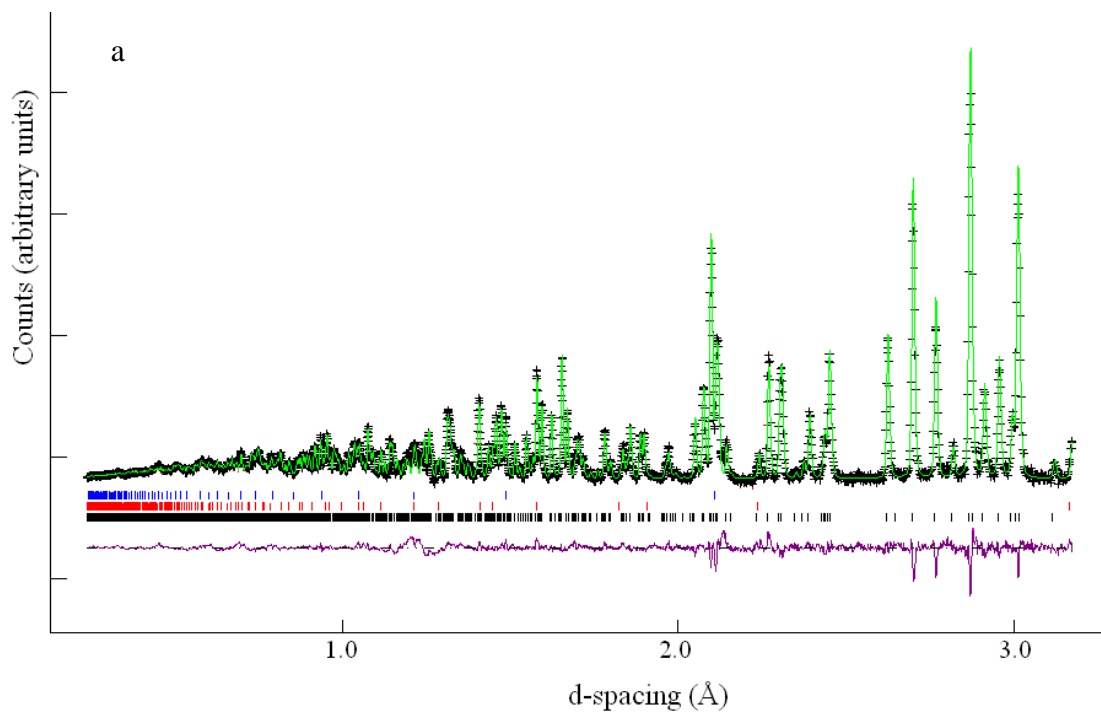


Figure 10.8 Rietveld refinement against X-ray diffraction data for $\text{Ba}_2\text{Co}_{0.2}\text{Zn}_{0.8}\text{S}_3$: Black line (observed), green line (calculated) and purple line (difference). Black tick marks correspond to $\text{Ba}_2\text{Co}_{0.2}\text{Zn}_{0.8}\text{S}_3$, blue to Ba_2SiS_4 and red to BaS

Table 10.8 Atomic positions, thermal parameters and fractional occupancies for $\text{Ba}_2\text{Co}_{0.2}\text{Zn}_{0.8}\text{S}_3$

Atom	x	y	z	U	F
Ba1	0.8262(3)	0.4813(4)	0.25	0.005	1
Ba2	0.4894(4)	0.6755(4)	0.25	0.005	1
Co	0.7447(7)	0.1989(7)	0.25	0.005	0.2
Zn	0.7447(5)	0.1989(7)	0.25	0.005	0.8
S1	0.8635(11)	0.0510(11)	0.25	0.005	1
S2	0.5540(14)	0.1413(13)	0.25	0.005	1
S3	0.2241(9)	0.7065(12)	0.25	0.005	1
$R_p = 13.26$		$R_{wp} = 14.34$		$\chi^2 = 1.89$	

10.2 Appendix 2



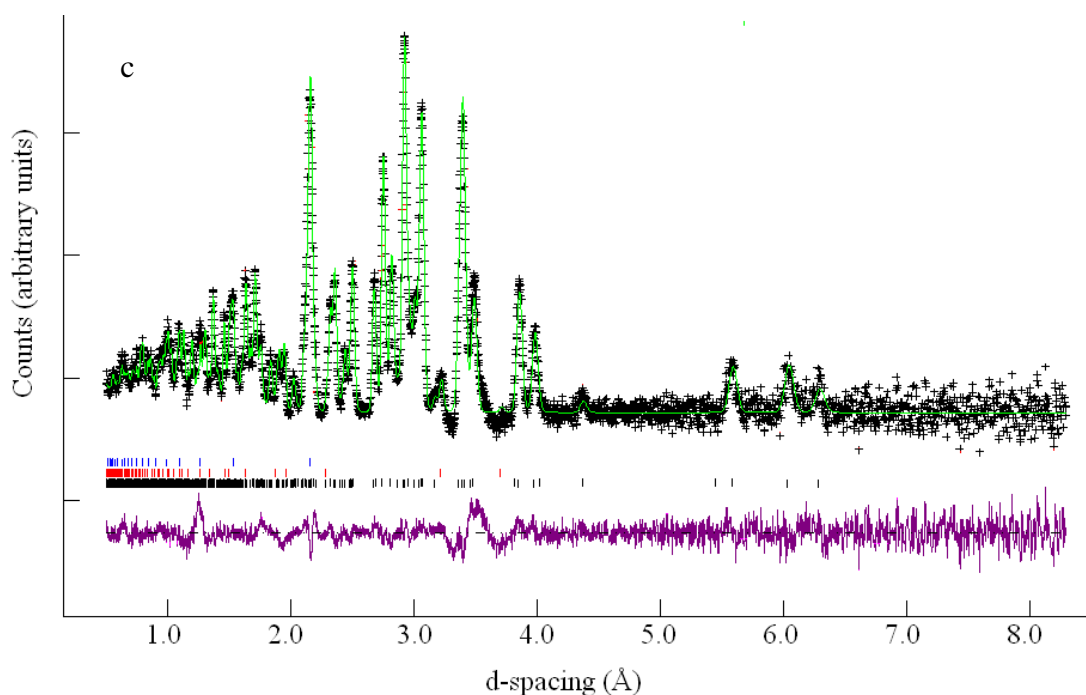
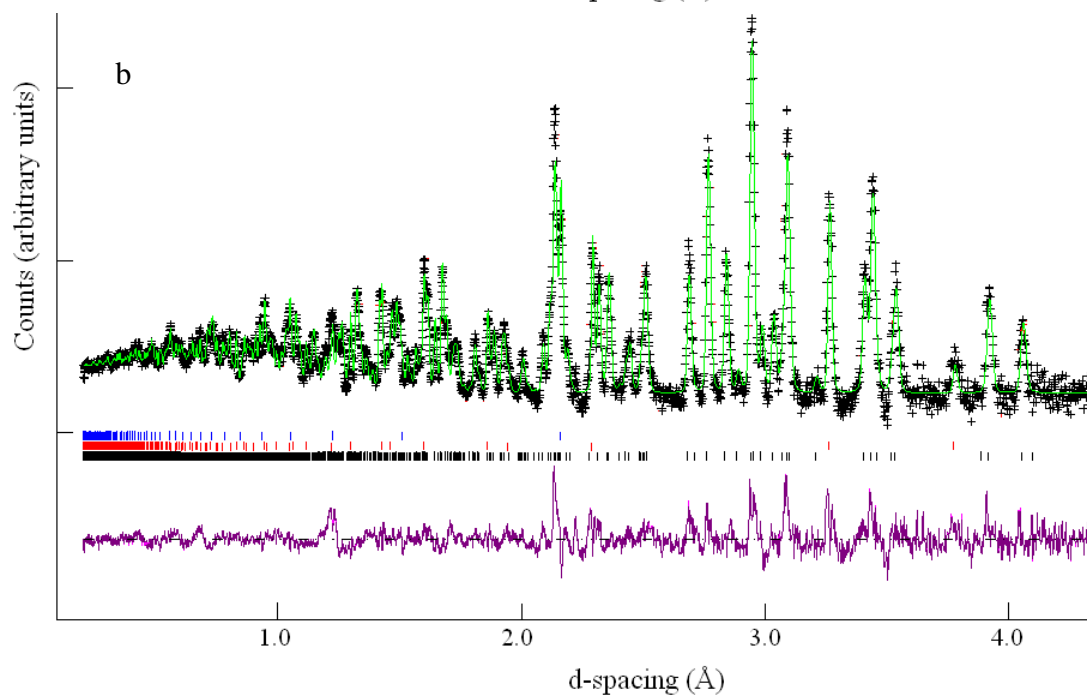
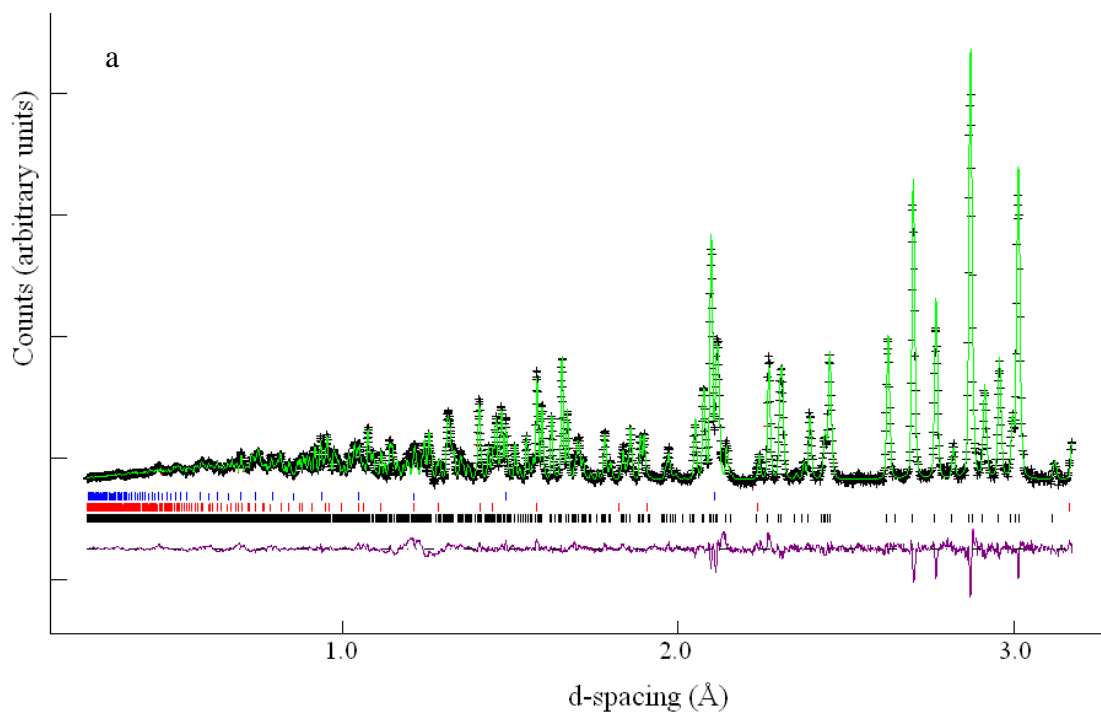


Figure 10.16 Rietveld refinement against neutron diffraction data for $\text{Ba}_2\text{Co}_{0.75}\text{Zn}_{0.25}\text{S}_3$ from banks 1, 2 and 3 (a, b and c respectively): Black line (observed), green line (calculated) and purple line (difference). Black tick marks correspond to $\text{Ba}_2\text{Co}_{0.75}\text{Zn}_{0.25}\text{S}_3$, blue to Ba_2SiS_4 and red to BaS

Table 10.9 Atomic positions, thermal parameters and fractional occupancies for $\text{Ba}_2\text{Co}_{0.75}\text{Zn}_{0.25}\text{S}_3$

Atom	x	y	z	U	F
Ba1	0.8285(1)	0.4808(1)	0.25	0.0090(3)	1
Ba2	0.4882(1)	0.6730(1)	0.25	0.0057(2)	1
Co	0.7488(2)	0.1984(2)	0.25	0.0030(4)	0.75
Zn	0.7488(2)	0.1984(2)	0.25	0.0030(4)	0.25
S1	0.8649(2)	0.0526(2)	0.25	0.0129(6)	1
S2	0.5612(2)	0.1410(2)	0.25	0.0036(4)	1
S3	0.2279(2)	0.7111(2)	0.25	0.0029(4)	1
$R_p = 3.18\%$		$R_{wp} = 2.30\%$		$\chi^2 = 3.94$	



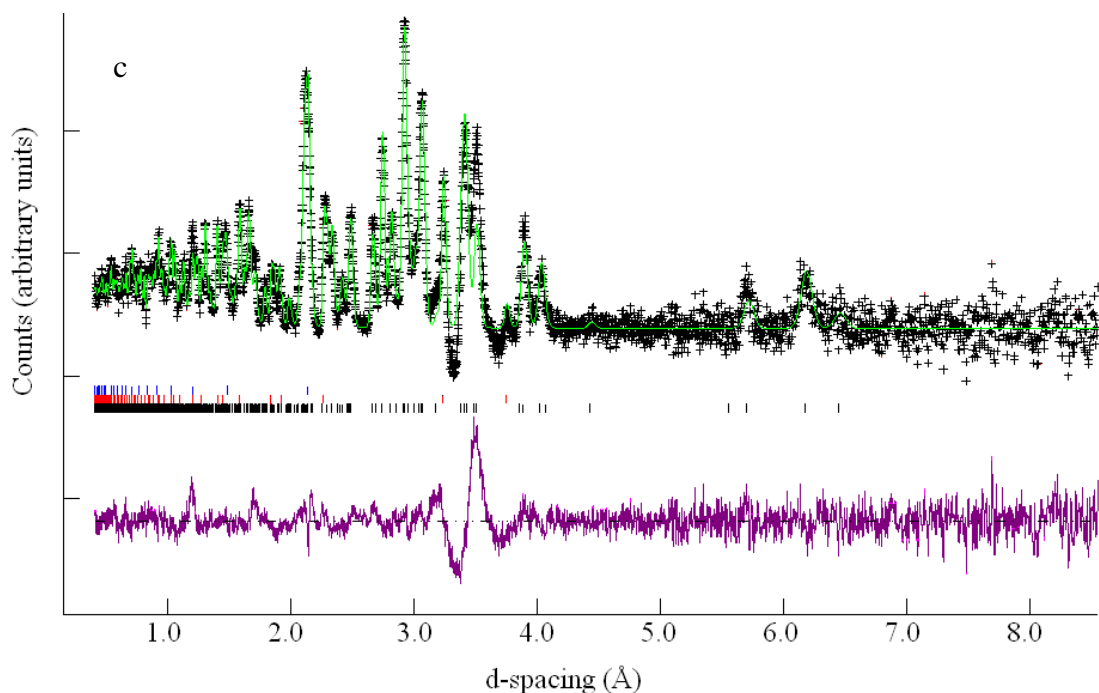
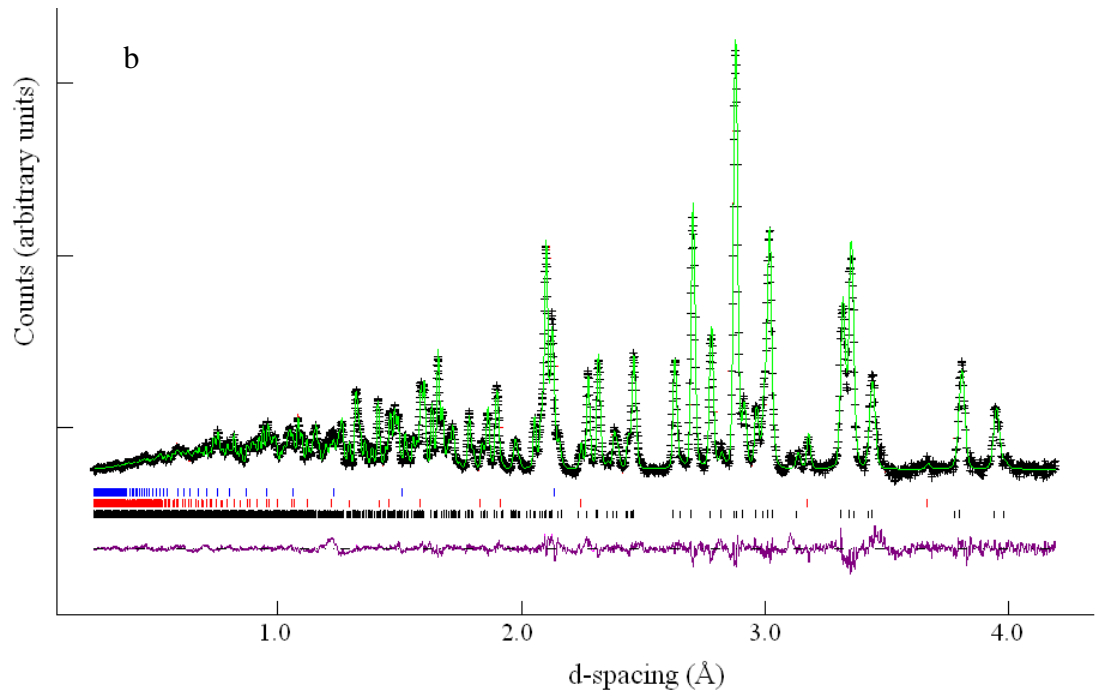
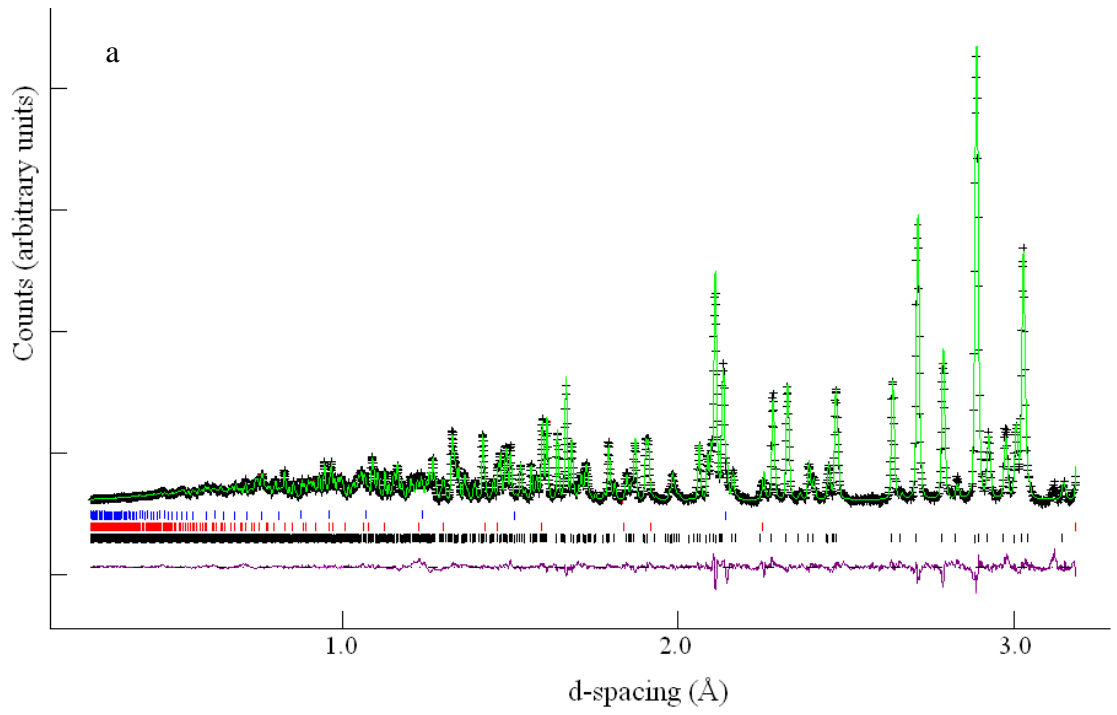


Figure 10.17 Rietveld refinement against neutron diffraction data for $\text{Ba}_2\text{Co}_{0.5}\text{Zn}_{0.5}\text{S}_3$: Black line (observed), green line (calculated) and purple line (difference). Black tick marks correspond to $\text{Ba}_2\text{Co}_{0.5}\text{Zn}_{0.5}\text{S}_3$, blue to Ba_2SiS_4 and red to BaS

Table 10.10 Atomic positions, thermal parameters and fractional occupancies for $\text{Ba}_2\text{Co}_{0.5}\text{Zn}_{0.5}\text{S}_3$

Atom	x	Y	z	U	F
Ba1	0.8264(2)	0.4812(1)	0.25	0.0041(3)	1
Ba2	0.4878(2)	0.6723(1)	0.25	0.0011(2)	1
Co	0.7484(2)	0.1986(2)	0.25	0.0002(3)	0.5
Zn	0.7484(2)	0.1986(2)	0.25	0.0002(3)	0.5
S1	0.8640(3)	0.0525(3)	0.25	0.0019(2)	1
S2	0.5594(2)	0.1421(3)	0.25	0.0028(2)	1
S3	0.2283(3)	0.7078(2)	0.25	0.0019(2)	1
$R_p = 2.42\%$		$R_{wp} = 1.45\%$		$\chi^2 = 3.94$	



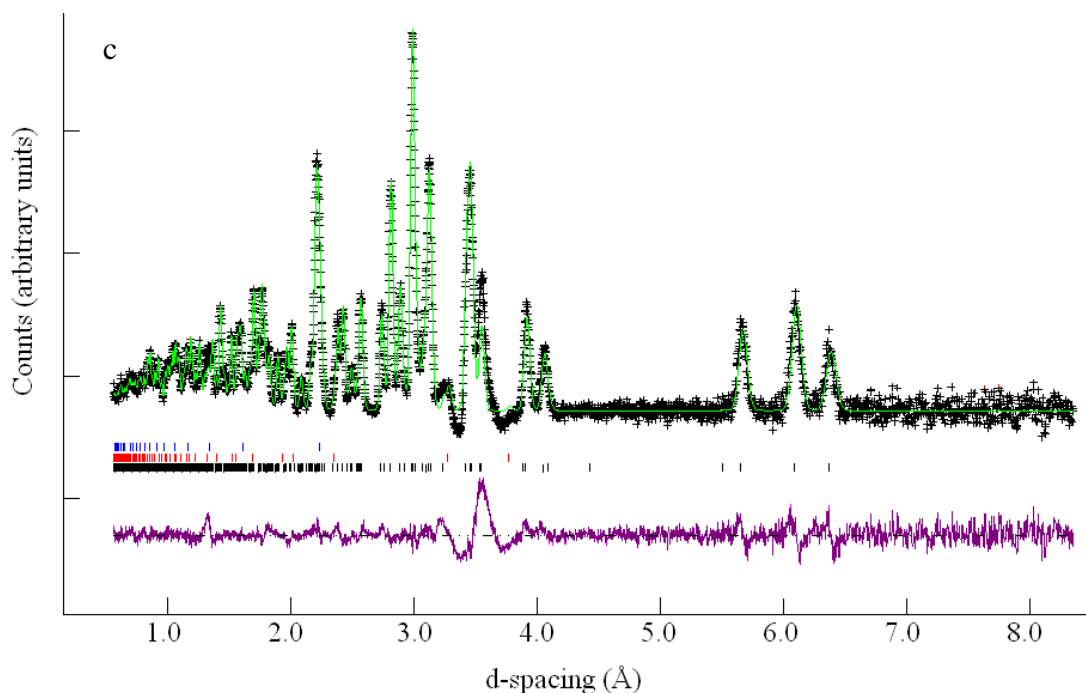
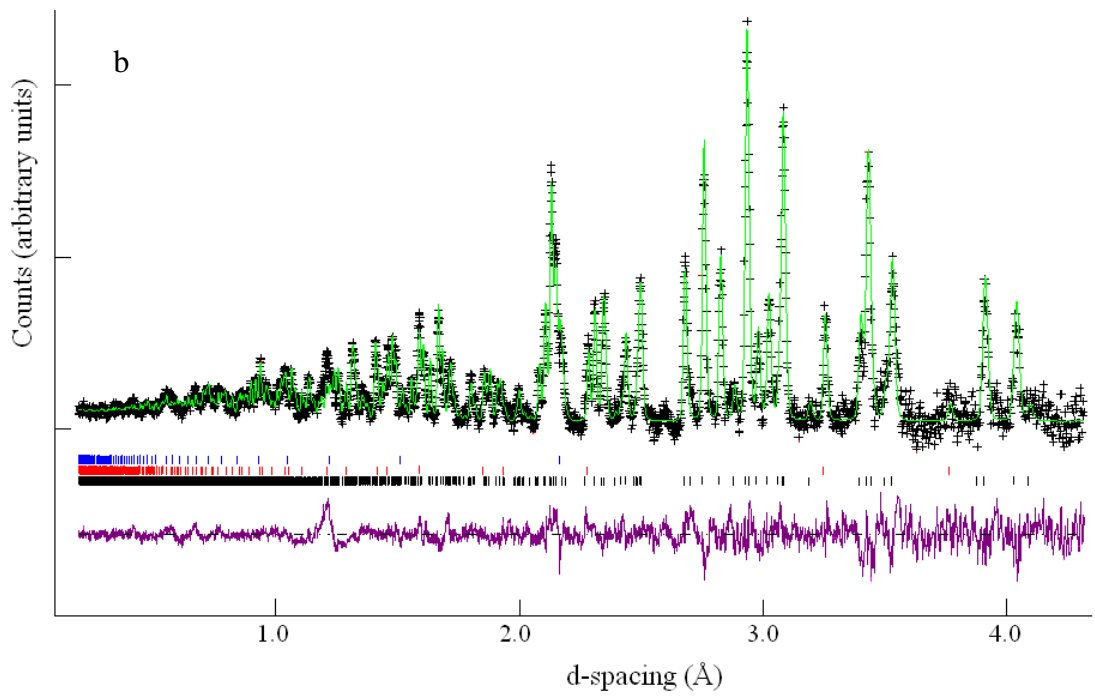
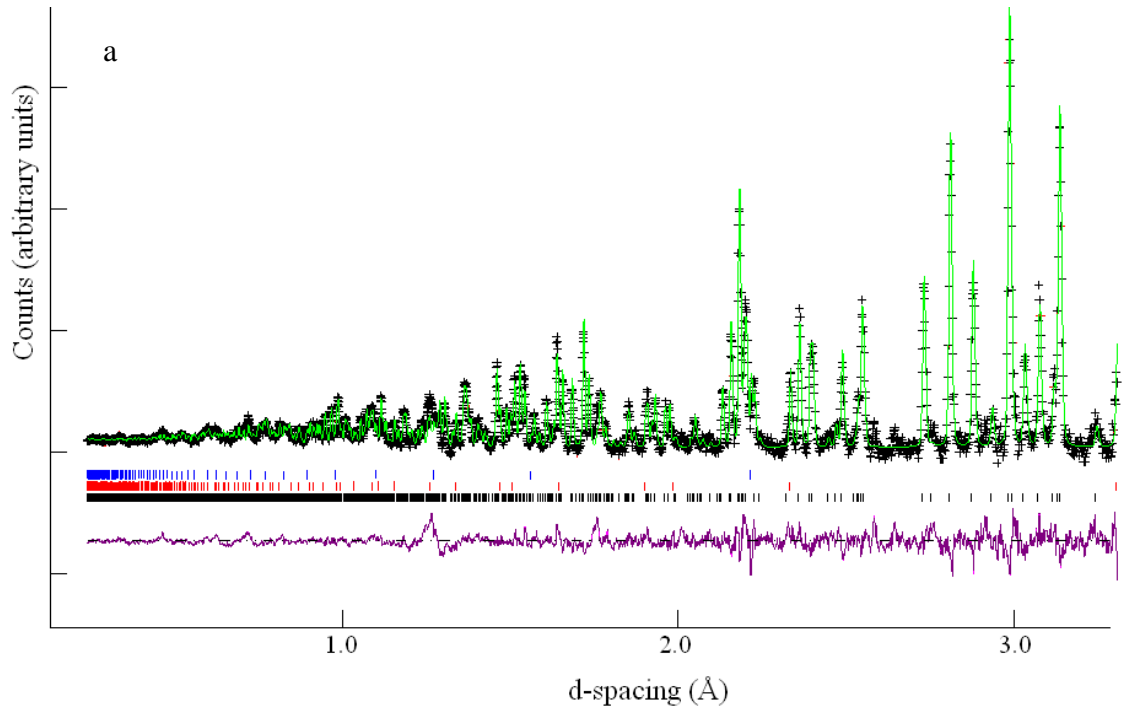


Figure 10.18 Rietveld refinement against neutron diffraction data for $\text{Ba}_2\text{Co}_{0.25}\text{Zn}_{0.75}\text{S}_3$: Black line (observed), green line (calculated) and purple line (difference). Black tick marks correspond to $\text{Ba}_2\text{Co}_{0.25}\text{Zn}_{0.75}\text{S}_3$, blue to Ba_2SiS_4 and red to BaS

Table 10.11 Atomic positions, thermal parameters and fractional occupancies for $\text{Ba}_2\text{Co}_{0.25}\text{Zn}_{0.75}\text{S}_3$

Atom	x	Y	z	U	F
Ba1	0.8278(1)	0.4822(1)	0.25	0.0087(2)	1
Ba2	0.4886(1)	0.6731(1)	0.25	0.0060(2)	1
Co	0.7472(1)	0.1981(1)	0.25	0.0052(2)	0.25
Zn	0.7472(1)	0.1981(1)	0.25	0.0052(2)	0.75
S1	0.8652(1)	0.0520(2)	0.25	0.0102(4)	1
S2	0.5593(1)	0.1406(2)	0.25	0.0086(4)	1
S3	0.2265(1)	0.7074(1)	0.25	0.0052(3)	1
$R_p = 3.64\%$		$R_{wp} = 2.12\%$		$\chi^2 = 3.07$	



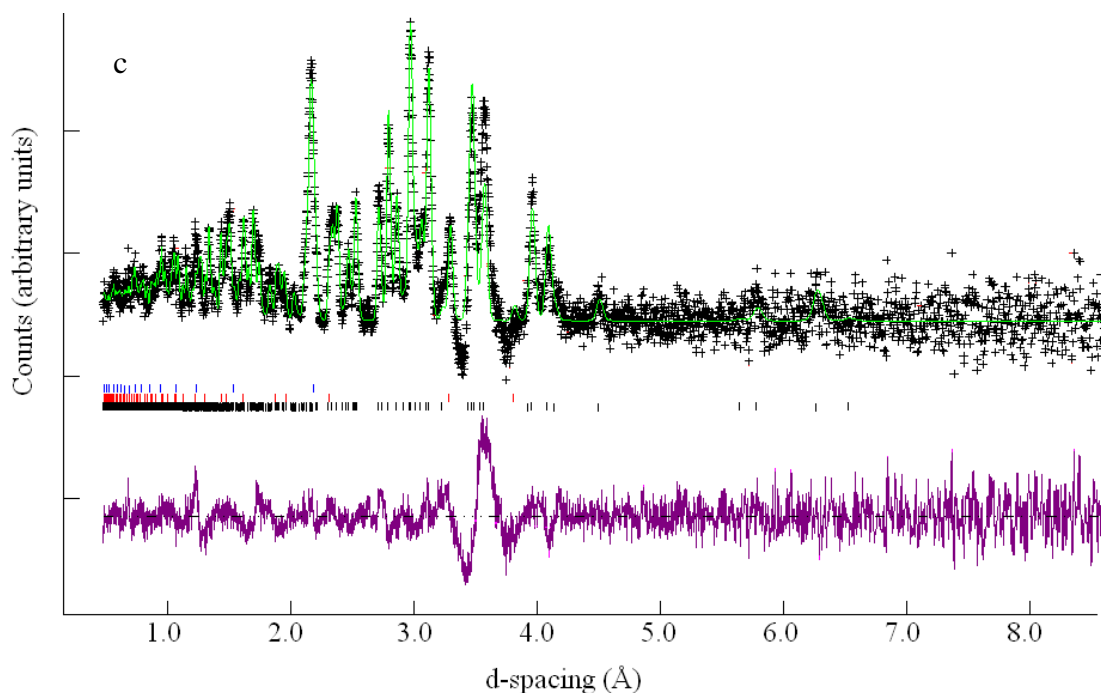
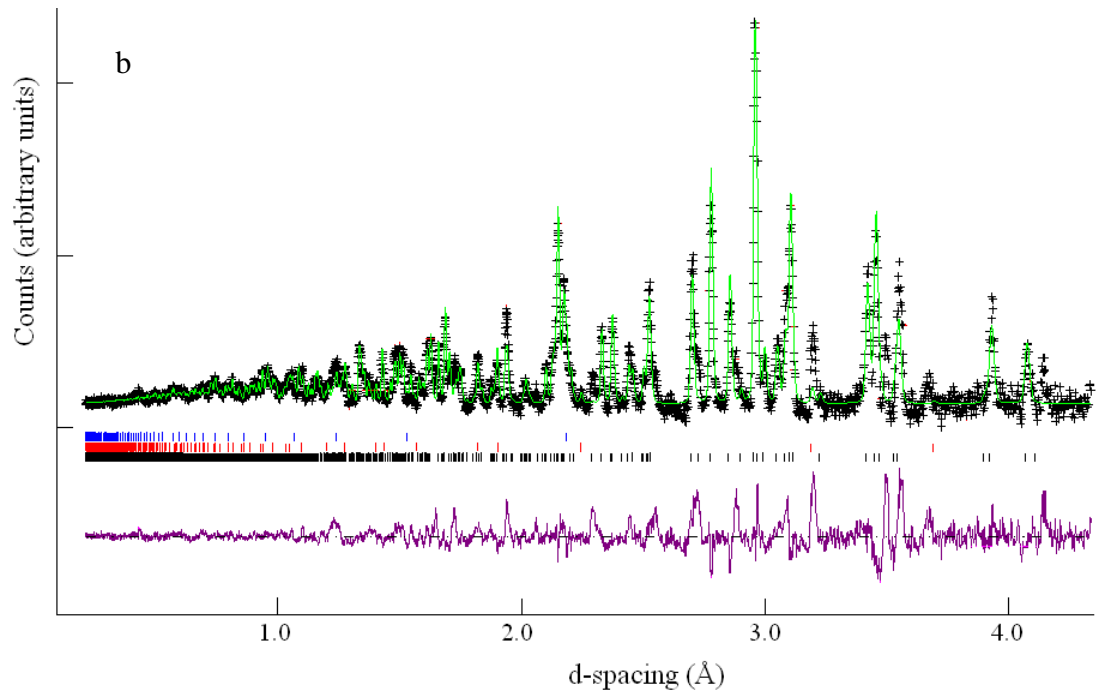
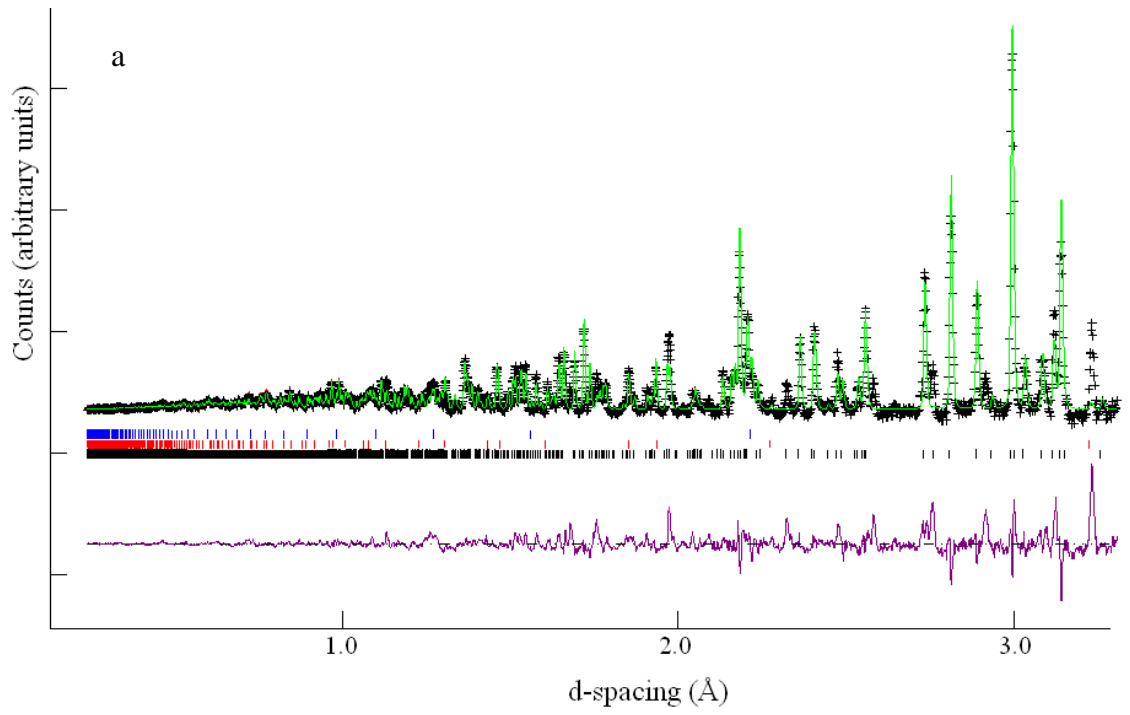


Figure 10.19 Rietveld refinement against neutron diffraction data for $\text{Ba}_2\text{Co}_{0.9}\text{Zn}_{0.1}\text{S}_3$: Black line (observed), green line (calculated) and purple line (difference). Black tick marks correspond to $\text{Ba}_2\text{Co}_{0.9}\text{Zn}_{0.1}\text{S}_3$, blue to Ba_2SiS_4 and red to BaS

Table 10.12 Atomic positions, thermal parameters and fractional occupancies for $\text{Ba}_2\text{Co}_{0.9}\text{Zn}_{0.1}\text{S}_3$

Atom	x	Y	z	U	F
Ba1	0.8275(2)	0.4808(2)	0.25	0.0123(5)	1
Ba2	0.4875(2)	0.6717(2)	0.25	0.0068(4)	1
Co	0.7524(4)	0.1978(3)	0.25	0.0006(2)	0.9
Zn	0.7524(4)	0.1978(3)	0.25	0.0006(2)	0.1
S1	0.8656(3)	0.0534(3)	0.25	0.0056(4)	1
S2	0.5603(3)	0.1425(3)	0.25	0.0056(4)	1
S3	0.2287(3)	0.7092(3)	0.25	0.0056(4)	1
$R_p = 4.18\%$		$R_{wp} = 2.58\%$		$\chi^2 = 2.66$	



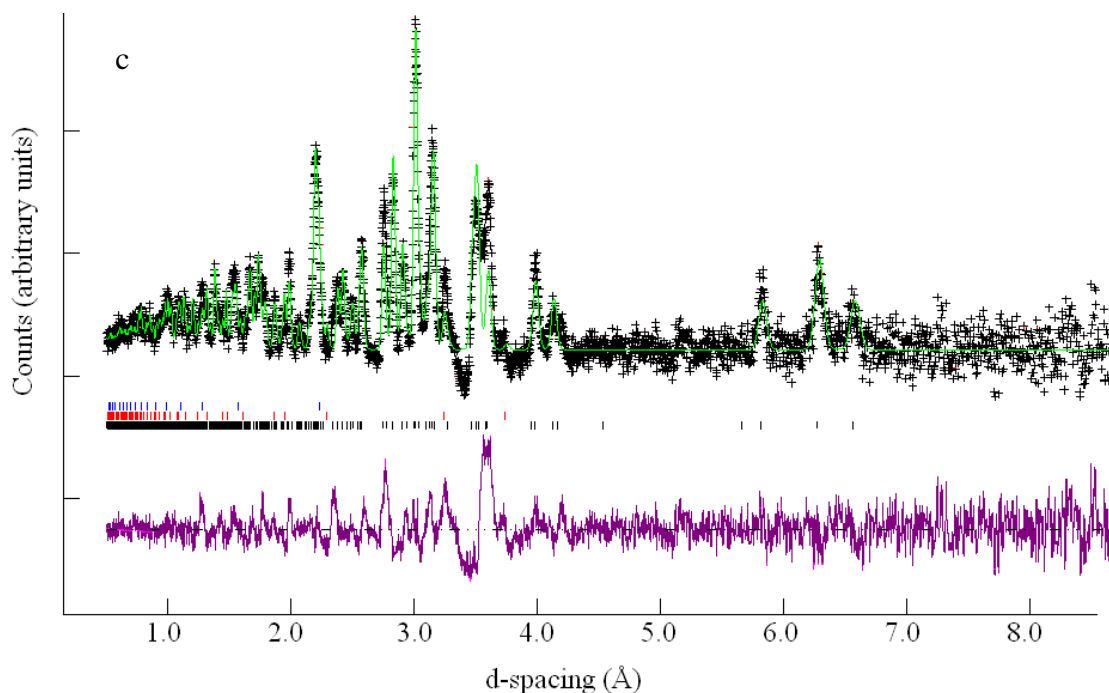


Figure 10.20 Rietveld refinement against neutron diffraction data for $\text{Ba}_2\text{Co}_{0.4}\text{Zn}_{0.6}\text{S}_3$: Black line (observed), green line (calculated) and purple line (difference). Black tick marks correspond to $\text{Ba}_2\text{Co}_{0.4}\text{Zn}_{0.6}\text{S}_3$, blue to Ba_2SiS_4 and red to BaS

Table 10.13 Atomic positions, thermal parameters and fractional occupancies for $\text{Ba}_2\text{Co}_{0.4}\text{Zn}_{0.6}\text{S}_3$

Atom	x	Y	z	U	F
Ba1	0.8258(3)	0.4843(2)	0.25	0.0138(6)	1
Ba2	0.4904(2)	0.6722(2)	0.25	0.0085(6)	1
Co	0.7484(3)	0.1994(2)	0.25	0.0067(6)	0.4
Zn	0.7484(3)	0.1994(2)	0.25	0.0067(6)	0.6
S1	0.8631(3)	0.0565(4)	0.25	0.0074(8)	1
S2	0.5572(3)	0.1421(4)	0.25	0.0056(8)	1
S3	0.2302(4)	0.7024(4)	0.25	0.0117(11)	1
$R_p = 6.01\%$		$R_{wp} = 2.93\%$		$\chi^2 = 3.11$	

10.3 Appendix 3

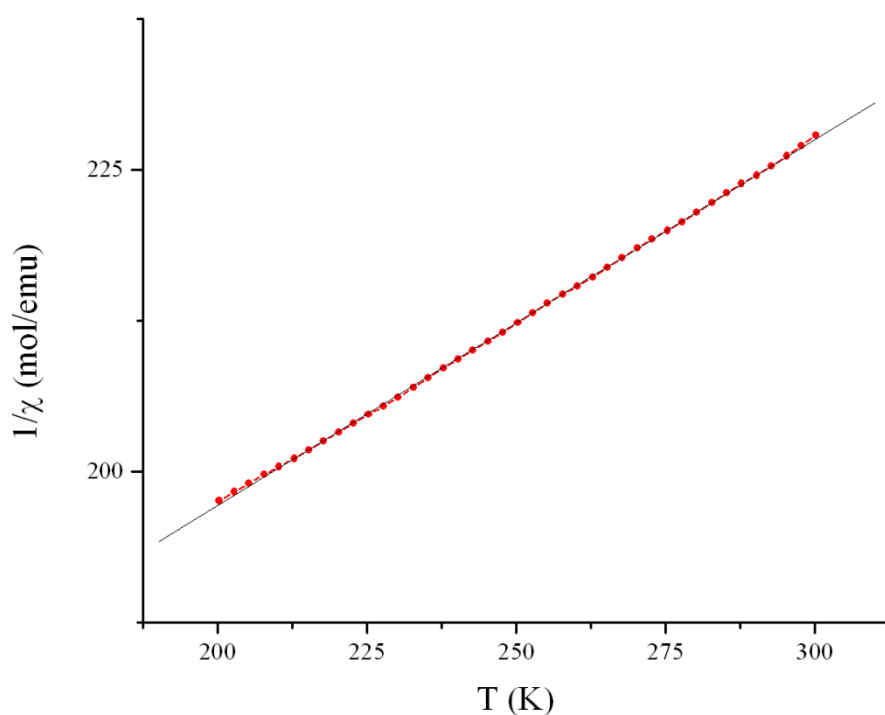


Figure 10.9 Linear fit (black line) of high temperature susceptibility data (red circles) for $\text{Ba}_2\text{Co}_{0.9}\text{Zn}_{0.1}\text{S}_3$

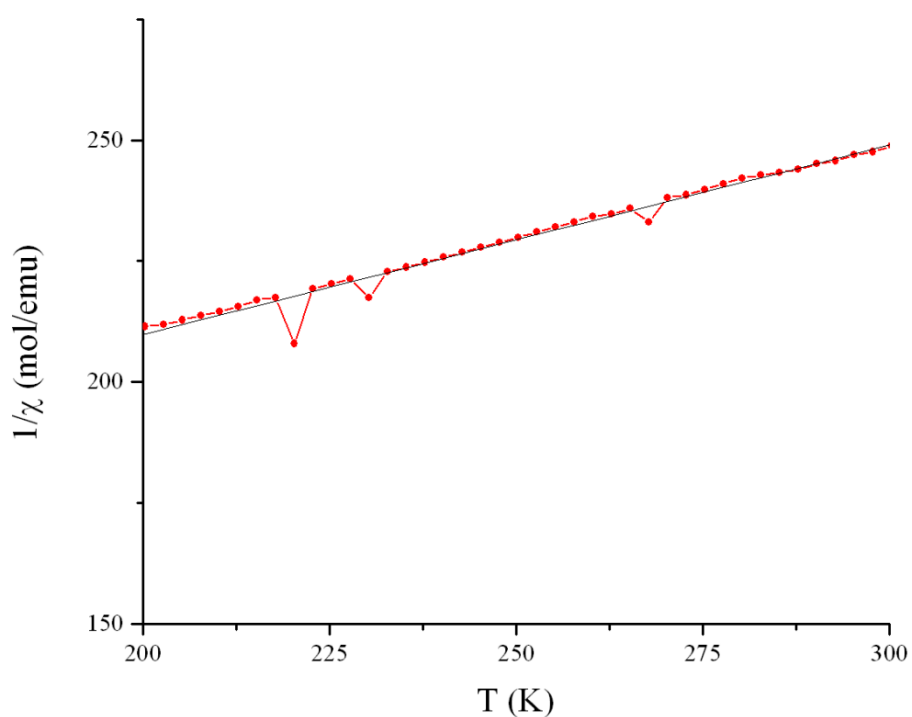


Figure 10.10 Linear fit (black line) of high temperature susceptibility data (red circles) for $\text{Ba}_2\text{Co}_{0.8}\text{Zn}_{0.2}\text{S}_3$

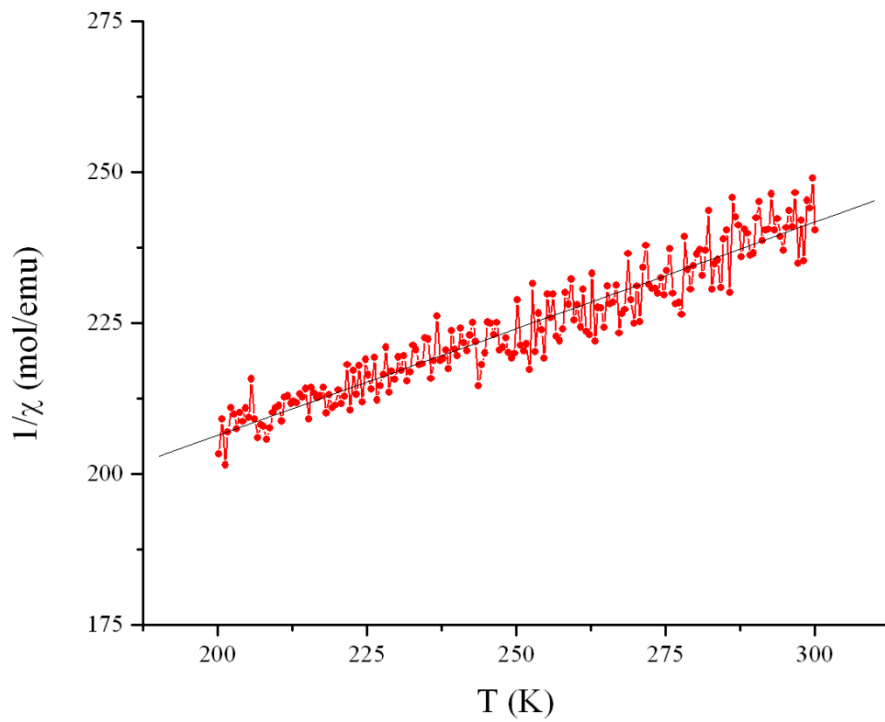


Figure 10.11 Linear fit (black line) of high temperature susceptibility data (red circles) for $\text{Ba}_2\text{Co}_{0.75}\text{Zn}_{0.25}\text{S}_3$

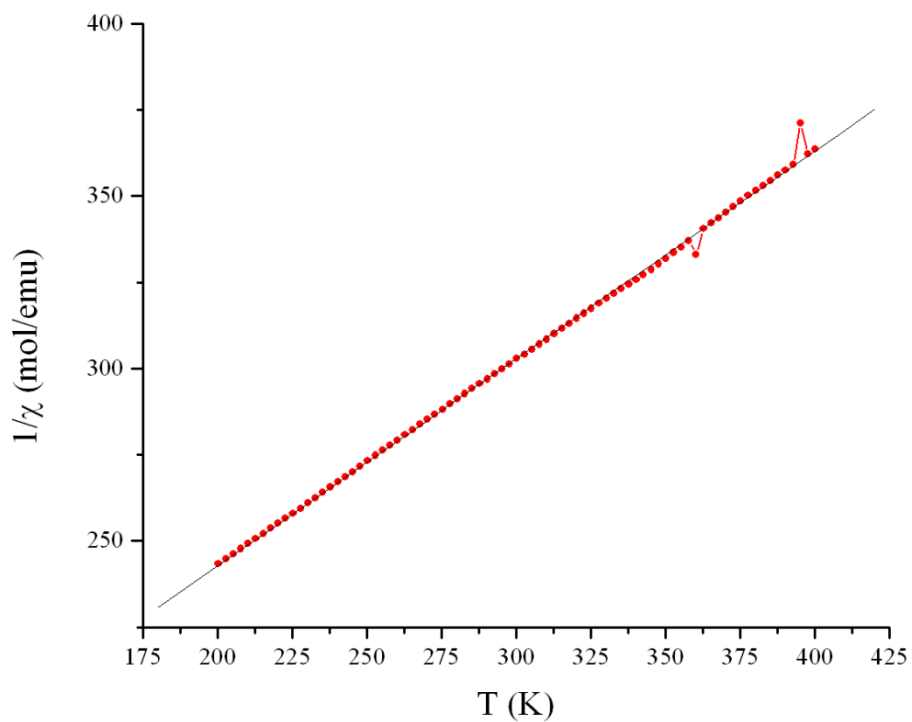


Figure 10.12 Linear fit (black line) of high temperature susceptibility data (red circles) for $\text{Ba}_2\text{Co}_{0.6}\text{Zn}_{0.4}\text{S}_3$

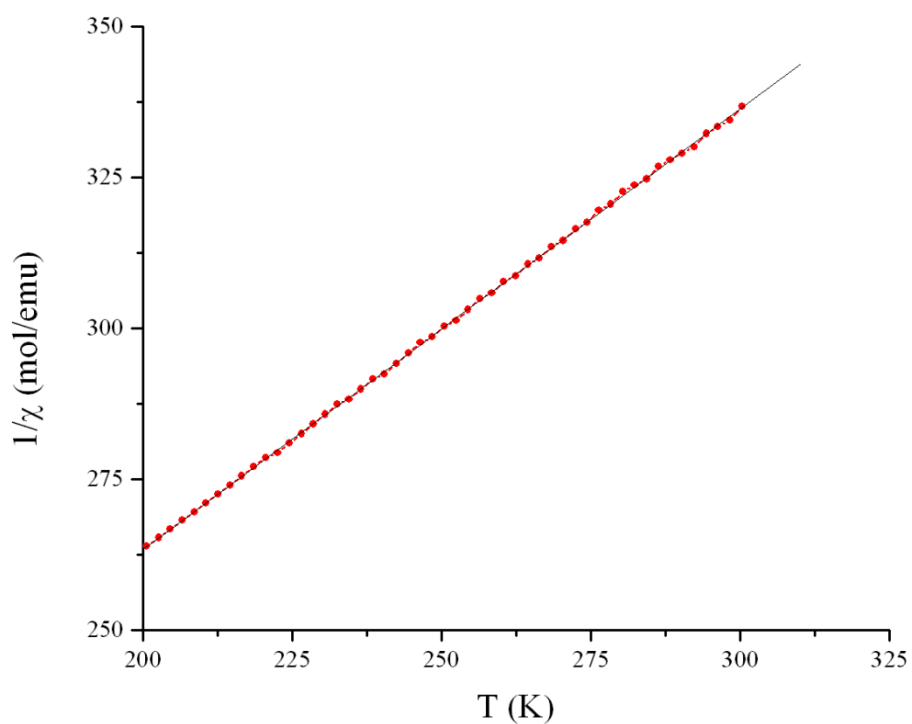


Figure 10.13 Linear fit (black line) of high temperature susceptibility data (red circles) for $\text{Ba}_2\text{Co}_{0.5}\text{Zn}_{0.5}\text{S}_3$

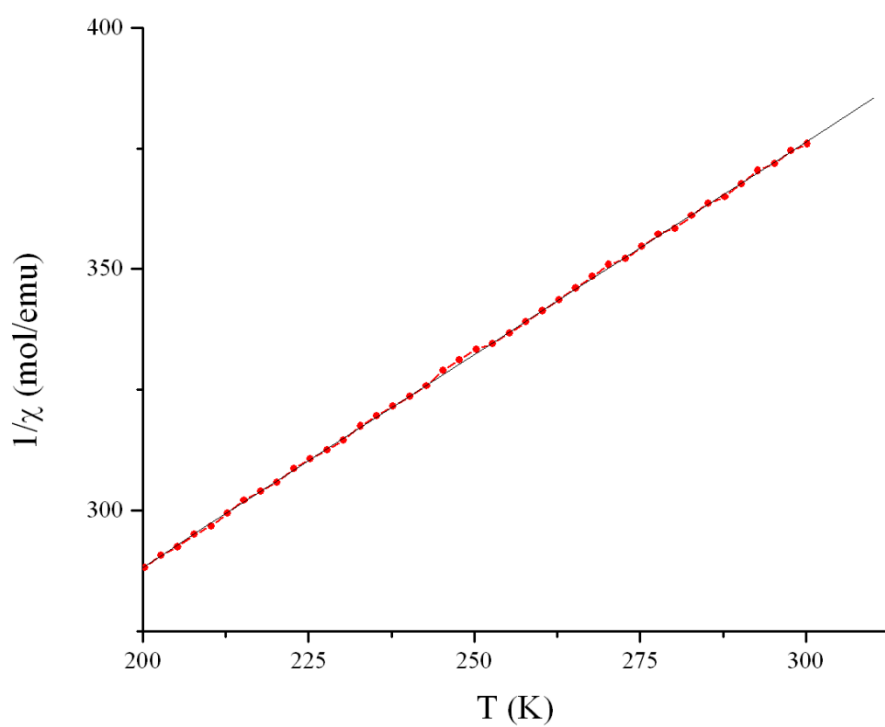


Figure 10.14 Linear fit (black line) of high temperature susceptibility data (red circles) for $\text{Ba}_2\text{Co}_{0.4}\text{Zn}_{0.6}\text{S}_3$

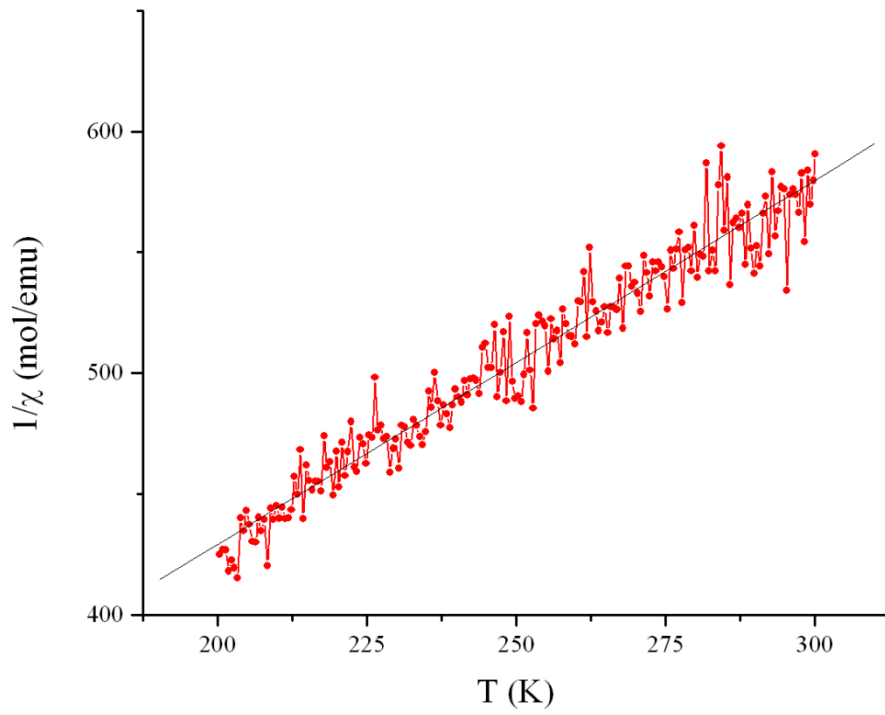


Figure 10.15 Linear fit (black line) of high temperature susceptibility data (red circles) for $\text{Ba}_2\text{Co}_{0.25}\text{Zn}_{0.75}\text{S}_3$

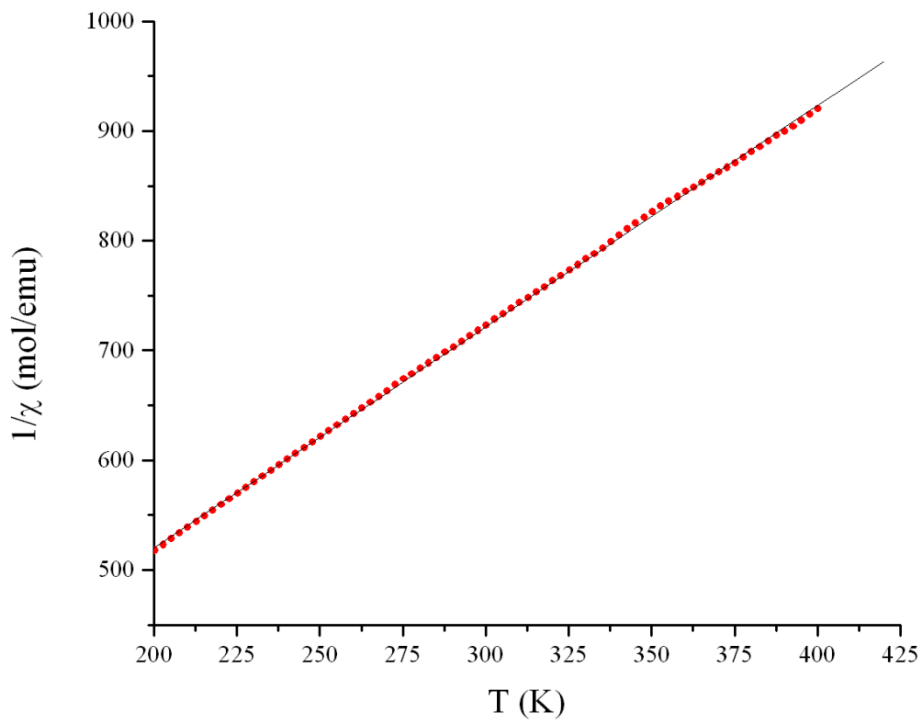


Figure 10.15 Linear fit (black line) of high temperature susceptibility data (red circles) for $\text{Ba}_2\text{Co}_{0.2}\text{Zn}_{0.8}\text{S}_3$

10.4 Appendix 4

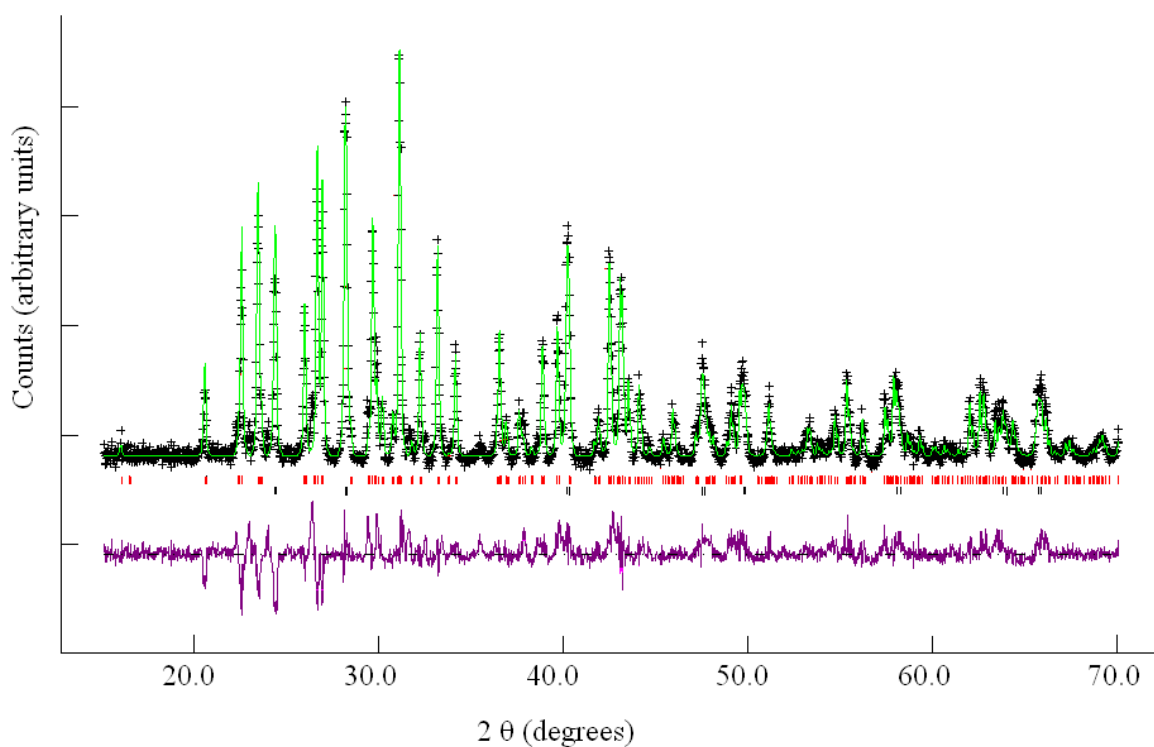


Figure 10.21 Rietveld refinement against X-ray diffraction data for $\text{Ba}_2\text{Zn}_{0.75}\text{Fe}_{0.25}\text{S}_3$: Black line (observed), green line (calculated) and purple line (difference). Red tick marks correspond to $\text{Ba}_2\text{Zn}_{0.75}\text{Fe}_{0.25}\text{S}_3$ and black to BaS.

Table 10.14 Refined atomic coordinates for $\text{Ba}_2\text{Zn}_{0.75}\text{Fe}_{0.25}\text{S}_3$

Atom	x	y	z	F
Ba1	0.8255(4)	0.4831(5)	0.25	1
Ba2	0.4874(5)	0.6757(4)	0.25	1
Zn	0.7485(9)	0.1950(9)	0.25	0.75
Fe	0.7485(9)	0.1950(9)	0.25	0.25
S1	0.8677(15)	0.0461(17)	0.25	1
S2	0.5519(17)	0.1353(19)	0.25	1
S3	0.2271(17)	0.7079(17)	0.25	1

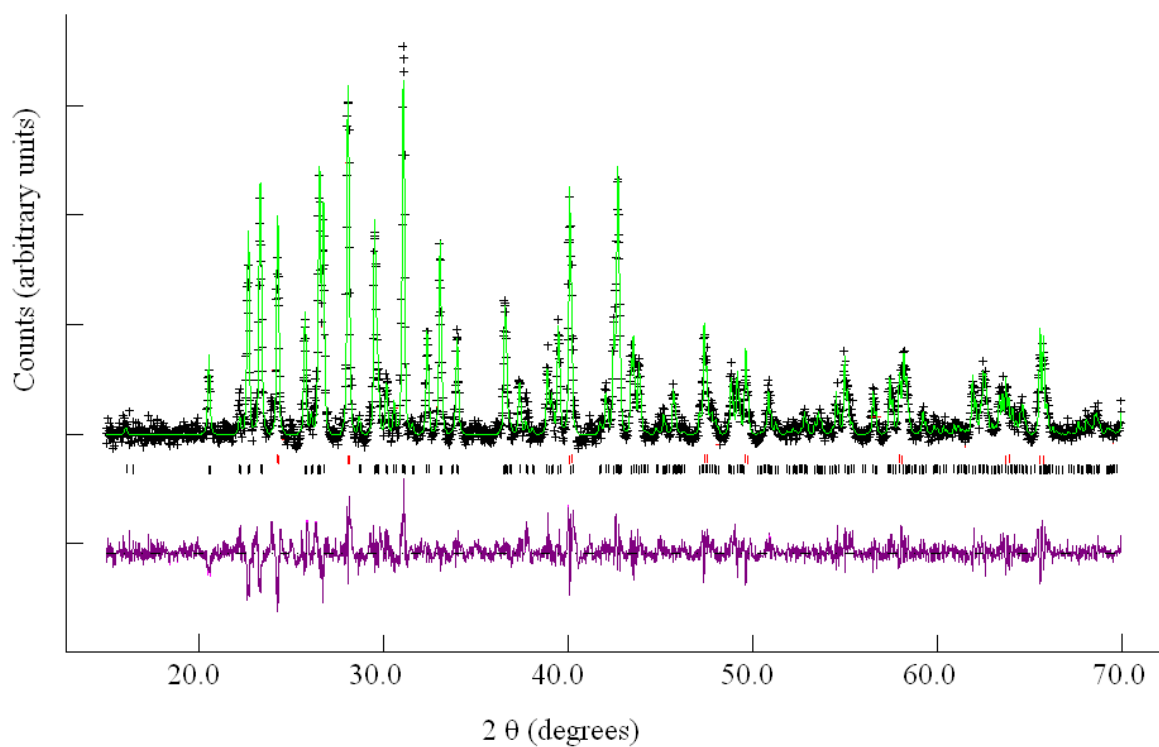


Figure 10.22 Rietveld refinement against X-ray diffraction data for $\text{Ba}_2\text{Zn}_{0.25}\text{Fe}_{0.75}\text{S}_3$: Black line (observed), green line (calculated) and purple line (difference). Black tick marks correspond to $\text{Ba}_2\text{Zn}_{0.25}\text{Fe}_{0.75}\text{S}_3$ and red to BaS.

Table 10.15 Refined atomic coordinates for $\text{Ba}_2\text{Zn}_{0.25}\text{Fe}_{0.75}\text{S}_3$

Atom	x	y	z	F
Ba1	0.8278(5)	0.4818(5)	0.25	1
Ba2	0.4889(6)	0.6748(5)	0.25	1
Zn	0.7464(11)	0.1931(11)	0.25	0.25
Fe	0.7464(11)	0.1931(11)	0.25	0.75
S1	0.8693(19)	0.0578(19)	0.25	1
S2	0.5570(19)	0.1418(21)	0.25	1
S3	0.2287(19)	0.7071(21)	0.25	1

10.5 Appendix 5

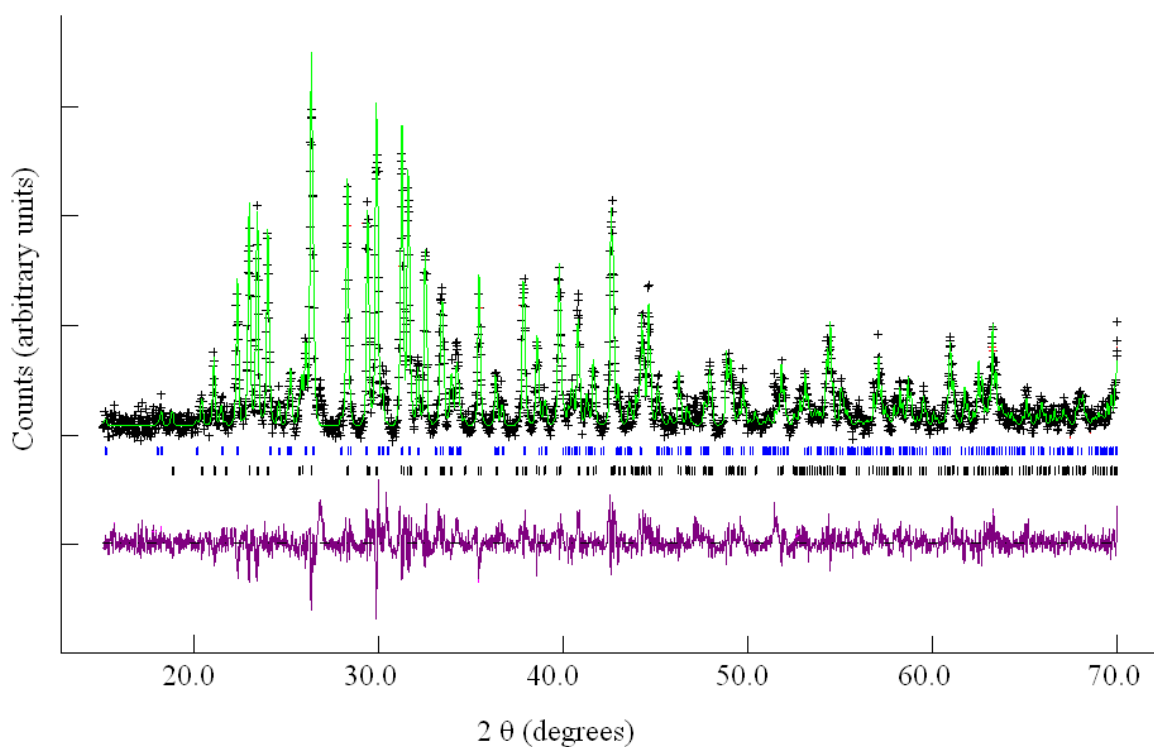
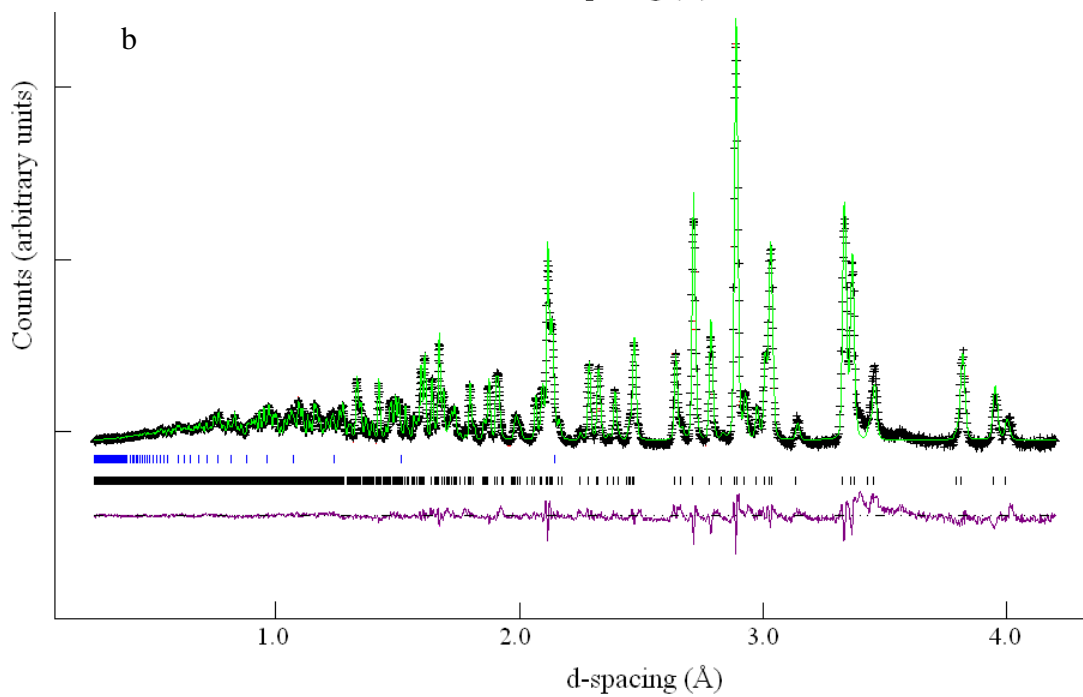
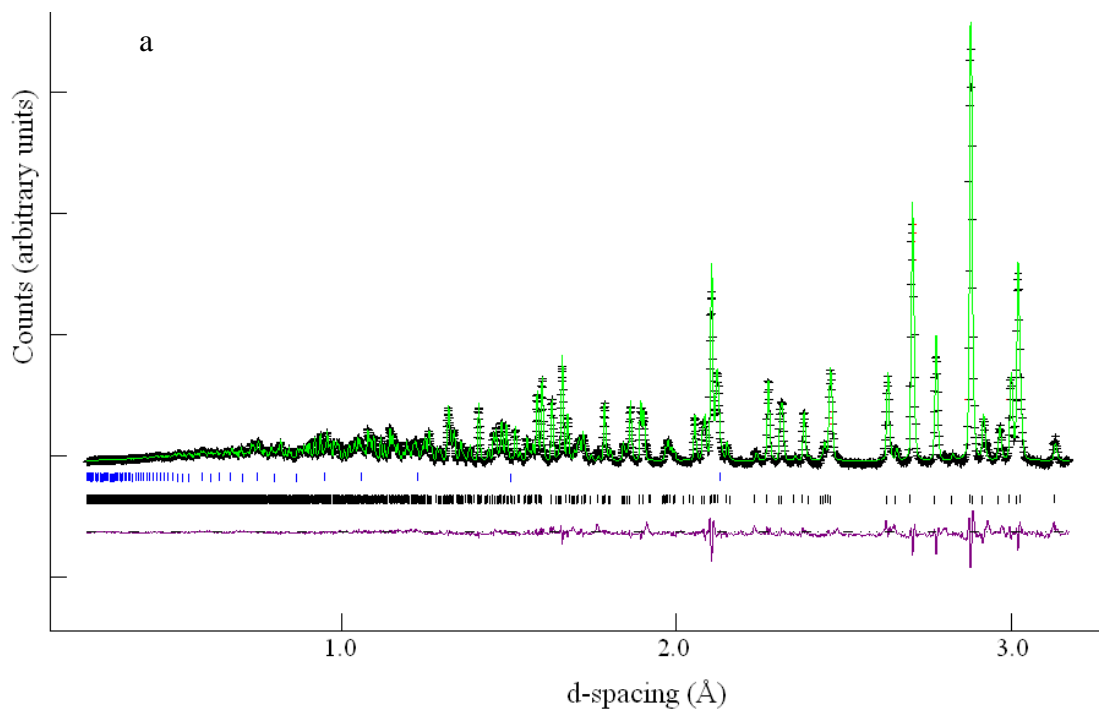


Figure 10.23 Rietveld refinement against X-ray diffraction data for $\text{Ba}_2\text{Zn}_{0.75}\text{Mn}_{0.25}\text{S}_3$: Black line (observed), green line (calculated) and purple line (difference). Black tick marks correspond to $\text{Ba}_2\text{Zn}_{0.75}\text{Mn}_{0.25}\text{S}_3$ and blue to BaSi_4 .

Table 10.16 Refined atomic coordinates for $\text{Ba}_2\text{Zn}_{0.75}\text{Mn}_{0.25}\text{S}_3$

Atom	x	y	z	F
Ba1	0.4194(8)	0.25	0.7122(5)	1
Ba2	0.4874(5)	0.25	0.4562(4)	1
Mn	0.3616(15)	0.25	0.1351(9)	0.25
Zn	0.3616(15)	0.25	0.1351(9)	0.75
S1	0.3100(28)	0.25	0.2772(2)	1
S2	0.1237(31)	0.25	0.0656(18)	1
S3	1.0043(27)	0.25	0.5959(15)	1

10.6 Appendix 6



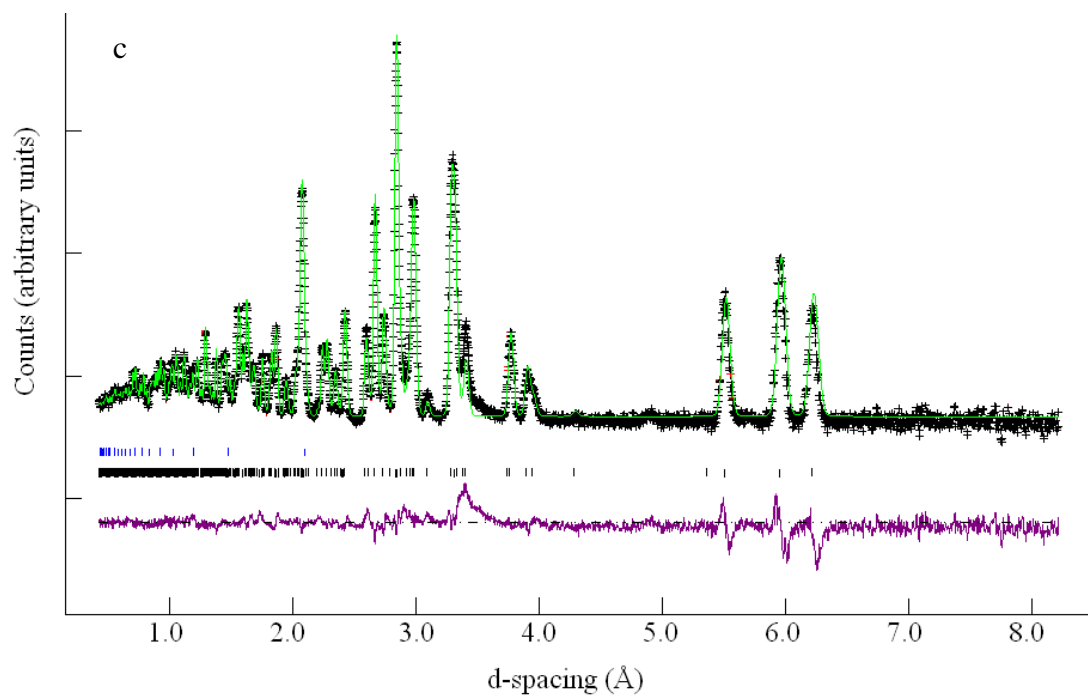
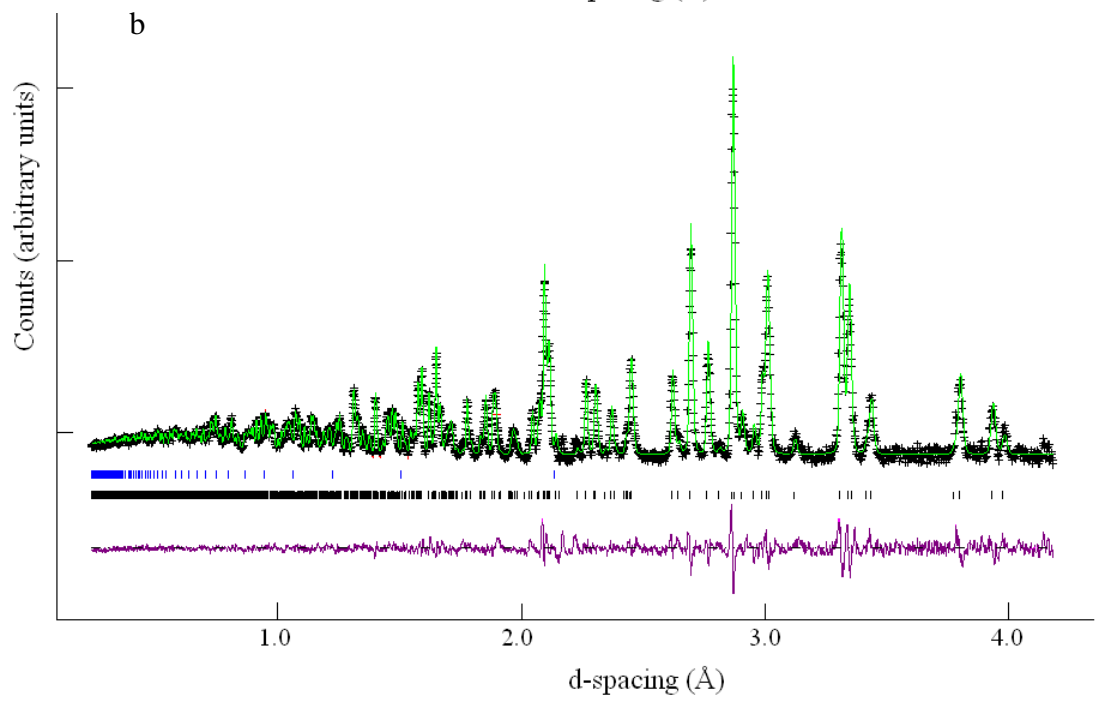
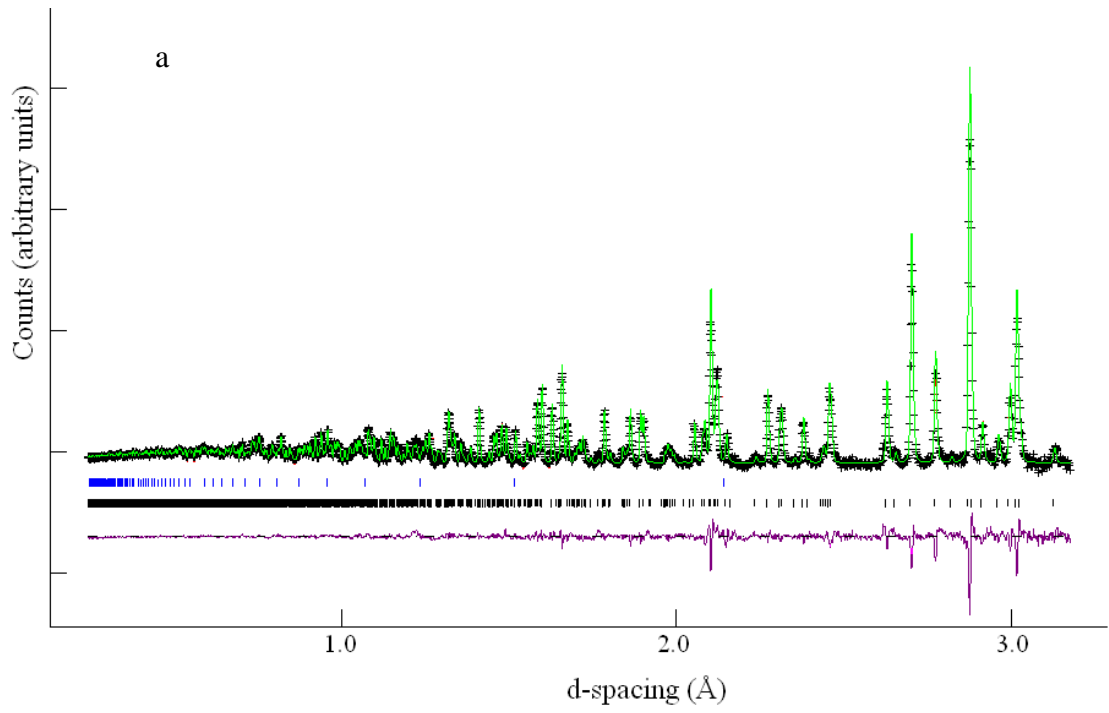


Figure 10.24 Rietveld refinement against neutron diffraction data for $\text{Ba}_2\text{Zn}_{0.75}\text{Fe}_{0.25}\text{S}_3$ from banks 1, 2 and 3 (a, b and c respectively) at room temperature: Black line (observed), green line (calculated) and purple line (difference). Black tick marks correspond to $\text{Ba}_2\text{Zn}_{0.75}\text{Fe}_{0.25}\text{S}_3$ blue to Ba_2SiS_4



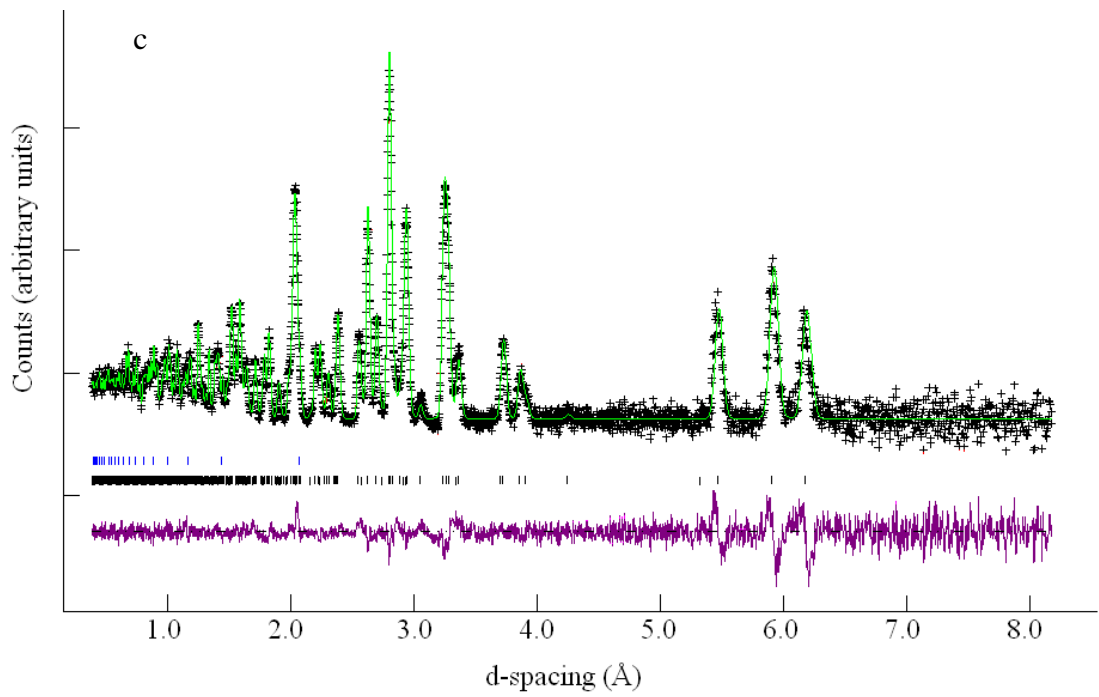
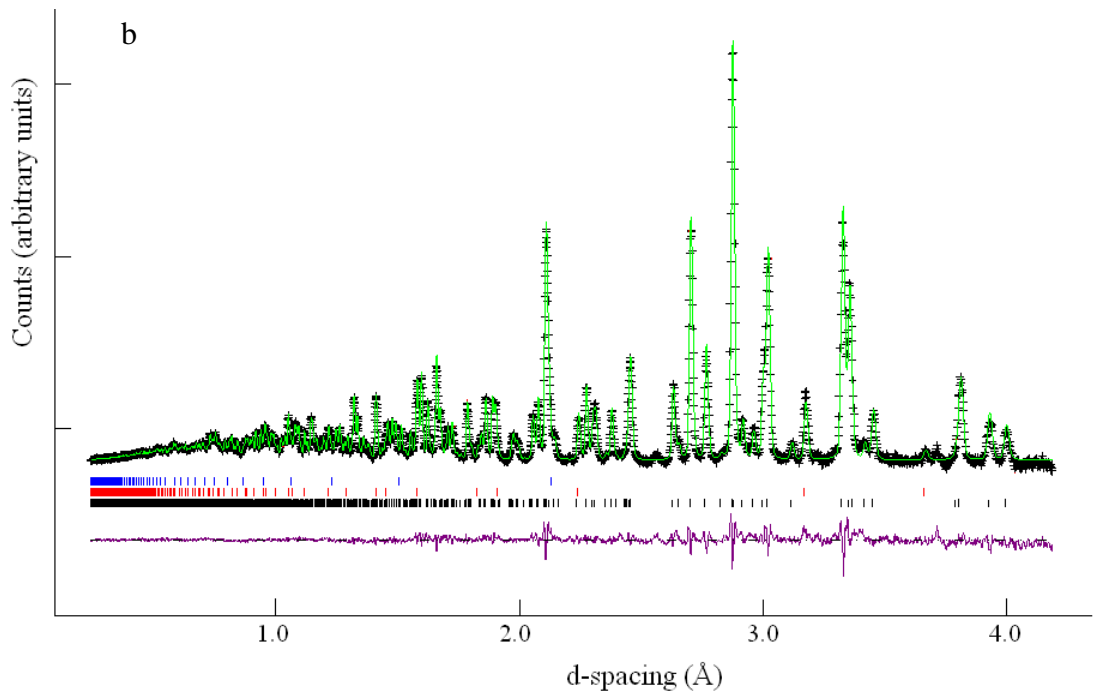
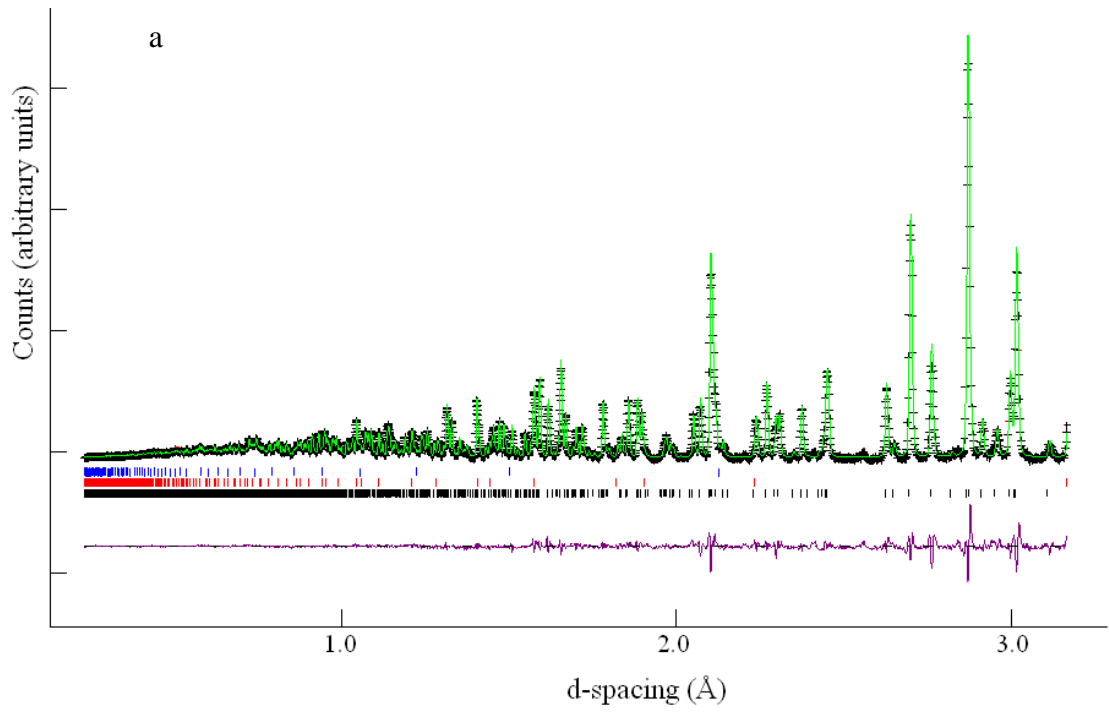


Figure 10.25 Rietveld refinement against neutron diffraction data for $\text{Ba}_2\text{Zn}_{0.75}\text{Fe}_{0.25}\text{S}_3$ from banks 1, 2 and 3 (a, b and c respectively) at 5 K: Black line (observed), green line (calculated) and purple line (difference). Black tick marks correspond to $\text{Ba}_2\text{Zn}_{0.75}\text{Fe}_{0.25}\text{S}_3$ blue to Ba_2SiS_4



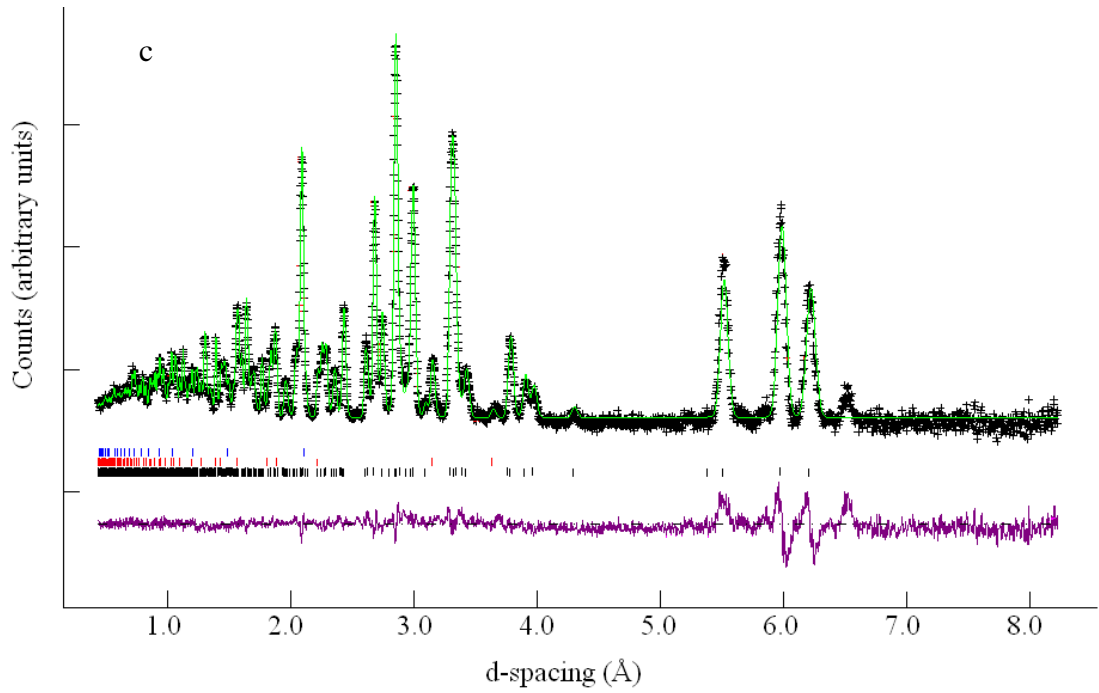
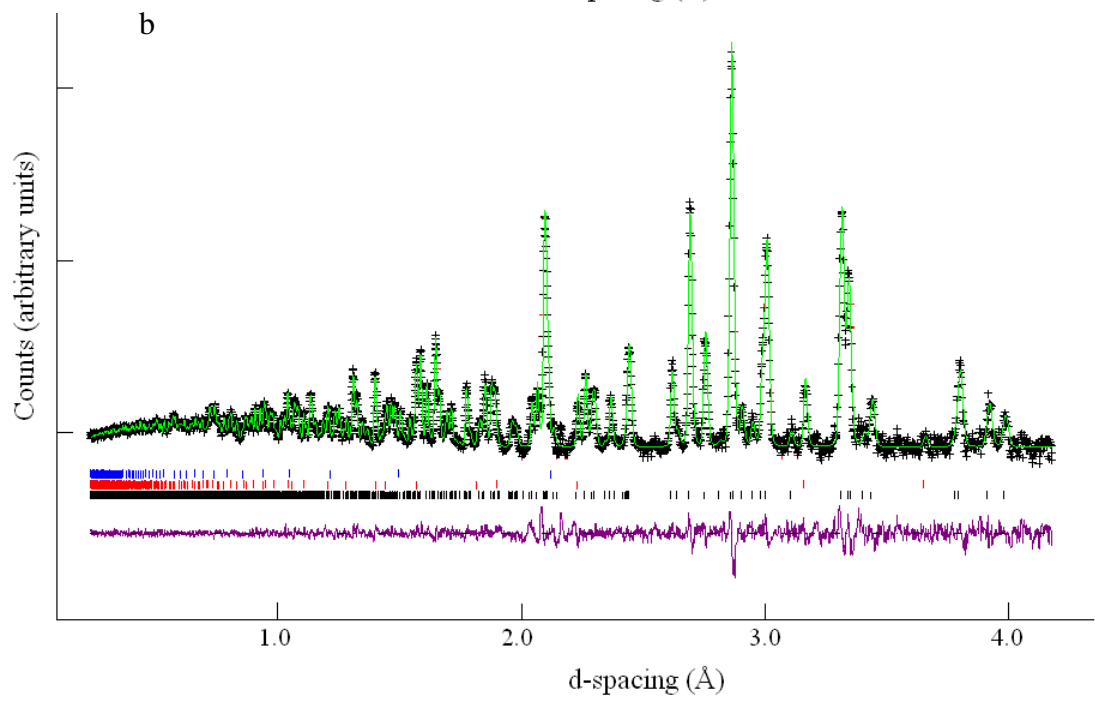
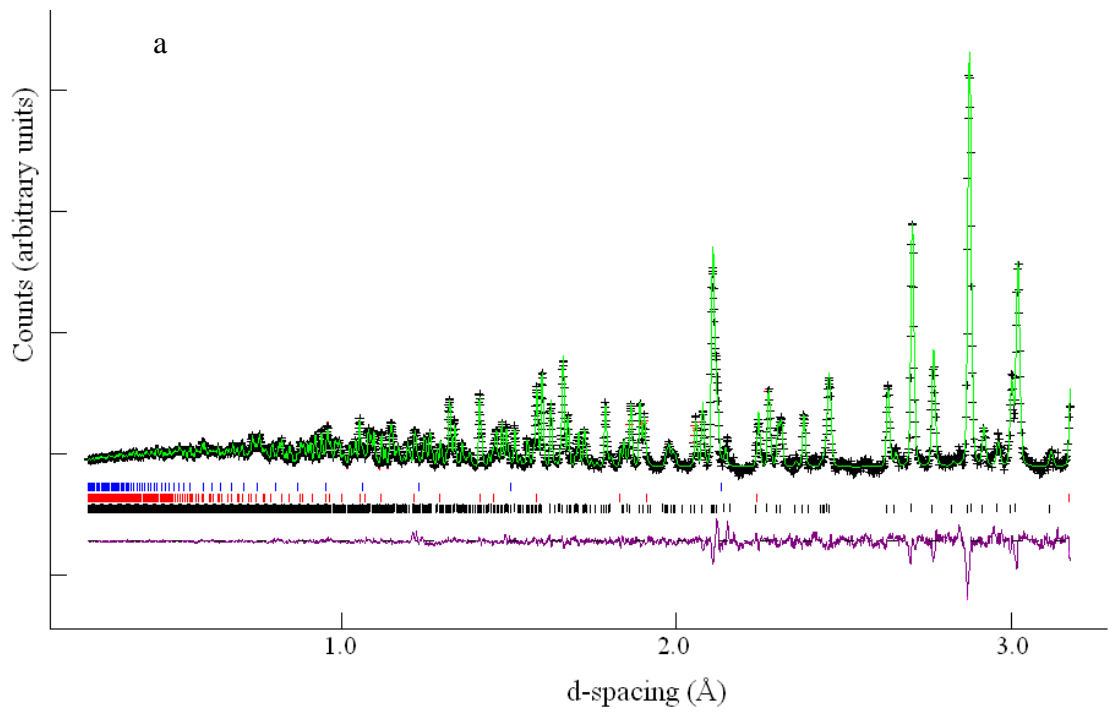


Figure 10.26 Rietveld refinement against neutron diffraction data for $\text{Ba}_2\text{Zn}_{0.5}\text{Fe}_{0.5}\text{S}_3$ from banks 1, 2 and 3 (a, b and c respectively) at room temperature: Black line (observed), green line (calculated) and purple line (difference). Black tick marks correspond to $\text{Ba}_2\text{Zn}_{0.5}\text{Fe}_{0.5}\text{S}_3$ blue to Ba_2SiS_4



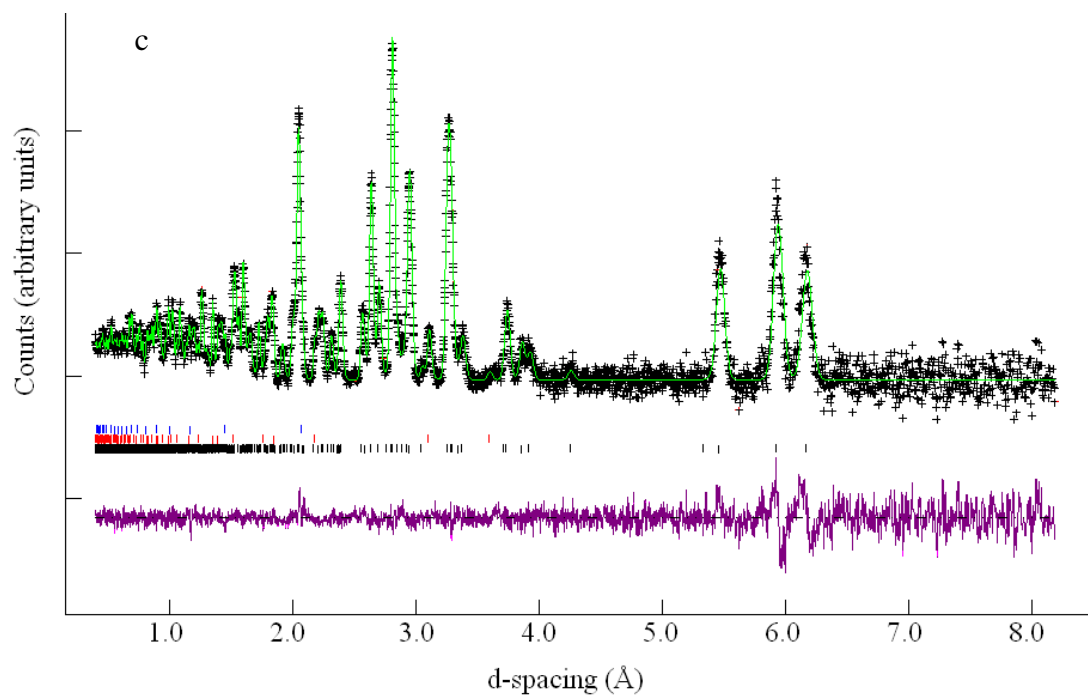
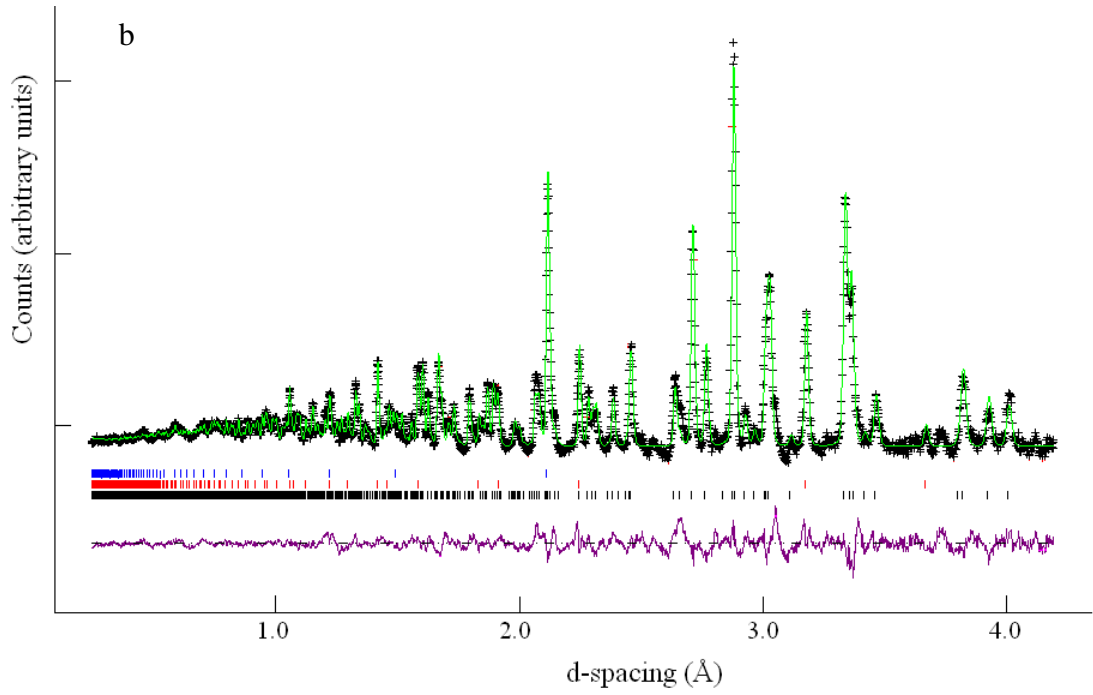
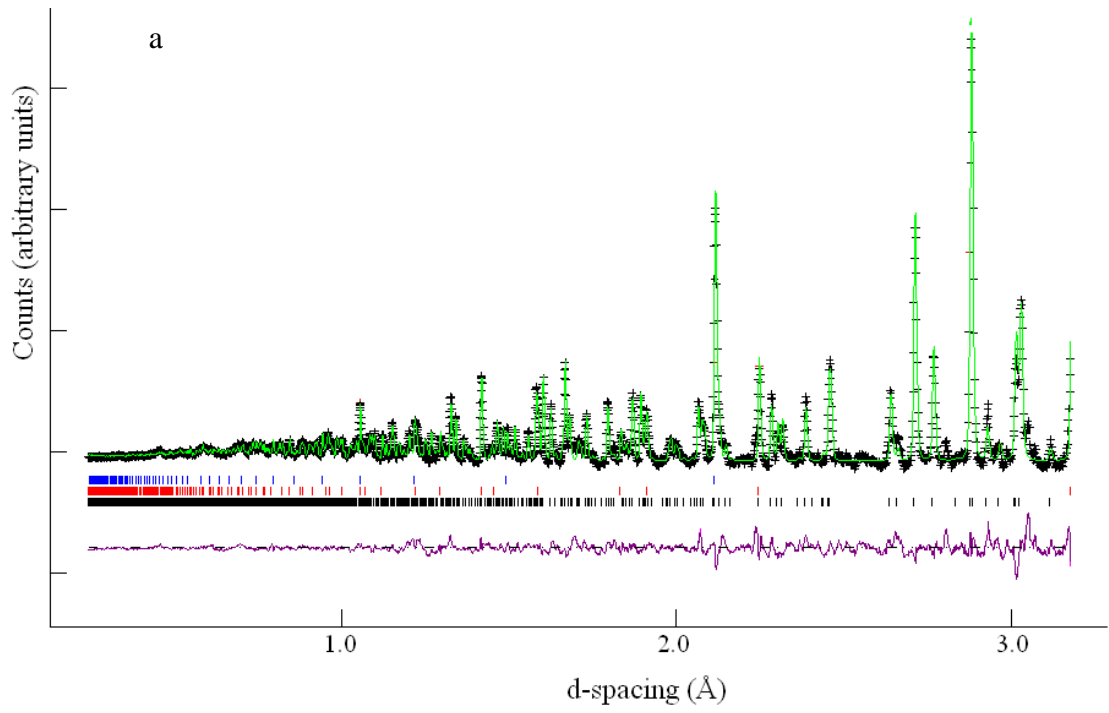


Figure 10.27 Rietveld refinement against neutron diffraction data for $\text{Ba}_2\text{Zn}_{0.5}\text{Fe}_{0.5}\text{S}_3$ from banks 1, 2 and 3 (a, b and c respectively) at 5 K: Black line (observed), green line (calculated) and purple line (difference). Black tick marks correspond to $\text{Ba}_2\text{Zn}_{0.5}\text{Fe}_{0.5}\text{S}_3$ blue to Ba_2SiS_4



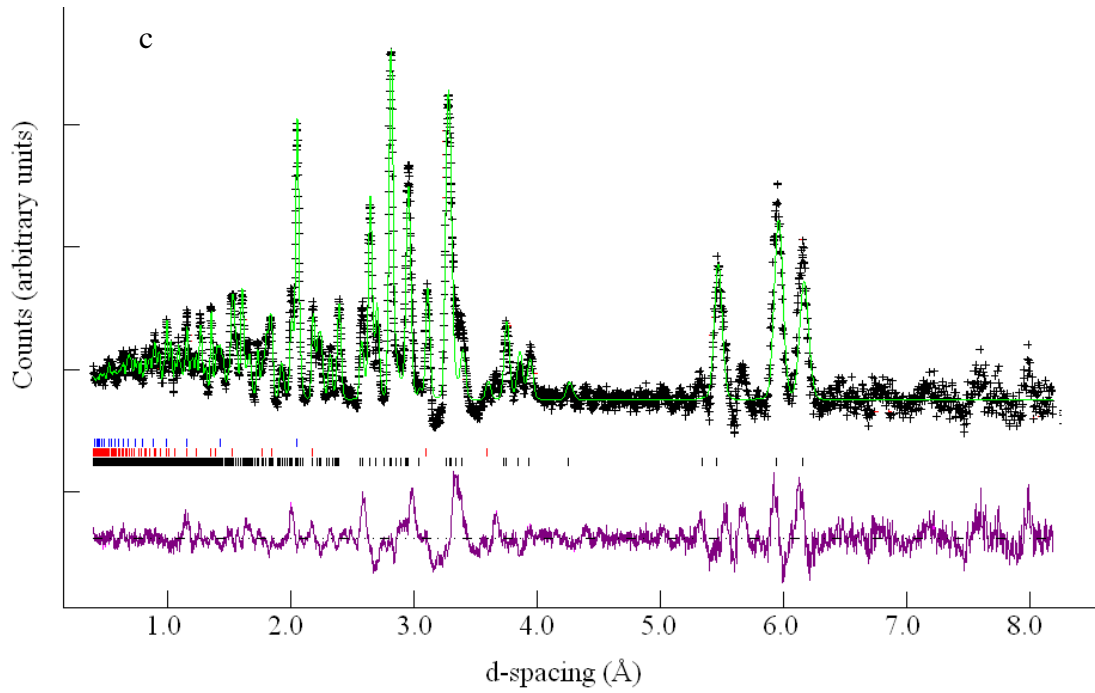
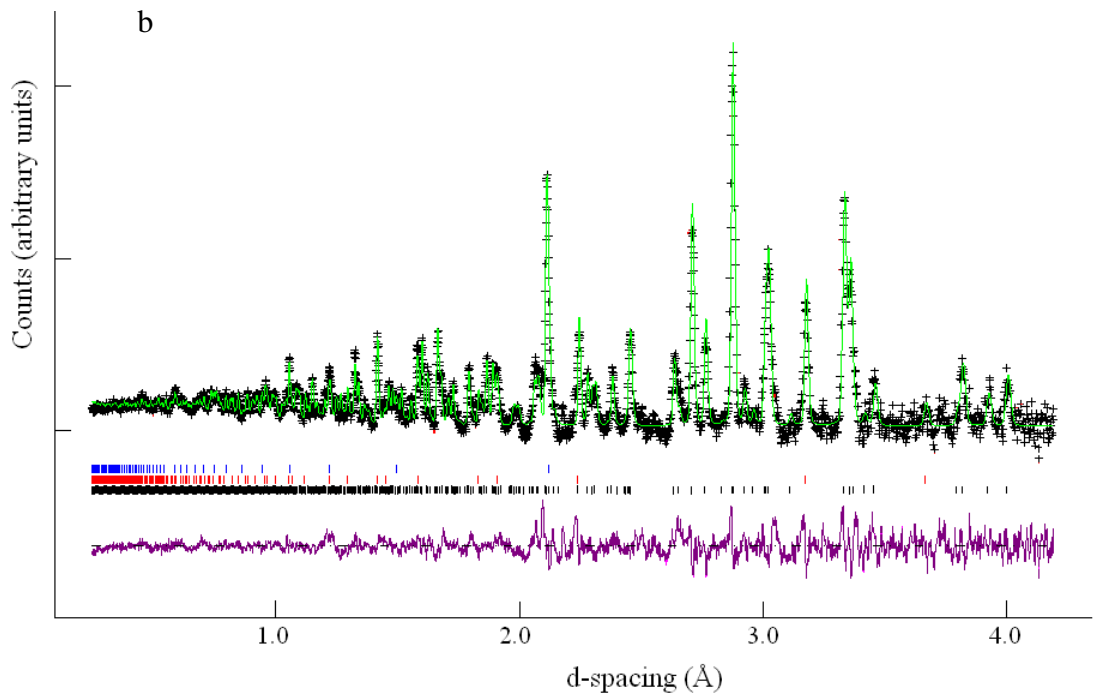
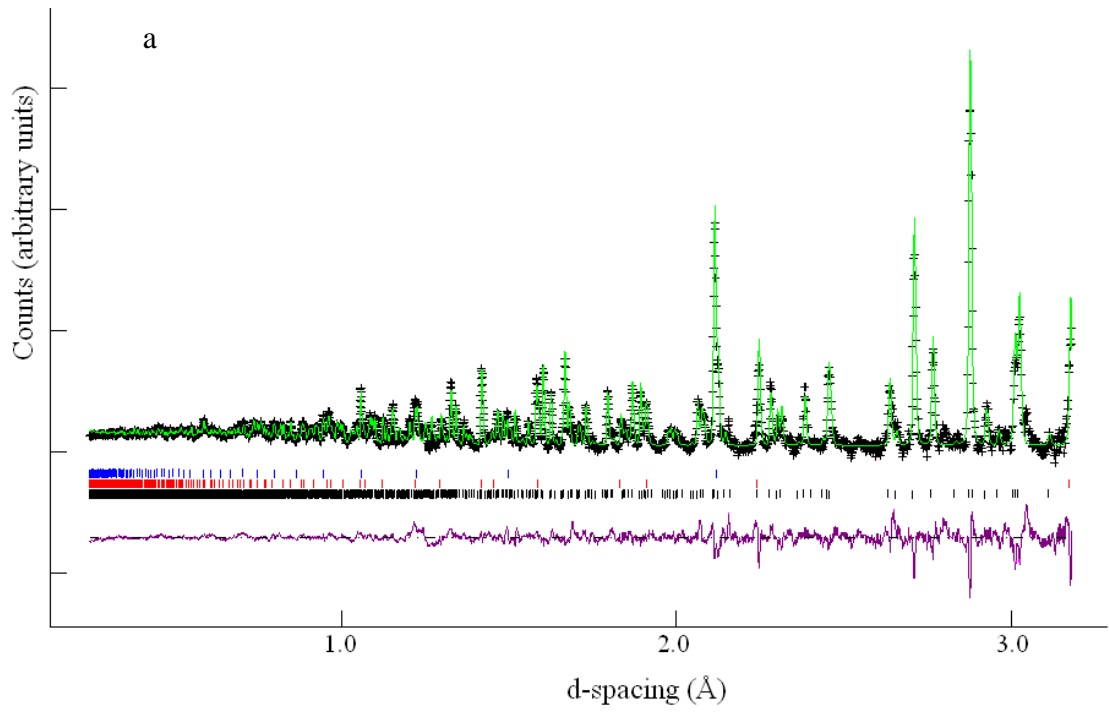


Figure 10.28 Rietveld refinement against neutron diffraction data for $\text{Ba}_2\text{Zn}_{0.25}\text{Fe}_{0.75}\text{S}_3$ from banks 1, 2 and 3 (a, b and c respectively) at room temperature: Black line (observed), green line (calculated) and purple line (difference). Black tick marks correspond to $\text{Ba}_2\text{Zn}_{0.25}\text{Fe}_{0.75}\text{S}_3$ blue to Ba_2Si_4



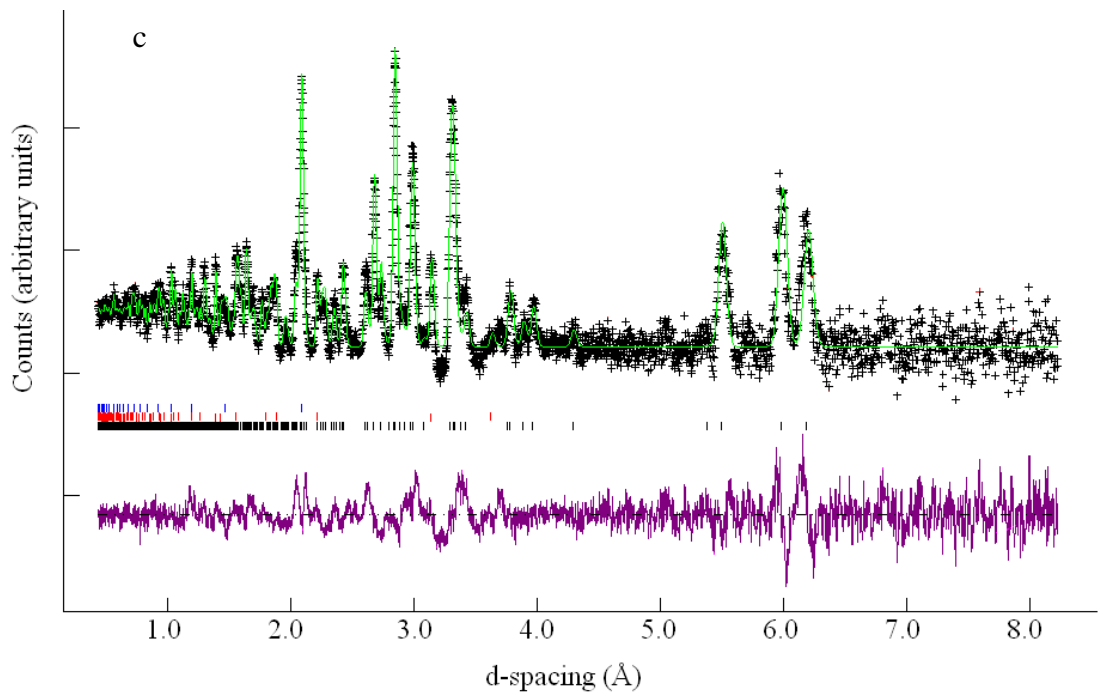
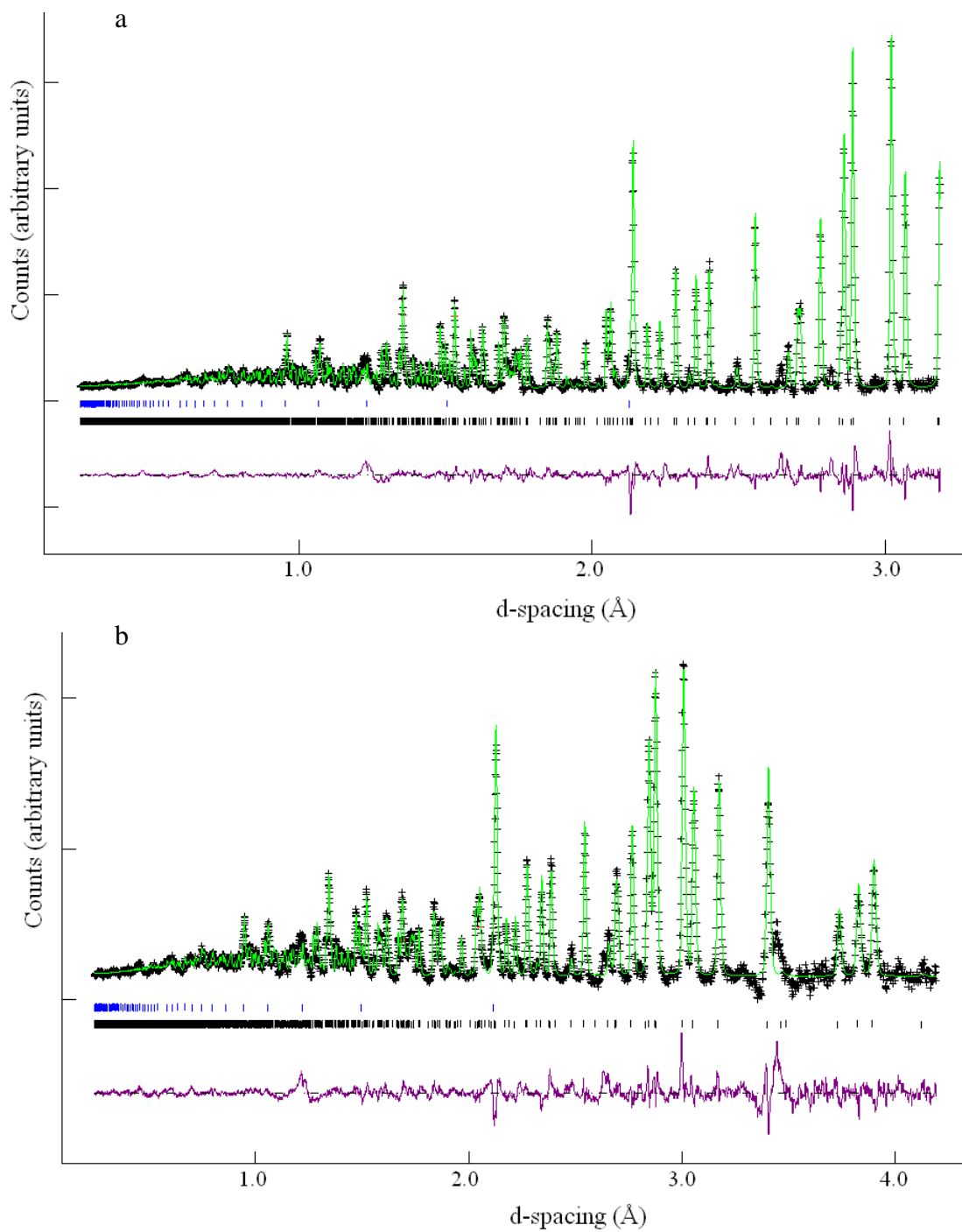


Figure 10.28 Rietveld refinement against neutron diffraction data for $\text{Ba}_2\text{Zn}_{0.25}\text{Fe}_{0.75}\text{S}_3$ from banks 1, 2 and 3 (a, b and c respectively) at 5 K: Black line (observed), green line (calculated) and purple line (difference). Black tick marks correspond to $\text{Ba}_2\text{Zn}_{0.25}\text{Fe}_{0.75}\text{S}_3$ blue to Ba_2SiS_4

10.7 Appendix 7



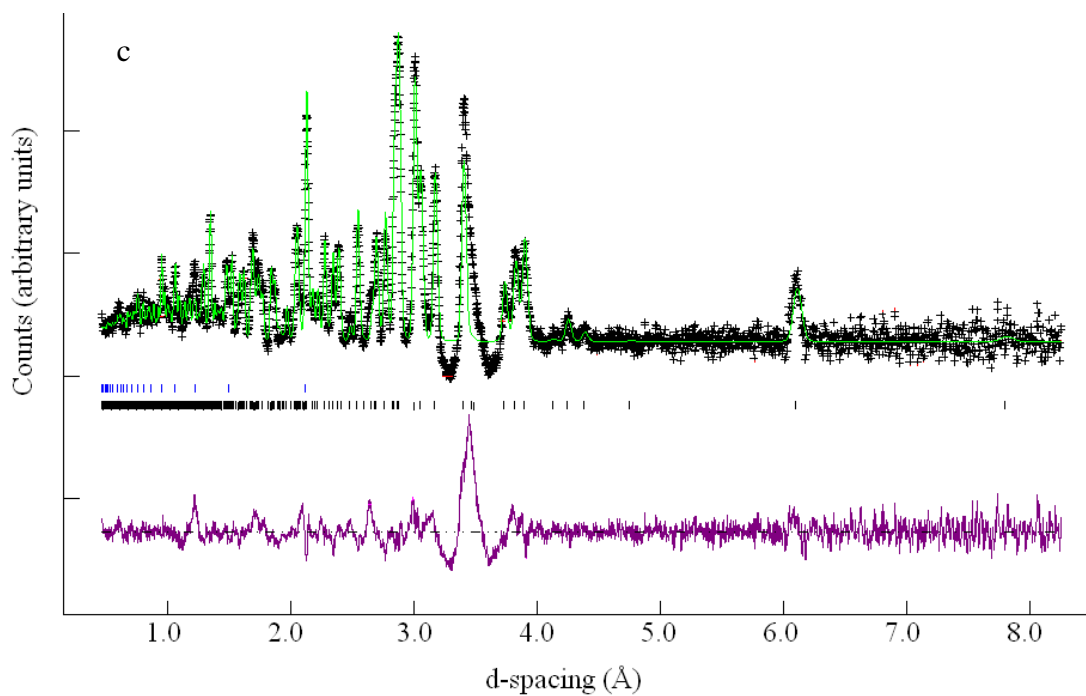
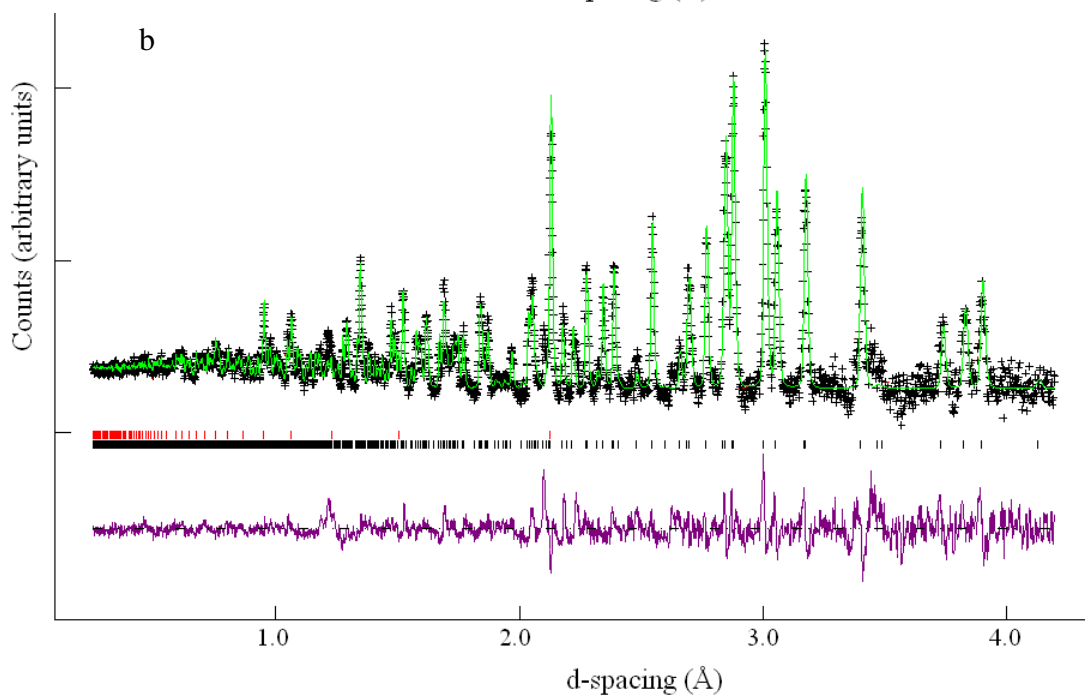
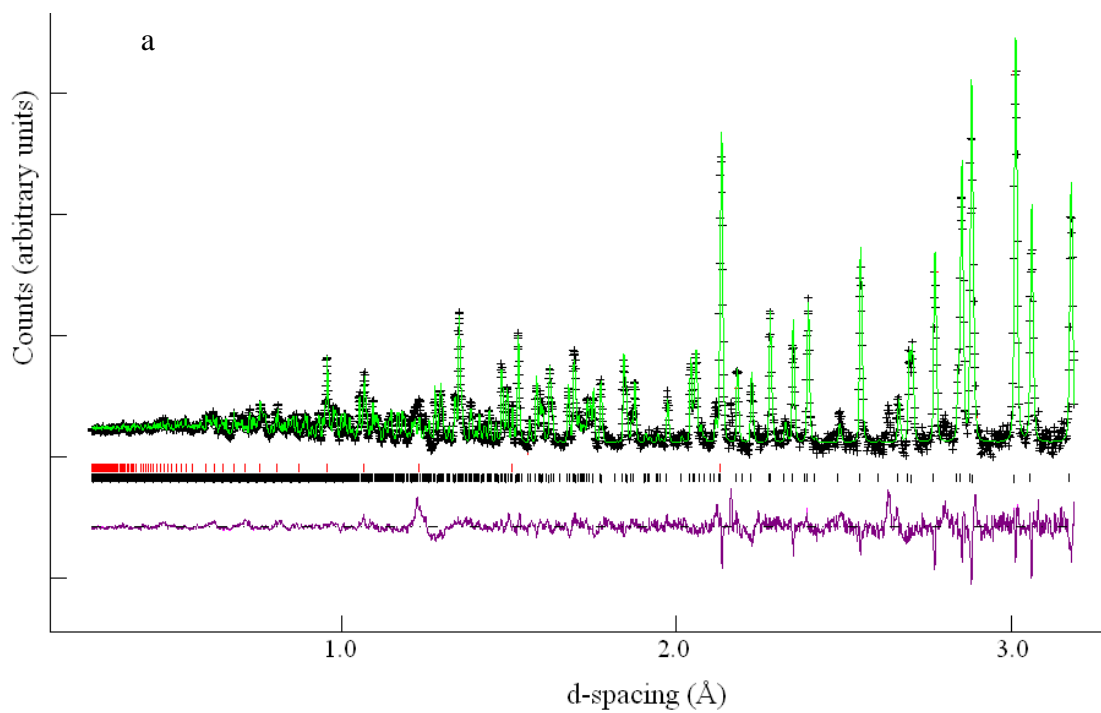


Figure 10.29 Rietveld refinement against neutron diffraction data for $\text{Ba}_2\text{Zn}_{0.75}\text{Mn}_{0.25}\text{S}_3$ from banks 1, 2 and 3 (a, b and c respectively) at room temperature: Black line (observed), green line (calculated) and purple line (difference). Black tick marks correspond to $\text{Ba}_2\text{Zn}_{0.75}\text{Mn}_{0.25}\text{S}_3$ blue to Ba_2SiS_4



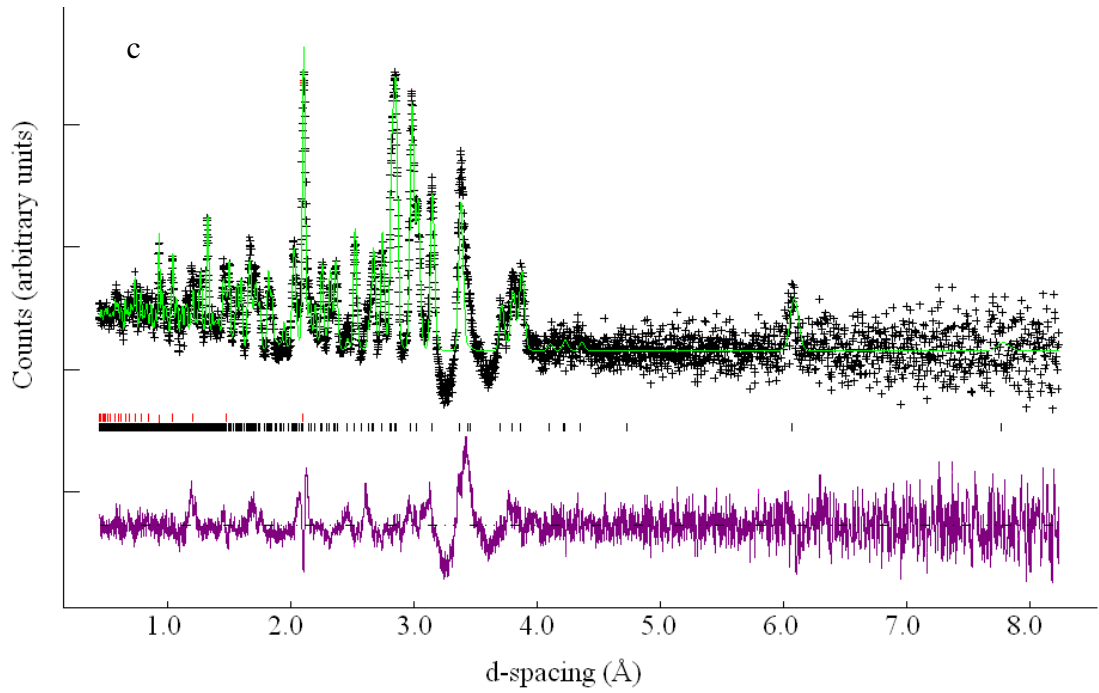
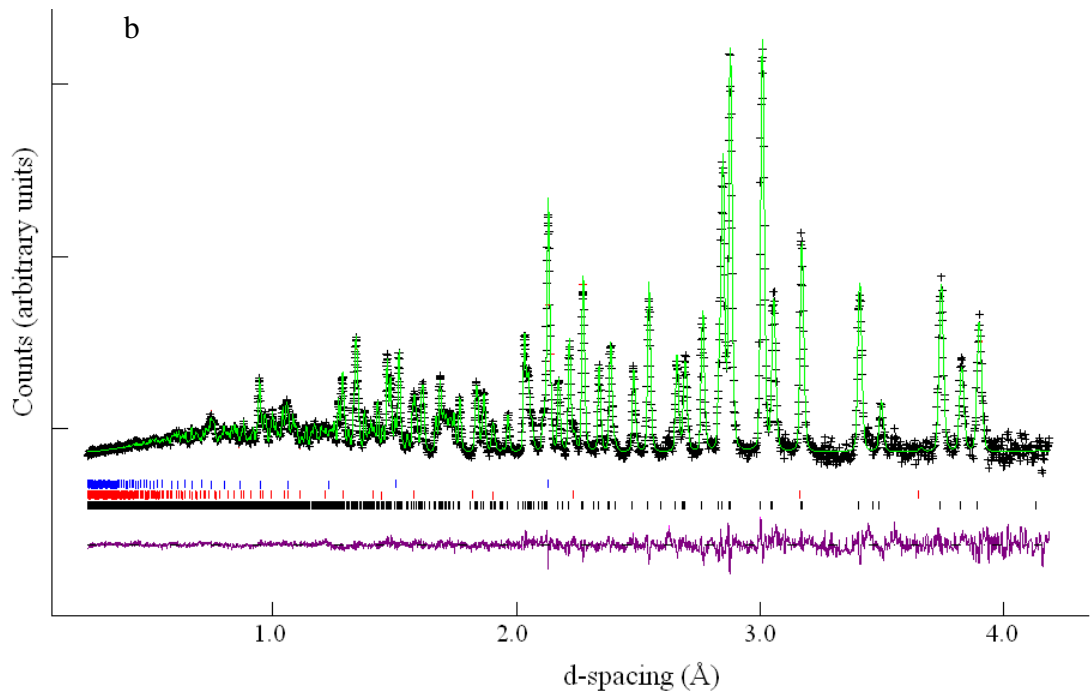
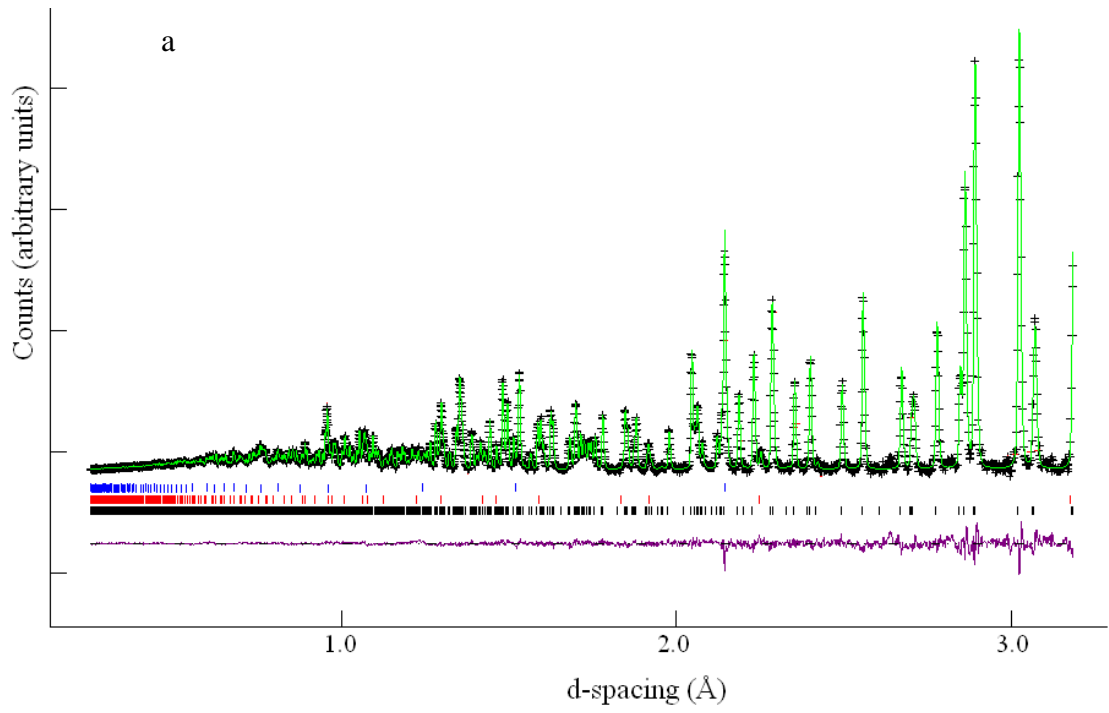


Figure 10.30 Rietveld refinement against neutron diffraction data for $\text{Ba}_2\text{Zn}_{0.75}\text{Mn}_{0.25}\text{S}_3$ from banks 1, 2 and 3 (a, b and c respectively) at 5 K: Black line (observed), green line (calculated) and purple line (difference). Black tick marks correspond to $\text{Ba}_2\text{Zn}_{0.75}\text{Mn}_{0.25}\text{S}_3$ blue to Ba_2SiS_4



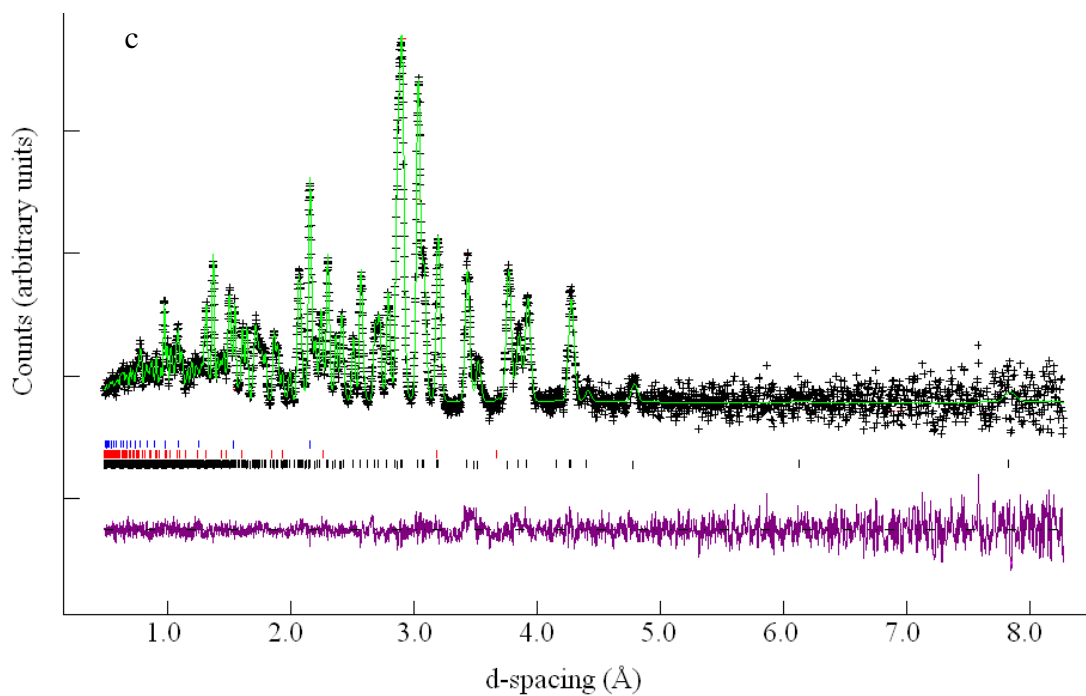
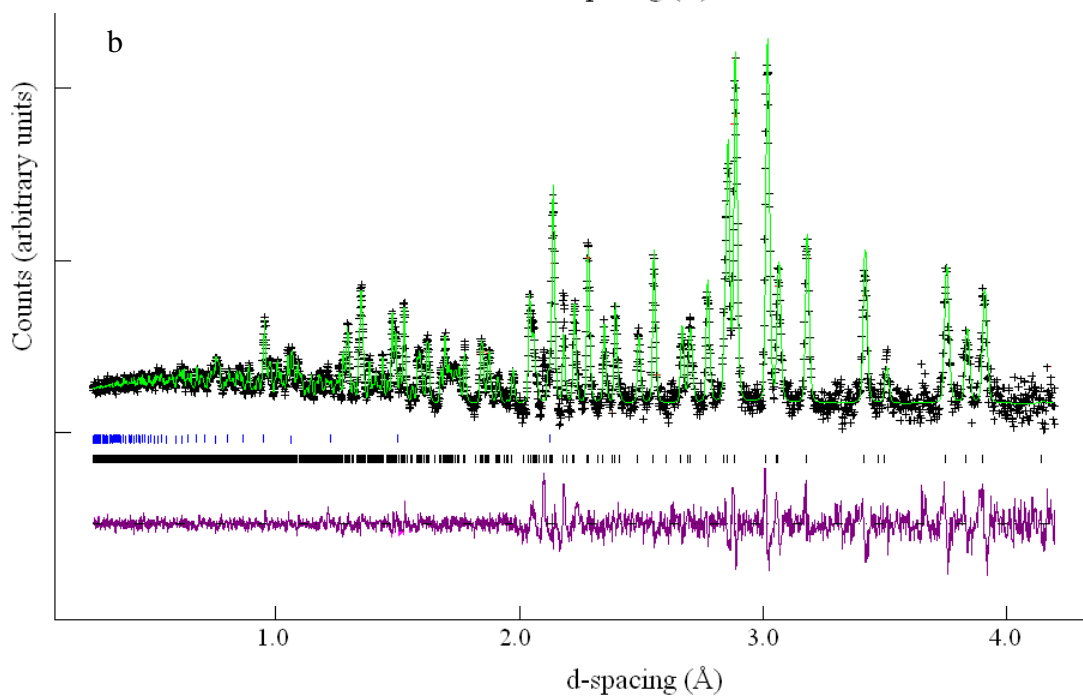
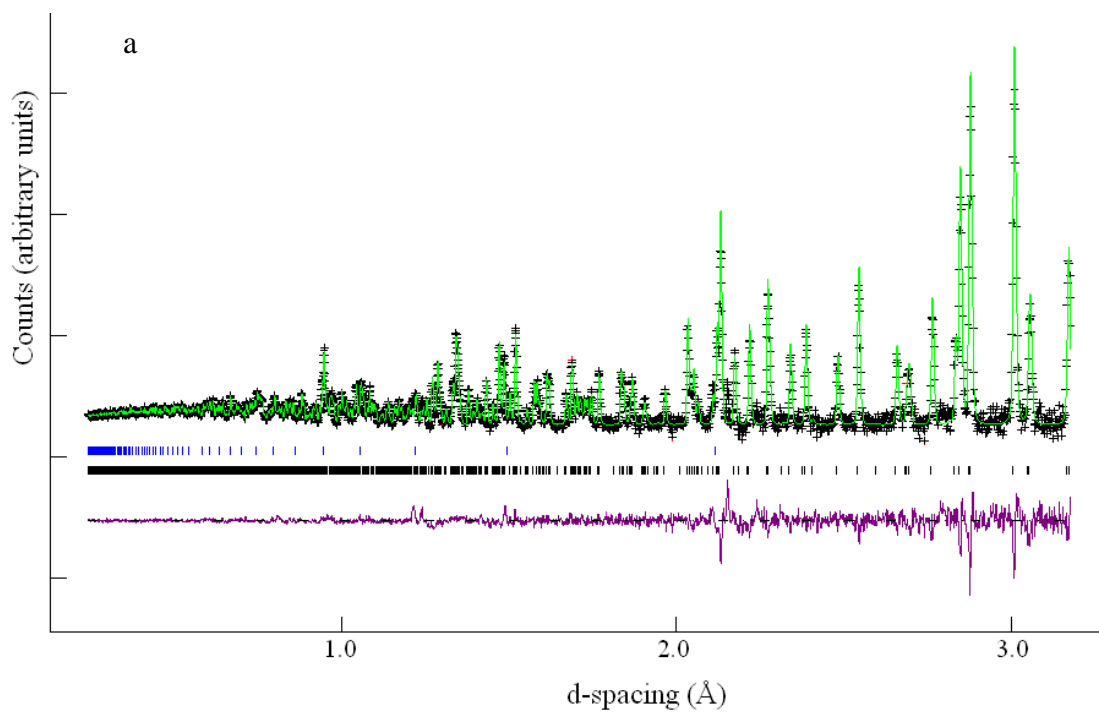


Figure 10.31 Rietveld refinement against neutron diffraction data for $\text{Ba}_2\text{Zn}_{0.5}\text{Mn}_{0.5}\text{S}_3$ from banks 1, 2 and 3 (a, b and c respectively) at room temperature: Black line (observed), green line (calculated) and purple line (difference). Black tick marks correspond to $\text{Ba}_2\text{Zn}_{0.5}\text{Mn}_{0.5}\text{S}_3$ blue to Ba_2SiS_4



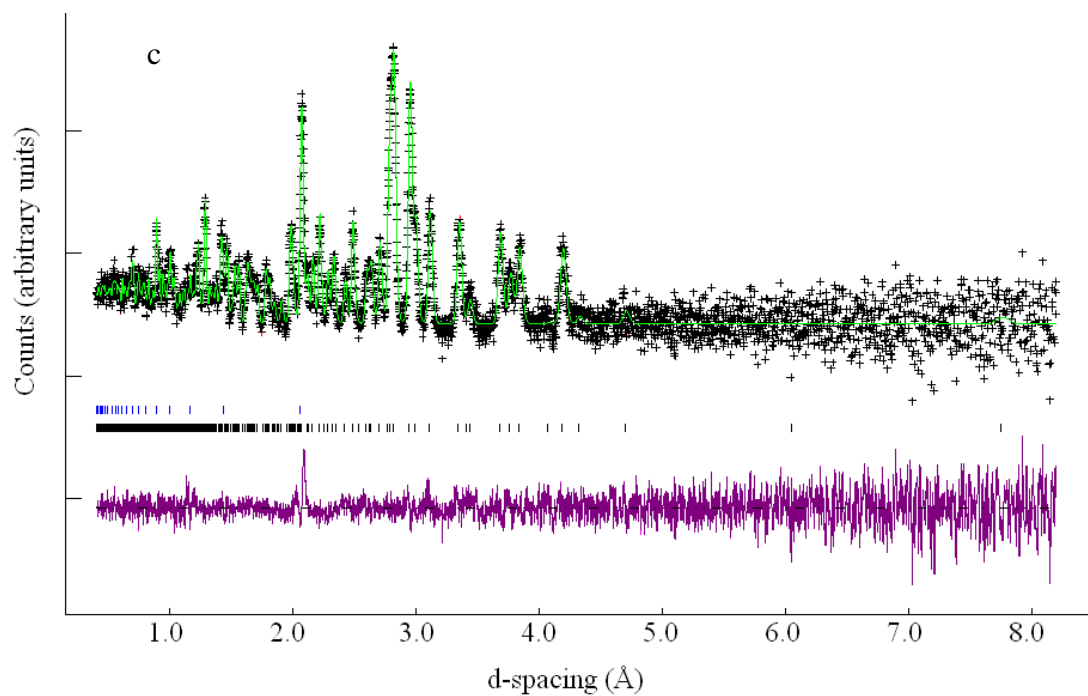
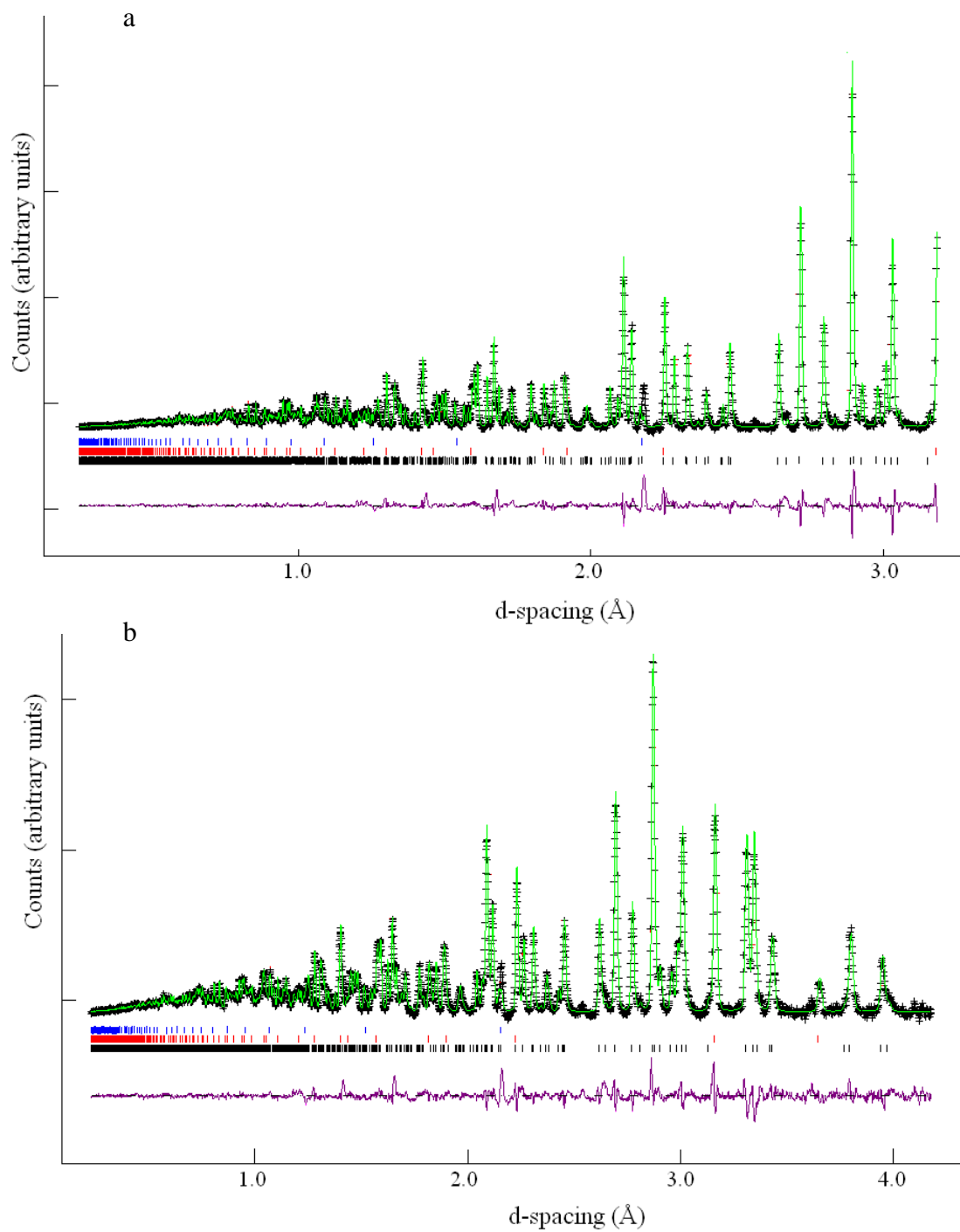


Figure 10.32 Rietveld refinement against neutron diffraction data for $\text{Ba}_2\text{Zn}_{0.5}\text{Mn}_{0.5}\text{S}_3$ from banks 1, 2 and 3 (a, b and c respectively) at 5 K: Black line (observed), green line (calculated) and purple line (difference). Black tick marks correspond to $\text{Ba}_2\text{Zn}_{0.5}\text{Mn}_{0.5}\text{S}_3$ blue to Ba_2Si_4

10.8 Appendix 8



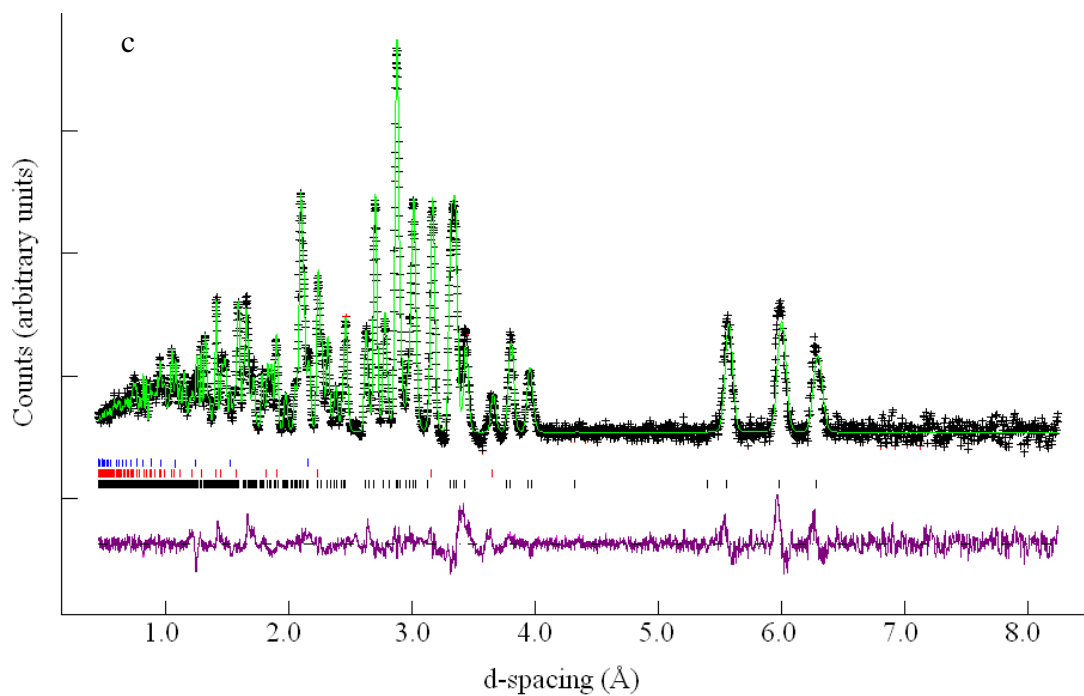
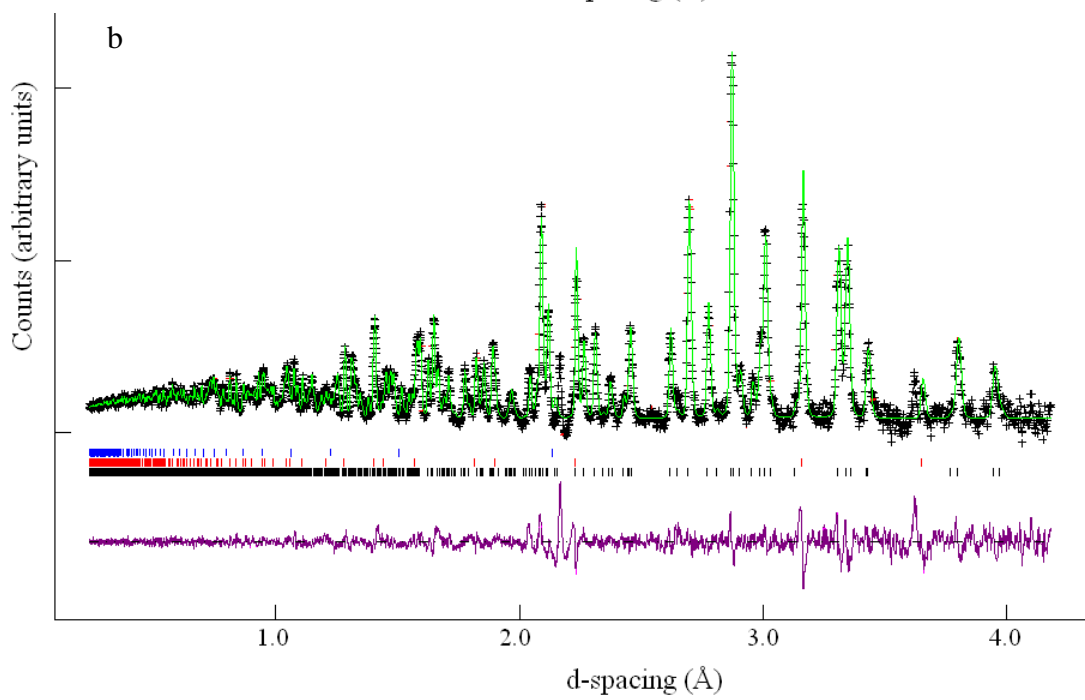
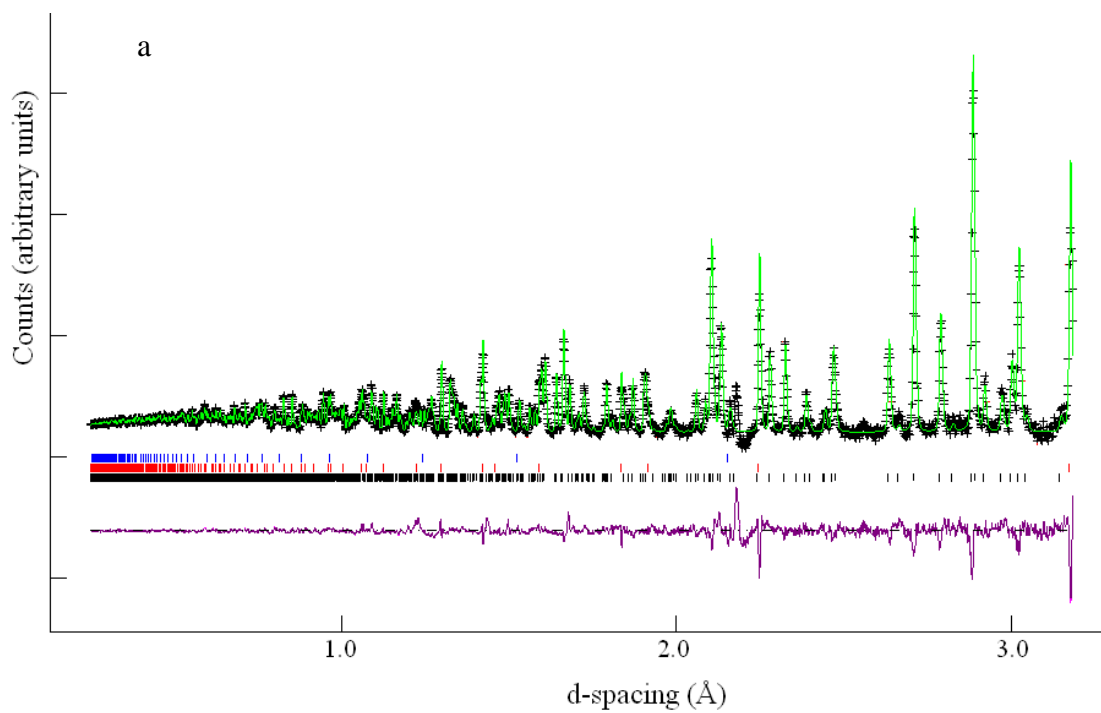


Figure 10.33 Rietveld refinement against neutron diffraction data for $\text{Ba}_2\text{Zn}_{0.75}\text{Cr}_{0.25}\text{S}_3$ from banks 1, 2 and 3 (a, b and c respectively) at room temperature: Black line (observed), green line (calculated) and purple line (difference). Black tick marks correspond to $\text{Ba}_2\text{Zn}_{0.75}\text{Cr}_{0.25}\text{S}_3$ blue to Ba_2Si_4 .



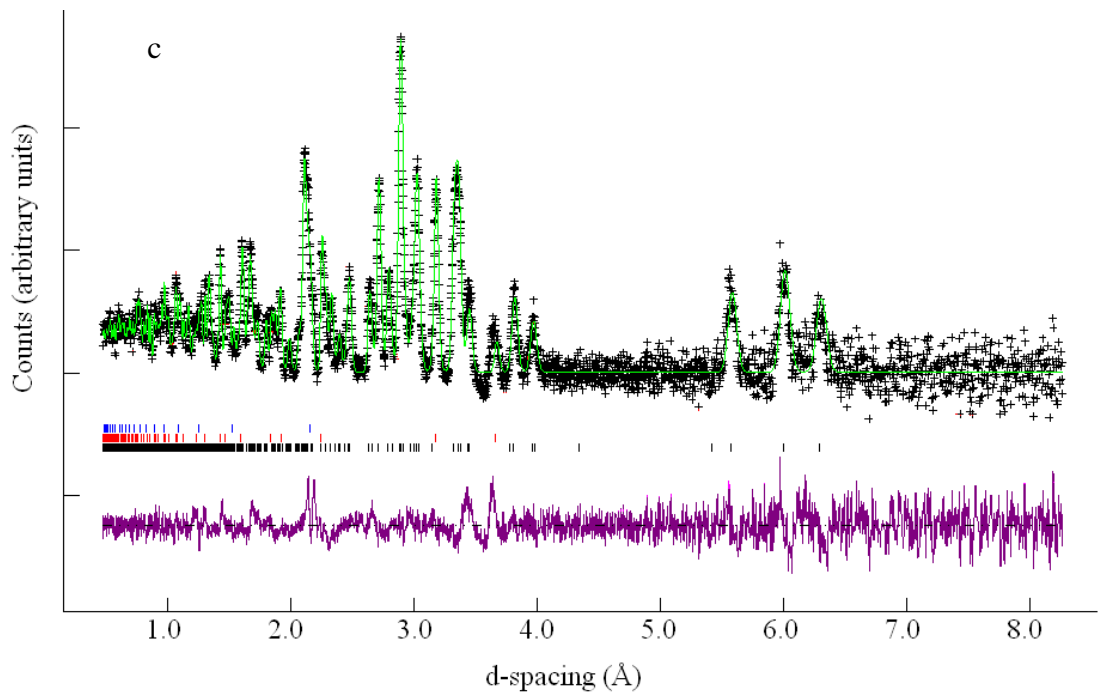
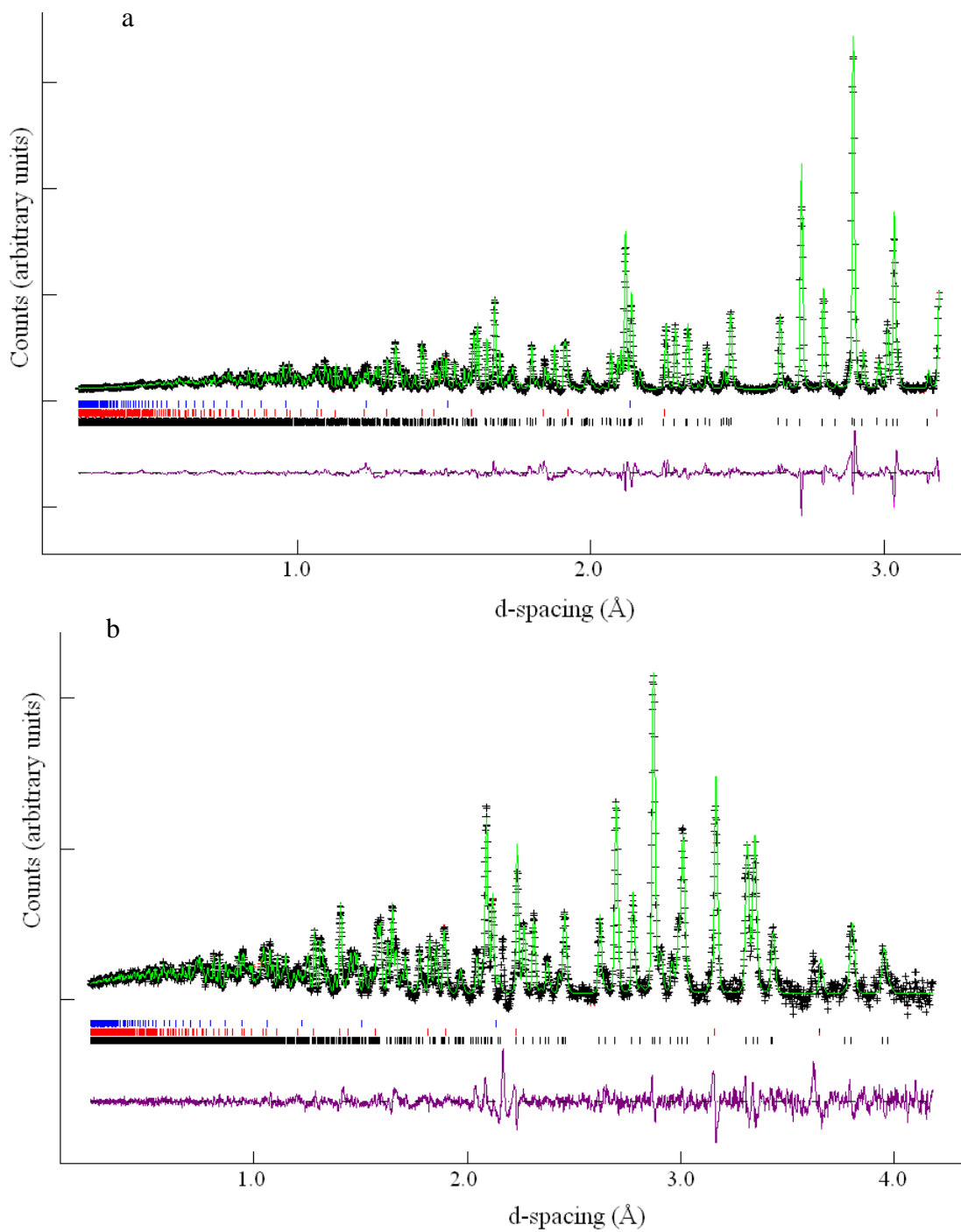


Figure 10.34 Rietveld refinement against neutron diffraction data for $\text{Ba}_2\text{Zn}_{0.75}\text{Cr}_{0.25}\text{S}_3$ from banks 1, 2 and 3 (a, b and c respectively) at 5 K: Black line (observed), green line (calculated) and purple line (difference). Black tick marks correspond to $\text{Ba}_2\text{Zn}_{0.75}\text{Cr}_{0.25}\text{S}_3$ blue to Ba_2SiS_4 .

10.9 Appendix 9



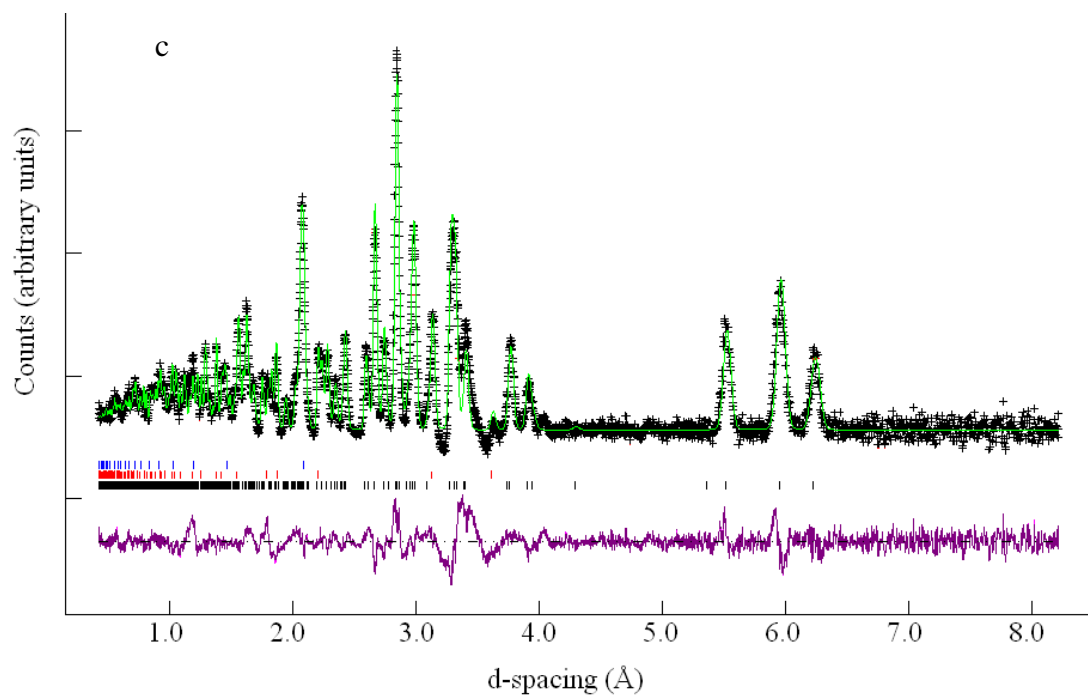


Figure 10.35 Rietveld refinement against neutron diffraction data for $Ba_2Zn_{0.75}Ni_{0.25}S_3$ from banks 1, 2 and 3 (a, b and c respectively) at room temperature: Black line (observed), green line (calculated) and purple line (difference). Black tick marks correspond to Ba_2ZnS_3 blue to Ba_2SiS_4 .

10.10 Appendix 10

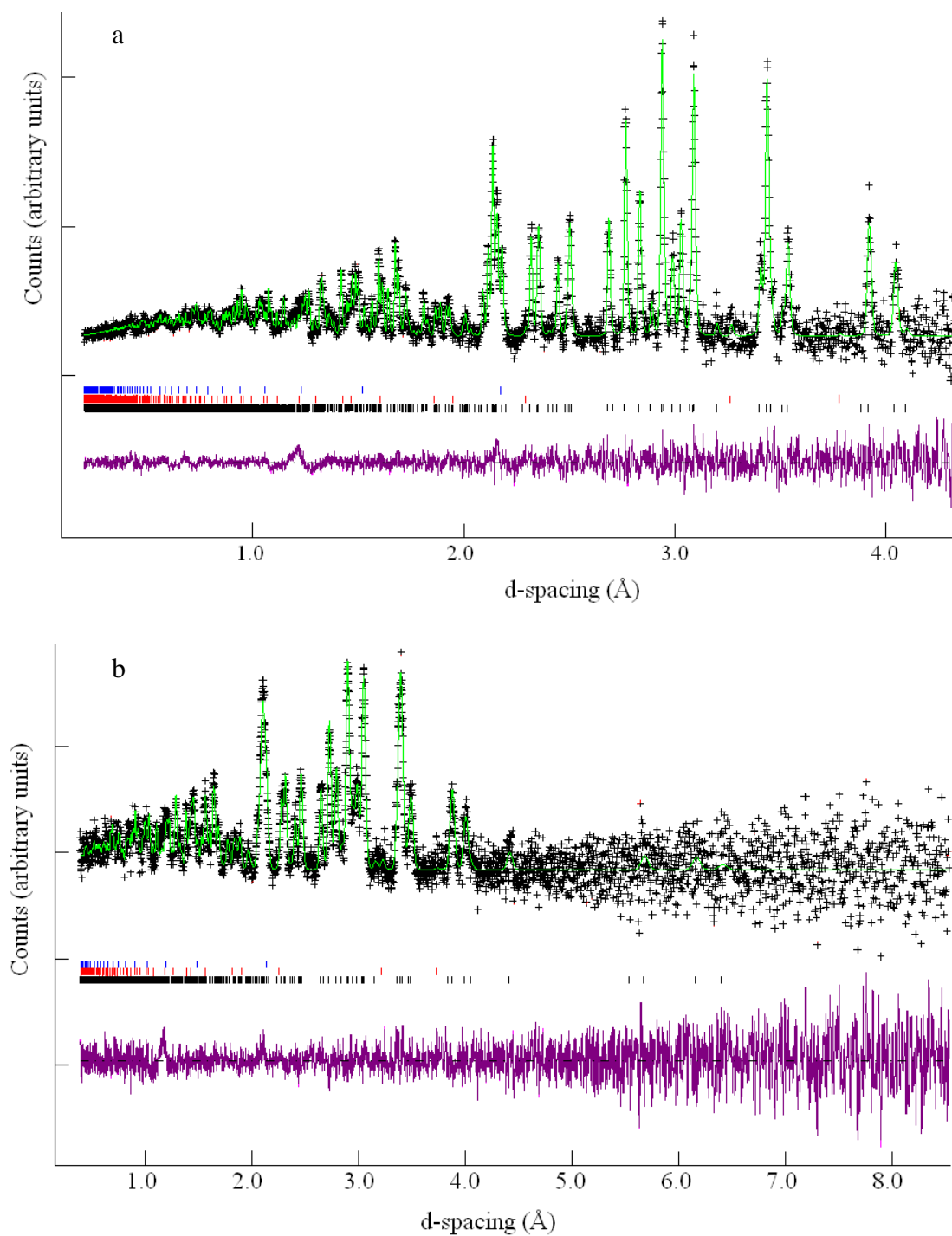


Figure 10.36 Rietveld refinement against neutron diffraction data for $\text{Ba}_{1.9}\text{K}_{0.1}\text{CoS}_3$ from banks 2 and 3 (a and b respectively) at room temperature: Black line (observed), green line (calculated) and purple line (difference). Black tick marks correspond to Ba_2CoS_3 red to BaS and blue to BaS.